EXPERIMENTAL STUDIES OF VISCO-PLASTIC LUBRICATION

by

CHUN KIT HUEN

BASc. (Mechanical Engineering), The University of British Columbia 2003

A THESIS SUBMITTED IN PARTIAL FULFILLMENT OF

THE REQUIREMENTS FOR THE DEGREE OF

MASTER OF APPLIED SCIENCE

in

THE FACULTY OF GRADUATE STUDIES

(MECHANICAL ENGINEERING)

THE UNIVERSITY OF BRITISH COLUMBIA

August 2005

© Chun Kit Huen, 2005

Abstract

A multi-layer flow of two purely viscous fluids is often unstable, at any Reynolds number, however small. The primary instability initiates at the interface through various mechanisms such as the Kelvin-Helmholtz instability. Here we demonstrate how interfacial instabilities of multi-layer flows can be eliminated by introducing a yield stress lubricating fluid. The basic flow geometry is that an inner core fluid flows in the central layer lubricated by a yield stress fluid adjacent to the wall of a pipe. Rheologies of the two fluids are such that the interface between fluid layers is surrounded by an unyielded layer of the lubricating fluid. In this thesis, first we model a typical multi-layer flow in a circular pipe geometry by solving the axisymmetric Navier-Stokes equations. A simple control model is derived for controlling the position of the interface by varying the flow rates of the two fluids. Second we present experimental results of a visco-plastic lubrication flow, where the lubricating fluid is a Carbopol solution and the inner core fluid is a Xanthan solution. After conducting over 100 experiments with 4 different fluid pairs over broad flow rate range, we can unequivocally state that stable multi-layer flows, of the visco-plastic lubrication type, can be achieved in a laboratory setting. The experiments have been designed with the aid of the control model which predicts the boundary between stable and unstable flows. Our experimental results do approximately identify this stability boundary. Results also strongly suggest that it would be possible to control the interfacial radius on-line, via regulation of the individual flow rates, in such flows.

Table of Contents

Abstract ..... **ii**

Table of Contents ..... **iii**

List of Tables ..... **vi**

List of Figures ..... **vii**

Acknowledgements ..... **xii**

Chapter 1. Introduction **1**

1.1 Problem Description 1

1.1.1 Applications 2

1.2 Interfacial Instabilities of a Multi-layer Flow 3

1.2.1 Viscous-viscous Shear Flow Instability 3

1.2.2 Kelvin-Helmholtz Instability 5

1.3 Idea of Visco-Plastic Lubrication 6

1.4 Background literature 6

1.5 Outline of the Thesis 8

Chapter 2. Multi-layer Visco-plastically Lubricated Flows **9**

2.1 Model Derivation 10

2.1.1 Equations of Motion 10

2.1.2 Flow of a Single Hershel-Bulkley Fluid 11

2.1.3 Flow of Two Herschel-Bulkley Fluids 14

2.1.3.1 Stable Visco-plastically Lubricated Case (STABLE) ... 15

2.1.3.2 Unstable Interface Case (UNSTABLE) 17

2.1.3.3 Static wall layer Case (STATIC) 19

2.1.4 Sample Solution with Analytical Model 20

2.2 Numerical Solution 24

2.3 Inverting the Flow Problem 27

Chapter 3. Experimental Apparatus and Fluids **30**

3.1 Multi-layer Flow Loop 30

3.2 Calibration of Apparatus 36
3.2.1 Objectives 36
3.2.2 Pressure Sensors 37
3.2.3 Magnetic Flowmeter and Monyo 332 PC Pump 37
3.2.4 Paddle-wheel Flowmeter and Monyo 1000 PC Pump 38
3.2.5 Cameras and Edge Detection Algorithm 38
3.3 Fluids and Characterizations 41
3.3.1 Fluid Characterizations 41
3.3.2 Carbopol 45
3.3.3 Xanthan Gum 49
3.4 Experiments 52
3.4.1 Classifying a Stable Flow with Spatiotemporal Plots 53
3.4.2 A Typical Experiment 62

Chapter 4. Results 70
4.1 Set 1 Experiment 70
4.2 Set 2 Experiment 72
4.3 Set 3 Experiment 74
4.4 Set 4 Experiment 76
4.5 Discussion of Observations 78
4.5.1 Experimental Observations 78
4.5.2 Stable and Unstable Regions 80
4.5.3 Measurement Errors for R_i 82
4.5.4 Abnormal Behaviours of Pressure Sensors 84

Chapter 5. Discussions and Conclusions 90
5.1 Summary of Principal Results 90
5.2 Discussions 91
5.3 Future Work 91

Bibliography 93

Appendix A. Calibrations for Pressure Sensors 96

Appendix B. Calibration for Magnetic Flowmeter and Monyo 332 PC Pump 97

Appendix C. Calibration for Paddle-wheel Flowmeter and Monyo 1000 PC Pump 98

Appendix D. Calibrations for Video Cameras 99

Appendix E. Flow Rate Plots for the Typical Experiment 101

Appendix F. Set 1 Experimental Data Table 102

Appendix G. Set 2 Experimental Data Table 105

Appendix H. Set 3 Experimental Data Table 107

Appendix I. Set 4 Experimental Data Table 109

Appendix J. Various Plots of Set 1 Experiments 111

Appendix K. Various Plots of Set 2 Experiments 114

Appendix L. Various Plots of Set 3 Experiments 117

Appendix M. Various Plots of Set 4 Experiments 120

Appendix N. Specifications of Monyo 332 Progressive Cavity Pump 123

Appendix O. Specifications of Monyo 1000 Progressive Cavity Pump 128

Appendix P. Top Pressure Sensor: EW-68075-40
Bottom Pressure Sensor: EW-68075-42 137

Appendix Q. Specifications of Magnetic Floweter FMG 423H 139

Appendix R. Specifications of Paddle Wheel Flowmeter DRG-1150N1F300 142

Appendix S. Specifications of Data Acquisition System 147

Appendix T. Rheology of a 0.3% Xanthan NF-C Solution 163

Appendix U. Model Utility Test for Set 1 Experiments 169

Appendix V. Model Utility Test for Set 2 Experiments 170

Appendix W. Model Utility Test for Set 3 Experiments 171

Appendix X. Model Utility Test for Set 4 Experiments 172

List of Tables

3.1 Parts descriptions of Figure 3.1 and 3.2 31
3.2 Properties of Carbopol 940 solutions of different concentrations at $T = 22^{o}C$. (Unit of yield stress is Pa and unit of consistency is $Pa \cdot s^{n}$) 47
3.3 Properties of Xanthan NF-C solution of different concentrations. $T = 22^{o}C$. (Unit of yield stress is Pa and unit of consistency is $Pa \cdot s^{n}$) 50
3.4 Factorial design of our experimental plan with 2 concentrations of each inner core fluid and lubricating fluid 53
3.5 Summary of the typical experiment 68

List of Figures

1.1 Schematic of a Poiseuille flow of two Bingham fluids. Velocity profile of the flow when both fluids are partially yielded is drawn 1

1.2 An axisymmetric Poiseuille flow of two iso-density immiscible fluids. Interface between fluid layers is at $y = 0$. More viscous fluid domain is in $y > 0$ while the less viscous fluid domain is in $y < 0$ 4

1.3 A Poiseuille flow of two iso-density immiscible fluids with a disturbed interface..... 4

1.4 Occurrence of the Kelvin-Helmholtz instability..... 5

2.1 (a) Inner core fluid surrounded by a yield stress lubricating fluid flowing in a pipe, (b) cross section of the pipe where the center region corresponds to the inner core fluid, and the outer region corresponds to the outer lubricating fluid, (c) desired velocity profile (inner core fluid surrounded by an unyielded plug region of the outer fluid) 10

2.2 Velocity profile of one single Herschel-Bulkley fluid in a circular pipe with radius R 14

2.3 Velocity profile of a stable visco-plastically lubricated case (STABLE). Inner fluid is surrounded by an un-yielded plug region of the outer fluid..... 17

2.4 Velocity profile of an unstable interface case (UNSTABLE). The lubricating fluid is completely yielded 18

2.5 Velocity profile of a static wall layer case (STATIC). The lubricating fluid is completely unyielded 20

2.6 Flow curve of a 0.3% Xanthan NF-C solution. Data points are fitted using MatLab nonlinear least-squares curve fitting function. $T = 22^{\circ}C$..... 21

2.7 Flow curve of a 0.3% Carbopol 940 solution (pH 5.0). Data points are fitted using MatLab nonlinear least-squares curve fitting function. $T = 22^{\circ}C$..... 21

2.8 Plot of analytically calculated flow rate of the inner core fluid with respect to the pressure gradient and interfacial radius. Inner core fluid is 0.3% Xanthan NF-C solution and lubricating fluid is 0.3% Carbopol 940 solution (pH 5.0) 22

2.9 Plot of analytically calculated flow rate of the lubricating fluid with respect

to the pressure gradient and interfacial radius. Inner core fluid is 0.3% Xanthan NF-C solution and lubricating fluid is 0.3% Carbopol 940 solution (pH 5.0) 22

2.10 Contours of analytically calculated Q_1 and Q_2 with respect to the pressure gradient and interfacial radius. Inner core fluid is 0.3% Xanthan NF-C solution and lubricating fluid is 0.3% Carbopol 940 solution (pH 5.0) 23

2.11 Plot of numerically calculated flow rate of the inner core fluid with respect to the pressure gradient and interfacial radius. Inner core fluid is 0.3% Xanthan NF-C solution and lubricating fluid is 0.3% Carbopol 940 solution (pH 5.0).. 25

2.12 Plot of numerically calculated flow rate of the lubricating fluid with respect to the pressure gradient and interfacial radius. Inner core fluid is 0.3% Xanthan NF-C solution and lubricating fluid is 0.3% Carbopol 940 solution (pH 5.0).. 26

2.13 Contours of numerically calculated Q_1 and Q_2 with respect to the pressure gradient and interfacial radius. Inner core fluid is 0.3% Xanthan NF-C solution and lubricating fluid is 0.3% Carbopol 940 solution (pH 5.0) 26

2.14 Inverted plot of interfacial radius with respect to flow rates of the inner core fluid and lubricating fluid. Inner core fluid is 0.3% Xanthan NF-C solution and the lubricating fluid is 0.3% Carbopol 940 solution (pH 5.0) 28

2.15 Inverted plot of pressure gradient with respect to flow rates of the inner core fluid and lubricating fluid. Inner core fluid is 0.3% Xanthan NF-C solution and the lubricating fluid is 0.3% Carbopol 940 solution (pH 5.0) 29

2.16 Contours of interfacial radius with respect to flow rates of both inner core fluid and lubricating fluid. Inner core fluid is 0.3% Xanthan NF-C solution and the lubricating fluid is 0.3% Carbopol 940 solution (pH 5.0) 29

3.1 Schematic of the multi-layer flow loop at UBC 31

3.2 A 4-meter multi-layer flow loop constructed at UBC 32

3.3 The exit manifold of the flow loop 33

3.4 Positions of the two pressure sensors 34

3.5 (a) Manifold at the bottom of the flow loop (b) Sectional view of the manifold (diagram is not to scale) 35

3.6 Pixel value versus distance from center of pipe 40

3.7 (a) A picture of a developing multi-layer flow. The interface is not perfectly straight and the flow consists of a small puff of the inner core fluid. The actual axial length of the image is 0.18 m. (b) The image reconstructed using our MatLab edge detection algorithm 41

3.8 Instantaneous viscosity curve of a 0.3% Carbopol 940 solution. The yield stress of the fluid corresponds to the maximum value of the viscosity curve, i.e. approximately 15 Pa 43
3.9 Creep test of a 0.3% Carbopol 940 solution at pH 5.0. Yield stress occurs at approximately 13 Pa 45
3.10 Flow curve of a 0.3% Carbopol 940 solution at pH 5.0. $T = 22$ °C. Data points are fitted using MatLab nonlinear least-squares curve fitting function 48
3.11 Flow curve of a 0.5% Carbopol 940 solution at pH = 5.0. $T = 22$°C. Data points are fitted using MatLab nonlinear least-squares curve fitting function . 48
3.12 Flow curve of 0.3% Xanthan NF-C solution. Test is done once every week for 6 weeks to show its thixtropic characteristics. $T = 22$°C..... 50
3.13 Flow curve of a 0.3% Xanthan NF-C solution. $T = 22$°C. Data points are fitted using MatLab nonlinear least-squares curve fitting function 51
3.14 Flow curve of a 0.5% Xanthan NF-C solution. $T = 22$°C. Data points are fitted using MatLab nonlinear least-squares curve fitting function 51
3.15 Flow is classified as unstable if corkscrew flow pattern is observed. Inner core fluid is water and lubricating fluid is 0.3% Carbopol 940 at pH 5.0. Q_1 = 15 ml/s and Q_2 = 10 ml/s..... 54
3.16 Spatiotemporal plot of a stable multi-layer flow experiment. Inner core and lubricating fluids are 0.3% Xanthan solution and 0.3% Carbopol solution at pH 5.00. Q_1 = 5 ml/s and Q_2 = 10 ml/s 56
3.17 Snap shots of a stable multi-layer flow experiment. Inner core and lubricating fluids are 0.3% Xanthan solution and 0.3% Carbopol solution (pH 5.00). Q_1 = 5 ml/s and Q_2 = 10 ml/s..... 57
3.18 Snap shots of a stable experiment. Inner core fluid is 0.3% Xanthan solution and lubricating fluid is 0.3% Carbopol solution at pH 5.0. Q_1 = 15 ml/s and Q_2 = 15 ml/s. Flow is disturbed artificially by squeezing the inner core fluid connection pipe. (a) t = 30s, (b) t = 35s, (c) t = 40.5s, (d) t = 43s, (e) t = 46s. (f) Spatiotemporal plot of the flow. Letters below indicate corresponding time for each of the images in (a) – (e). L = 0.18 m and T_f = 15 59
3.19 Snap shots of an unstable experiment. Inner core and lubricating fluids are 0.3% Xanthan solution and 0.3% Carbopol solution at pH 5.0. Q_1 = 25 ml/s and Q_2 = 25 ml/s. (a) t = 67 s, (b) t = 71 s, (c) t = 75 s, (d) t = 79 s, (e) t = 82 s. (f) Spatiotemporal plot of the flow. Letters below indicate corresponding time for each of the images in (a) – (e). L = 0.18 m and T_f = 15 s..... 61

3.20 Snap shots of the typical experiment discussed in section 4.1. The actual length of the snap shots is 2.2 m 63
3.21 Close-up snap shots of the typical experiment discussed in section 4.1. Camera is focusing at 0.5 m above the manifold and capturing 0.18 m of images..... 64
3.22 Spatiotemporal plot of the typical experiment discussed in section 3.4.2. The inner core fluid enters the video capture region at $t/T_f = 0.5$ s 65
3.23 Spatiotemporal plot of the experiment discussed in section 3.4.2. The flow is stable and irregularities of the interface travel at the interfacial velocity..... 66
3.24 Spatiotemporal plot of the stable experiment discussed in section 3.4.2..... 66
3.25 (a) A close up snap shot of the flow loop after the flow becomes fully developed. The actual axial length of the image is 0.18 m. The flow is stable and the image is used to measure the width of the inner core fluid. (b) A black and white image created with a Matlab code for determining the width of the inner core fluid 68

4.1 (a) Set 1 experimental observations plotted with respect to flow rates of the two fluids. Stable: 'O', unstable 1: 'Δ', and unstable 2: 'x'. Predicted transition region is shaded with grey. (b) Measured R_i versus calculated R_i 71
4.2 (a) Set 2 experimental observations plotted with respect to flow rates of the two fluids. Stable: 'O', unstable 1: 'Δ', and unstable 2: 'x'. Predicted transition region is shaded with grey. (b) Measured R_i versus calculated R_i 73
4.3 (a) Set 3 experimental observations plotted with respect to flow rates of the two fluids. Stable flows are marked with 'o' and no unstable flows were observed. Predicted transition region is shaded with grey. (b) Measured R_i versus calculated R_i. 75
4.4 (a) Set 4 experimental observations plotted with respect to flow rates of the two fluids. Stable: 'O', unstable 1: 'Δ', and unstable 2: 'x'. Predicted transition region is shaded with grey. (b) Measured R_i versus calculated R_i. ... 77
4.5 Snap shots of an unstable experiment. The inner core fluid is 0.3% Xanthan NF-C solution and the lubricating fluid is 0.3% Carbopol 940 solution at pH 5.0. Q_1 = 15 ml/s and Q_2 = 25 ml/s. 80
4.6 Pressure readings from bottom sensors during Set 1 Test 17 84
4.7 Pressure gradient along the pipe during Set 1 Test 17 85
4.8 Pressure measurements from sensors. Test fluid was water. Steady measurement was achieved as soon as the water column reached the top of the loop at t = 300s 87

4.9 Pressure gradient calculated from Figure 4.8 87
4.10 Pressure measurements from sensors. Test fluid was 0.3% Carbopol 940 solution (pH 5.0) 88
4.11 Pressure gradient calculated from Figure 4.10 88
4.12 Schematics drawing of a typical pressure sensor 89

Acknowledgements

This project has been financially supported by B.C. Advanced System Institute, the Canada foundation for Innovation and NSERC Canada.

I would like to thank many individuals that had helped in the completion of this thesis. My supervisors, Dr. Ian Frigaard and Dr. Mark Martinez have shown constant encouragement and provided invaluable guidance throughout.

I wish to thank my family for encouraging me to pursue my dreams and continue onto my academic career.

Chapter 1

Introduction

1.1 Problem Description

A Poiseuille, pressure driven, multi-layer flow of two iso-density immiscible fluids in a circular pipe is studied experimentally. This thesis concerns the non-linear stability of the interface between the two fluid layers. The primary objective is to prove that the visco-plastic lubrication flows in [3, 7] can be achieved in a laboratory setting. The secondary objective is to observe whether the position of the interface between fluid layers is controllable. Our basic flow is an axisymmetric flow in which a generalized Newtonian fluid is flowing in the center, fully surrounded and lubricated by a yield stress fluid adjacent to the wall of the pipe. Flow rates and rheologies of the two fluids are such that the lubricating fluid remains unyielded at the interface as illustrated in Figure 1.1.

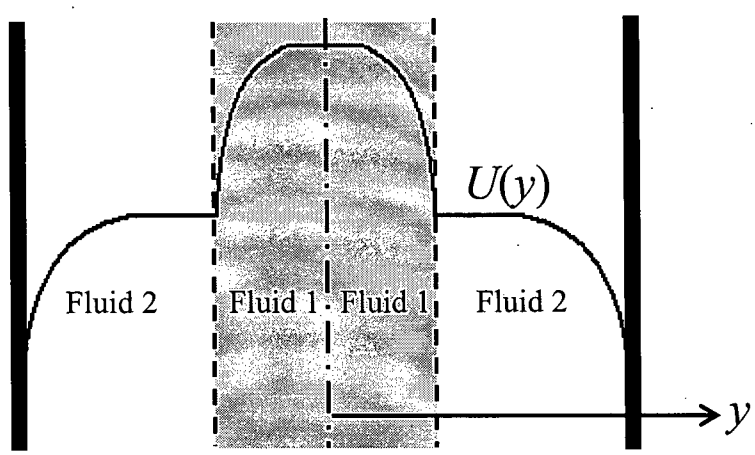

Figure 1.1: Schematic of a Poiseuille flow of two Bingham fluids. Velocity profile of the flow when both fluids are partially yielded is drawn.

1.1.1 Applications

A primary motivation for studying instabilities of multi-layer shear flows is their industrial relevance. Two potential application areas are co-extrusion processes and lubricated pipelining.

- **Co-extrusion processes**: Co-extrusion processes are widely used in the plastics and metal industries to manufacture bi-layer and multi-layer films, sheets, and pipes, conjugate fibers and concentric coatings of two or more polymers in the fiber industry. The principle advantage for employing co-extrusion processes is the ability to create composite materials with tailor-made properties. The fundamental process of a co-extrusion operation is to combine multiple melt streams in a feed block which directs all flows to a die where the layers take their final dimensions. In co-extrusion operations the rate of production is limited by flow instabilities and especially interfacial instabilities between adjacent layers. These instabilities could result in slow production rates and defected products. The ability to maintain multi-layer flows stable at low or moderate Reynolds numbers certainly allows one to manufacture better products at an improved production rate.

- **Lubricated pipelining**: There is a strong tendency for two immiscible iso-density fluids to arrange themselves so that the low-viscosity constituent is in the region of high shear, i.e. typically closest to the wall in a duct flow. We can imagine that it is possible to introduce a beneficial effect in any flow of a very viscous fluid by introducing small amounts of a lubricating fluid. For example transportation of heavy crude oils. Viscosities of crude oils can be as high as 1000 poise at room temperature and cannot be transported by usual pipeline methods due to the fact that fiction at the pipe wall accumulates and tremendous motor power would be needed. One may reduce the viscosity of the oil either through the addition of hydrocarbon diluent or through the installation of heating equipment at short intervals along the pipeline. Unfortunately both solutions are inconvenient and costly. A possible solution is to introduce a much less viscous immiscible fluid, for example water, into the flow and let it migrate to the high shear region. Work required to transport the oil would then be reduced significantly. Similar methods are used in coal-water slurry transport.

Common needs for both applications just mentioned are to maintain a stable interface between the fluid layers and be able to control the configuration of the flow. The instabilities at the interfaces and their onsets limit the rate of production and transport. Thus, before we can truly utilize the benefits of a stable multi-layer flow in an industrial process, we must understand how to eliminate any interfacial instability and determine where the two fluids will be.

1.2 Interfacial Instabilities of a Multi-layer Flow

Linear stability analyses have identified three main types of instability. Two of them, a long-wavelength instability [11, 23] and a short-wavelength instability [14], are low-Reynolds-number and arise from the interfaces between fluid layers. The third type of instability arises from a "wall mode" [13], and corresponds to the classical instability of shear flows. It occurs at high shear rates, with a wavelength of the order of the thickness of the fluid layers [21]. Interfacial instability is most relevant to this thesis and we will overview some interfacial instability mechanisms in this section.

1.2.1 Viscous-viscous Shear Flow Instability

Consider an infinite axisymmetric Poiseuille flow of two iso-density immiscible fluids in $y > 0$ and $y < 0$ with respective viscosities μ_+ and μ_- as shown in Figure 1.2. The rheologies of the two fluids are such that the top fluid is always more viscous than the bottom fluid, i.e. $\mu_+ > \mu_-$. With no perturbation shear stress and velocities of the two fluids are continuous at the interface.

Now consider the flow is perturbed by displacing the interface with a small amplitude wave from $y = 0$ to $y = \eta(x) = \eta_0\cos(kx)$ as shown in Figure 1.3. At the peak of the disturbed interface, A, the undisturbed velocity of the less viscous fluid is slower than that of the more viscous fluid. Thus for the velocities of the two fluids remain continuous at the interface, the more viscous fluid must slow down at the disturbed interface while the less viscous fluid must speed up relatively. In contrast, at trough B the more viscous fluid must speed up while the less viscous fluid must slow down for the continuity condition to remain valid. The adjustments of the horizontal velocity can be considered as disturbance velocities. These disturbance velocities are maximum at the disturbed interface and decay away into the interior of the fluids. The disturbance velocities may also be interpreted as

disturbance vorticities, i.e. counter clockwise vorticities are expected at peak A while clockwise vorticities are expected at trough B. These vorticities magnify the amplitude of the disturbance on the interface and lead the entire flow into an unstable flow. This is the classical viscous-viscous flow instability.

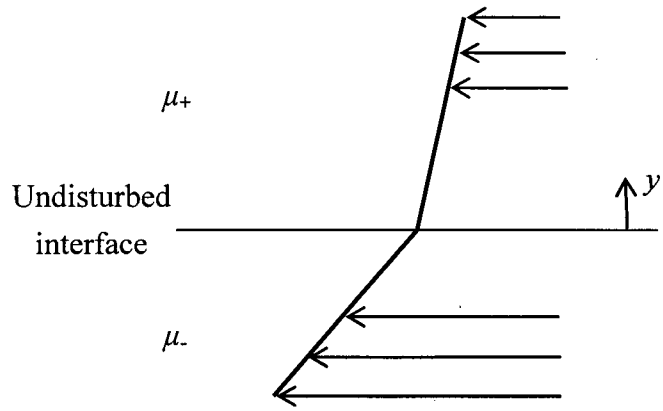

Figure 1.2: An axisymmetric Poiseuille flow of two iso-density immiscible fluids. Interface between fluid layers is at $y = 0$. More viscous fluid domain is in $y > 0$ while the less viscous fluid domain is in $y < 0$.

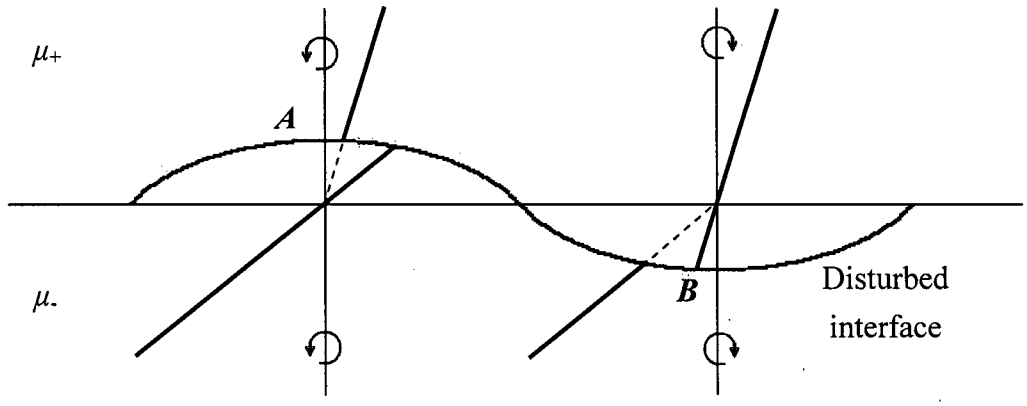

Figure 1.3: A Poiseuille flow of two iso-density immiscible fluids with a disturbed interface.

1.2.2 Kelvin-Helmholtz Instability

Another well studied phenomenon is called the Kelvin-Helmholtz instability. Again, consider an axisymmetric Poiseuille flow of two iso-density immiscible fluids in $y > 0$ and $y < 0$ with respective mean velocities U_+ and U_- as shown in Figure 1.4. In contrast to the viscous-viscous shear flow instability, the Kelvin-Helmholtz instability does not arise from the viscosity difference, but instead the velocity difference of the two fluids. The flow experiences a sharp velocity change at the interface between the fluid layers, i.e. velocities are not continuous at the interface. Now again consider the flow is perturbed by displacing the interface with a small amplitude wave from $y = 0$ to $y = \eta(x) = \eta_0\cos(kx)$. The flow in concavities is slower than the flow in convexities causing a pressure difference at both the peak and trough of the interface. The pressure difference amplifies the amplitude of the perturbation and the upper part of the interface is now carried by the faster fluid while the lower part is dragged by the slower fluid. Very quickly the interface is rolled up and a mixing layer is observed.

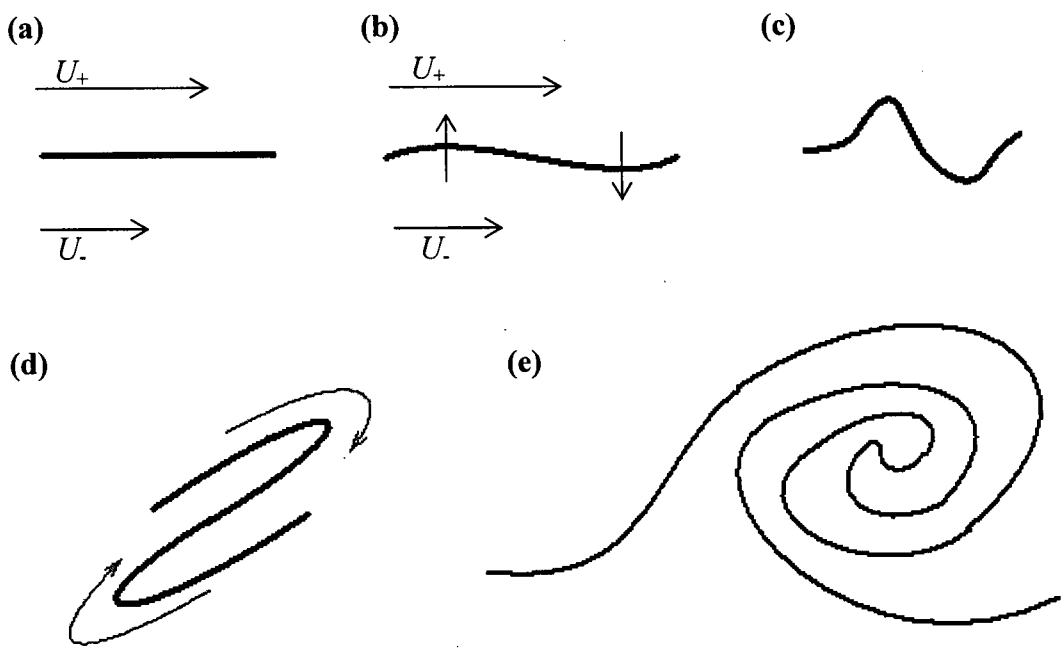

Figure 1.4: Occurrence of the Kelvin-Helmholtz instability.

1.3 Idea of Visco-Plastic Lubrication

The idea of visco-plastic lubrication was first discussed by Frigaard in 2001 [3]. In summary, consider an axisymmetric Poiseuille flow in a channel or a pipe with two Bingham fluids that behave as elastic solids while the apply stress is lower than their critical yield stresses. The flow configuration is a three-layer flow, with a central fluid 1 lubricated by two layers of fluid 2 at the wall as shown in Figure 1.1. Now consider the shear stress in the pipe is not sufficient to yield the lubricating fluid completely, i.e. the interface is surrounded by an unyielded, or plug, region of the lubricating fluid. Since a yield stress fluid has elastic solid behaviour under yield point, apparently the central fluid is flowing inside a moving elastic pipe that is made of the lubricating fluid. The interface is no longer a fluid-fluid interface, but instead a fluid-solid interface, i.e. perturbations on the interface are suppressed by the solid behaviour of the lubricating fluid, and even if the interface is perturbed, the amplitude of perturbation is not going to be amplified by the two instability mechanisms discussed in the previous section. Thus, interfacial instabilities are wholly eliminated.

1.4 Background Literature

There have been a number of studies of interfacial instabilities of multi-layer flows. The three fundamental systems that have been studied are gravity-driven flows such as multi-layer films on an inclines plane, shear-driven flows such as plane Couette flow, and pressure-drive flows such as core-annular [15] and plane Poiseuille flows [16, 19, 20, 22]. The earliest theoretical investigation of instability due to viscosity stratification is probably the classical study of Yih [23]. Stability of two superposed fluids of different viscosities in plane Couette and Poiseuille flows was studied, using an asymptotic method based on long wavelengths. His study shows that for iso-density fluids the flow can be unstable at any Reynolds number, however small. Various aspects of this problem for multi-layer Couette, Poiseuille, and Couette-Poiseuille flows of Newtonian fluids have been studied, e.g. [9, 13, 22], and a fairly extensive review is given in [18]. In summary the linear stability of immiscible iso-density flows requires a sufficiently large surface tension and that the lubricating fluid is less viscous. The latter case suppresses long wave length instabilities, while large surface tension tends to stabilize short wave length instabilities. Explanations of physical mechanisms that govern these interfacial

instabilities are given in [10].

The axisymmetric flow that we consider corresponds to what is known as perfect core annular flow (PCAF). PCAF has been extensively studied and general reviews are given in [15, 18]. Hickox [9] studied the linear stability of PCAF with Yih's long wavelength method and concluded that no situations were encountered where the primary flow was stable to asymmetric and axisymmetric disturbances, simultaneously. Therefore, parallel flows and countercurrent flows are always unstable in the sense that any small perturbations to the flow will grow with time at an exponential rate regardless of the size of the Reynolds number.

Pinarbasi and Liakopoulos [20] performed a linear stability analysis of the interface between two inelastic non-Newtonian fluid layers in a Poiseuille flow in a straight channel. Both Bingham-like and Carreau-Yasuda fluids were considered. Their works have shown that it is possible to stabilize the fluid-fluid interface for intermediate and large wave numbers by replacing the bottom Newtonian fluid with a visco-plastic fluid. However, Pinarbasi and Liakopoulos do not model a true Binham fluid with a yield stress. Instead they choose a form of regularized velocity model in which the effective viscosity attains a Newtonian limit of high viscosity at zero shear rate. Therefore the results in [20] are best interpreted as effects of having a nonlinearly viscous fluid and are qualitatively similar to those found for the corresponding Newtonian fluid flows.

In this thesis we will use a Herschel-Bulkley fluid in place of a purely viscous lubricating fluid. Frigaard [3] uses a visco-plastic fluid as the lubricating fluid in the study of a three-layer plane Poiseuille flow. The fluids are immiscible with no stabilising surface tension. His work has shown that interfacial instabilities can be wholly eliminated by surrounding the interface between fluid layers by an unyielded region of the lubricating fluid. Comparini and Mannucci [2] have considered the reverse of our flow configuration, i.e. lubricating a Bingham fluid with a Newtonian fluid. Although their flow configuration is completely opposite and therefore his results are not directly applicable, their work has proven that the interface between the yielded Bingham fluid and Newtonian fluid would still suffer from the classical interfacial instabilities.

Recent experiments by Gabard [6] are interesting in the sense that the flow configuration is very similar to the basic flow we will consider in this thesis. The influence of rheology on the miscible displacement of a viscous fluid by a less viscous, Newtonian one in a

vertical (non-capillary) tube is studied experimentally as a function of the flow velocity. He considers the transient residual film thickness of the Newtonian displaced fluids, and concludes from experimental results that the film thickness is as high as 38% of the tube radius at large viscosity ratios between the two fluids in agreement with numerical results. Gabard displaces aqueous solutions of both Xanthan and Carbopol with a less viscous glycerol solution along a long vertical tube. The Xanthan solutions are Carreau-like with a very high viscosity at low shear rate while the Carbopol solutions exhibit a true yield stress. The viscosity and flow rates of the glycerol solutions are such that the displacement is incomplete. A thick layer of fluid 2 is left behind on the walls of the tube directly after the initial displacement in each case. The glycerol solution is pumped past the wall layers for sufficient long time after the displacement front has passed. The Xanthan solutions were observed to become unstable slowly while the Carbopol solutions remained stable. Gabard's work has proved that the yield stress of the displaced fluid is able to stabilize the interface between fluid layers. In this thesis we will focus mainly on the case when the lubricating fluid does not remain static.

In this thesis we consider a parallel multi-layer flow of two Herschel-Bulkley fluids experimentally; where the lubricating fluid must exhibit a true yield stress while the central fluid not necessary has a yield stress. We show that the flow is stable for sufficiently small Reynolds number.

1.5 Outline of the Thesis

In Chapter 2 we first introduce the axisymmetric basic flow that consists of an inner core fluid and a lubricating fluid. Then we solve the basic flow analytically and numerically, and predict flow to be stable or unstable with respect to the flow rates of the two fluids. The experimental flow loop that is built to carry out the study experimentally will be discussed in Chapter 3. We will discuss components of the flow loop and calibration processes for all measuring equipments. Experimental plans will also be discussed. In Chapter 4, results of 120 experiments are summarized and presented. Chapter 5 concludes this thesis with a discussion of the experimental results, conclusions and future work recommended.

Chapter 2

Multi-layer Visco-plastically Lubricated Flows

In [1, 3, 7, 8] where 2- and 3-dimensional stability of a multi-layer flow is studied, analytically and numerically, a 3-dimensional model of the flow is required. However for experimental design, we need only a simple 1-dimensional hydraulic model that will be derived in this chapter. We focus on the case where the pipe cross-section is separated into two distinct fluid domains, with the outer lubricating fluid providing a lubricating layer for the inner core fluid, i.e. the cross-sectional domain occupied by the inner core fluid is completely surrounded by the lubricating fluid, which abuts the wall of the pipe as shown in Figure 2.1. We consider a pipe with radius R and a finite length L. It is assumed that both fluids have the same density ρ and surface tension is neglected. We model the basic flow by assuming both fluids have a rheological behaviour characterized by the Herschel-Bulkley model, and the inner core fluid always has a yield stress smaller than that of the lubricating fluid. The inner core fluid is characterized by its yield stress τ_{y1}, consistency κ_1, and power index n_1. Similarly, the outer lubricating fluid is characterized by the three parameters τ_{y2}, κ_2, and n_2.

$$\text{Herschel-Bulkey Model}\begin{cases} \text{Inner Core Fluid 1:} \quad \tau_1 = \tau_{y1} + \kappa_1 \cdot \dot{\gamma}^{n_1} & (2.1) \\ \text{Lubricating Fluid 2:} \quad \tau_2 = \tau_{y2} + \kappa_2 \cdot \dot{\gamma}^{n_2} & (2.2) \end{cases}$$

where:

τ_k = shear stress in fluid k, $k = 1, 2$
$\dot{\gamma}$ = resultant shear rate of the fluid

In this chapter we first study the flow problem by solving the hydraulics model analytically and numerically. By doing so, we are able to understand how flow rates of the two fluids behave with respect to the primary independent parameters such as the

pressure gradient along the pipe and the interfacial radius, i.e. we solve the flow problem $Q_1 = \mathbf{f_1}(R_i, |\partial P / \partial z|)$ and $Q_2 = \mathbf{f_2}(R_i, |\partial P / \partial z|)$. Then, for experimental design since we can control merely the flow rates of the two fluids, Q_1 and Q_2, we invert the results obtained and study the resultant interfacial radius and the pressure gradient for a given pair of Q_1 and Q_2, i.e. we solve the problem in the reverse direction for $R_i = \mathbf{g_1}(Q_1, Q_2)$ and $|\partial P / \partial z| = \mathbf{g_2}(Q_1, Q_2)$.

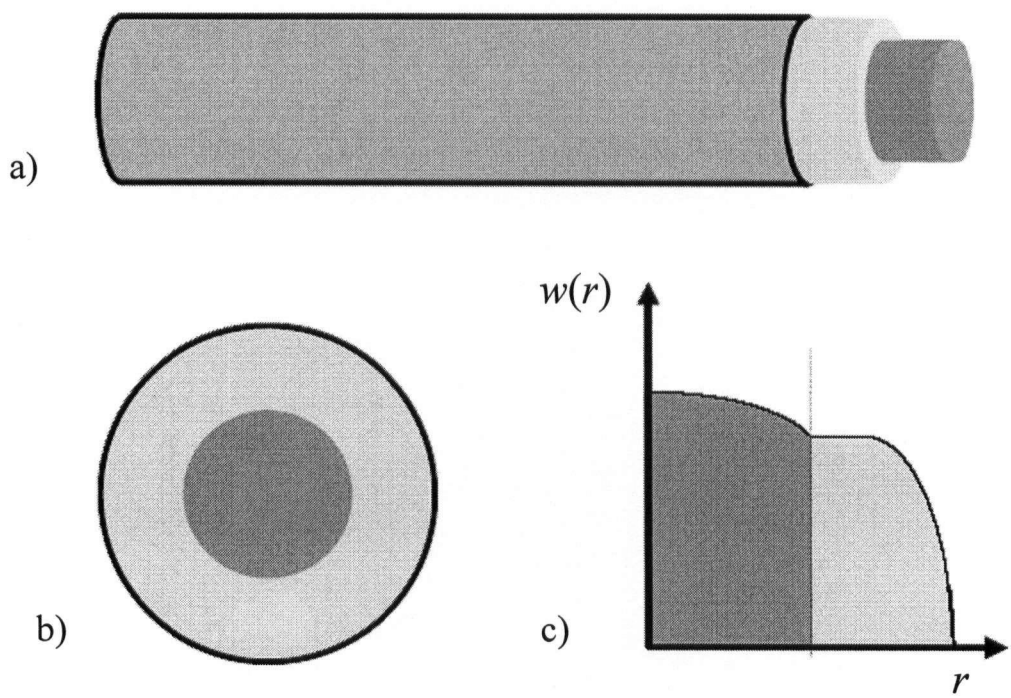

Figure 2.1: (a) Inner core fluid surrounded by a yield stress lubricating fluid flowing in a pipe, (b) cross section of the pipe where the center region corresponds to the inner core fluid, and the outer region corresponds to the outer lubricating fluid, (c) desired velocity profile (inner core fluid surrounded by an unyielded plug region of the outer fluid).

2.1 Model Derivation

2.1.1 Equations of Motion

The continuity and momentum equations in cylindrical coordinates are satisfied in both fluid domains for $k = 1, 2$.

$$\frac{1}{r}\frac{\partial}{\partial r}(ru_r)+\frac{1}{r}\frac{\partial u_\theta}{\partial \theta}+\frac{\partial w}{\partial z}=0 \tag{2.3}$$

$$\rho\left(\frac{\partial u}{\partial t}+u\frac{\partial u}{\partial r}+\frac{v}{r}\frac{\partial u}{\partial \theta}-\frac{v^2}{r}+w\frac{\partial u}{\partial z}\right)=\left[\frac{1}{r}\frac{\partial}{\partial r}(r\tau_{k,rr})+\frac{1}{r}\frac{\partial \tau_{k,r\theta}}{\partial \theta}+\frac{\partial \tau_{k,rz}}{\partial z}-\frac{\tau_{k,\theta\theta}}{r}\right]-\frac{\partial P}{\partial r} \tag{2.4}$$

$$\rho\left(\frac{\partial v}{\partial t}+u\frac{\partial v}{\partial r}+\frac{v}{r}\frac{\partial v}{\partial \theta}+\frac{uv}{r}+w\frac{\partial v}{\partial z}\right)=\left[\frac{1}{r^2}\frac{\partial}{\partial r}(r^2\tau_{k,r\theta})+\frac{1}{r}\frac{\partial \tau_{k,\theta\theta}}{\partial \theta}+\frac{\partial \tau_{k,\theta z}}{\partial z}\right]-\frac{1}{r}\frac{\partial P}{\partial \theta} \tag{2.5}$$

$$\rho\left(\frac{\partial w}{\partial t}+u\frac{\partial w}{\partial r}+\frac{v}{r}\frac{\partial w}{\partial \theta}+w\frac{\partial w}{\partial z}\right)=\left[\frac{1}{r}\frac{\partial}{\partial r}(r\tau_{k,zr})+\frac{1}{r}\frac{\partial \tau_{k,z\theta}}{\partial \theta}+\frac{\partial \tau_{k,zz}}{\partial z}\right]-\frac{\partial P}{\partial z} \tag{2.6}$$

Here the pressure P is the modified pressure: $P = p+\rho gz$. The basic flow is modeled assuming that the velocity of the fluids in the radial and angular directions is zero, and the axial velocity in the z-direction, upwards, depends on only distance from center of the pipe, r, i.e. $U = (0,0,w(r))$. We further assume when the fluid is un-yielded, all stress terms are zero except $\tau_{k,zr}$ and $\tau_{k,rz}$. By substituting $U = (0,0,w(r))$ into the continuity and momentum equations, (2.3) vanishes, and (2.4) and (2.5) become:

$$\frac{\partial P}{\partial r}=0 \qquad \frac{\partial P}{\partial \theta}=0 \tag{2.7}$$

Therefore, the pressure P depends only on z and (2.6) can be rewritten as:

$$0=\frac{1}{r}\frac{\partial}{\partial r}(r\cdot\tau_{k,zr})-\frac{\partial P}{\partial z} \qquad k=1,2 \tag{2.8}$$

2.1.2 Flow of a Single Hershel-Bulkley Fluid

We consider first the case of a single Herschel-Bulkley fluid in the pipe and drop the subscript k. We rearrange and integrate (2.8):

$$\frac{\partial P}{\partial z}=\frac{1}{r}\frac{\partial}{\partial r}(r\cdot\tau_{zr})$$

$$\tau_{zr}=\frac{\partial P}{\partial z}\frac{r}{2}+\frac{C}{r}$$

Now we assume the symmetry condition $\tau_{zr}\big|_{r=0} = 0$, and therefore:

$$\tau_{zr} = \frac{\partial P}{\partial z}\frac{r}{2}$$

For a forward flow the pressure gradient will be negative and hence:

$$\tau = |\tau_{zr}| = \left|\frac{\partial P}{\partial z}\right|\frac{r}{2} = -\frac{\partial P}{\partial z}\frac{r}{2} \tag{2.9}$$

Equation (2.9) indicates that the shear stress increases linearly from zero at the center of the pipe to a maximum at the wall of the pipe.

$$\tau_w = \frac{R}{2}\left|\frac{\partial P}{\partial z}\right| \tag{2.10}$$

Assuming the yield stress of the Herschel-Bulkley fluid is lower than the maximum value of shear stress in the pipe, its velocity profile is differentiable but piece-wise as shown in Figure 2.2, and we consider two regions separately:

Unyielded region:	$0 \le r < R_y$
Yielded region:	$R_y \le r \le R$

where the yield radius is defined as:

$$R_y = \frac{2 \cdot \tau_y}{\left|\frac{\partial P}{\partial z}\right|} = \frac{\tau_y}{\tau_w} \cdot R \tag{2.11}$$

Within the yielded region, the velocity profile can be calculated by integrating the velocity gradient with respect to r from the wall of the pipe:

$$w(r) = \int_R^r \frac{dw}{dr} \cdot dr = \int_R^r -\dot{\gamma}(r) \cdot dr \qquad R_y \le r \le R \tag{2.12}$$

Substitute from the constitutive law, (2.1) into (2.12)

$$w(r) = -\int_R^r \left(\frac{\tau - \tau_y}{\kappa} \right)^{\frac{1}{n}} \cdot dr$$

$$= -\int_R^r \left[\frac{1}{\kappa} \cdot \left(\left| \frac{\partial P}{\partial z} \right| \cdot \frac{r}{2} - \left| \frac{\partial P}{\partial z} \right| \cdot \frac{R_y}{2} \right) \right]^{\frac{1}{n}} \cdot dr$$

$$= -\left(\frac{1}{2\kappa} \cdot \left| \frac{\partial P}{\partial z} \right| \right)^{\frac{1}{n}} \cdot \int_R^r (r - R_y)^{\frac{1}{n}} \cdot dr$$

$$= -\left(\frac{1}{2\kappa} \cdot \left| \frac{\partial P}{\partial z} \right| \right)^{\frac{1}{n}} \cdot \left[\frac{(r - R_y)^{\frac{1}{n}+1}}{\frac{1}{n}+1} \right]_R^r$$

$$= \frac{\left(\frac{1}{2\kappa} \cdot \left| \frac{\partial P}{\partial z} \right| \right)^{\frac{1}{n}}}{\frac{1}{n}+1} \cdot \left[(R - R_y)^{\frac{1}{n}+1} - (r - R_y)^{\frac{1}{n}+1} \right] \qquad (2.13)$$

For the unyielded region, since the fluid remains unyielded, the velocity gradient is equal to zero and therefore:

$$w(r) = w(R_y) \qquad 0 \le r < R_y \qquad (2.14)$$

In summary, the velocity profile for one Herschel-Bulkley fluid in a circular pipe is:

$$w(r) = \begin{cases} \beta \cdot (R - R_y)^{\frac{1}{n}+1} & 0 \le r < R_y \quad (2.15) \\ \beta \cdot \left[(R - R_y)^{\frac{1}{n}+1} - (r - R_y)^{\frac{1}{n}+1} \right] & R_y \le r \le R \quad (2.16) \end{cases}$$

where:

$$\beta = \frac{\left(\frac{1}{2\kappa}\cdot\left|\frac{\partial P}{\partial z}\right|\right)^{\frac{1}{n}}}{\frac{1}{n}+1}$$

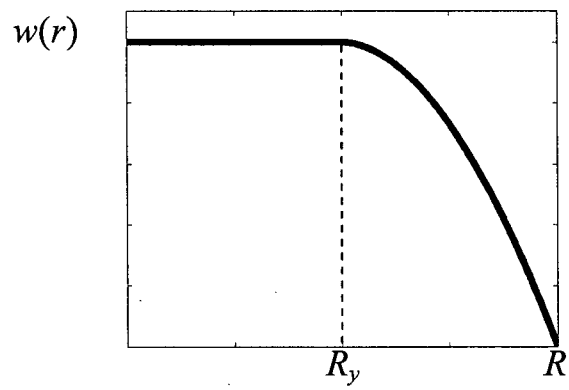

Figure 2.2: Velocity profile of one single Herschel-Bulkley fluid in a circular pipe with radius R.

2.1.3 Flow of Two Herschel-Bulkley Fluids

The basic flow we consider is the case when one Herschel-Bulkley fluid is lubricated by another Herschel-Bulkley fluid in a circular pipe. We start with (2.8), which we integrate in fluid 1 with $k = 1$ using $\tau_{1,zr} = 0$ at $r = 0$. This gives:

$$\tau_{1,zr} = \left|\frac{\partial P}{\partial z}\right|\frac{r}{2} \qquad 0 \le r \le R_i. \tag{2.17}$$

At the interface the stress is continuous and therefore:

$$\tau_{1,zr}(R_i) = \tau_{2,zr}(R_i) = \left|\frac{\partial P}{\partial z}\right|\frac{R_i}{2} \tag{2.18}$$

We now integrate (2.8) with $k = 2$, from R_i outwards to give:

$$\tau_{2,zr} = \left|\frac{\partial P}{\partial z}\right| \frac{r}{2} \qquad R_i < r \le R \tag{2.19}$$

Therefore stress is linear throughout fluid 1 and fluid 2. Depending on the pressure gradient and yield stress of the fluids, there are three distinct cases to be considered.

1. Stable visco-plastically lubricated case (STABLE): fluid 2 partially yielded.
2. Unstable interface case (UNSTABLE): fluid 2 fully yielded.
3. Static wall layer case (STATIC): fluid 2 fully un-yielded.

The stability theory in [3, 7] states that for a multi-layer flow to be stable, the interface between the fluid layers must be surrounded by a plug region of the lubricating fluid.

2.1.3.1 Stable Visco-plastically Lubricated Case (STABLE)

The first case to be considered is the stable visco-plastically lubricated case. In this case the interface is stable, and is surrounded by an unyielded plug region of the lubricating fluid. This case occurs when the lubricating fluid begins to yield for some $r \in (R_i, R)$. The two fluid domains are separated into different velocity regions and their velocity profiles are represented by equations below. The velocity is continuous everywhere across the two fluid domains and is given by:

$$w(r) = \begin{cases} u_c & 0 \le r < R_{y1} \quad (2.20) \\ u_c - \beta_1 \cdot \left(r - R_{y1}\right)^{\frac{1}{n_1}+1} & R_{y1} \le r < R_i \quad (2.21) \\ u_i & R_i \le r < R_{y2} \quad (2.22) \\ u_i - \beta_2 \cdot \left(r - R_{y2}\right)^{\frac{1}{n_2}+1} & R_{y2} \le r \le R \quad (2.23) \end{cases}$$

where the yield radii are given by:

$$R_{yk} = \frac{2 \cdot \tau_{yk}}{\left|\frac{\partial P}{\partial z}\right|} \qquad k = 1, 2 \tag{2.24}$$

and where:

$$\beta_1 = \frac{\left(\left|\frac{\partial P}{\partial z}\right| \cdot \frac{1}{2\kappa_1}\right)^{\frac{1}{n_1}}}{\frac{1}{n_1}+1} \qquad \beta_2 = \frac{\left(\left|\frac{\partial P}{\partial z}\right| \cdot \frac{1}{2\kappa_2}\right)^{\frac{1}{n_2}}}{\frac{1}{n_2}+1}$$

$$u_i = \beta_2 \cdot \left(R - R_{y2}\right)^{\frac{1}{n_2}+1} \qquad u_c = \beta_1 \cdot \left(R_i - R_{y1}\right)^{\frac{1}{n_1}+1} + u_i$$

u_i and u_c are defined as the interfacial velocity and center line velocity respectively. Flow rates of the inner core fluid, Q_1, and the lubricating fluid, Q_2, can be calculated by integrating the velocity profiles with respect to r.

$$Q_1 = \int_0^{R_{y1}} 2 \cdot \pi \cdot r \cdot u_c \cdot dr + \int_{R_{y1}}^{R_i} 2 \cdot \pi \cdot r \cdot \left[u_c - \beta_1 \left(r - R_{y1}\right)^{\frac{1}{n_1}+1}\right] \cdot dr$$

$$= \pi \cdot u_c \cdot R_i^{\,2} - 2 \cdot \pi \cdot \beta_1 \cdot \left(R_i - R_{y1}\right)^{\frac{1}{n_1}+2} \cdot \left(\frac{R_i - R_{y1}}{\frac{1}{n_1}+3} + \frac{R_{y1}}{\frac{1}{n_1}+2}\right) \tag{2.25}$$

$$Q_2 = \int_{R_i}^{R_{y2}} 2 \cdot \pi \cdot r \cdot u_i \cdot dr + \int_{R_{y2}}^{R} 2 \cdot \pi \cdot r \cdot \left[u_i - \beta_2 \left(r - R_{y2}\right)^{\frac{1}{n2}+1}\right] \cdot dr$$

$$= \pi \cdot u_i \cdot \left(R^2 - R_i^{\,2}\right) - 2 \cdot \pi \cdot \beta_2 \cdot \left(R - R_{y2}\right)^{\frac{1}{n_2}+2} \cdot \left(\frac{R - R_{y2}}{\frac{1}{n_2}+3} + \frac{R_{y2}}{\frac{1}{n_2}+2}\right) \tag{2.26}$$

The above equations assume that fluid 1 is yielded, i.e. $R_{y1} < R_i$. If this is not the case then (2.20) and (2.21) are replaced by $w(r) = u_i$, and $Q_1 = \pi R_i^2 u_i$.

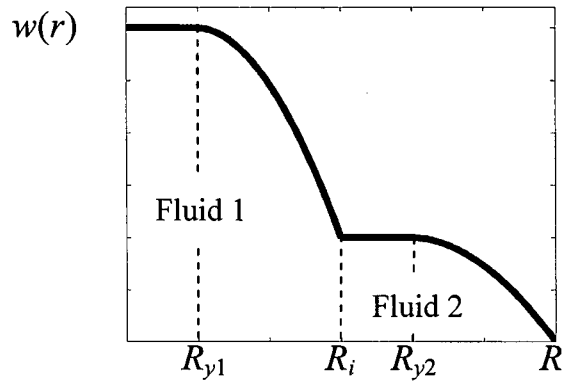

Figure 2.3: Velocity profile of a stable visco-plastically lubricated case (STABLE). Inner fluid is surrounded by an un-yielded plug region of the outer fluid.

2.1.3.2 Unstable Interface Case (UNSTABLE)

In this case the lubricating fluid is completely yielded. This happens if the yield stress of the lubricating fluid is relatively low. Since the lubricating fluid is fully yielded, the interface is no longer surrounded by a plug region and is sensitive to interfacial perturbations, as with classical viscous-viscous flow instabilities.

$$w(r) = \begin{cases} u_c & 0 \le r < R_{y1} \quad (2.27) \\ u_c - \beta_1 \cdot \left(r - R_{y1}\right)^{\frac{1}{n_1}+1} & R_{y1} \le r < R_i \quad (2.28) \\ u_i + \beta_2 \cdot \left[\left(R_i - R_{y2}\right)^{\frac{1}{n_2}+1} - \left(r - R_{y2}\right)^{\frac{1}{n_2}+1}\right] & R_i \le r \le R \quad (2.29) \end{cases}$$

where:

$$\beta_1 = \frac{\left(\left|\frac{\partial P}{\partial z}\right| \cdot \frac{1}{2\kappa_1}\right)^{\frac{1}{n_1}}}{\frac{1}{n_1}+1} \qquad \beta_2 = \frac{\left(\left|\frac{\partial P}{\partial z}\right| \cdot \frac{1}{2\kappa_2}\right)^{\frac{1}{n_2}}}{\frac{1}{n_2}+1}$$

$$u_i = \beta_2 \cdot \left[\left(R - R_{y2}\right)^{\frac{1}{n_2}+1} - \left(R_i - R_{y2}\right)^{\frac{1}{n_2}+1}\right] \qquad u_c = \beta_1 \cdot \left(R_i - R_{y1}\right)^{\frac{1}{n_1}+1} + u_i$$

Flow rates of the two fluids:

$$Q_1 = \int_0^{R_{y1}} 2\cdot\pi\cdot r\cdot u_c\cdot dr + \int_{R_{y1}}^{R_i} 2\cdot\pi\cdot r\cdot\left[u_c - \beta_1\left(r - R_{y1}\right)^{\frac{1}{n_1}+1}\right]\cdot dr$$

$$= \pi\cdot u_c\cdot R_i^{\,2} - 2\cdot\pi\cdot\beta_1\cdot\left(R_i - R_{y1}\right)^{\frac{1}{n_1}+2}\cdot\left(\frac{R_i - R_{y1}}{\frac{1}{n_1}+3} + \frac{R_{y1}}{\frac{1}{n_1}+2}\right) \qquad (2.30)$$

$$Q_2 = \int_{R_i}^{R} 2\cdot\pi\cdot r\cdot\left\{u_i + \beta_2\cdot\left[\left(R_i - R_{y2}\right)^{\frac{1}{n_2}+1} - \left(r - R_{y2}\right)^{\frac{1}{n_2}+1}\right]\right\}\cdot dr$$

$$= \pi\cdot\left(R^2 - R_i^{\,2}\right)\cdot\left[u_i + \beta_2\left(R_i - R_{y2}\right)^{\frac{1}{n_2}+1}\right] - 2\cdot\pi\cdot\beta_2\cdot\alpha \qquad (2.31)$$

where:

$$\alpha = \left(R - R_{y2}\right)^{\frac{1}{n_2}+2}\cdot\left(\frac{R - R_{y2}}{\frac{1}{n_2}+3} + \frac{R_{y2}}{\frac{1}{n_2}+2}\right) - \left(R_i - R_{y2}\right)^{\frac{1}{n_2}+2}\cdot\left(\frac{R_i - R_{y2}}{\frac{1}{n_2}+3} + \frac{R_{y2}}{\frac{1}{n_2}+2}\right)$$

Again, (2.27), (2.28) and (2.30) are valid when fluid 1 is yielded, i.e. $R_{y1} < R_i$. When this is not satisfied, (2.27) and (2.28) are replaced with $w(r) = u_i$, and $Q_1 = \pi R_i^2 u_i$.

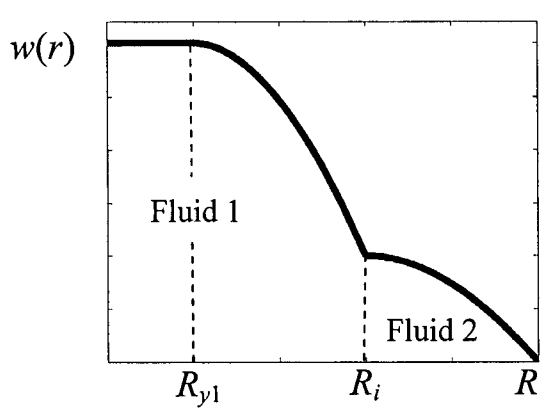

Figure 2.4: Velocity profile of an unstable interface case (UNSTABLE). The lubricating fluid is completely yielded.

2.1.3.3 Static Wall Layer Case (STATIC)

This case is merely the opposite of the previous case. Yield stress of the lubricating fluid is so high that it remains completely un-yielded. In fact, since the fluid 2 region is fully occupied by the un-yielded lubricating fluid which has elastic solid behaviour, the inner core fluid is essentially flowing in a pipe with a reduced diameter. This type of flow is extremely stable. Nonetheless, we are more interested in flows where inner core fluid and lubricating fluid are both moving.

$$w(r) = \begin{cases} u_c & 0 \le r \le R_{y1} \quad (2.32) \\ u_c - \beta_1 \cdot \left(r - R_{y1}\right)^{\frac{1}{n_1}+1} & R_{y1} < r \le R_i \quad (2.33) \\ 0 & else \quad (2.34) \end{cases}$$

where:

$$\beta_1 = \frac{\left(\left|\frac{\partial P}{\partial z}\right| \cdot \frac{1}{2\kappa_1}\right)^{\frac{1}{n_1}}}{\frac{1}{n_1}+1} \qquad u_c = \beta_1 \cdot \left(R_i - R_{y1}\right)^{\frac{1}{n_1}+1}$$

Flow rates of the two fluids:

$$Q_1 = \int_0^{R_{y1}} 2 \cdot \pi \cdot r \cdot u_c \cdot dr + \int_{R_{y1}}^{R_i} 2 \cdot \pi \cdot r \cdot \left[u_c - \beta_1 \left(r - R_{y1}\right)^{\frac{1}{n_1}+1}\right] \cdot dr$$

$$= \pi \cdot u_c \cdot R_i^2 - 2 \cdot \pi \cdot \beta_1 \cdot \left(R_i - R_{y1}\right)^{\frac{1}{n_1}+2} \cdot \left(\frac{R_i - R_{y1}}{\frac{1}{n_1}+3} + \frac{R_{y1}}{\frac{1}{n_1}+2}\right) \qquad (2.35)$$

$$Q_2 = 0$$

Again, (2.32), (2.33) and (2.35) are valid only if fluid 1 is yielded, i.e. $R_{y1} < R_i$. When this is not the case, fluid 1 is also unyielded therefore $w(r) = 0$, and $Q_1 = 0$.

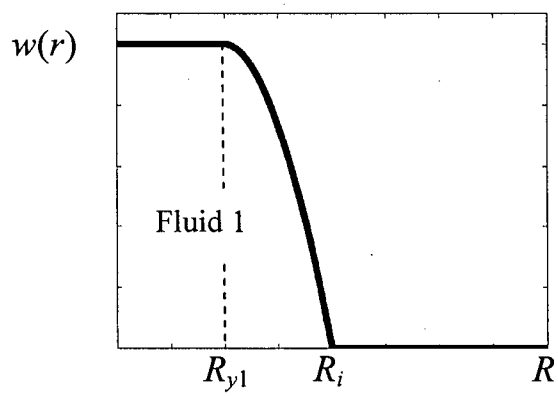

Figure 2.5: Velocity profile of a static wall layer case (STATIC). The lubricating fluid is completely unyielded.

2.1.4 Sample Solution with Analytical Model

Our main purpose in developing the analytical solutions above is to determine the relation between the flow rates of the two fluids, and the pressure gradient and interfacial radius, i.e. for any given pair of fluids. To utilize the analytical solutions just derived, rheological properties, such as the power index, consistency and yield stress, of the two fluids are needed. The preliminary pair of fluids that are chosen to be used as the inner core fluid and lubricating fluid are 0.3% Xanthan solution and 0.3% Carbopol solution respectively. Flow curves of the two fluids are obtained with a Bohlin C-VOR control stress rotational rheometer. The two test fluids and methods on how to measure their properties will be discussed in more details in Chapter 3. Flow curves of the two fluids are presented in Figure 2.6 and 2.7, and their properties are calculated by fitting the data points with the Herschel-Bulkley model.

0.3% Xanthan gum solution: $\tau = 0 + 0.2 \cdot \dot{\gamma}^{0.6}$

0.3% Carbopol 940 solution (pH 5.0): $\tau = 13.0 + 90 \cdot \dot{\gamma}^{0.2}$

Having fitted the rheological parameters, we compute Q_1 and Q_2 as functions of (R_i, $|\partial P/\partial z|$) for our flow loop, $R = 0.0254$ m. The results are shown in Figure 2.8 and 2.9.

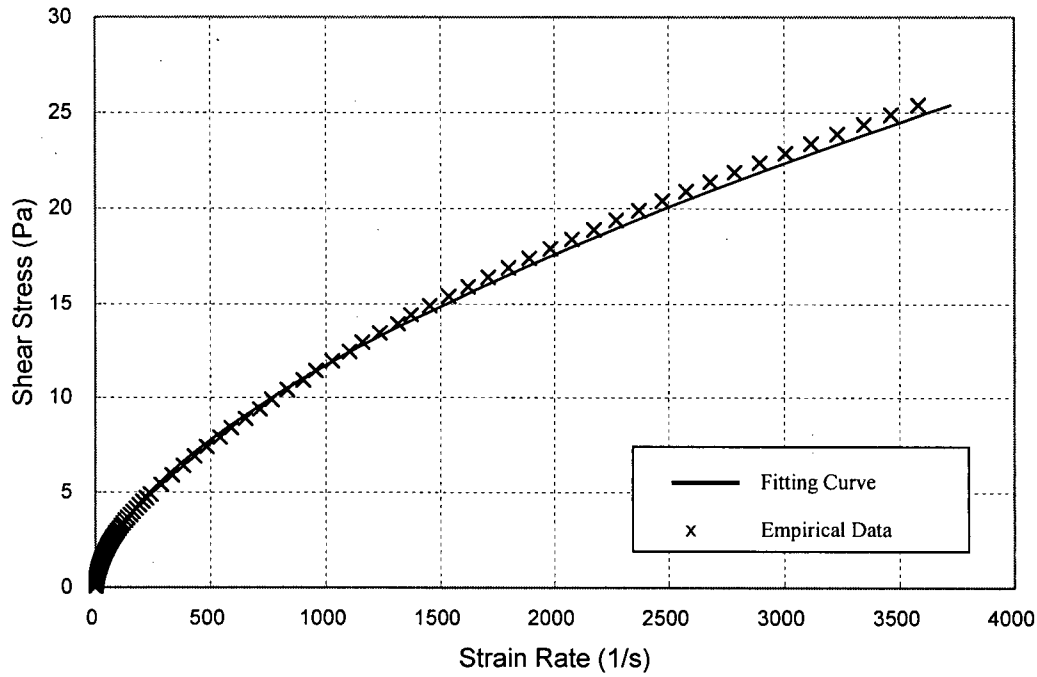

Figure 2.6: Flow curve of a 0.3% Xanthan NF-C solution. Data points are fitted using MatLab nonlinear least-squares curve fitting function. $T = 22^{\circ}C$.

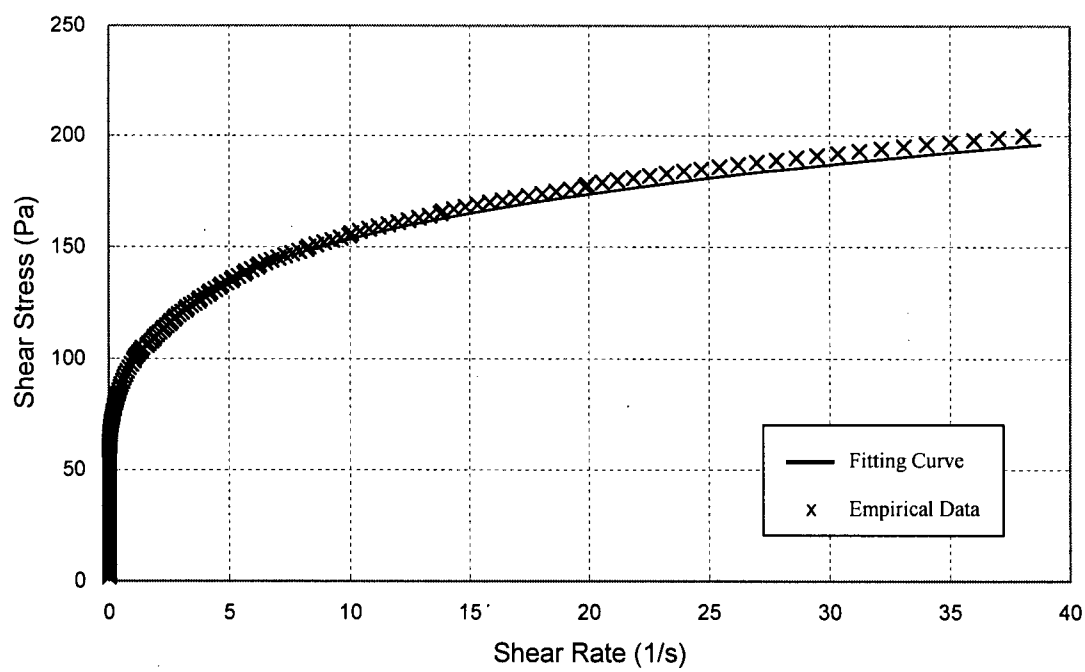

Figure 2.7: Flow curve of a 0.3% Carbopol 940 solution at pH 5.0. Data points are fitted using MatLab nonlinear least-squares curve fitting function. $T = 22^{\circ}C$.

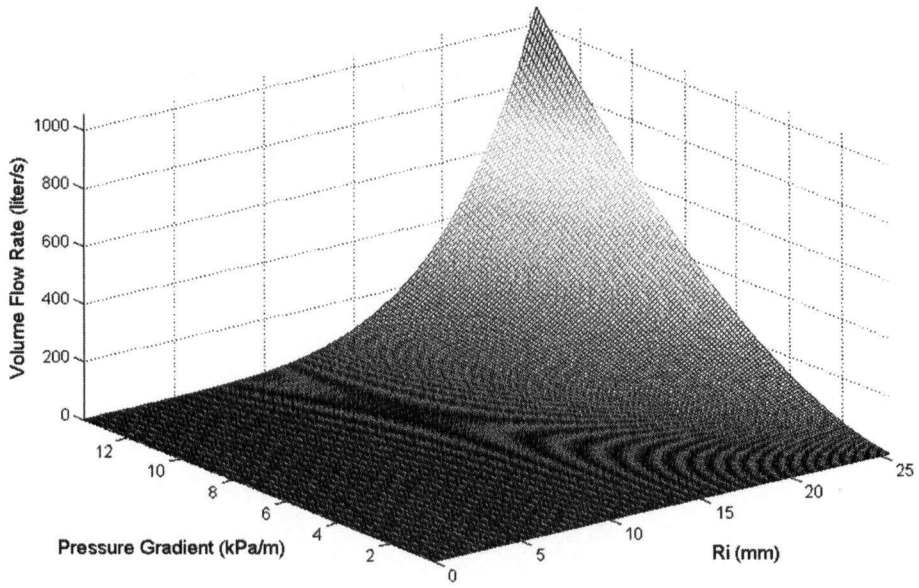

Figure 2.8: Plot of analytically calculated flow rate of the inner core fluid with respect to the pressure gradient and interfacial radius. Inner core fluid is 0.3% Xanthan NF-C solution and lubricating fluid is 0.3% Carbopol 940 solution (pH 5.0).

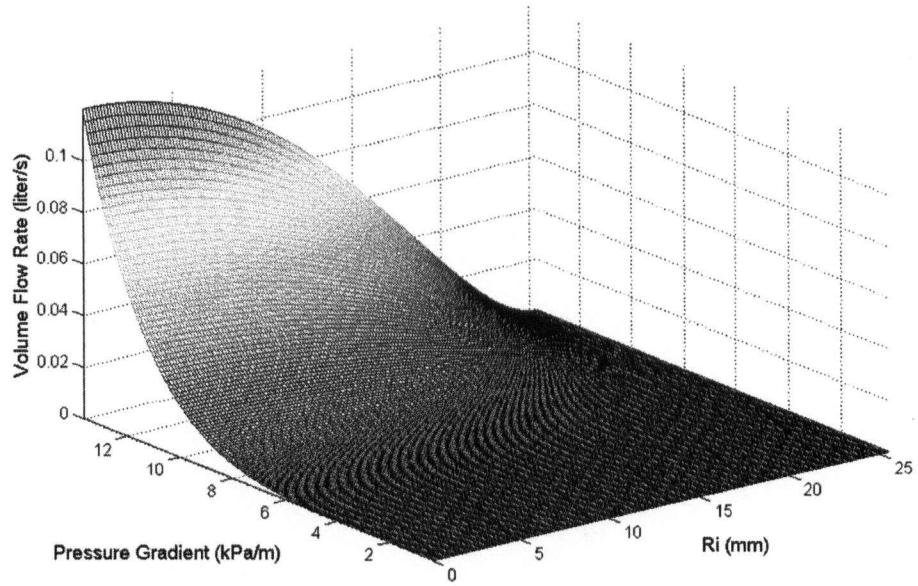

Figure 2.9: Plot of analytically calculated flow rate of the lubricating fluid with respect to the pressure gradient and interfacial radius. Inner core fluid is 0.3% Xanthan NF-C solution and lubricating fluid is 0.3% Carbopol 940 solution (pH 5.0).

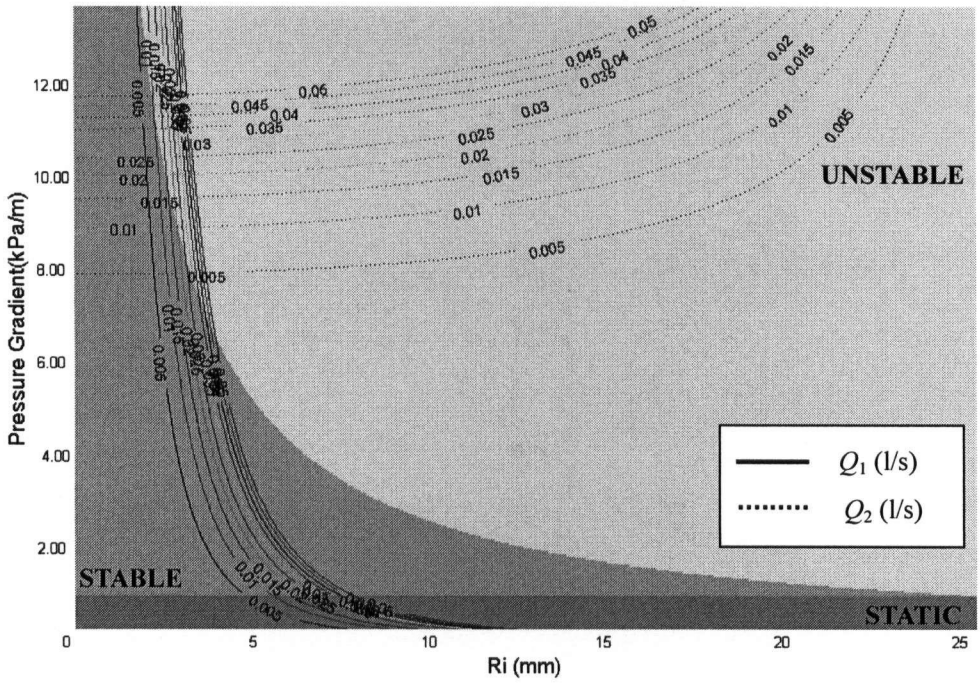

Figure 2.10: Contours of analytically calculated Q_1 and Q_2 with respect to the pressure gradient and interfacial radius. Inner core fluid is 0.3% Xanthan NF-C solution and lubricating fluid is 0.3% Carbopol 940 solution (pH 5.0).

A secondary objective of this thesis is to investigate control of R_i by varying Q_1 and Q_2. Therefore it is important to observe what size of R_i a particular pair of Q_1 and Q_2 leads to. The flow rate plots in Figure 2.8 and 2.9 are combined to generate a contour plot, with contour lines indicating Q_1 and Q_2 in liters per second. On the same plot we mark the different flow regions as shown in Figure 2.10.

From the contour plot we see that the $(R_i, |\partial P / \partial z|)$ mapping is invertible, at least in the region where Q_1 and Q_2 are both greater than 0, i.e. a single pair $(R_i, |\partial P / \partial z|)$ maps to a single pair (Q_1, Q_2). This suggests that we can use (Q_1, Q_2) as our control variables, i.e. by fixing (Q_1, Q_2) we can select R_i (and also $|\partial P / \partial z|$, although this is less important). We later use plots such as Figure 2.16, to design our experiments, selecting (Q_1, Q_2) to lie inside the STABLE region.

2.2 Numerical Solution

As presented in the previous section, flow rates of the two fluids can be calculated analytically. However, using these solutions requires the rheological parameters of the two fluids, τ_y, n and κ, to be determined by fitting their flow curves with fluid models. Similar to all curve fitting problems, there is no perfect fitting curve which goes through all data points and hence errors are introduced. This is well demonstrated in Figure 2.7. The fitting curve does not follow exactly the empirical data at high shear stress. To calculate the velocity and flow rate in a more robust way and to minimize errors introduced by curve fitting, another MatLab code is written to calculate the flow rates and velocity profiles of the two fluids numerically with their empirical rheological data. Similar to the analytical approach, $|\partial P/\partial z|$ and R_i are taken as the two input parameters. An outline of the numerical algorithm for approximating the velocity profile is presented below.

1. Begin iteration at the wall of the pipe, and define $w(R) = 0$, no slip condition.
2. Calculate shear stress, τ_j, at current location, r_j, according to (2.9).
3. If shear stress is higher than the yield stress of the domain fluid, then compute velocity gradient from the flow curve, i.e. evaluate $\dot{\gamma}(\tau_j)$ by linear interpolation from the empirical data. If not, define $\dot{\gamma}(\tau_j) = 0$.
4. Velocity at next position is calculated using 1st order Euler approximation, i.e.

   $$w_{j+1} = w_j + \dot{\gamma}(\tau_j) \cdot \Delta r .$$

5. Repeat step 2 – 4 until $r_j = R_i$.
6. At R_i, assume $w^+ = w^-$.
7. Repeat step 2 – 4 until $r_j = 0$.

The algorithm has been improved by calculating one extra point within each step and using a 4th order Simpson's Rule approximation. By doing so the number of iteration steps can be reduced significantly and yet the order of accuracy is maintained.

$$w(r_{j+1}) = w(r_j) + \left\{ \frac{1}{6}\left[\dot{\gamma}(r_j) + \dot{\gamma}(r_{j+1})\right] + \frac{2}{3}\dot{\gamma}(r_{j+0.5}) \right\} \cdot \Delta r \qquad (2.36)$$

After obtaining the velocity profile, flow rates can be calculated numerically using

Simpson's rule, again giving 4th order accuracy:

$$\int_a^b 2\pi \cdot w(r) \cdot dr = \left[w(r_1) + 4w(r_2) + 2w(r_3) + \ldots\right.$$

$$\left.\ldots + 2w(r_{n-2}) + 4w(r_{n-1}) + w(r_n)\right] \cdot \frac{2\pi \cdot \Delta r}{3} \qquad (2.37)$$

Examples of the flow rate computations are given in Figure 2.11 and 2.12. In Figure 2.13 we show the corresponding flow design contour plot. It is obvious that the numerical and analytical approach yield different results due to the difference in interpretation of the two fluid rheologies. In this case the Herschel-Bulkley model fitted to the flow curve data seems to over estimate the shear-stress-strain-rate relation of both the lubricating fluid and inner core fluid in the high strain rate region, causing at one pressure gradient more fluids are driven in the analytical result than that of the numerical result. For the results presented hereafter we have used the numerical method. This avoids any curve fitting errors, at the expense of longer computational time.

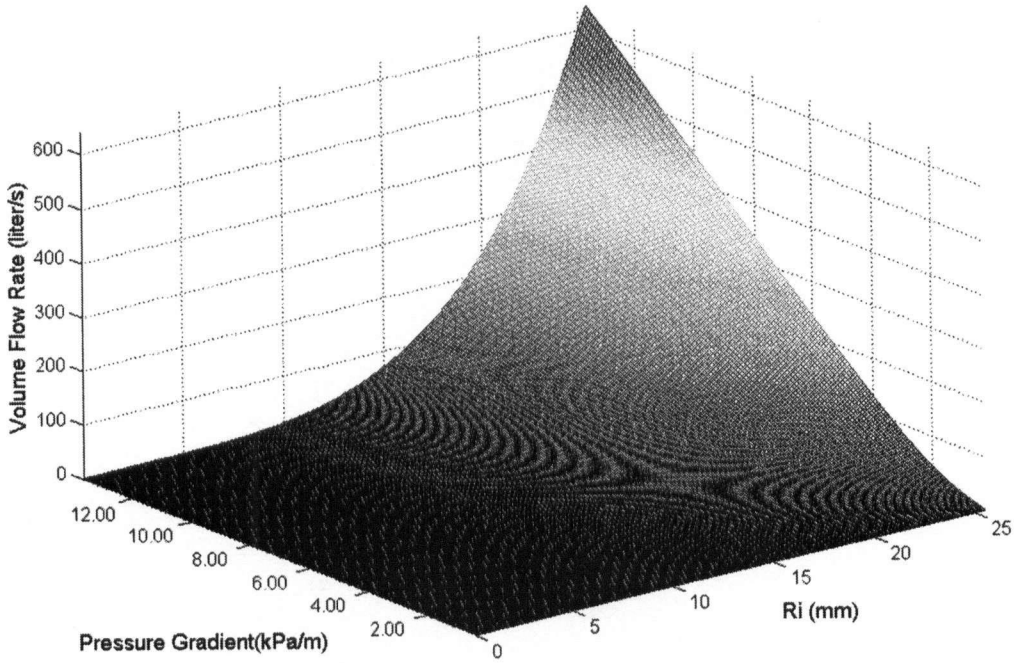

Figure 2.11: Plot of numerically calculated flow rate of the inner core fluid with respect to the pressure gradient and interfacial radius. Inner core fluid is 0.3% Xanthan NF-C solution and lubricating fluid is 0.3% Carbopol 940 solution (pH 5.0).

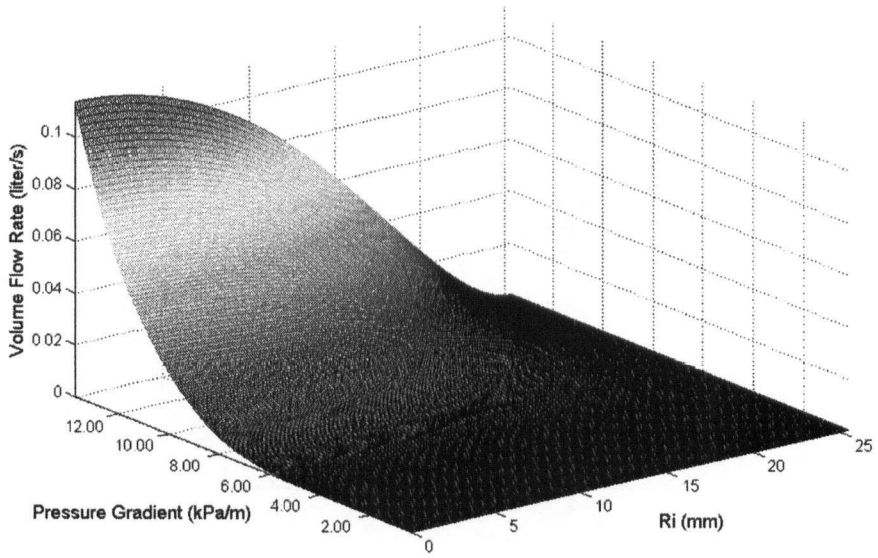

Figure 2.12: Plot of numerically calculated flow rate of the lubricating fluid with respect to the pressure gradient and interfacial radius. Inner core fluid is 0.3% Xanthan NF-C solution and lubricating fluid is 0.3% Carbopol 940 solution (pH 5.0).

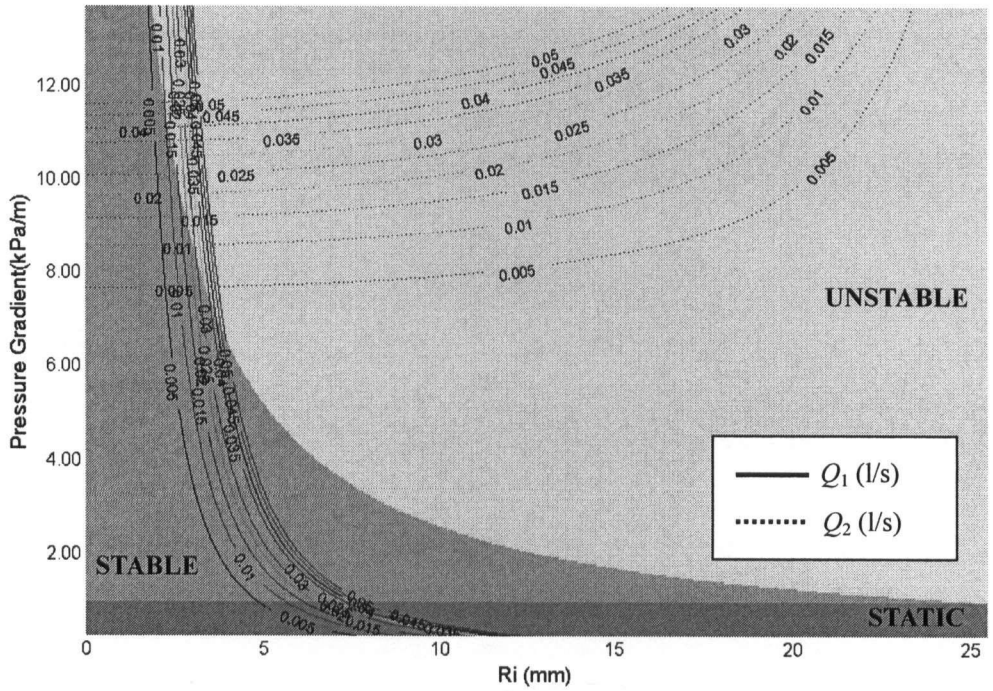

Figure 2.13: Contours of numerically calculated Q_1 and Q_2 with respect to the pressure gradient and interfacial radius. Inner core fluid is 0.3% Xanthan NF-C solution and lubricating fluid is 0.3% Carbopol 940 solution (pH 5.0).

2.3 Inverting the Flow Problem

The multi-layer flow problem is straight forward and it is obvious that for given rheological properties, the flow rates of the two fluids can be calculated easily with respect to the two independent parameters R_i and $|\partial P/\partial z|$:

$$Q_1 = \mathbf{f}_1(R_i, |\partial P/\partial z|) \tag{2.38}$$
$$Q_2 = \mathbf{f}_2(R_i, |\partial P/\partial z|) \tag{2.39}$$

Although the relation is simple to solve with either analytical or numerical approach, it is in fact the inverse relation that we want for experimental design, i.e. we would like to observe directly the variation in R_i by varying Q_1 and Q_2. One can vary Q_1 and Q_2 directly by controlling the individual pumps, but there is no clear way to control R_i directly. As a result, it is essential that we are able to invert the problem, i.e. we have to solve the relation in the reverse direction:

$$R_i = \mathbf{g}_1(Q_1, Q_2) \tag{2.40}$$
$$|\partial P/\partial z| = \mathbf{g}_2(Q_1, Q_2) \tag{2.41}$$

A MatLab code has been written to perform the inversion for a range of Q_1 and Q_2. The functions $\mathbf{g}_1(x, y)$ and $\mathbf{g}_2(x, y)$ are defined implicitly by finding the zero's $(R_i, |\partial P/\partial z|)$ of the system.

$$\left(x - \mathbf{f}_1\left(R_i, \left|\frac{\partial P}{\partial z}\right|\right)\right)^2 = 0$$

$$\left(y - \mathbf{f}_2\left(R_i, \left|\frac{\partial P}{\partial z}\right|\right)\right)^2 = 0$$

The zeros are found using the built-in function *fsolve( )*. *fsolve( )* utilizes the non-linear least squares method with a user defined initial guess to find the root or solution of a non-linear system of equations. Limitations of *fsolve( )* are that the system must be continuous and its solution must be unique, or else *fsolve( )* either not converges or the solution depends on the initial guess. We have seen that the forward problem (2.38) and

(2.39) produce smooth solutions (Q_1, Q_2). However, in order for the code to work properly, the range of Q_1 and Q_2 to be considered must be selected carefully. For instance, we must define the flow rates of the two fluids to be outside the STATIC region, i.e. Q_1 and Q_2 must be non-zero. The code is unable to resolve anything inside the STATIC region due to the fact that multiple combinations of R_i and $|\partial P/\partial z|$ can lead to the same zero flow rate. The problem is numerically unstable inside the STATIC region since it does not consist of unique solution. Since we anyway want $Q_2 > 0$ ml/s therefore the restriction to (R_i, $|\partial P/\partial z|$) outside the static region is not a problem.

The ranges of Q_1 and Q_2 are selected to be from 5 ml/s to 50 ml/s based on the possible operational regions of the two pumps. In Figure 2.14 we show the result of this inversion, for the same 2 fluids considered previously. From the control chart in Figure 2.16 it is very clear which combinations of Q_1 and Q_2 yield a stable flow, and this is perfect for experimental design.

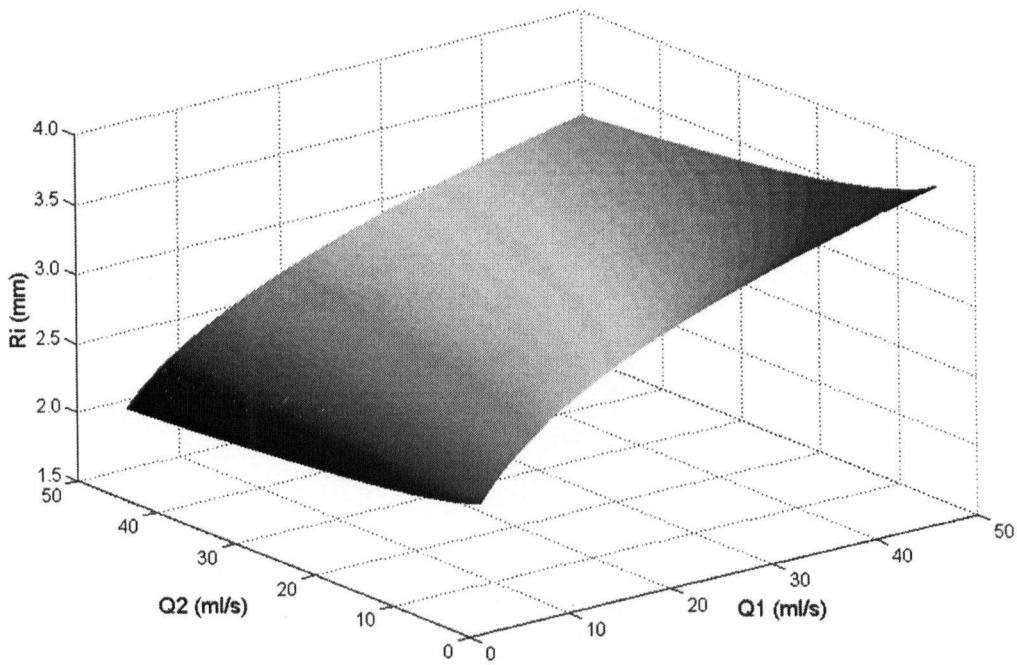

Figure 2.14: Inverted plot of interfacial radius with respect to flow rates of the inner core fluid and lubricating fluid. Inner core fluid is 0.3% Xanthan NF-C solution and the lubricating fluid is 0.3% Carbopol 940 solution (pH 5.0).

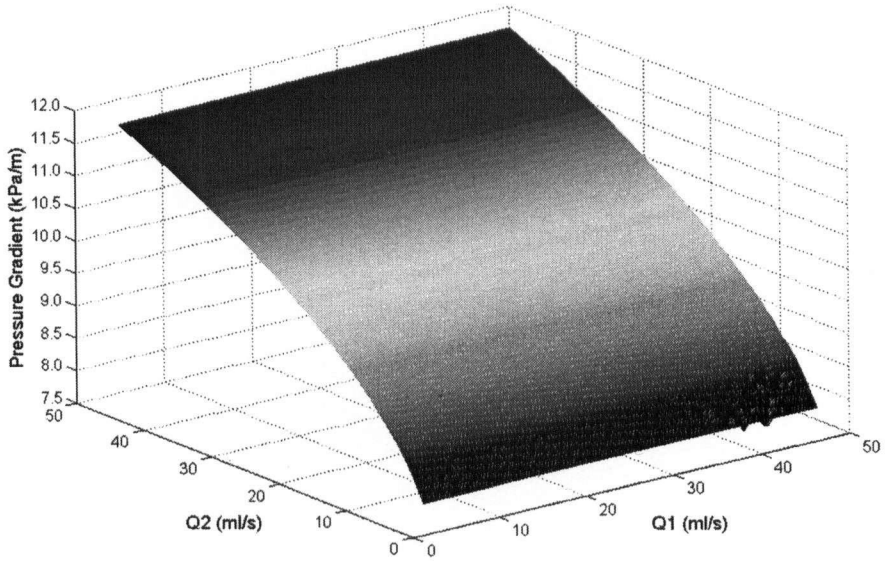

Figure 2.15: Inverted plot of pressure gradient with respect to flow rates of the inner core fluid and lubricating fluid. Inner core fluid is 0.3% Xanthan NF-C solution and the lubricating fluid is 0.3% Carbopol 940 solution (pH 5.0).

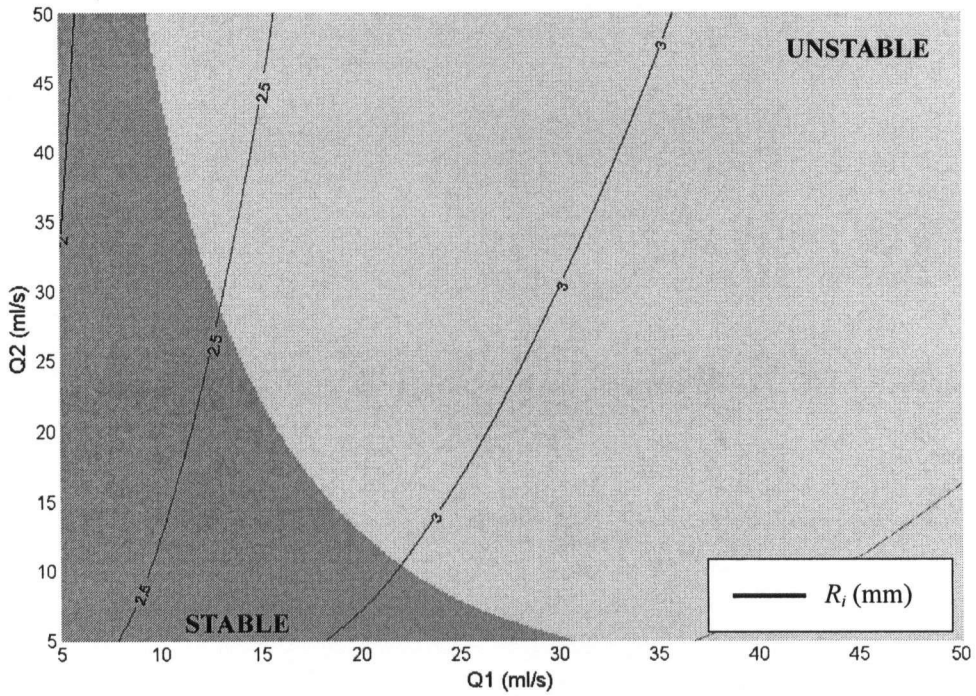

Figure 2.16: Contours of interfacial radius with respect to flow rates of both inner core fluid and lubricating fluid. Inner core fluid is 0.3% Xanthan NF-C solution and the lubricating fluid is 0.3% Carbopol 940 solution (pH 5.0).

Chapter 3

Experimental Apparatus and Fluids

In this chapter we will discuss the multi-layer flow loop constructed at the University of British Columbia. The two primary fluids that are used as the inner core fluid and lubricating fluid will be discussed, and finally the experimental plan will be presented.

3.1 Multi-layer Flow Loop

The primary objective of this thesis is to provide experimental verification that the stable visco-plastic lubrication flows studied in [3, 7, 8] can be achieved in a laboratory setting. Multi-layer fluid flows of Newtonian fluids have been studied through various approaches such as analytical and numerical modeling, experimental and CFD simulation. However, experimental validation of analytical theory is still most widely accepted as demonstration that a particular flow phenomenon can be achieved. Experimental results are compared with model predictions and used to gauge the validity of assumptions made in the modeling process.

It is important for the experimental flow loop to meet the following requirements for validation of the modeling results:

1. The flow must be fully visible.
2. Optical devices should be used to record and measure movement and properties of the interface between the inner core fluid and lubricating fluid.
3. The size of inner core fluid inlet should be adjustable.

With the requirements listed above, the following multi-layer flow loop was constructed. A schematic of the loop is shown in Figure 3.1.

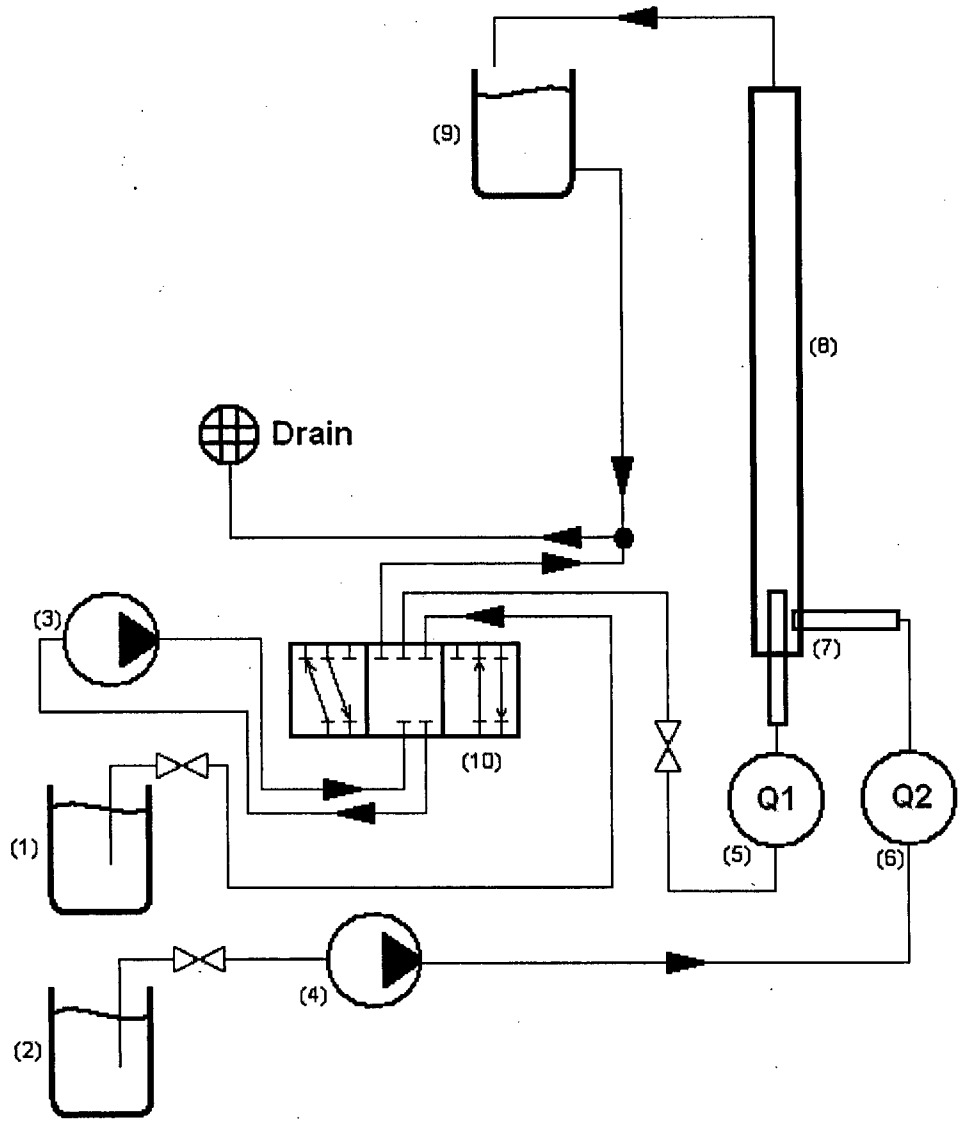

Figure 3.1: Schematic of the multi-layer flow loop at UBC.

Part #	Description	Part #	Description
1	Reservoir (1) for inner core fluid	8	Circular plexiglass pipe, 4-meter long, ID = 50.8 mm
2	Reservoir (2) for lubricating fluid		
3	Monyo 1000 PC pump	9	Open tank for collecting return fluids
4	Monyo 332 PC pump	10	3-way valve
5	Paddle wheel flow meter	11	Panasonic video camera
6	Magnetic flow meter	12	Canon video camera
7	Flow loop inlet manifold	13	DAQ computer

Table 3.1 Parts descriptions of Figure 3.1 and 3.2

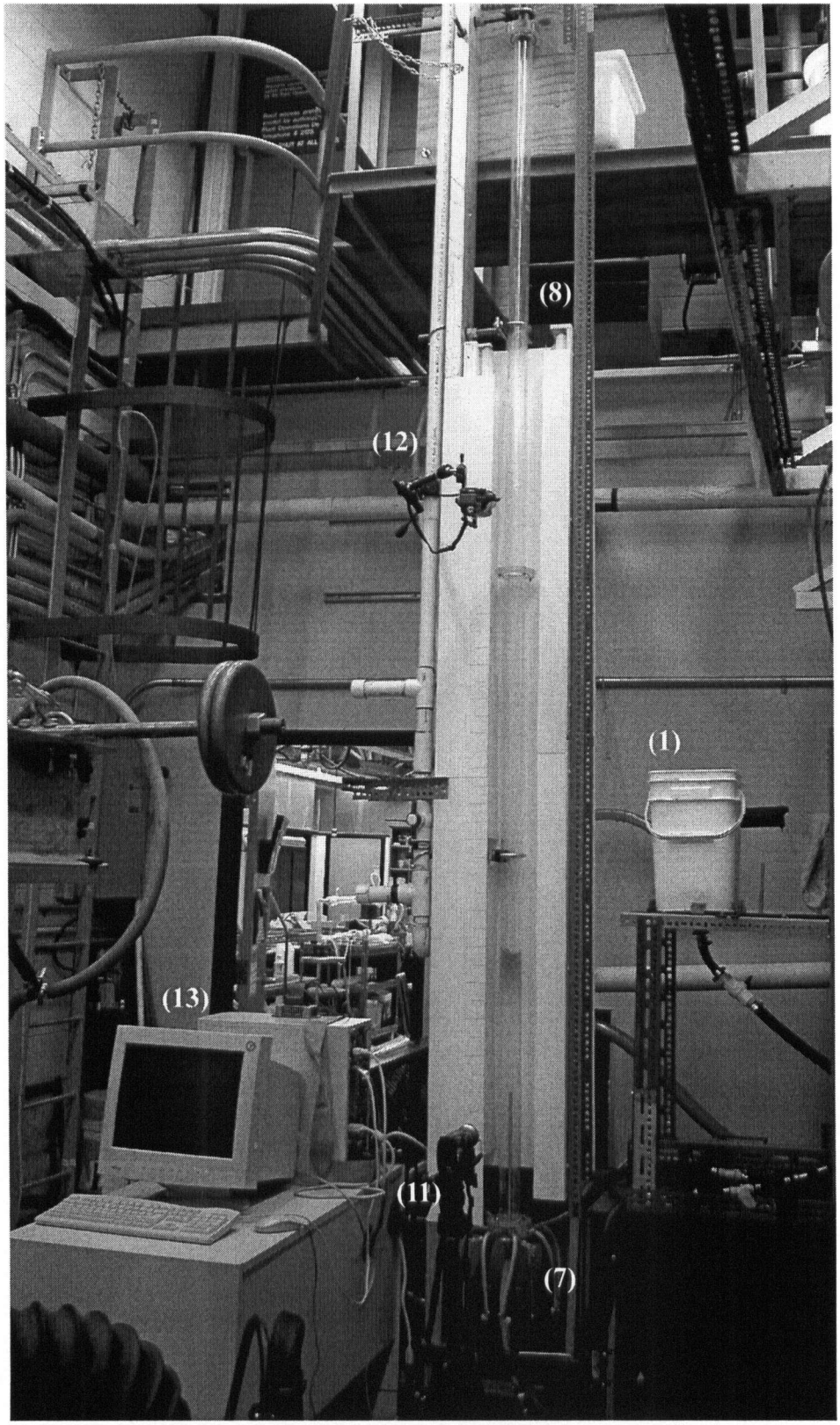

Figure 3.2: A 4-meter multi-layer flow loop constructed at UBC.

A 4-meter long plexiglass pipe (part #8) is attached to a C-Channel which is bolted to the ground. The tilt angle of the channel is adjustable in the range of -20° to +20° measured from vertical. All measurements and observations regarding the interface of the two fluids have been performed along the axis of the pipe. As shown in Figure 3.1, both fluids are first stored in reservoirs. A progressive cavity pump (part #4) is used to pump the lubricating fluid directly from the reservoir (part #2) to the manifold inlet (part #7), which is located at the bottom of the plexiglass pipe. Its flow rate is measured with a magnetic flow meter (part #6) which is connected to a computer for data logging. Reservoir 1 (part #1) is equipped with a quick-connect female adaptor (part #10), as well as the manifold inlet for the inner core fluid. In addition, the suction and discharge of a second progressive cavity pump (part #3) are equipped with quick-connect male adaptors. This setup is for easily reversing the flow direction to facilitate clean out. During an experiment, suction inlet of the pump (part #3) is connected to reservoir 2 while the discharge outlet is connected to the manifold inlet. After each experiment, suction inlet of the pump may be connected to the manifold inlet and the discharge outlet may be connected to a drain path, which is also equipped with a quick-connect female adaptor. The flow rate of the inner core fluid is measured with a paddle wheel flow meter (part #5) which is also connected to a computer. The fluids discharge into an open tank (part #9) attached to the pipe as shown in Figure 3.3.

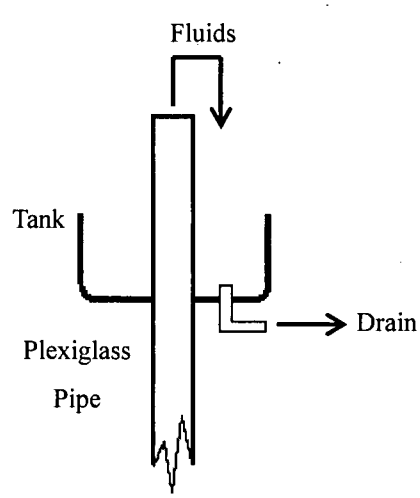

Figure 3.3: The exit manifold of the flow loop.

To minimize the possibilities that the rheological characteristics of a test fluid be damaged or altered, a Monyo 332 PC (part # 4) and a Monyo 1000 PC (part # 3) pumps were chosen to deliver the lubricating fluid and the inner core fluid respectively. Technical specification sheets of the two pumps are attached in Appendix N and O. Both pumps are controlled with variable frequency drives. According to manufacturers' specifications the maximum flow rates of Monyo PC 332 and Monyo 1000 PC are 250 ml/s and 50 ml/s respectively.

Two pressure transducers are installed to observe the pressure changes along the pipe. The two transducers are 2 m apart and the bottom transducer is 0.5 m above the manifold as shown in Figure 3.4. The pressure gradient along the pipe can be calculated by subtracting pressure readings at the bottom from those at the top, and then dividing by their distance apart. A Cole-Parmer pressure transmitter (EW-68075-40) with measuring range between 0-34.5 kPa is installed at the top sensor position while another Cole-Parmer pressure transmitter (EW-68075-42) with measuring range between 0-68.9 kPa is used at the bottom. Both transmitters output voltage signals of 0.5-5.5 V and have a accuracy of ± 0.25% of the full scale.

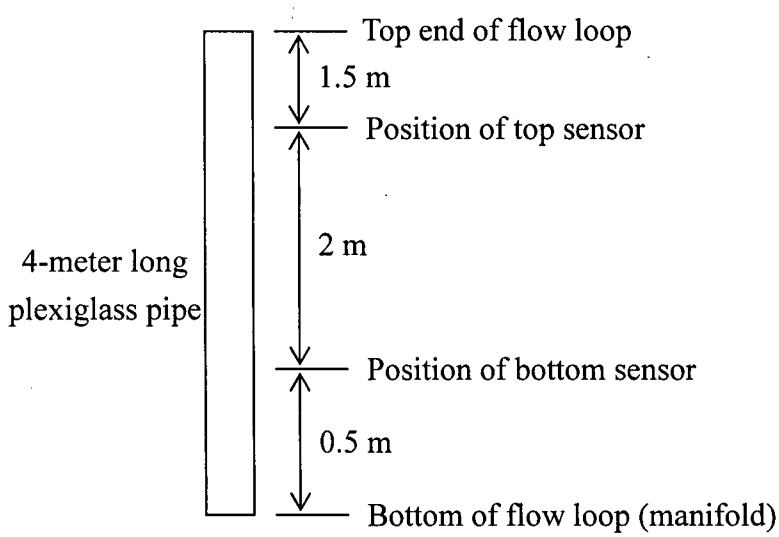

Figure 3.4: Positions of the two pressure sensors.

The inlet manifold has been designed and machined to merge the two test fluids at the entrance of the plexiglass pipe forming a multi-layer flow as shown in Figure 3.5. The center part of the manifold is an annular plexiglass block with an aluminum flange attached to the bottom. One end of the aluminum flange is a 19.08 mm NPT threaded hole while the other end is a very thin 254 mm long aluminum pipe with an inner diameter of 6.35 mm. The narrow end points into the plexiglass pipe while the wide end is connected to Monyo 1000 PC pump which supplies the inner core fluid. To ensure the outer fluid is evenly distributed into the loop, there are eight 6.35 mm ports, separated by 45°, around the plexiglass glass block. Below the aluminum flange is a 1-to-8 manifold constructed with household ABS piping. It is used to distribute the lubricating fluid evenly into 8 portions for the inlets around the plexiglass block.

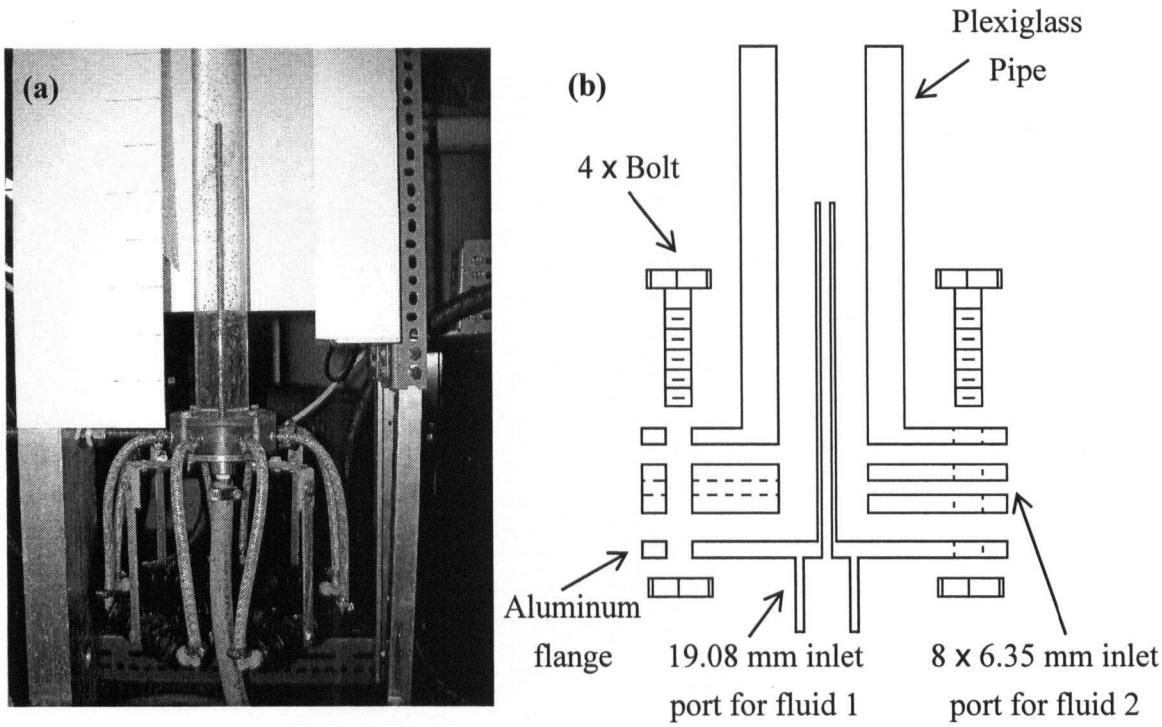

Figure 3.5: (a) Manifold at the bottom of the flow loop (b) Sectional view of the manifold (diagram is not to scale).

Prior to the manifold inlets for both the inner core fluid and the lubricating fluid, two flowmeters are installed. An Omega magnetic flowmeter (FMG-423H) is used for the lubricating fluid while a Kobold paddle-wheel flowmeter (DRG-1150N1F300) is used for the inner core fluid. Technical specification sheets for both devices can be found in Appendix Q and R. In addition to the flowmeters, since both pumps are equipped with

variable frequency drives, the pumps are calibrated such that the flow rates of the two fluids can be monitored via the motor rotational speeds as a backup. Details regarding the calibration are presented in a later section.

Data must be collected and logged from all flowmeters and pressure sensors during experiments. An Iotech DaqBoard 2000 is selected for data acquisition. It is a PC based PCI board that is capable to sample at a maximum rate of 200 kHz. The DaqBoard 2000 consists of 16 analog voltage input channels that can be used for our pressure sensors, and 4 digital counters that can be used for the flowmeters. DaqView 7.0 is the software used to operate the DaqBoard 2000 and log data. The data are stored in both ANSI text file and MatLab file formats such that MS Excel and MatLab can be used for any post experimental data calculations.

Two digital video camcorders, Panasonic PV-DV951-K and Canon Optura 30, are used to capture videos of the experiments. The videos are transferred directly from the camcorders to the computers for post image processing via Firewire IEEE1394 connections. The output video resolution for both cameras is 720 pixels by 480 pixels. The recorded videos serve two purposes: first, for creating spatiotemporal plots, second, for measuring the width of the inner core fluid. Post processing of the images will be discussed in later chapters. The closest possible distance we can place the cameras from the flow loop without any focusing problems is approximately 150 mm. At this distance the cameras yield a resolution of 0.25 mm/pixel.

3.2 Calibration of Apparatus

3.2.1 Objectives

When a measuring device is used, it is important to verify how dependable the result is, i.e. how far is the measurement apart from the true value? Moreover, today most measurements are taken with electronic devices that give out voltage signals which are proportional to the measure quantities, and therefore calibrations are required to determine their relationship. In general new sensors come with calibration reports; however, behaviours of sensors vary over time and are altered by different working conditions. It is always ideal to perform calibrations at locations where measurements are taken.

3.2.2 Pressure Sensors

The flow loop itself is used as a calibrating device for the two pressure transmitters. Each of the transmitters is initially installed at the lower sensor position one after another, i.e. half meter above the inlet of the flow loop as shown in Figure 3.4. Pressure is then increased by pumping water into the loop and is approximated by using the static hydraulics relation $P = \rho g h$, where ρ is the density of water, g is gravitational acceleration, and h is the vertical height of the water column. The pump is stopped after each half meter of water is delivered into the loop, and then one thousand voltage measurements are taken with the software DaqView at a frequency of 100 Hz. We start the pump again, and procedures are repeated until water reaches the top of the loop. The whole calibration process is repeated three times to ensure repeatability of each sensor. The results are averaged to obtain relations shown in Appendix A. A quick calibration is performed before each experiment to verify the validity of the *Pressure-Voltage* relations.

3.2.3 Magnetic Flowmeter and Monyo 332 PC Pump

The Monyo 332 PC Pump is connected in series with the magnetic flowmeter and is responsible for pumping the lubricating fluid from one of the reservoirs into the flow loop. The pump is equipped with an analog variable frequency drive (VFD) which has a dial knob with 0 – 100% markings on the operation panel. Since the flowmeter and pump are in series, it is possible to calibrate both of them at the same time using the stop-watch-and-bucket method. The flowmeter is able not only to display the flow rate on the built-in LCD display, but also to send out a pulsated voltage signal to a computer. The flowmeter is set to generate a voltage pulse for every 2 ml of fluid passing through the flowmeter. With DaqView we are only able to record the total number of pulses received since the start of the program, and in other words we measure the cumulative volumetric flow of the fluid instead of its instantaneous flow rate. Therefore data is post-processed with MatLab to determine the instantaneous flow rate with respect to time by performing numerical differentiation. The test fluid, Carbopol solution, is pumped through the flowmeter into a bucket at some constant flow rate for three minutes. Data is logged with computer during the process and after each minute the mass of bucket is measured. By knowing the density of the fluid, the standard flow rate can be calculated by dividing the volume of fluid in the bucket with time. The procedure is repeated with five different flow rates, and the whole calibration is repeated three times to ensure consistency of the flowmeter and VFD. The following relationship is obtained for the 0.3% Carbopol

solution.

$$\text{Flow rate (ml/s)} = 2.72\,x - 10.33 \qquad 4 \leq x \leq 100$$

where x is the pump speed in percentage of full speed. The linear fit of the flow rate and corresponding motor speed indicates an approximately 10 ml/s offset, i.e. the motor speed must be at least 4% to induce a flow. This offset is mainly due to the static friction within pump, and power is required to overcome the friction and yield stress of the fluid when pump is first started. In addition the pump is not designed to run at speeds lower than 10 ml/s. The calibration plot is shown in Appendix B. Calibration plots are shown in Appendix B.

3.2.4 Paddle-wheel Flowmeter and Monyo 1000 PC Pump

The Monyo 1000 PC pump is connected in series with the paddle-wheel flowmeter and is responsible for pumping the inner core fluid into the flow loop. This Monyo pump is equipped with a digital VFD which allows the rotational speed of the motor to be varied from 0 RPM to the maximum speed 1720 RPM at 1 RPM increment. Identical calibration procedures to those performed for the magnetic flowmeter and Monyo 320 PC pump are used to calibrate the paddle-wheel flowmeter and Monyo 1000 PC pump.

$$\text{Flow rate (ml/s)} = 0.0264\,x \qquad 0 \leq x \leq 100$$

where x is pump speed in RPM. The calibration is shown in Appendix C. The two concentrations of Xanthan solution we used for our experiments are 0.3% and 0.5%. The absolute error for the flowmeter is ± 2.0 ml independent of the flow rate of the fluid. Calibration plots are shown in Appendix C.

3.2.5 Cameras and Edge Detection Algorithm

Due to the fact that the surface of the plexiglass pipe is not flat but circular, and that the refractive indexes of the test fluids, plexiglass, and air are not identical, light rays are deflected as they travel form inside of the pipe to the outside. As a result, objects inside the plexiglass pipe appear larger on the recorded images than they actually are in real life. In order to acquire the width of the inner core fluid using the recorded images, it is important to determine the relationship between the actual size of an object inside the

pipe and its distorted size on the recorded images. To do so, a section of plexiglass pipe is filled with the lubricating fluid, 0.3% Carbopol solution. Five metal rods with different sizes are inserted into the center of the pipe one after another and imaged.

A MatLab code is written to determine the size of the inserted metal rod. The code utilizes the color difference between the lubricating fluid and the metal rod. The color of the lubricating fluid is transparent and the metal rod is not. It is expected to see that values of the pixels around the interfaces between the lubricating fluid and the metal rod should experience drastic changes. Matlab converts each frame of the video clip, approximately 30 frames per second, into a matrix and each entry in the matrix contains information of the color intensity of the corresponding pixel in the original frame. Built-in functions included in Matlab are used to locate any edges by performing a second derivative test, i.e. to determine any concavity changes within the matrix. For instance, the value of a black pixel is 0 while the value of a white pixel is 255. Since the lubricating fluid is transparent and the metal is not, we expect that the value of metal rod pixels to be dark, i.e. low, and the value of lubricating fluid pixels to be bright, i.e. high. If we plot the pixel value at one height across the width of the pipe, theoretically there should be a discontinuity or jump for the pixel value at the interface however, due to various issues such as the background lighting and resolution of images, the plot is smooth as shown in Figure 3.6. The concavity of the plot changes from positive to negative between the two regions so to determine the position of the interface, we calculate where the concavity changes sign. The width of the metal rod is then calculated by determining the distance between the left and right interfaces and compared with a known length scale in the picture, usually the width of the plexiglass pipe that is 63.5 mm wide. The code is later used to determine the width of the inner core fluid during actual experiments. It is essential to assign distinctive colors to the two fluids in order for the MatLab code to work properly. Throughout most experiments the lubricating fluid is kept transparent and black color dye is mixed with the inner core fluid.

Results show that relation between the measured size and actual size of an object inside the pipe filled with the lubricating fluid is linear and is scaled by 1.34 for the Panasonic camera and 1.38 for the Panasonic Camcorder. The calibration is repeated with 0.5% Carbopol solution and no significant difference of the two scaling coefficients is observed. Calibration plots are shown in Appendix D.

To estimate R_i, we locate our cameras such that each of them can capture 180 mm of the

loop. Figure 3.7a is a picture of a stable multi-layer flow with a small puff of the inner core fluid. The flow is not fully developed yet and therefore the flow path of the inner core fluid is not completely straight. Figure 3.7b is the black and white image created by MatLab. Figure 3.7b shows that our code is robust enough to follow the shape of the puff of the inner core fluid and the bent interface.

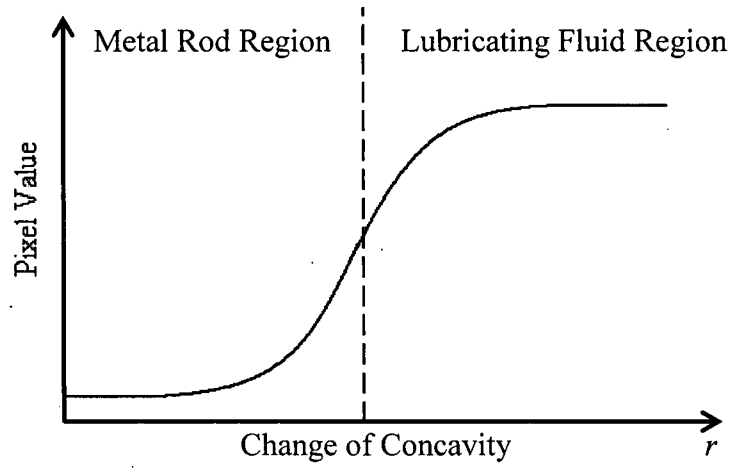

Figure 3.6: Pixel value versus distance from center of pipe.

The resolution of all our images is 0.25 mm/pixel. In other words excluding the error contributed by the edge detection algorithm, the error from our camera for each interface measurement is ± 0.25 mm. Since R_i is calculated by finding the distance between two interfaces, the error for a R_i measurement is therefore equal to ± 2 x 0.25 mm, i.e. ± 0.50 mm. It is unclear that how much error the edge detection algorithm contributes to the measurement. The algorithm could be tested with artificial images or matrixes, or a sensitive test could be done to estimate its error contribution. However this process is computationally complex and is outside of the expertise of the author.

Due to the small axial length of the captured image, it is reasonable to assume that R_i is independent of the axial position, z, within the video frame. To fully utilize the number of video frames, we first select a range of time which the flow is visually stable. Then we perform the edge detection algorithm over the entire range, i.e. typically 15 s. For each second we have about 30 frames and from each frame we can make about 700 measurements of R_i. Therefore in total we have approximately 315,000 measurements.

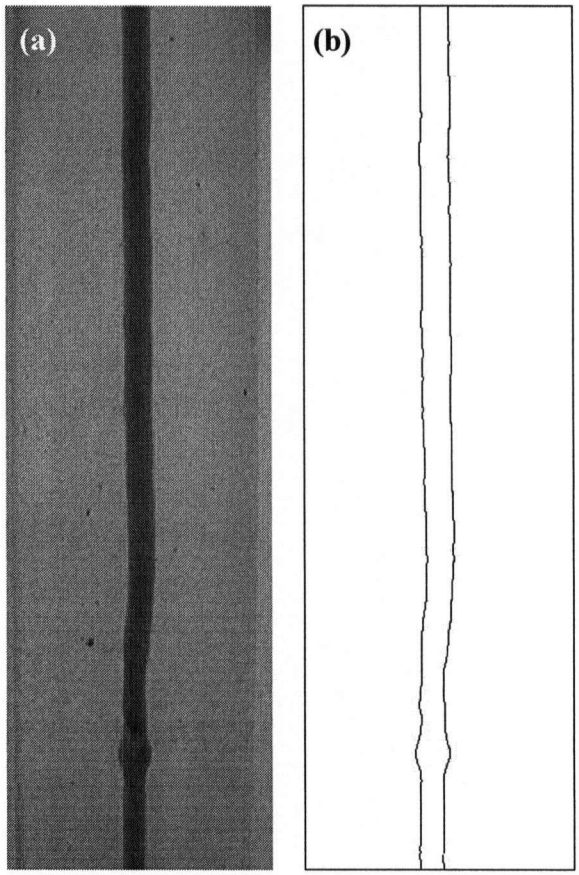

Figure 3.7: (a) A picture of a developing multi-layer flow. The interface is not perfectly straight and the flow consists of a small puff of the inner core fluid. The actual axial length of the image is 0.18 m. (b) The image reconstructed using our MatLab edge detection algorithm.

3.3 Fluids and Characterizations

3.3.1 Fluid Characterizations

Flow Curve

For this thesis the flow curve of a fluid refers to the graph of its shear stress versus strain rate. A Bohlin C-VOR digital controlled shear stress and strain rate rotational rheometer is used to characterize all test fluids. To obtain the flow curve of a test fluid, approximately 3 ml of the test fluid is put in the test platform of the rheometer and another metal plate is lowered from the top until the desired gap size is achieved. Then, the rheometer either applies a known shear stress via the top plate, and measures the resultant strain and strain rate, or it can apply a known shear rate and measure the

frictional force, i.e. shear stress, observed by the top plate with a built-in torque sensor. Throughout the study a cone and plate 4/40 geometry (CP 4/40) is used. The geometry consists of a stationary flat bottom plate, and a rotating upper cone which has a diameter of 40 mm and an angle of 4°. As per the manufacturer's specification, shear rate along the radial position of the cone is constant (within 0.3%) and is ideal for testing fluids with high viscosity.

Yield Stress Determination

Yield stress from a rheologist's point of view is defined as the minimum shear stress that must be applied to a material to induce flow. A yield stress fluid exhibits solid-like behaviour below its yield point. Its behaviour is associated with elasticity. In other words, the material strains to a fixed value when subjected to a given stress, and there is complete strain recovery upon the removal of the stress. Within this stress region, the relationship between shear stress and strain is usually linear and is a reason why the yield stress sometimes is referred as the proportional limit. On the other hand, above the yield point, it acts like a nonlinear viscous fluid. When shear is applied to a material, it strains continuously and there is no strain recovery even after the stress is removed. The yield stress represents the transition between solid-like and fluid-like behaviour. This transition usually occurs not at a single value of shear stress, but over a range of stresses. It is therefore very difficult to justify how accurate one measuring technique is. Throughout the study two methods are used simultaneously to ensure the accuracy of yield stress determination.

Viscosity Inspection

The first technique that is used to determine the yield stress of one fluid is to look at the instantaneous viscosity of the sample with respect to shear stress. Instantaneous viscosity is sometimes referred to as the effective viscosity, and is equal to the slope of the flow curve. As discussed a yield stress fluid acts like solid below its yield point. Thus if one applies a stress, it would be like stretching an elastic band, the more stress you apply, the more the fluid resists to flow. Since viscosity is the measure of how much one fluid resists to flow, it should increase with stress as well, in the elastic region. Once we get over the yield point, the fluid starts to flow and its viscosity decreases instantly. Therefore the yield stress should occur at the maximum of the viscosity curve. We may also look at this test as searching for the smallest applied stress which the fluid begins to flow. In

general this test is less accurate than the creep test which will be discussed, but it allows us to approximate the value of yield stress in a rapid test, i.e. as fast as 4 minutes. The approximated value can also be used as an initial guess for performing the creep test. An example plot of viscosity versus shear stress of a 0.3% Carbopol solution is shown in Figure 3.8. The yield stress of the fluid corresponds to the maximum value of the viscosity curve, and therefore it is approximately equal to 15 Pa.

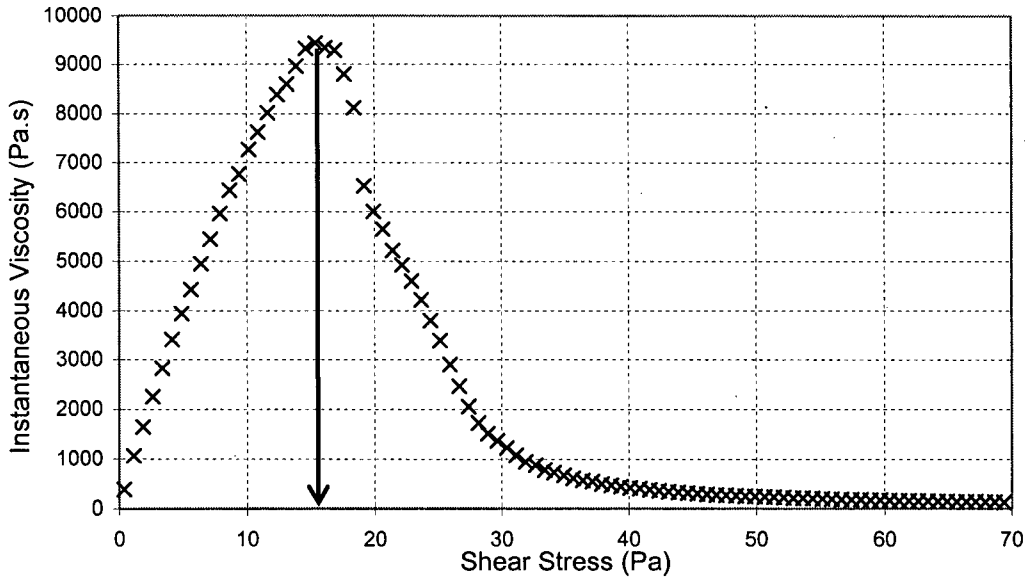

Figure 3.8: Instantaneous viscosity curve of a 0.3% Carbopol 940 solution. The yield stress of the fluid corresponds to the maximum value of the viscosity curve, i.e. approximately 15 Pa.

Creep Test

The second technique for determining the yield stress of one fluid is called the creep test. The working principle of the creep test is based on the Hooke's law. A known shear stress is applied to the test sample for a fixed amount of time. If the applied stress is below the critical yield stress value, the sample should strain to one finite value regardless how long the shear stress is applied. On the other hand if applied stress is above the yield stress, the sample should strain continuously until the stress is removed. If stress is plotted versus strain, one should observe there is a critical stress where strain increases dramatically and we define that critical stress as the yield stress.

To perform a creep test we first load the correct amount, i.e. 3 ml, of sample on the test

platform and the top plate is lowed to the correct gap clearance, i.e. 500 μm. A known constant shear stress is applied to the sample for 60 seconds. Then resultant strain is measured and the procedure is repeated for another value of shear stress with the same amount of shearing time. The procedure is repeated until the desired resolution is achieved. Finally, a plot of applied stress versus strain is generated and a sample plot is generated with a 0.3% Carbopol solution and shown in Figure 3.9. Straight lines are extended from below and above yield point and their intersection is defined as the yield stress. In this example the yield stress is defined as 13 Pa. Again, since the yield stress does not physically occur at one shear stress value, but over a range of shear stress. The final result usually depends on how a rheologist interprets the data and it is difficult to define the error bound for the yield stress measurement. From the creep test plot it is reasonable to believe the yield stress occurs between 10 Pa and 16 Pa, i.e. a ± 3 Pa error bound. In this thesis the yield stress of the lubricating fluid is mainly used to determine the transition between the stable and unstable cases. As shown in Figure 4.1, an error bound of ± 1 Pa, instead of ± 3 Pa, is used for our contour plot calculations to indicate that the transition can occur over a range of flow rates. In reality the error bound could be larger than ± 1 Pa, but this error bound is used just to indicate that it is reasonable to observe a transition not exactly at the calculated flow rates during an actual experiment. Moreover if a ± 3 Pa error bound is used, the transition region is going to cover the entire graph, which totally neglects the purpose of transition prediction. Using a small error bound also implies a small tolerance is allowed on our model. During our experiments all the observed transitions occurred within our ± 1 Pa error bound.

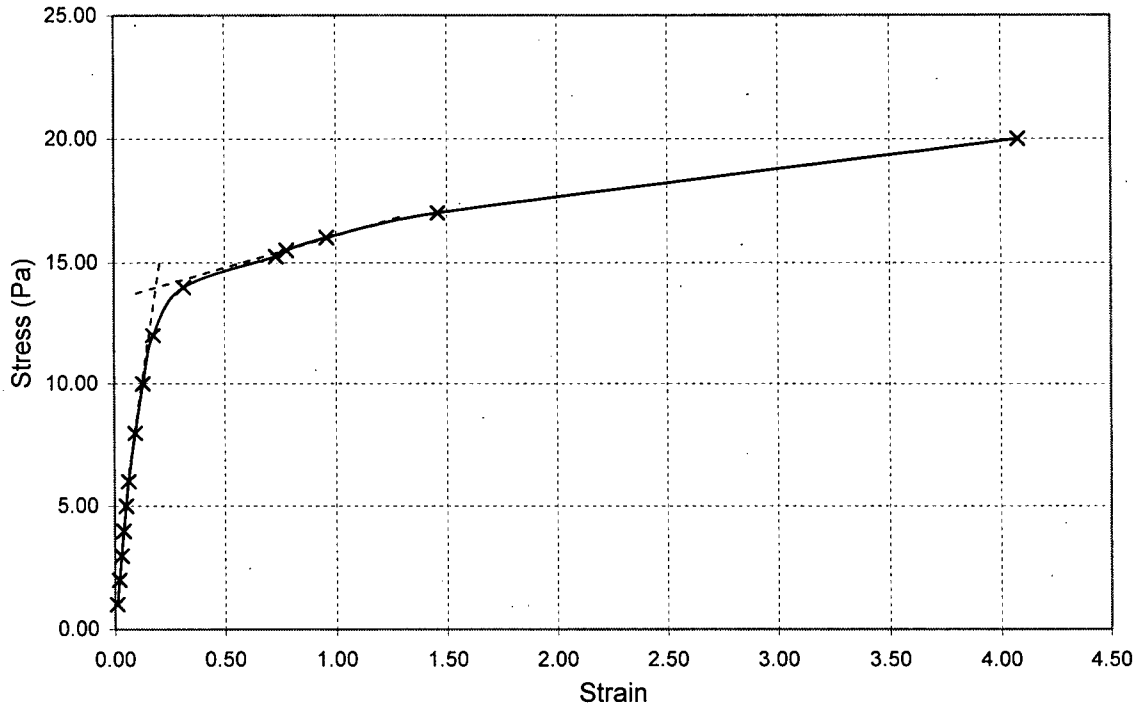

Figure 3.9: Creep test of a 0.3% Carbopol 940 solution at pH 5.0. Yield stress occurs at approximately 13 Pa.

3.3.2 Carbopol

A yield stress fluid named Carbopol 940 is used as the lubricating fluid for our experiments. For the last 50 years, Carbopol, a B.F. Goodrich commercial polymeric thickener has been one of the most widely used thickening and gelling agents for commercial aqueous products in the personal, homecare and pharmaceutical areas. A typical Carbopol solution is shear thinning in nature, and is a yield stress fluid whose yield stress value increases with its concentration. Its shear thinning characteristics is one of the major reasons why it is so widely used in the cosmetic industry. For instant Carbopol solution can be used to produce hand creams, or hand lotions. Hand creams are generally formulated to have a high viscosity at low shear rate and a low viscosity at high shear rate. The high viscosity at low shears gives the cream a good stand up appearance in the pot, inferring a rich creamy product. On the other hand a low viscosity at high shear allows the product to be absorbed into the skin when being rubbed.

The rheology of a Carbopol solution is very interesting. As mentioned the yield stress value of a carbopol solution increases with concentration, but it is also sensitive to the pH

level of the aqueous solution. Without the addition of any neutralizing agents, the pH level of a 0.3% Carbopol dispersion is roughly 2.7. At this pH level the solution is milky and watery. Experimental measurements show that the yield stress of such solution is zero, and is verified by observing air bubbles entrapped within the solution move to the top very slowly and escape. To thicken the solution it is best to increase the pH level of the polymers by the addition of an alkaline neutralizing agent, e.g. sodium hydroxide. The neutralization ionizes the polymers and generates negative charges along the backbone of the polymers. Repulsion of like charges causes polymers to uncoil and turn into extended structures. This reaction gives instantaneous thickening and emulsion stabilization. In general between pH 5 – 10, Carbopol is in the form of gel and its properties are relatively consistent. Beyond pH 10, due to the excessive neutralizing agent Carbopol breaks down and becomes watery again. In summary, the behaviour of Carbopol can be distinguished into three regions:

1. $pH < 5$: pregelification; milky and watery.
2. $5 \leq pH \leq 10$: gel; transparent, most viscous with finite yield stress, consistent properties.
3. $pH > 10$: gel breaks down; milky and watery.

Carbopol comes as a fine polymer powder and therefore must be dispersed in an aqueous solution to form Carbopol in the form of gel. The outline listed below summarizes the overall fluid preparation procedures. The same procedures are repeated closely whenever a new batch of solution is prepared, to ensure properties of all test fluids are consistent.

1. Amount of Carbopol powder needed is calculated according to desired concentration, dry weight of carbopol powder / volume of water, i.e. to achieve a 0.1% Carbopol solution we need 1 g of Carbopol powder for every litre of water.
2. Carbopol powder required is transferred into a beaker and its weight is measured with an electrical weight scale.
3. Carbopol powder is added to water and mixed rapidly for 8 hours, to ensure complete hydration of the powder.
4. The dispersion is covered and left to sit for at least 48 hours before neutralization. This procedure is to ensure all air bubbles within the solution will have enough time to escape. Thus, final solution will be free of bubbles.

5. An alkaline neutralizing agent, sodium hydroxide, is added to bring the pH level of the solution to 5.0. Instead of measuring the pH level of the solution for each mix, the mass of bulk sodium hydroxide added in solid form is measured. For all different batches, same mass of sodium hydroxide is added to ensure we have consistent fluid properties. Sodium hydroxide crystals are dissolved into 250 ml of water before adding into the Carbopol dispersion. 1.25 g and 1.70 g of sodium hydroxide is used for every liter of 0.3% and 0.5% Carbopol solution respectively. The sodium hydroxide solution is slowly poured into the Carbopol container while the Carbopol solution is being mixed.
6. A clear, gel-like Carbopol solution is ready to be used.

During the entire mixing process, the solution is covered to prevent evaporation. Throughout the experiments two different concentrations of Carbopol 940 are used and they are 0.3% and 0.5%. Their flow curves are shown in Figure 3.10 and 3.11. Using regression, we have estimated the Herschel-Bulkley parameters for the data, and their parameters are shown in Table 3.2. We emphasize however, that the flow curve data is used directly for our control model computations (see section 2.2). One may notice all Carbopol solutions are neutralized to a pH level of 5.0, but not any other values. The primary reason why a pH level of 5.0 is chosen for all Carbopol solutions is that the rheology of Carbopol remains relatively consistent within the range of pH 5 – 10. Neutralizing the solution from pH 5 to pH 10 consumes roughly double the amount of sodium hydroxide required for neutralizing the solution from pH 2.7 to pH 5, and yet we observe no significant changes in the rheology. In addition, for our initial test a Carbopol solution with a pH level of 5.0 was used, and we have decided to be consistent with the pH level for the rest of the experiments.

Fluid	**Herschel-Bulkley Model**
0.3% Carbopol 940 solution (pH 5.00)	$\tau = 13 + 90 \cdot \dot{\gamma}^{0.19}$
0.5% Carbopol 940 solution (pH 5.00)	$\tau = 20 + 92 \cdot \dot{\gamma}^{0.24}$

Table 3.2: Properties of Carbopol solutions of different concentrations at $T = 22^{\circ}C$. (Unit of yield stress is Pa and unit of consistency is $Pa \cdot s^{n}$.)

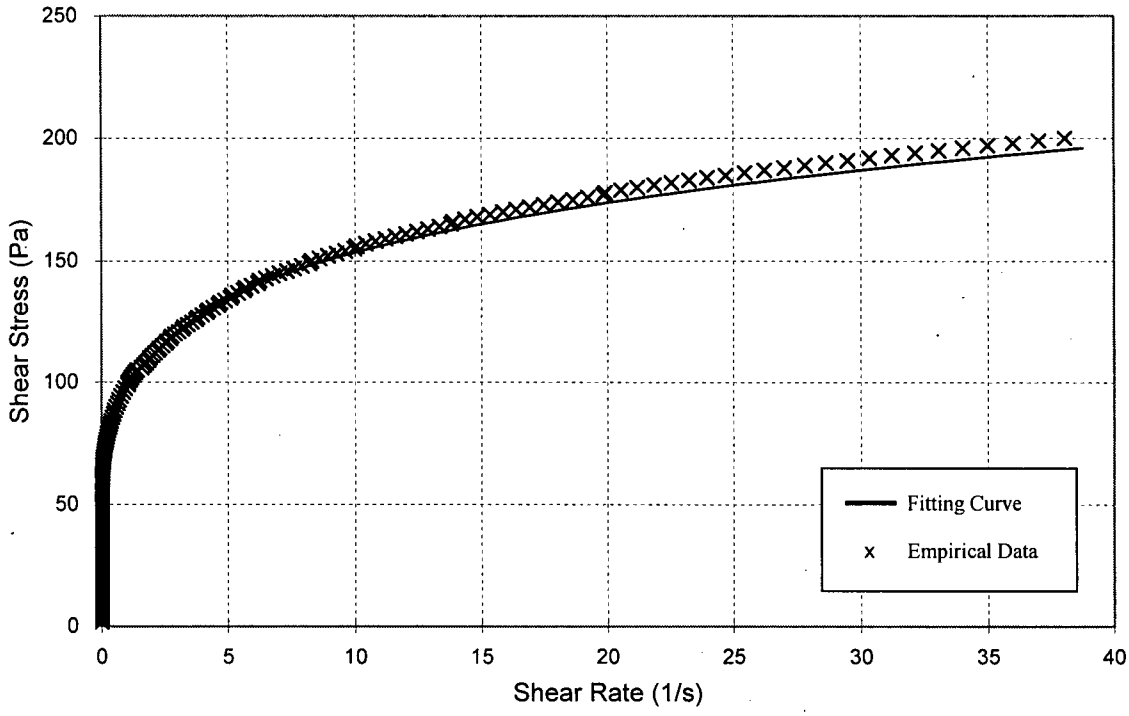

Figure 3.10: Flow curve of a 0.3% Carbopol 940 solution at pH 5.0. T = 22°C. Data points are fitted using MatLab nonlinear least-squares curve fitting function.

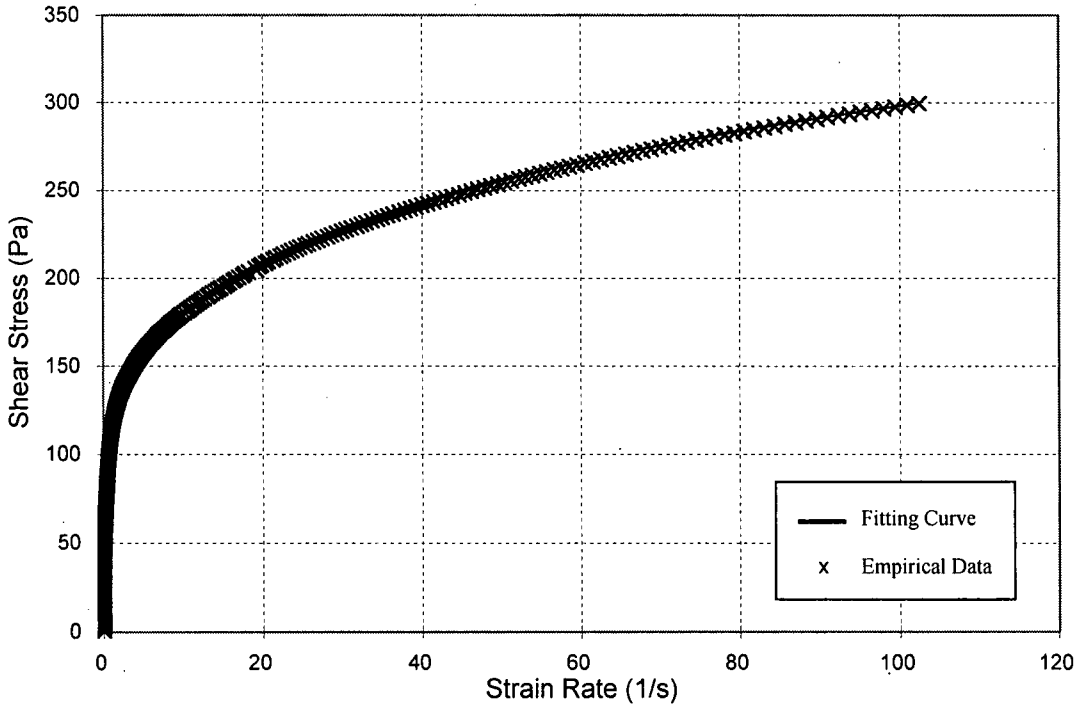

Figure 3.11: Flow curve of a 0.5% Carbopol 940 solution at pH = 5.0. T = 22°C. Data points are fitted using MatLab nonlinear least-squares curve fitting function.

3.3.3 Xanthan Gum

A shear thinning fluid called Xanthan gum NF-C is used as the inner core fluid for our experiments. Xanthan is similar to Carbopol which is shear thinning but with no yield stress. Xanthan is mainly considered to be non-gelling and used for the control of viscosity due to its shear-thinning properties. Another interesting fact of Xanthan solution is its thixotropic character, i.e. a fluid that thins out with time. To better understand Xanthan's thixotropic characteristics, approximately 1 liter of Xanthan solution has been prepared and kept in a sealed container to ensure no evaporation of water. The sample is tested once every week and it is verified that Xanthan solution is time dependent as shown in Figure 3.12. It is observed that it begins to thin out slowly after sitting for one week, and the change is dramatic after two weeks. Therefore, all prepared Xanthan solutions should be used within one week time. The key features of Xanthan are listed below:

1. Pseudoplastic rheology (shear reversible behavior);
2. soluble in water;
3. stable over a range of pH and temperatures;
4. compatible with and stable in systems containing high concentrations of salt;
5. excellent suspension for insoluble solids and oil droplets;
6. resistant to enzymatic degradation;

The preparation procedure for Xanthan solutions is simpler than the one for Carbopol solution since Xanthan solution does not require any neutralization. The preparation procedures are straight forward and listed below:

1. Amount of Xanthan powder needed is calculated according to the desired final concentration, dry weight of Xanthan powder / volume of water, i.e. to achieve a 0.1% Xanthan solution we need 1g of carbopol powder for every litre of water.
2. Xanthan powder required is transferred into a beaker and its weight is measured with an electrical weight scale.
3. Xanthan powder is added to water and mixed rapidly for 8 hours, to ensure complete hydration of the powder. Solution should be homogenous by the end of mixing, and has a pH level of approximately 7.
4. The solution is now ready to be used and good for approximately 1 week.

During the entire mixing process, the solution is covered to prevent evaporation. The two concentrations of Xanthan solutions that are used for our experiments are 0.3% and 0.5%. Their flow curves are shown in Figure 3.13 and 3.14. Similar to what we have done for the Carbopol solutions, we have curve fitted Herschel-Bulkley parameters to the flow curves, and their parameters are shown in Table 3.3. Again, the flow curve data is used directly for our control model computations.

Fluid	**Herschel-Bulkley Model**
0.3% Xanthan NF-C Solution	$\tau = 0 + 0.20 \cdot \dot{\gamma}^{0.60}$
0.5% Xanthan NF-C Solution	$\tau = 0 + 2.26 \cdot \dot{\gamma}^{0.33}$

Table 3.3: Properties of Xanthan solution of different concentrations. $T = 22^{\circ}$C. (Unit of yield stress is Pa and unit of consistency is Pa·s^{n}.)

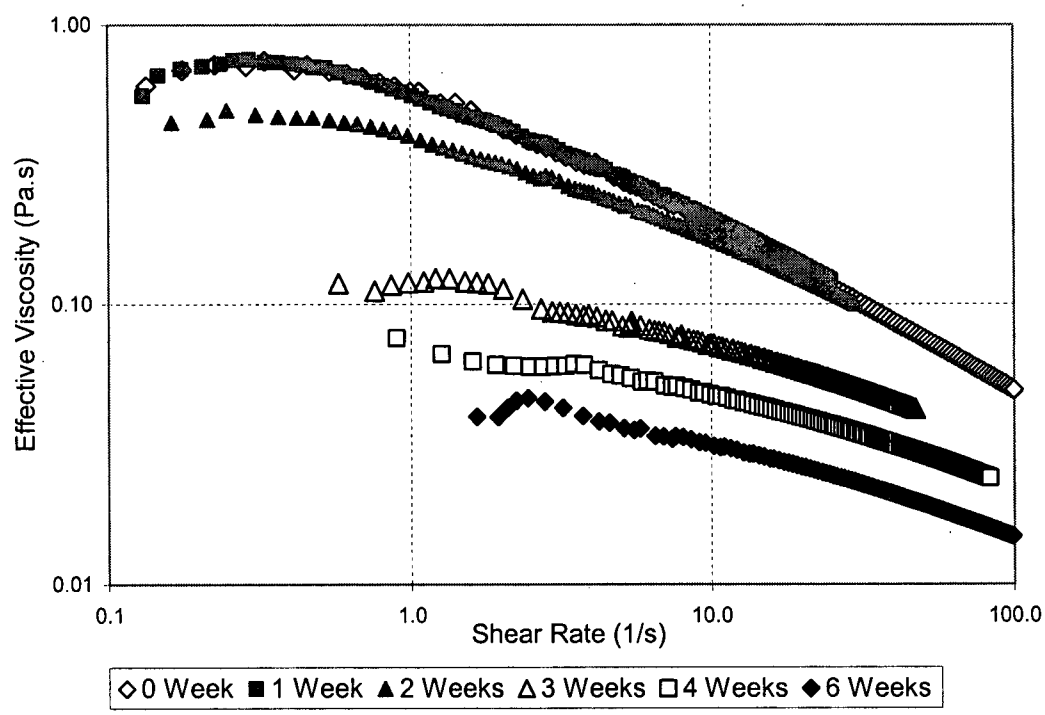

Figure 3.12: Flow curve of 0.3% Xanthan NF-C solution. Test is done once every week for 6 weeks to show its thixtropic characteristics. $T = 22^{\circ}$C.

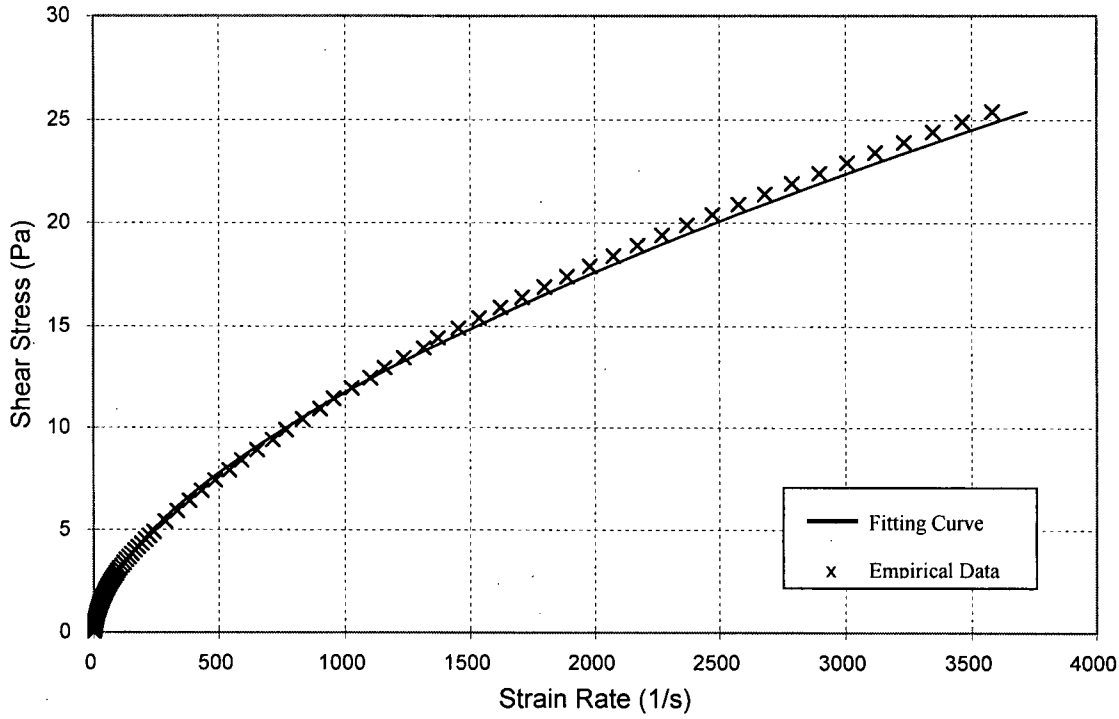

Figure 3.13: Flow curve of a 0.3% Xanthan NF-C solution. T = 22°C. Data points are fitted using MatLab nonlinear least-squares curve fitting function.

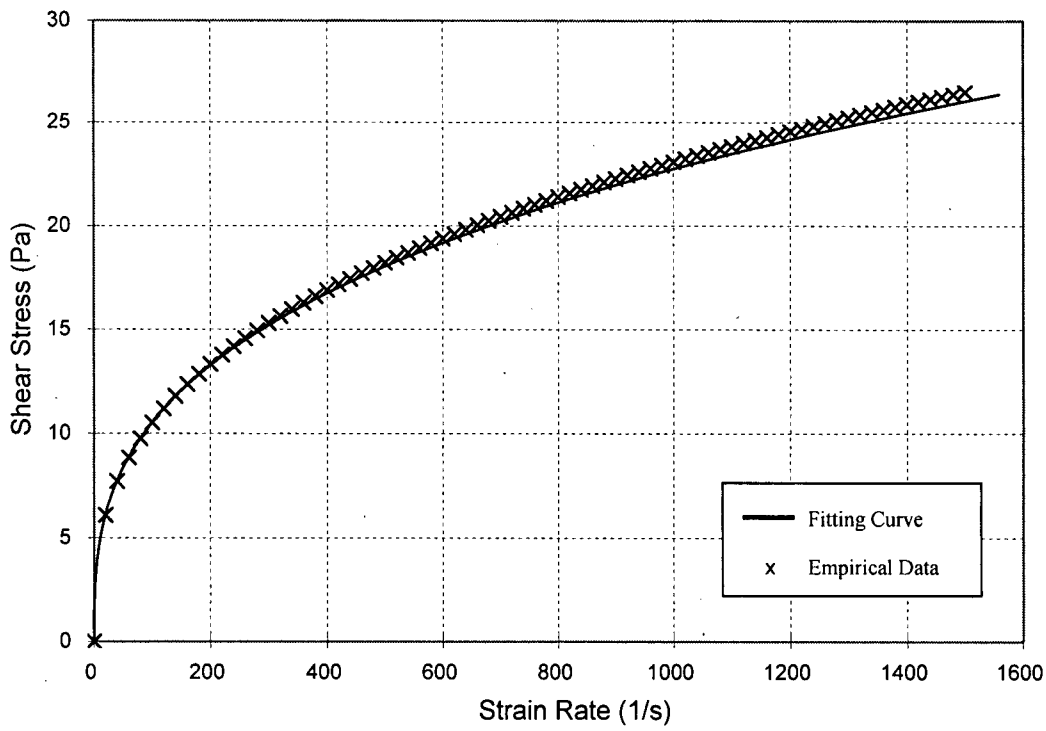

Figure 3.14: Flow curve of a 0.5% Xanthan NF-C solution. T = 22°C. Data points are fitted using MatLab nonlinear least-squares curve fitting function.

For Xanthan solution it is clear that its consistency and shear thinning characteristics increase with concentration. Similarly, for Carbopol its yield stress and consistency increase with concentration. However, it becomes less shear thinning for high concentration. To select a proper range of shear stress to perform a controlled stress test on one fluid, we do a quick estimation by using Equation 2.9. For a given pressure gradient, the largest possible shear stress occurs at the wall of the pipe so does the strain rate of the fluid. In our experimental plan the flow rates of the two fluids have been designated to be 0 to 50 ml/s. Since a large flow rate implies a large pressure gradient, we may use the two 50 ml/s lines in Figure 2.13 and find the pressure gradient for the corresponding interception. Apparently the pressure gradient for such flow rates is approximately 12 kPa/m. Thus for the lubricating fluid the greatest shear stress it may experience in our flow loop is:

$$\tau = \frac{0.0254}{2} \cdot 12 \times 10^3 = 152.4 Pa$$

And from the inner fluid the greatest shear stress that it may experience should occur at R_i. From our mathematical model we know that $R_i \approx 3$ mm.

$$\tau = \frac{0.003}{2} \cdot 12 \times 10^3 = 18 Pa$$

To ensure the range of our rheological data is large enough for our mathematical model, for a controlled stress test we always set the upper limit to be at least 200 Pa for the lubricating fluid, and 25 Pa for the inner core fluid.

3.4 Experiments

Achieving a stable multi-layer flow is complicated. The stability of the flow and the interfacial radius depends on many parameters such as the yield stresses, viscosities, densities and flow rates of both inner and lubricating fluids, the pressure gradient, and the length of the pipe, etc. To completely observe effects contributed by each of the parameters on the interface, hundreds of experiments might be needed. Thus instead of doing experiments with respect to each of the parameter, we have decided to focus on the concentration of the inner core fluid and lubricating fluid, which is anyways a more

industrial relevant parameter. In this section we first discuss how we design our experimental plan by performing a factorial design. Second, we discuss how we classify a flow as stable for our experiments. Finally, we discuss how a typical experiment is done.

Factorial Design

Factorial design technique is used to generate a detailed experimental plan. It is ideal to observe how a multi-layer flow reacts with different fluids of different concentration with the minimum number of experiments. A 2 X 2 factorial is generated with a high and a low concentration of each of the two fluids. This yields a total of 4 sets of experiments as shown in Table 3.4. It is expected that flow rates of the two fluids should alter the location of the interface. Thus, for each set of the experiment, flow rates of the two fluids are varied from 5 ml/s to 50 ml/s, with 10 ml/s increments. This yields a total of approximately 30 experiments for each set. With this number of experiments we should be able to identify for each pair of fluids, their stable and unstable regions. Measurements of the interfacial radius are also compared with the ones predicted from the fluid rheologies, at fixed (Q_1, Q_2), as discussed in Chapter 2. The test values for high and low concentration are 0.5% and 0.3% respectively, and are selected based on capabilities of the two pumps.

Experiment Set #	Xanthan NF-C Solution	Carbopol 940 Solution at pH 5.0
1	—	—
2	+	+
3	—	+
4	+	—
	+ = 0.5%, — = 0.3%	

Table 3.4: Factorial design of our experimental plan with 2 concentrations of each inner core fluid and lubricating fluid.

3.4.1 Classifying a Stable Flow with Spatiotemporal Plots

From the numerical model we discussed in Chapter 2, it is clear that for a given pair of fluids we should measure the pressure gradient, interfacial radius, and the flow rates of the inner core fluid and lubricating fluid. However, looking at these quantities does not tell us if one flow is stable or not. Guidelines are needed for classifying a flow as stable

or unstable. For all our experiments the following conditions must be satisfied for a flow to be classified as a stable flow.

1. It must become fully developed after a sufficient long time, i.e. behaviour of the flow should become constant after a time of L/U_i (see section 4.5).
2. The inner core fluid and lubricating fluid must not mix anywhere within the entire length of the pipe.
3. Inner core fluid must flow along the center line of the pipe for the entire length of the pipe, i.e. if a corkscrew flow pattern as shown in Figure 3.15 is observed for the inner core fluid then the flow is classified unstable.
4. The interface between the inner core fluid and lubricating fluid must remain sharp and clean for the entire length of the pipe. A fuzzy interface implies the flow is becoming unstable.
5. Interfacial perturbations must not propagate downstream, at any velocity other than the interfacial velocity. This means that an interfacial non-uniformity may be "frozen" into the unyielded interface and advected stably along the pipe. This condition is confirmed by inspecting the spatiotemporal plot of the flow.

Flows that are not classified as stable are classified as unstable. This classification is made based on examination of the video record of an experiment and by examining spatiotemporal plots of each displacement (see below for description). In most cases it is obvious whether the flow is stable or not.

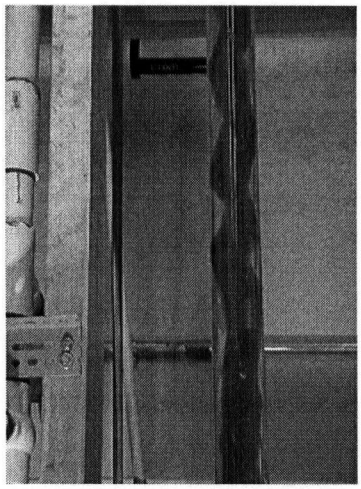

Figure 3.15: Flow is classified as unstable if corkscrew flow pattern is observed. Inner core fluid is water and lubricating fluid is 0.3% Carbopol 940 at pH 5.0. Q_1 = 15 ml/s and Q_2 = 10 ml/s.

Spatiotemporal Plot

A spatiotemporal plot is a qualitative way to represent variations in the width of the inner core fluid with respect to time and axial position of the pipe. Each experiment is video taped. We capture a video frame of the fully developed flow and process it using MatLab. From each frame we are able to obtain an estimate of the interfacial radius as a function of axial position. In general they are averaged to one value and compared with the value obtained from the mathematical model. However this does not allow us to present our interfacial measurements versus time and axial position of the pipe. To solve this problem we generate spatiotemporal plots. The plot is generated by averaging the pixel values across the width of the pipe at each height. The color intensity of each pixel of a spatiotemporal plot indicates the amount of the inner core fluid. Assuming the inner core fluid remains in a central column, a dark color pixel on the spatiotemporal plot implies a large interfacial radius value. A completely black pixel may imply the pipe is completely filled with the inner core fluid or the two fluids have mixed together. Another way to generate the spatiotemporal plot is to use the R_i values from the edge detection algorithm. However such detection requires a relatively clean interface and the algorithm often fails when the two fluids start mixing. Thus, the time domain of the spatiotemporal plot must be when the flow is approaching fully developed if values from the edge detection algorithm are used. However spatiotemporal plots are more interesting when the flow is developing, perturbed, or unstable, and it is not efficient to use the edge detection algorithm during such time domain. Thus, the edge detection algorithm is not used for generating spatiotemporal plots.

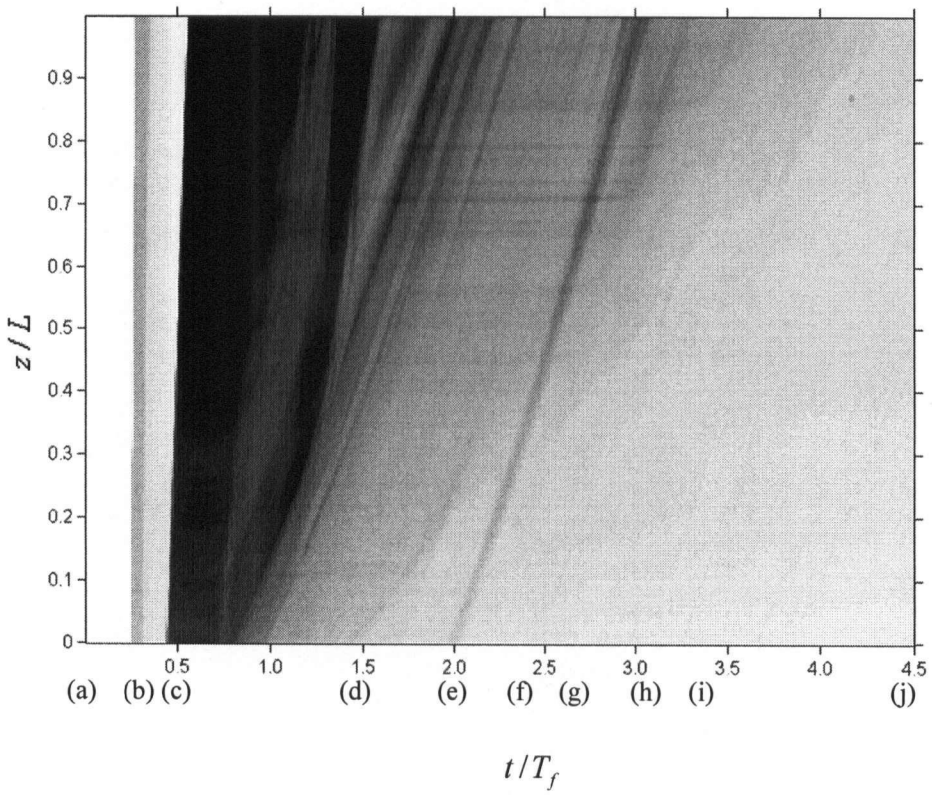

Figure 3.16: Spatiotemporal plot of a stable multi-layer flow experiment. Inner core and lubricating fluids are 0.3% Xanthan solution and 0.3% Carbopol solution at pH 5.0. Q_1 = 5 ml/s and Q_2 = 10 ml/s. The capture length, L, of the video is 0.18 m, and time is normalized by T_f, which is defined as L/U_i and is approximately equal to 42 s. A puff of the inner core fluid is observed near the bottom at $t/T_f = 2.0$. Letters below indicate the corresponding time for each of the images in Figure 3.17.

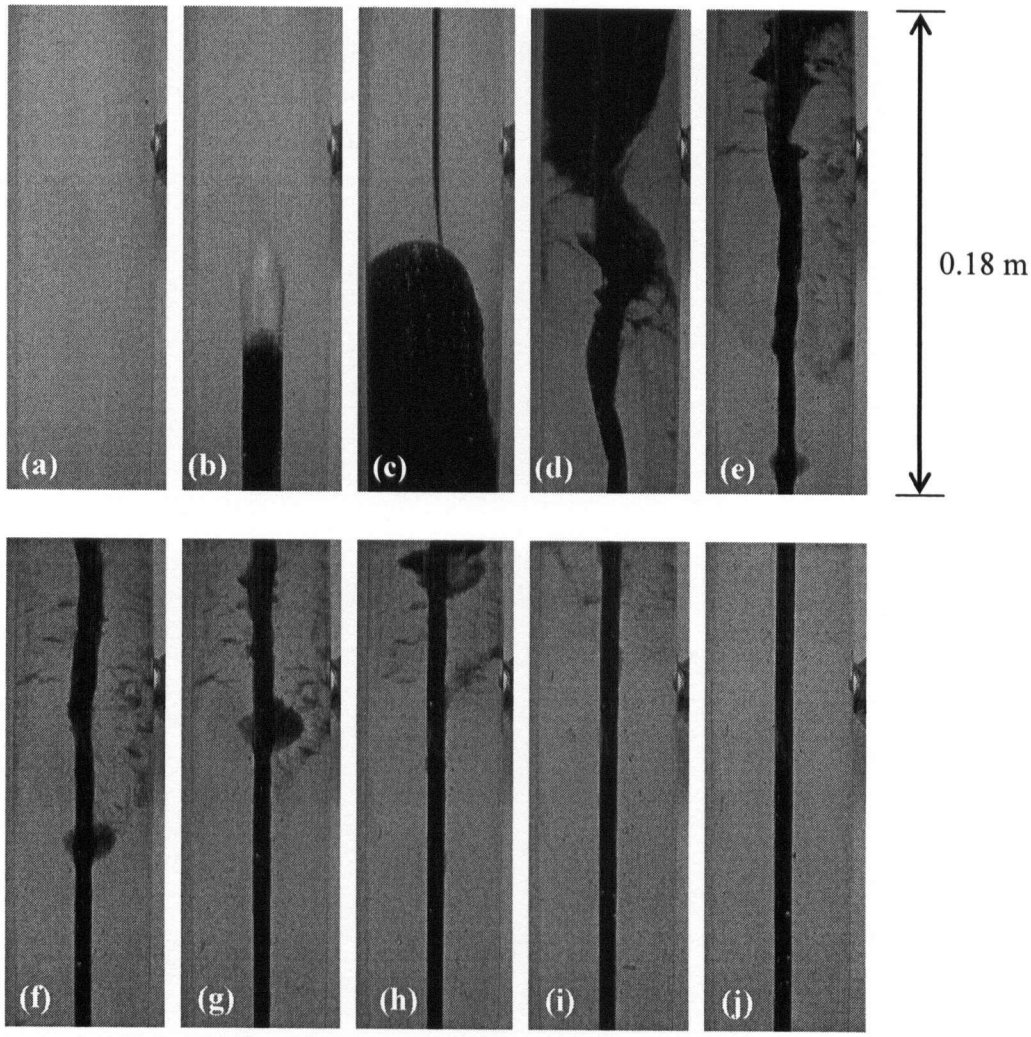

Figure 3.17: Snap shots of a stable multi-layer flow experiment. Inner core and lubricating fluids are 0.3% Xanthan solution and 0.3% Carbopol solution (pH 5.0). $Q_1 = 5$ ml/s and $Q_2 = 10$ ml/s. A puff of the inner core fluid is observed near the bottom in (e), and (f) to (h) show that the puff expands as it travels along the pipe. (a) $t = 0$ s, (b) $t = 10$ s, (c) $t = 20$ s, (d) $t = 60$ s, (e) $t = 85$ s, (f) $t = 100$ s, (g) $t = 110$ s, (h) $t = 123$ s, (i) $t = 140$ s, (j) $t = 185$ s.

An example of a spatiotemporal plot from the initial phase of a stable experiment is shown in Figure 3.16. For the spatiotemporal plot, the axial position, z, is normalized by the length of the video capture region, L, which is 0.18 m. Time is scaled by T_f which is defined as the time required for the interface to travel from the bottom to the top of the image, i.e. $L/U_i = 42$ s. The camera is located 0.5 m away and capturing 0.18 m of the loop. The inner core fluid and lubricating fluid are 0.3% Xanthan solution and 0.3% Carbopol solution. Their respective flow rates are 5 ml/s and 10 ml/s. We see the displacement front of the inner core fluid as it is pumped into the tube as shown in Figure 3.17. Initially the loop is occupied by the mixture of the two fluids. Quickly a fresh and non-uniform interface and the two fluid domains appear starting at the inlet. As the flow develops, the interface become sharp, clear, and uniform as all irregularities of the interface are frozen in the unyielded fluid layer and pumped out at the end of the pipe. From the spatiotemporal plot, it is clear that the flow establishes into a stable multi-layer flow at $t/T_f = 3.5$. One interesting point to look at is the dark line origins at $t/T_f = 2.0$. It corresponds to a puff of the inner core fluid as shown in Figure 3.17(e). The spatiotemporal plot indicates that the puff expands as it travels downstream and agrees with our video record. The light black horizontal lines between $t/T_f = 1.5$ and $t/T_f = 3.5$ indicate some of the inner core fluid rests in the lubricating layer without moving, i.e. there is residual layer of the lubricating fluid on the wall of the pipe, or the lubricating layer is partially static.

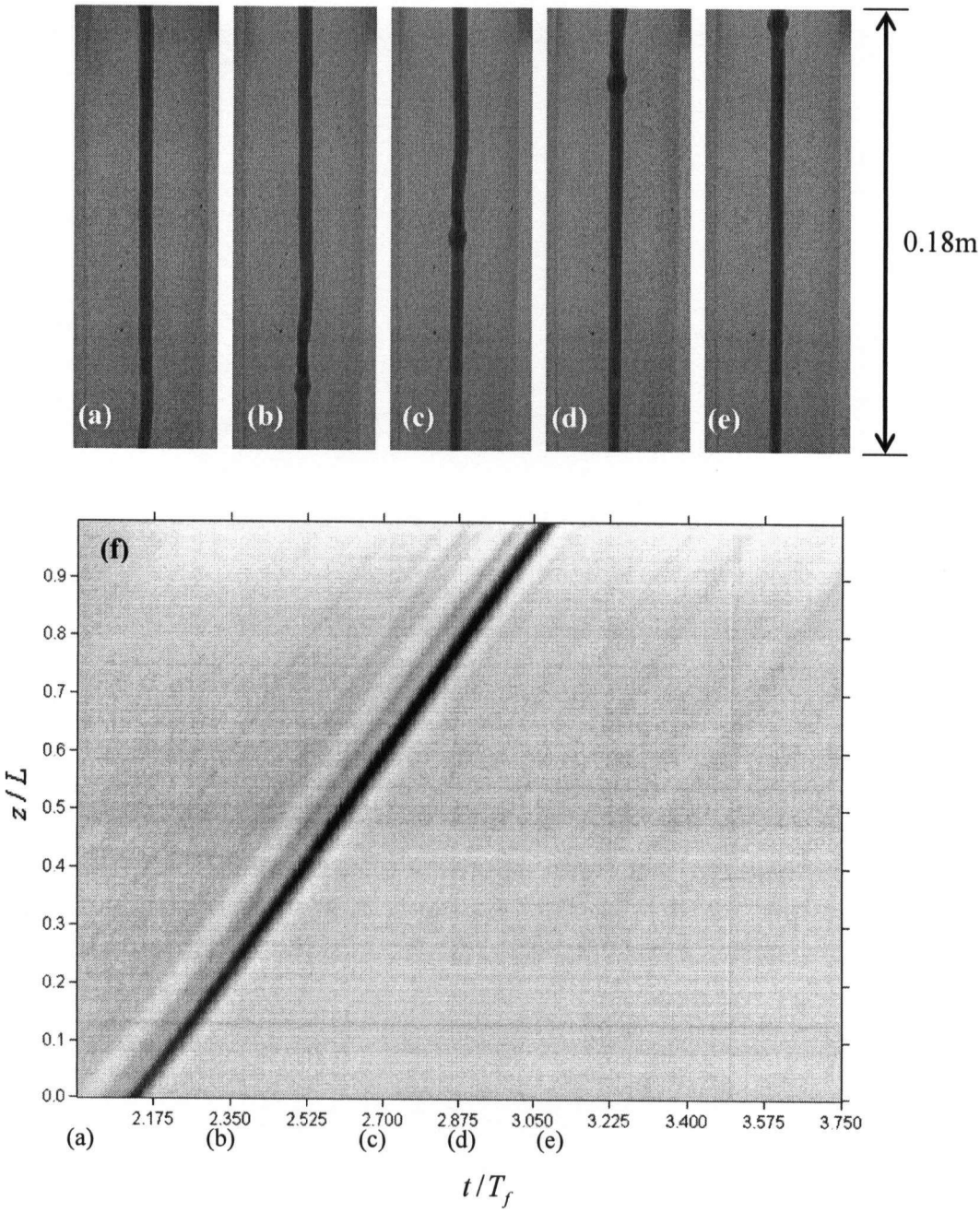

Figure 3.18: Snap shots of a stable experiment. Inner core fluid is 0.3% Xanthan solution and lubricating fluid is 0.3% Carbopol solution at pH 5.0. Q_1 = 15 ml/s and Q_2 = 15 ml/s. Flow is disturbed artificially by squeezing the inner core fluid connection pipe. No propagation of disturbance is observed. t/T_f = (a) 2.0, (b) 2.3, (c) 2.7, (d) 2.9s, (e) 3.1. (f) Spatiotemporal plot of the flow. Letters below indicate corresponding time for each of the images in (a) – (e). L = 0.18 m and T_f = 15 s.

A second example, from later in a stable run is shown in Figure 3.18. Again the axial position of the spatiotemporal plot is scaled by the length of the capture region, L, i.e. 0.18 m, and time is scaled by T_f which is approximately equal to 15 s. For a stable flow, theoretically the corresponding spatiotemporal plot could be monotonous, i.e. the plot should be identical everywhere with the same colour since the interface is uniform and stable. However in reality there are inevitable perturbations on the flow such as vibrations from pumps and the surface roughness of the pipe wall. Therefore, the spatiotemporal plot of an actual experiment, stable or unstable, should consist of dark and light color regions due to inconsistent interfacial radius along the axial position of the pipe. The slope of the line patterns indicates the velocity of the interface. To classify a flow as stable or unstable, we can pay attention to the line patterns. If the dark colour regions expand as they travel downstream, it implies the interface is not stable and interfacial perturbations propagate downstream. On the other hand, if no expansion of dark color region is observed, it shows that interfacial perturbations are suspended in the unyielded fluid and not being amplified. Again, the purpose of a spatiotemporal plot is not to present the interfacial radius value quantitatively, but to show whether one flow is stable or not, qualitatively. In Figure 3.18, after the flow becomes fully developed, we disturb the flow artificially by squeezing the inner core fluid connection pipe. A puff of the inner core fluid is observed with no expansion as it travels downstream. The vertical and horizontal lines in the spatiotemporal plot are the background light intensity. The sloped lines show propagation of interfacial irregularities. It is clear that the slope is constant and disturbances are simply adverted along the pipe.

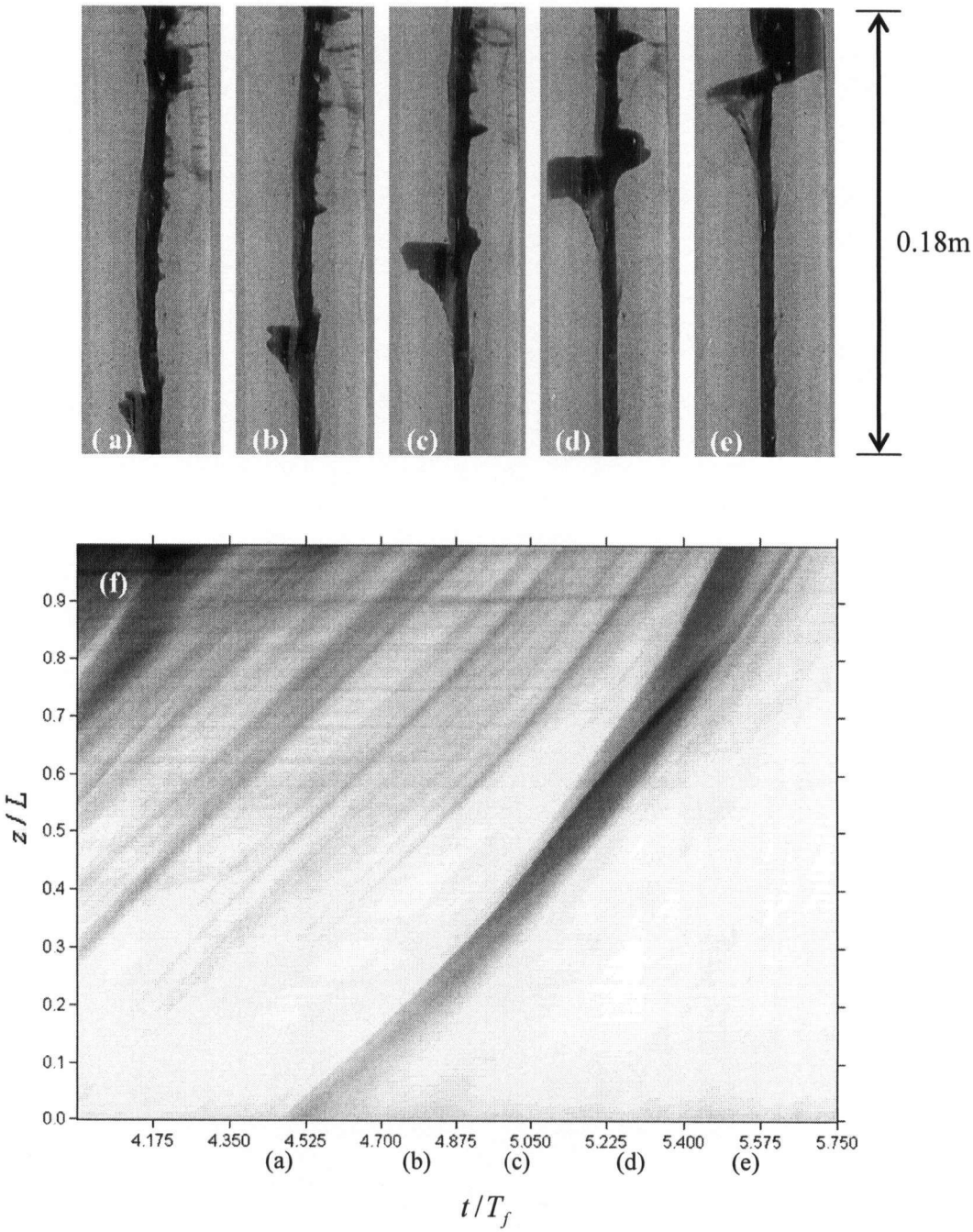

Figure 3.19: Snap shots of an unstable experiment. Inner core and lubricating fluids are 0.3% Xanthan solution and 0.3% Carbopol solution at pH 5.0. Q_1 = 25 ml/s and Q_2 = 25 ml/s. t/T_f = (a) 4.5, (b) 4.7, (c) 5.0, (d) 5.3, (e) 5.5. (f) Spatiotemporal plot of the flow. Letters below indicate corresponding time for each of the images in (a) – (e). L = 0.18 m and T_f = 15 s.

An example of a spatiotemporal plot of an unstable flow is shown in Figure 3.19. Between $t/T_f = 4.5$ and 5.6, a puff of the inner core fluid appears at the bottom of the video record and expands into the lubricating layer quickly as it travels downstream. From the spatiotemporal plot one may notice sloped lines do not have constant slope, which indicates that irregularities of the interface propagate at speeds other than the interfacial velocity, i.e. the non-uniformity of the interface is no longer frozen in the unyielded layer and the flow is unstable.

3.4.2 A Typical Experiment

In this section we show in illustrated form the typical sequence of events that take place in an experiment. The inner core fluid is 0.3% Xanthan NF-C solution and the lubricating fluid is 0.3% Carbopol 940 with a pH level of 5.0. The respective designated flow rates are 10 ml/s and 25 ml/s (Set 1 Test 17). The flow is expected to be stable according to the numerical model. To begin the experiment, reservoir 1 and 2 are first filled with the inner core fluid and lubricating fluid respectively. Then, inner core fluid is pumped up to the inlet of the plexiglass pipe and stopped. The ball valve between reservoir 1 and the loop is closed to prevent any inner core fluid get drawn into the loop by the movement of the lubricating fluid. We start pumping the lubricating fluid at the designated flow rate, i.e. the Monyo 332 PC pump is set to 13% of full speed which should give a flow rate of 25 ml/s. As soon as it reaches the top of the loop, we open the ball valve in the path of the inner core fluid, and start pumping the inner core fluid at its designated flow rate, i.e. we set the speed of the Monyo 1000 PC pump to 378 RPM which should give a flow rate of 10 ml/s. All pressure sensors, flowmeters, and digital video cameras are turned on for monitoring and data acquisition purposes. It is important to allow sufficient time for the flow to become fully developed. In general each experiment lasts for roughly 30 minutes and consumes 38 liters of each fluid.

Initially when the flow starts up, the displacement front is messy and the two fluids mix together as shown in Figure 3.20 and 3.21. To illustrate the experiment more clearly, one camera is posited far enough from the loop to capture the entire length of the pipe, i.e. roughly 2.2 m of the loop. Another camera is posited 0.5 m above the manifold to capture the detailed behaviour of the interface, i.e. 0.18 m of the loop. As the flow develops, a clear interface appears starting at the manifold at the bottom of the loop. After 5 minutes, the mixed zone exits the pipe and the flow approaches steady state. The interface is sharp and clear, and no new mixing or puff of the two fluids is observed. The experiment

carries on for another 10 minutes. No instability of the interface is observed, and therefore the flow is now classified as stable by visual inspection. In fact, visually there is no difference between the flow at t = 300 s and t = 600 s. We turn off all the equipment such as the data acquisition system, pumps, and pressure sensors etc, and we start post processing our data and video record. Although no actual measurements are taken regarding the symmetry of the flow, by visual inspection the assumption of a stable multi-layer be axisymmetric is reasonable.

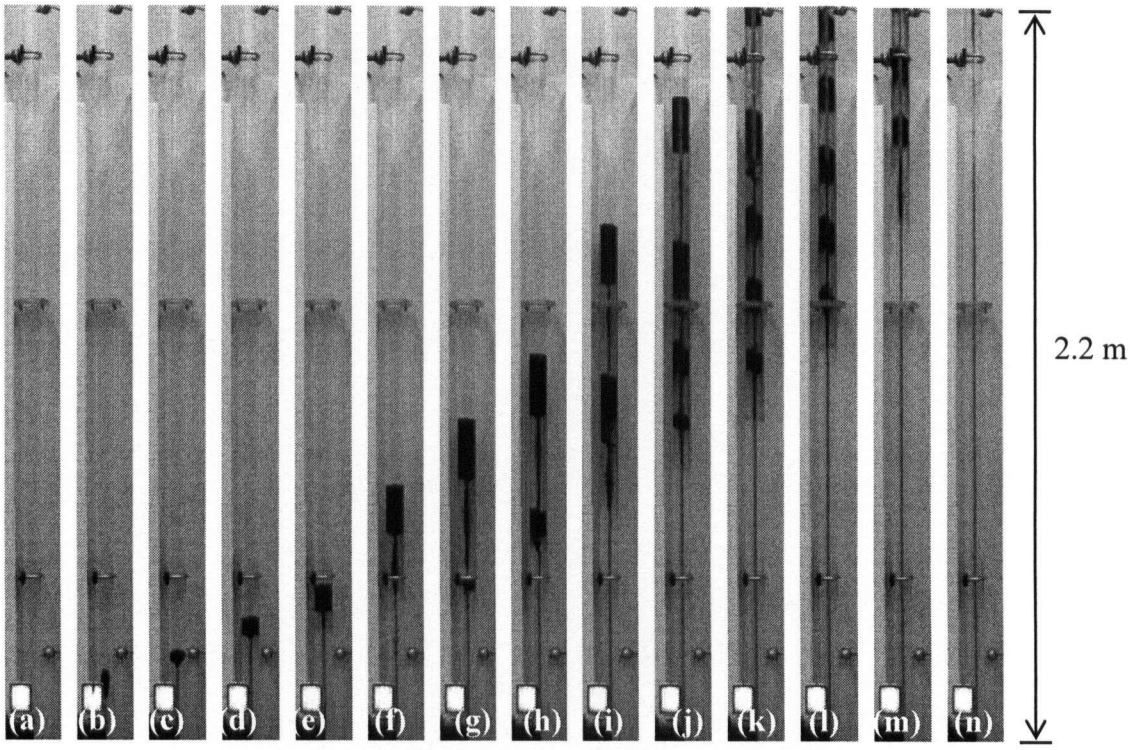

Figure 3.20: Snap shots of the typical experiment discussed in section 4.1. The actual length of the snap shots is 2.2 m. (a) t = 0 s, (b) t = 3 s, (c) t = 5 s, (d) t = 10 s, (e) t = 15 s, (f) t = 30 s, (g) t = 40 s, (h) t = 50 s, (i) t = 70 s, (j) t = 90 s, (k) t = 110 s, (l) t = 140 s, (m) t = 200 s, (n) t = 300 s.

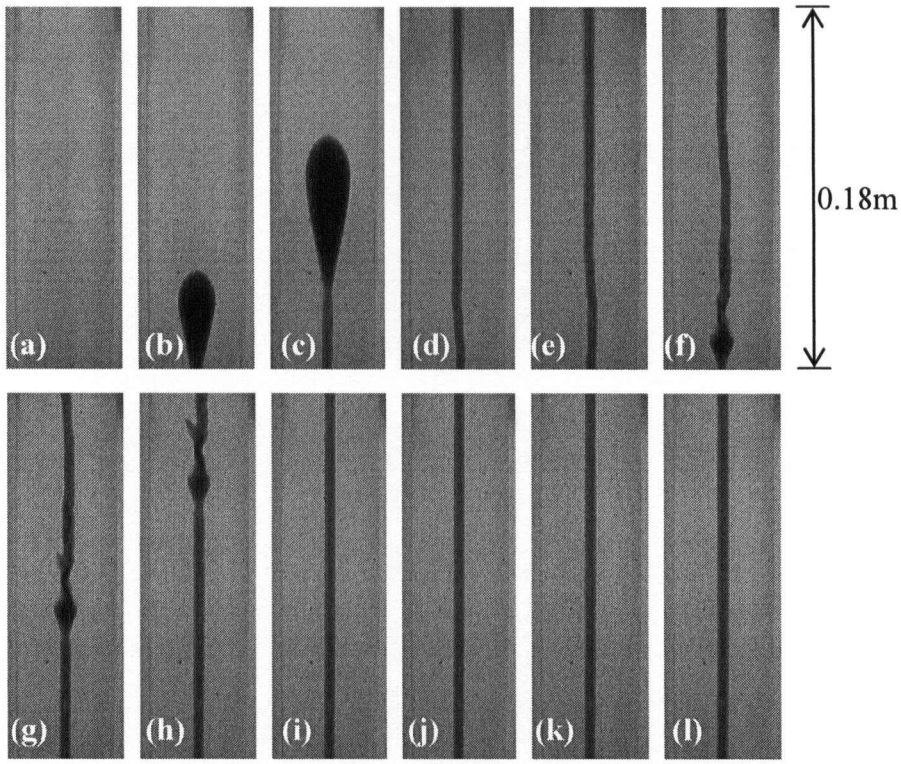

Figure 3.21: Close-up snap shots of the typical experiment discussed in section 4.1. Camera is focusing at 0.5 m above the manifold and capturing 0.18 m of images. (a) $t = 0$ s, (b) $t = 1$ s, (c) $t = 2$ s, (d) $t = 5$ s, (e) $t = 7$ s, (f) $t = 12$ s, (g) $t = 17$ s, (h) $t = 22$ s, (i) $t = 32$ s, (j) $t = 42$ s, (k) $t = 52$ s, (l) $t = 300$ s.

Classifying the Flow with Spatiotemporal Plots

Although the flow has been classified as stable by visual inspection, it is important to generate spatiotemporal plots to inspect any interfacial instabilities that are less obvious. For the spatiotemporal plots generated for this experiment, the time is scaled by T_f which is 13.5 s and axial position, z, is scaled by the length of the capture region, L, which is 0.18 m. It is sensible to pay attention on the beginning, middle, and the end of the experiment. Three spatiotemporal plots are generated with the close up video captured 0.5 m above the manifold and shown in Figure 3.22 to 3.24. In the first spatiotemporal plot, it is clear that from $t/T_f = 0$ to 0.52, the loop is filled with only the lubricating fluid. At $t/T_f = 0.52$, a black line appears and consists of a relatively steep slope compared with the two obvious light grey lines which appear later at $t/T_f = 1.33$. It implies the inner core fluid displacement front appears in the camera at $t/T_f = 0.52$ and travels at a speed slightly faster than the interfacial velocity. At $t/T_f = 1.33$, a noticeable puff of the inner core fluid is observed but frozen in the unyielded layer. It is advected downstream without

expansion or propagation. The capture region becomes fully developed as all the disturbances exit the camera at t/T_f = 2.67. Again it does not mean the entire flow becomes fully developed at t/T_f = 2.67, but only the bottom half of the loop that is inside the capture region. According to Figure 3.20, the entire flow does not become steady until t = 22.22 s.

The time domains for the second and third spatiotemporal plots are t/T_f = 22.00 to 24.44, and 39.78 to 44.00. The two plots are less interesting due to the fact that the flow is very stable and the interface is very uniform. In Figure 3.23, a dark line appears across the entire plot and has a slope much smaller than the interfacial velocity. It has been verified that it is a small metal chip that sits near the pipe wall. Since it is so close to the wall, its velocity is much slower than the interfacial velocity. One should notice there are dark vertical lines shown in the plots indicating the entire tube is oscillating between bright and dark. It is suspected that this noise comes from the background lighting which is provided with fluorescent light tubes. Other than the vertical lines, one should also observe grey sloped lines due to minor irregularities of the interface. Their slopes are constant which implies all disturbances are advected downstream at interfacial velocity. It is evident enough to classify this experiment as a stable experiment.

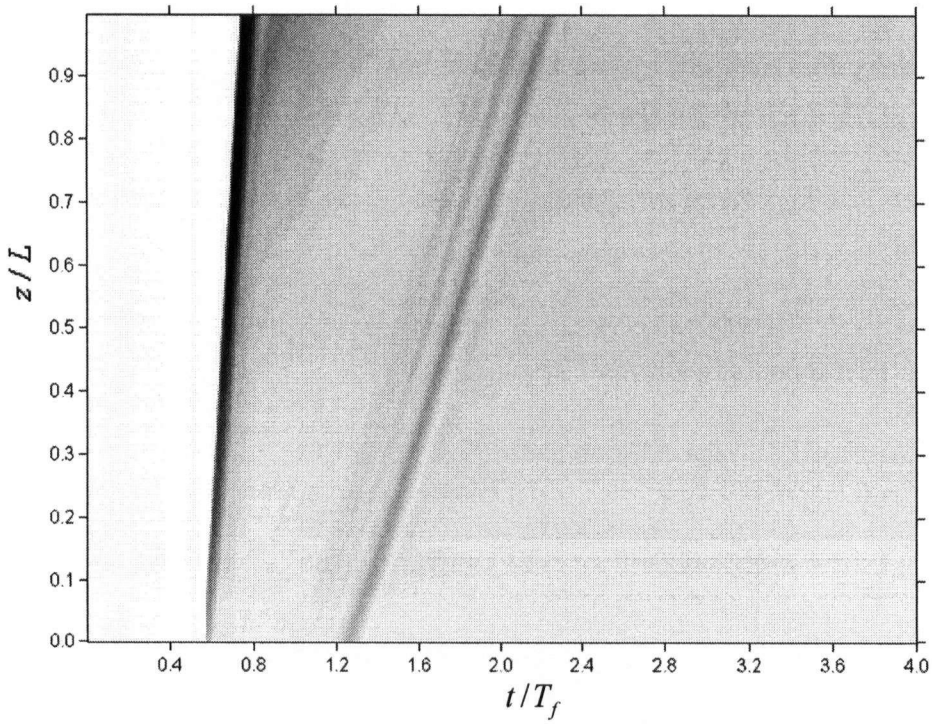

Figure 3.22: Spatiotemporal plot of the typical experiment discussed in section 3.4.2. The inner core fluid enters the video capture region at t/T_f = 0.5 s.

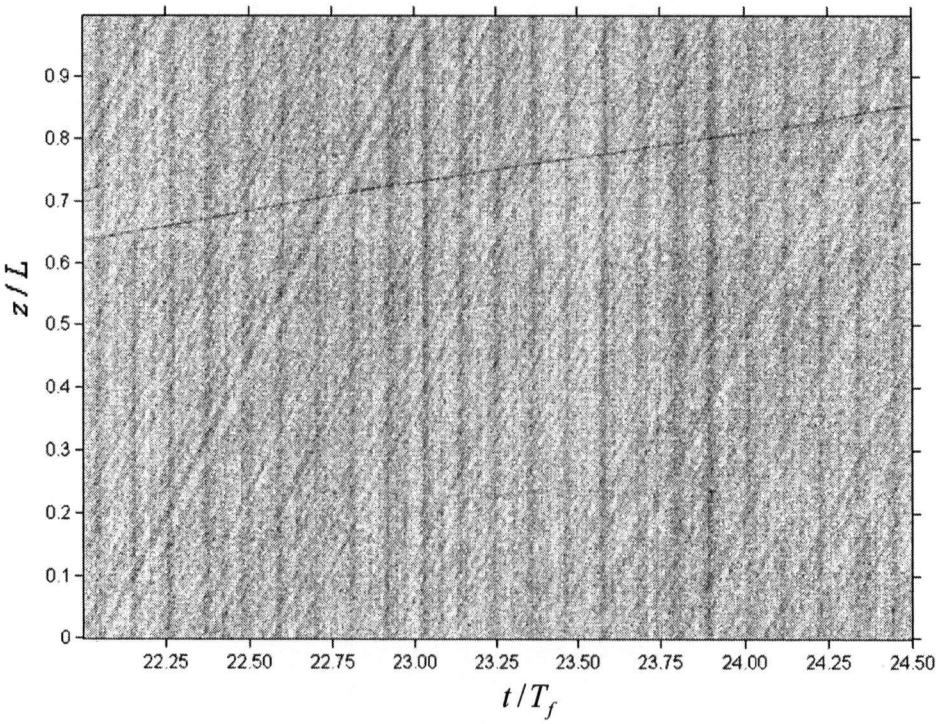

Figure 3.23: Spatiotemporal plot of the experiment discussed in section 3.4.2. The flow is stable and irregularities of the interface travel at the interfacial velocity.

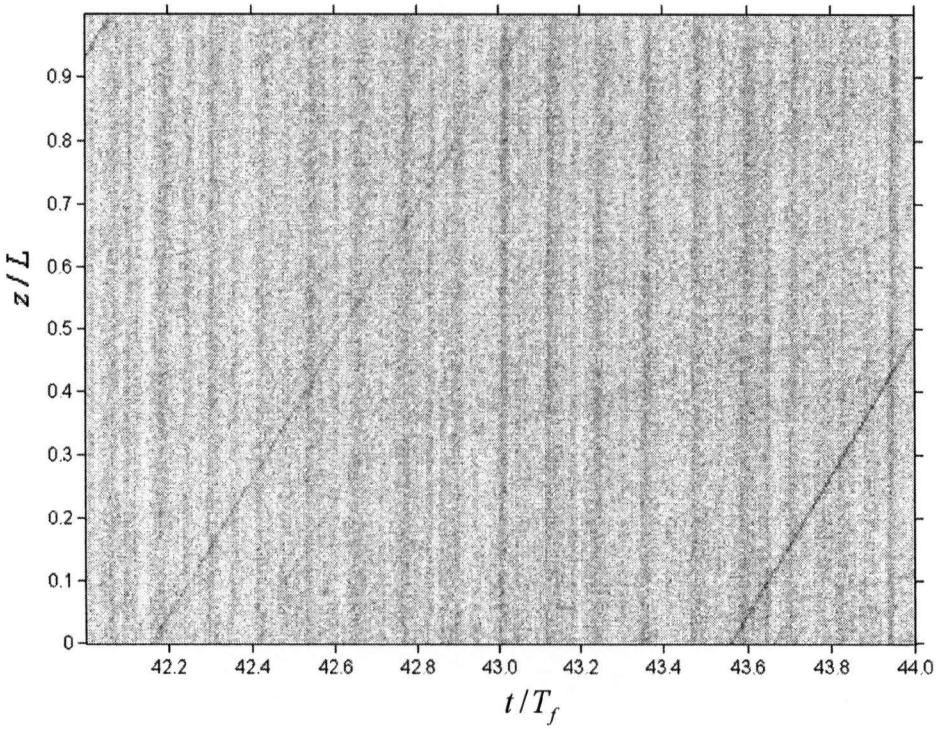

Figure 3.24: Spatiotemporal plot of the stable experiment discussed in section 3.4.2.

Flow Rate Measurement

After confirming the flow is stable, we begin processing the flow rate data. As mentioned our data acquisition system records only the net volumetric flows of the two fluids, and thus to calculate the actual instantaneous flow rates of the two fluids a MatLab code is used to numerically differentiate the data. The flow rate plots of the two fluids are shown in Appendix E, and the average Q_1 and Q_2 over the entire experiment are 9.7 ± 2.0 ml/s and 24.7 ± 1.5 ml/s respectively. With Q_1 and Q_2, we can predict R_i and $\partial P/\partial z$ with our surface plots generated with our mathematical model as shown in Figure 2.14 and 2.15. We model predicts that for the given Q_1 and Q_2, R_i is 2.39 mm and $\partial P/\partial z$ is 10.06 kPa/m.

R_i Measurement

As shown in Figure 3.25, a 15-second video clip of the experiment is used to estimate R_i. 315,500 measurement values are obtained through image analysis and the averaged R_i is 2.47 ± 0.5 mm at the 95% confidence interval (2.45, 2.49). Comparing the R_i measurement with the predicted value:

$$\begin{aligned} \%\ \text{Difference} &= \frac{2.47 - 2.39}{2.39} \times 100 \\ &= 3.35\% \end{aligned}$$

which means our measured R_i is 3.35% larger than the predicted value.

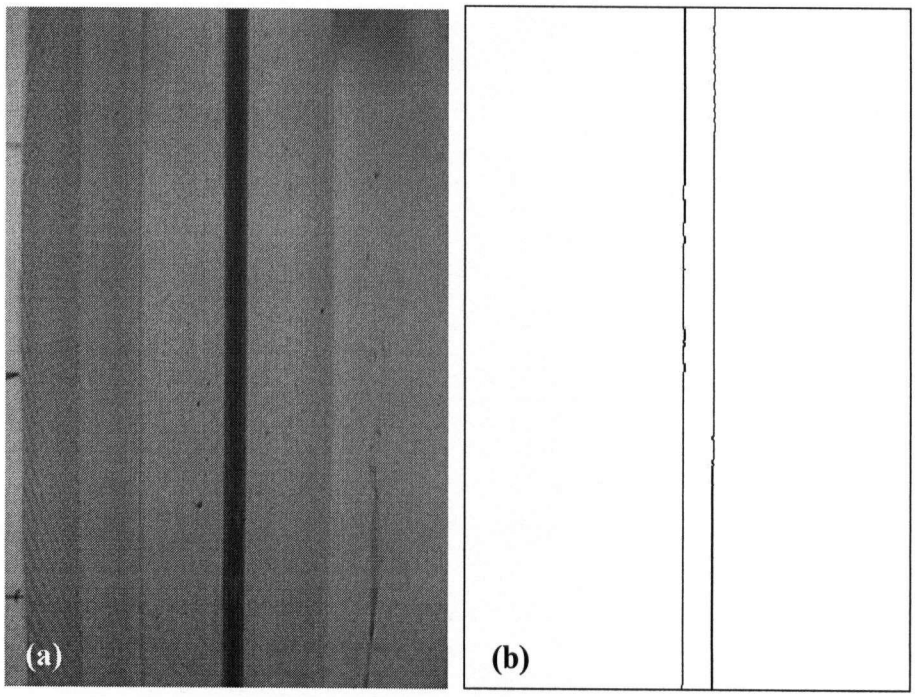

Figure 3.25: (a) A close up snap shot of the flow loop after the flow becomes fully developed. The actual axial length of the image is 0.18 m. The flow is stable and the image is used to measure the width of the inner core fluid. (b) A black and white image created with a Matlab code for determining the width of the inner core fluid. The width is measured by finding the distance between the two interfaces.

Summary of the typical experiment

The following table summarized the results obtained from this experiment.

Inner Core Fluid	Lubricating Fluid	Q_1 (ml/s)	Q_2 (ml./s)	Measured R_i (mm)	Calculated R_i (mm)	R_i % Difference	Observa-tion
0.3% Xanthan NF-C solution	0.3% Carbopol 940 solution (pH 5.0)	9.7	24.7	2.47	2.39	3.35	Stable

Table 3.5: Summary of the typical experiment.

The "Observation" column is filled with one of the followings:

1. Stable: The flow was stable and satisfied all the conditions listed in section

3.4.1.

2. Unstable 1: The flow became stable, then unstable, i.e. the flow satisfied the conditions listed in section 3.4.1 for a short duration. The interface became fuzzy and then at some height puffs of the inner core fluid appeared and perturbed the downstream of the flow either because there was no unyielded layer of the lubricating fluid or the unyielded layer was not strong enough to suspend the puffs.

3. Unstable 2: The flow never became stable or fully developed, i.e. mixing of the two fluids was observed throughout the experiment.

Chapter 4

Results

In this chapter we present results of 4 different sets of experiments as outlined in Table 3.4. Experimental results are compared with values obtained from the numerical model discussed in Chapter 2. All data tables are included in the appendices.

4.1 Set 1 Experiment

The inner core fluid for this set of experiments was 0.3% Xanthan NF-C solution and the lubricating fluid was 0.3% Carbopol 940 solution with a pH level of 5.0. Flow rates of the two fluids were between 5 ml/s to 50 ml/s. In Figure 4.1a, stable, unstable 1, and unstable 2 observations are marked with 'o', 'Δ' and 'x' respectively. Our mathematical model predicted well the transition between stable and unstable. As mentioned we assume the error for our yield stress measurements is ± 1 Pa. The shaded region represents the transition region and the dotted lines represent the corresponding transition boundaries. In Figure 4.1b experimental measurements of R_i for stable flows are plotted against mathematically calculated R_i. All unstable measurements are omitted since we do not expect them to follow our control model. Ideally we hope to see all data points lie on the line $y = x$ which implies our mathematical model can accurately predict the interfacial radius in an actual multi-layer flow. Although not all data points lie on the line, all stable measurements are within ± 10% of the calculated values as shown in Appendix F. A model utility test is included in Appendix U. One may notice data points are plotted with only y-error bars, i.e. only the measurement error is considered. The error for the predicted R_i (x-axis) mainly comes from the rheological data of the two fluids. However, according to the specifications of the rheometer the error for a strain measurement is tiny, i.e. in the order of 10^{-5}. In addition, the rheological data tables of the two fluids in Appendix T show that for a given stress there is no significant deviation between the strain measurements. Thus it is concluded that the error for a calculated R_i is small and all

x-error bars are omitted.

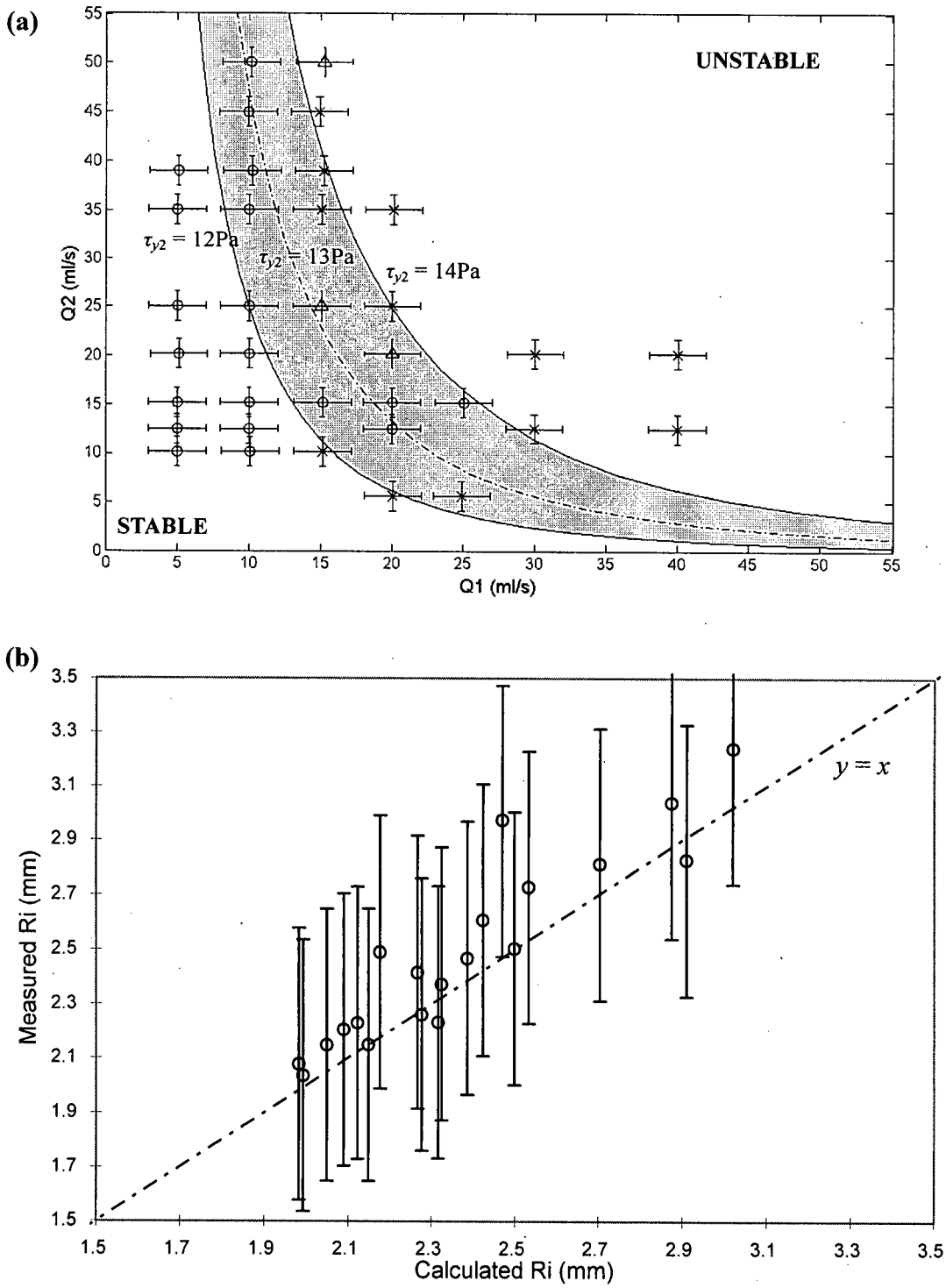

Figure 4.1: (a) Set 1 experimental observations plotted with respect to flow rates of the two fluids. Stable: 'O', unstable 1: 'Δ', and unstable 2: 'x'. Predicted transition region is shaded with grey. (b) Measured R_i versus calculated R_i.

4.2 Set 2 Experiment

For this second set of experiments, the inner fluid was 0.5% Xanthan NF-C solution and the lubricating fluid was 0.5% Carbopol 940 solution with a pH level of 5.0. The transition between stable and unstable was predicted well when Q_2 was between 30 ml/s and 50 ml/s. When Q_2 was smaller than 30ml/s, the actual transition occurred at a higher Q_1 than expected. Again, all stable measurements of the interfacial radius are within ±10% of the calculated values as shown in Appendix G. A model utility test is provided in Appendix V.

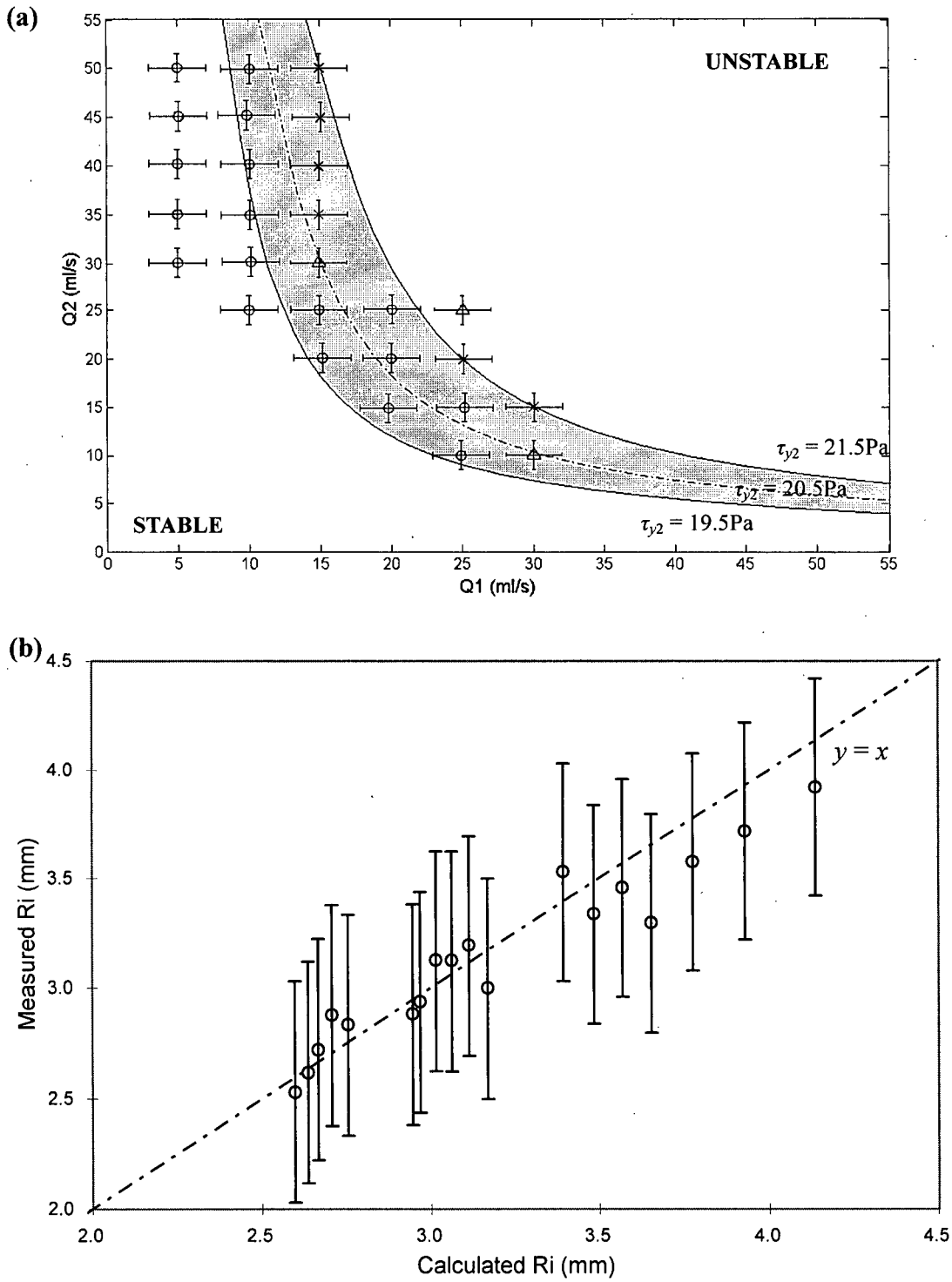

Figure 4.2: (a) Set 2 experimental observations plotted with respect to flow rates of the two fluids. Stable: 'O', unstable 1: 'Δ', and unstable 2: 'x'. Predicted transition region is shaded with grey. (b) Measured R_i versus calculated R_i.

4.3 Set 3 Experiment

For the third set of experiment the inner core and lubricating fluid were 0.3% Xanthan NF-C solution and 0.5% Carbopol 940 solution with a pH level of 5.0. According to our mathematical model for this given pair of fluid, the flow should always be stable within our operational region and we expected to see no unstable trials. Experiments for Q_1 greater than 30 ml/s were all omitted due to relatively high Reynolds number of the inner fluid (see section 4.5.2). Again, all stable measurements of interfacial radius are within ±10% of the calculated values as shown in Appendix H. A model utility test is provided in Appendix W.

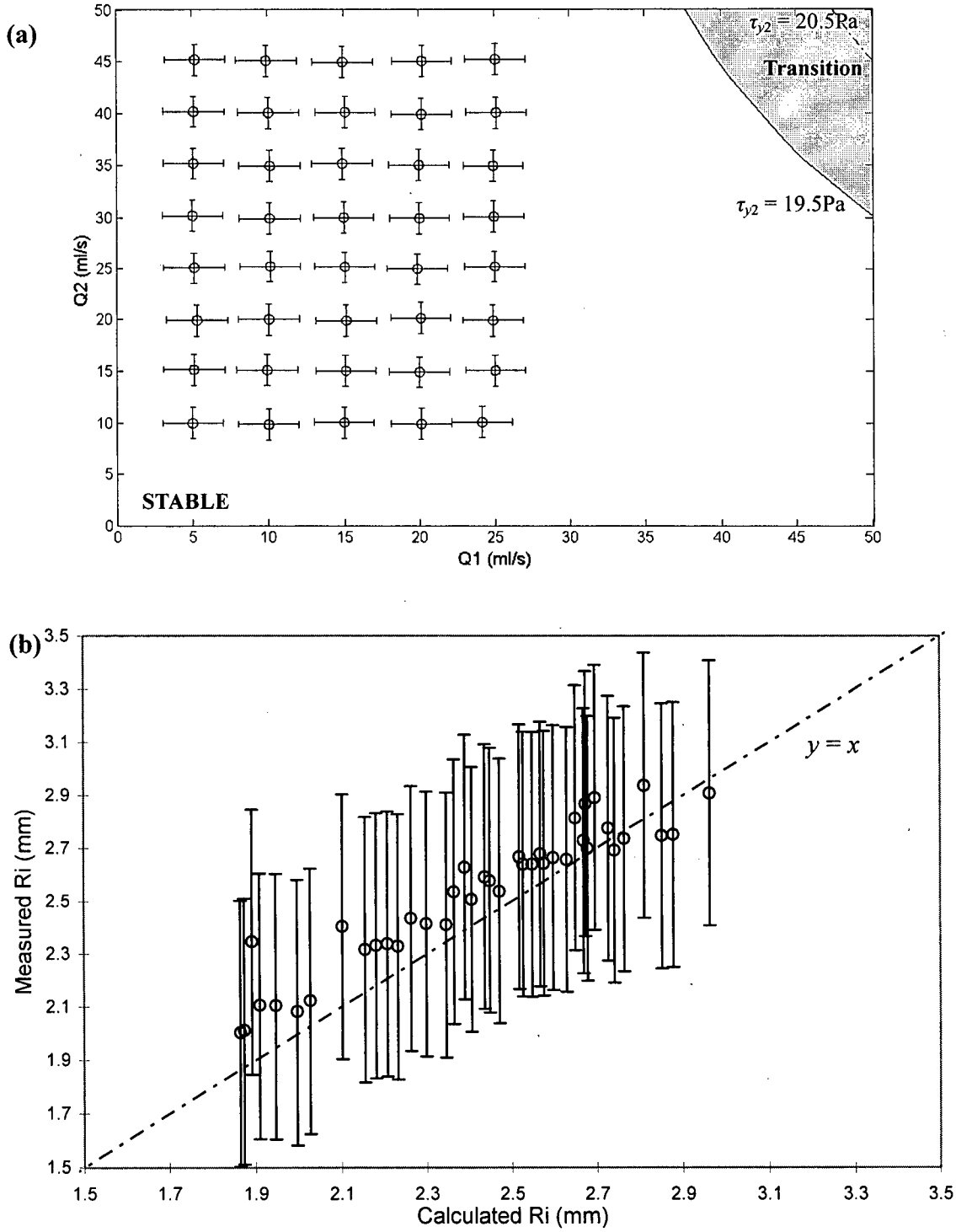

Figure 4.3: (a) Set 3 experimental observations plotted with respect to flow rates of the two fluids. Stable flows are marked with 'o' and no unstable flows were observed. Predicted transition region is shaded with grey. (b) Measured R_i versus calculated R_i.

4.4 Set 4 Experiment

For the final set of experiments, we used 0.5% Xanthan NF-C solution and 0.3% Carbopol 940 solution with a pH level of 5.0 as the inner core fluid and lubricating fluid respectively. Unlike the third set of experiments, we expected to have no stable observation according to our mathematical model. Surprisingly, flow seemed to be stable when the inner core fluid moved at low speed, i.e. approximately 5 ml/s. Flow became unstable very quickly as we increased the flow rate of the inner core fluid. The data table is shown in Appendix I. A model utility test is provided in Appendix X.

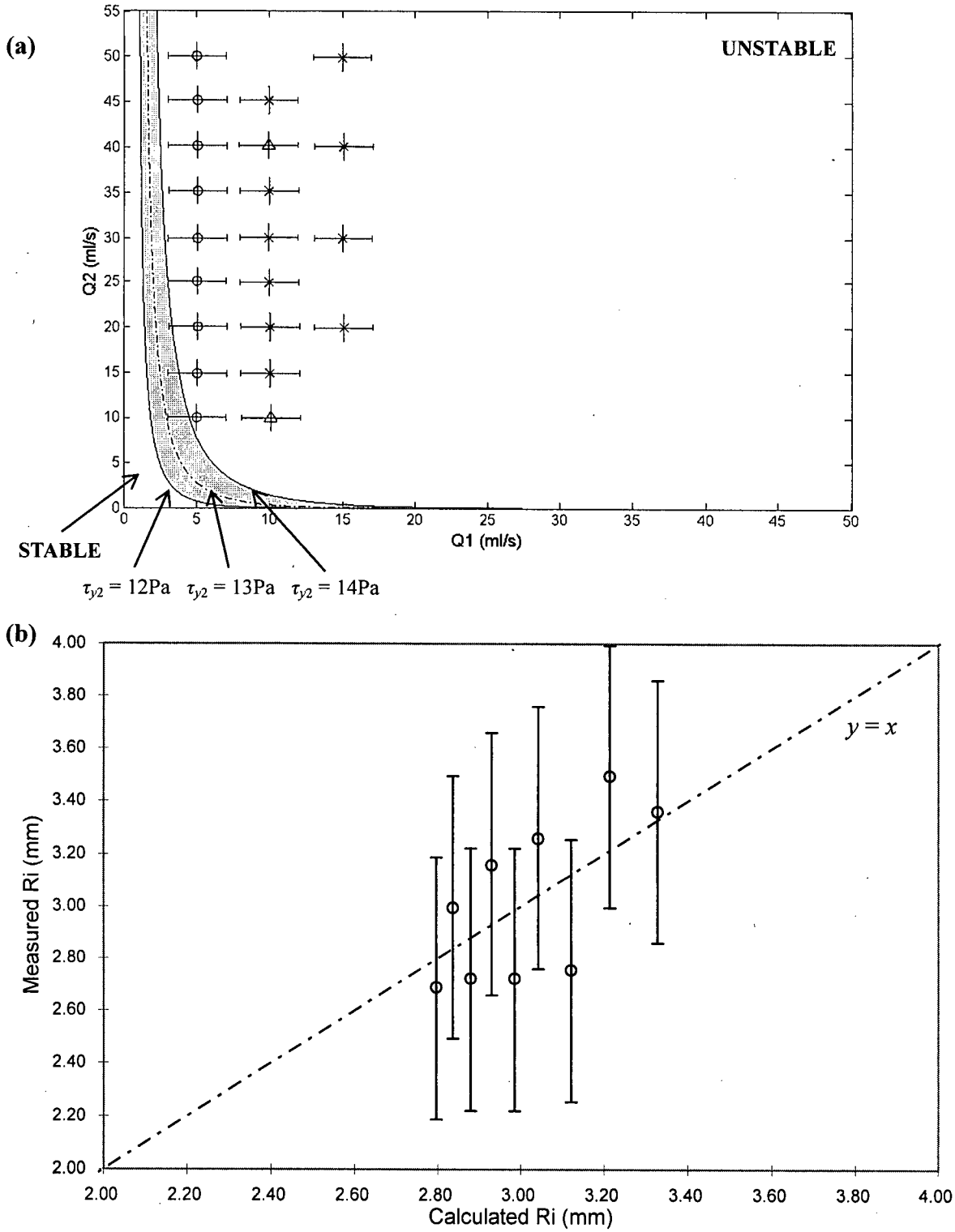

Figure 4.4: (a) Set 4 experimental observations plotted with respect to flow rates of the two fluids. Stable: 'O', unstable 1: 'Δ', and unstable 2: 'x'. Predicted transition region is shaded with grey. (b) Measured R_i versus calculated R_i.

4.5 Discussion of Observations

4.5.1 Experimental Observations

The followings were observed from our experiments.

At the beginning of each experiment:

- Loop was initially filled with the lubricating fluid and was flowing at the designated flow rate, Q_2.

- When the multi-layer flow was first established by introducing the inner core fluid at Q_1, mixing of the two fluids was observed as shown in Figure 3.20.

- For a stable flow, the flow became stable and fully developed as the "fresh" interface travelled the entire tube length, i.e. the time scale , T_F, required for a fully developed stable flow is approximately:

$$T_F = \frac{L}{U_i}$$

  where U_i is the interfacial velocity and L is the length of the flow loop.

For a stable flow, the interface is observed to be sharp and clear as shown in Figure 3.25. While the flow was stable, for a give pair of fluids:

- R_i increased with Q_1.

- R_i decreased with increased Q_2.

- The pressure gradient along the pipe is expected to increase with both Q_1 and Q_2 from our mathematical model. However, we were not able to verify such prediction from our experimental measurements.

While the flow was stable, for a given combination of flow rates:

- R_i increased with the concentration of the inner core fluid.
- R_i decreased with increasing concentration of the lubricating fluid.
- A large yield stress of the lubricating fluid implies a large stable region for a multi-layer flow. The reason is that the flow is stable as long as R_i is smaller than R_{y2}. For a given pressure gradient a large yield stress of the lubricating fluid shifts the R_{y2} closer to the wall of the pipe, i.e. R_i can be closer to the pipe wall as well.

All of the above observations agree with our mathematical model. For an unstable flow:

- The interface near the manifold remained sharp and clear. At some characteristic distance form the manifold, the interface becomes fuzzy.
- The fuzzy interface evolved into puffs eventually. Puffs of inner core fluid were observed along the pipe at some interval as shown in Figure 4.5.
- The size of puffs increased as they travelled downstream. Eventually homogenous mixing of the two fluids was observed.
- Unlike the stable flows, as the mixed zone exited the pipe, the interface did not stabilize along the entire length. New puffs appeared.

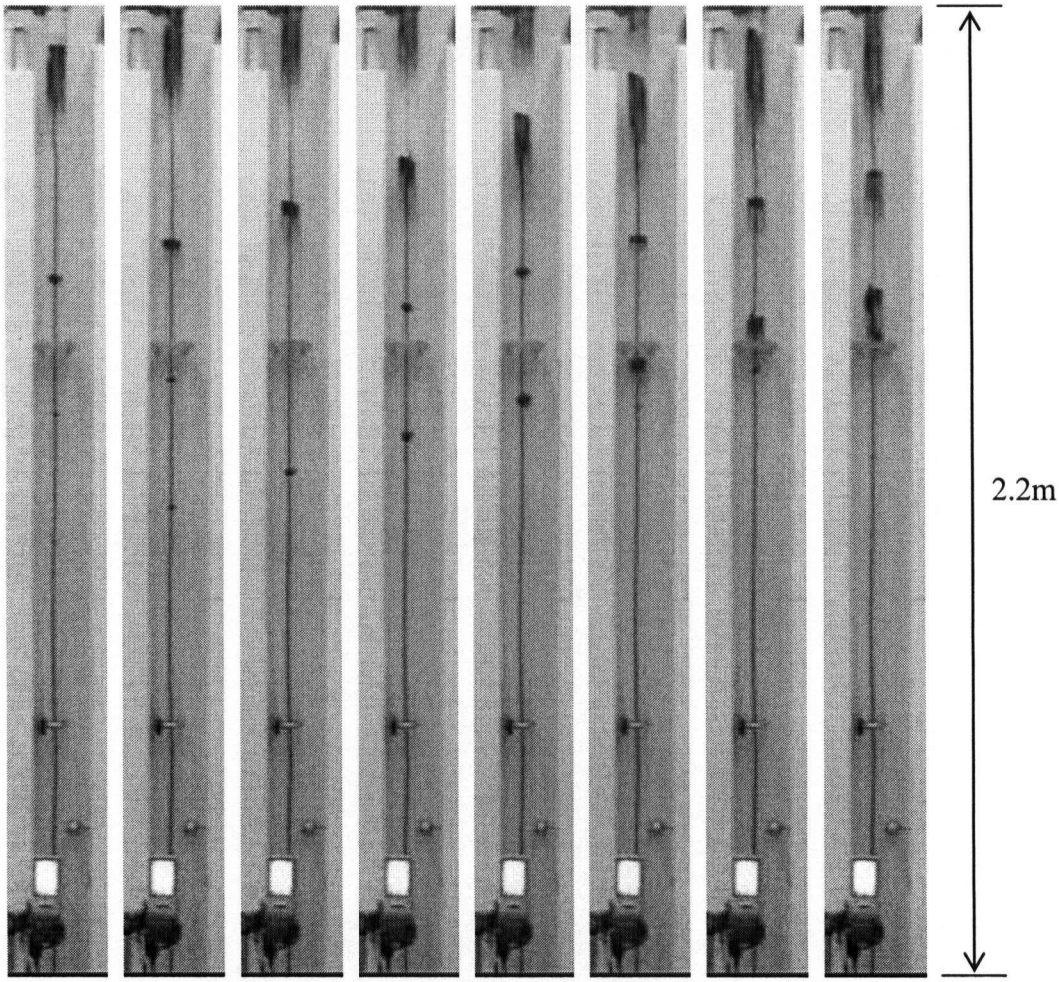

Figure 4.5: Snap shots of an unstable experiment. The inner core fluid is 0.3% Xanthan NF-C solution and the lubricating fluid is 0.3% Carbopol 940 solution at pH 5.0. Q_1 = 15 ml/s and Q_2 = 25 ml/s. The flow never stabilizes. New puffs appear as old ones exit the pipe.

4.5.2 Stable and Unstable Regions

For a given pair of fluid our mathematical model can easily predict where the transition between stable and unstable is. However, the calculation is completely based on the position of the interfacial radius and the yield radius of the lubricating fluid, i.e. as long as the lubricating fluid is partially unyielded, $R_{y2} > R_i$, then the flow is said to be stable. Thus, the precise boundary depends on τ_{y2}, which is quite uncertain (see section 3.3.1). Therefore, we should really consider a transition region corresponding to the yield stress range.

During the third set of experiments, at large Q_1 we observed unstable flows even though

our model indicated such flows should be stable. Our experiments reminded us there should be one more condition to add to our model for predicting the transition boundary. To ensure a multi-layer flow is stable, not only the interface must be surrounded by a plug region of the lubricating fluid, but also that the inner core fluid must be itself stable, i.e. the flow at center must be a steady laminar flow. To verify whether the inner core fluid is in the laminar flow region we calculate the corresponding Reynolds number.

$$Re = \frac{\rho U D}{\mu} \tag{4.1}$$

where ρ and μ are density and viscosity of the fluid, and U and D are the mean velocity and diameter of the flow. Calculating the Re for a Newtonian fluid is straight forward since the viscosity of the fluid is well defined. However for a shear thinning fluid since its viscosity is a function of shear stress, and therefore so is the corresponding Re. To simplify our calculation, from Figure 3.17 we assume μ of a 0.3% Xanthan solution is always 6×10^{-3} Pa·s. The inlet port for the inner core fluid is about 6 mm. Unstable observations were made when Q_1 was roughly about 30 ml/s. The mean velocity is defined as:

$$U = \frac{Q}{\pi \cdot r^2} \tag{4.2}$$

Substitute (4.2) into (4.1),

$$\begin{aligned} Re &= \frac{\rho \cdot D \cdot Q}{\mu \cdot \pi \cdot r^2} = \frac{2 \cdot \rho \cdot Q}{\mu \cdot \pi \cdot r} \\ &= \frac{2 \cdot 1032 \cdot 30 \times 10^{-6}}{6 \times 10^{-3} \cdot \pi \cdot 3 \times 10^{-3}} \\ &= 1095 \end{aligned}$$

The high Re suggests why flows were always unstable when Q_1 was greater than 30 ml/s. Again this is only a very rough approximation. The transitional Re for this type of flow is not known. However, this indicates that inertial effects are very significant in the inner core fluid when we reach $Q_1 \approx 30$ ml/s. One may as well define D as the interfacial radius instead of the diameter of the inlet. Due to the fact that all experiments with $Q_1 > 30$ ml/s were expected to be unstable, such experiments were omitted.

Further evidence that the instabilities are often high *Re* instabilities of the inner core fluid comes from observations such as those in Figure 4.5. The observed onset is strongly localized, just as the initial turbulent puffs in a shear flow transition. It appears that these localized disturbances have sufficient energy to break the unyielded layer of the lubricating fluid and then propagate. In the case we are just in the unstable region, the lubricating fluid is still very viscous or close to unyielded and it seems again that a localized disturbance is needed.

In addition to the unstable flow observed when $Q_1 > 30$ ml/s, flow was observed unstable when $Q_2 < 10$ ml/s. The instability mainly arose from the mechanical limitation of our pump system. The maximum flow rate of our Monyo 332 PC pump is 250 ml/s, i.e. when $Q_2 < 10$ ml/s we were operating the pump at less than 5% of its maximum capacity. This is not ideal and various problems were observed such as heating, significant vibration of the pump, and un-steady pump speed. It is suspected that due to the various problems just mentioned, they caused a pulsating output flow rate and significantly perturbed the interface.

In summary, the following flow rate limits were used for our experiments:

$$0 \text{ ml/s} \leq Q_1 \leq 30 \text{ ml/s}$$
$$10 \text{ ml/s} \leq Q_2 \leq 50 \text{ ml/s}$$

4.5.3 Measurement Errors for R_i

In section 4.1 – 4.4 we have shown that for a stable flow the experimental interfacial radius value was approximately ± 10% of the value calculated with our mathematical model. The deviation is probably caused by the following factors.

Inaccurate Rheological Data of the Two Fluids Used

It is very important to provide precise and proper range of rheological data of the inner core fluid and lubricating fluid in order for our mathematical model to accurately predict the value of R_i. Unlike other measuring quantities such as length scale and temperature, rheological data is difficult to verify. In addition, to ensure the range of our data is enough, we estimated the potential maximum shear stress that the two fluids might experience inside the flow loop as discussed in section 3.3. For viscous fluid such as Carbopol there

is no problem achieving such range since the maximum resultant rotational speed of the spindle of the test plate is relatively low compared with the measurable range of our rheometer. However, since Xanthan is much less viscous than Carbopol, to achieve the estimated range of shear stress, the maximum resultant rotational speed of the test spindle approaches the upper limit of the measurable speed of our rheometer. The signal to noise ratio (SNR) decreases significantly at this high speed and inconsistent measurements are observed. Currently the problem is minimized by averaging at least 3 trials of rheology tests. To minimize the error further, rheological data should be achieved from at least two rheometers and compared.

Poor Resolution of the Two Cameras

Two household purpose digital camcorders are used to measure the width of the inner fluid. The output of the cameras is 720 pixels by 480 pixels and the resolution of the recorded images is 0.25 mm/pixel. To determine R_i we need to measure the positions of the left and right interfaces and therefore the net error bound is ± 0.5 mm as discussed in section 3.2.5. This small error bound is very impressive while no high end laboratory camera is used. However, since the typical R_i value is only 3 mm, the cameras contribute a significant error to the measurements, i.e. 16%, and almost 25% when the actual R_i is 2 mm. In other words, it is reasonable why there is a 10% deviation between our measurements and predicted values. This problem may be solved by employing cameras with higher resolution or other measuring techniques.

Inaccuracy of the Control Model

A third source of error comes from the control model discussed in Chapter 2. Firstly, although the experiments appear to be axisymmetric, this symmetry is not perfect. Although we can compute asymmetry flows of this type [7, 8], it is very time consuming. Apart from symmetry consideration, the base flow also assumes no extensional stresses. This is not necessarily realistic. In particular, extensional stresses will present as the flow develops near the inflow port, and will be caused by any slight non-uniformity in the flow geometry downstream. For example, an interfacial asymmetry "frozen" in as the unyielded plug establishes will be carried downstream, but will create extensional stresses locally. All these effects are difficult to estimate reliably.

4.5.4 Abnormal Behaviours of Pressure Sensors

During actual experiments, unfortunately abnormal readings from both our pressure sensors are observed. For example, Figure 4.6 and 4.7 are the pressure measurements taken during Set 1 Test 17 (see section 4.1). The flow was stable and it was surprised that the pressure gradient never approached a constant value after the entire experiment which lasted for more than 10 minutes.

As long as the flow rates of the two fluids are constant, we expect the pressure gradient along the pipe should increase linearly to a maximum and approach a constant value. At t = 0 s, we start pumping the inner core fluid into the loop which is already filled with the lubricating fluid. A constant pressure reading is expected as soon as the flow becomes fully developed at t = 300 s. However, none of the sensor reports a steady reading. Although the pressure gradient seems to approach a constant value of approximately -19 kPa/m, readings from both sensors seem to increase indefinitely. It is not understood why the pressure in the pipe drop significantly between t = 100 s and t = 200 s either.

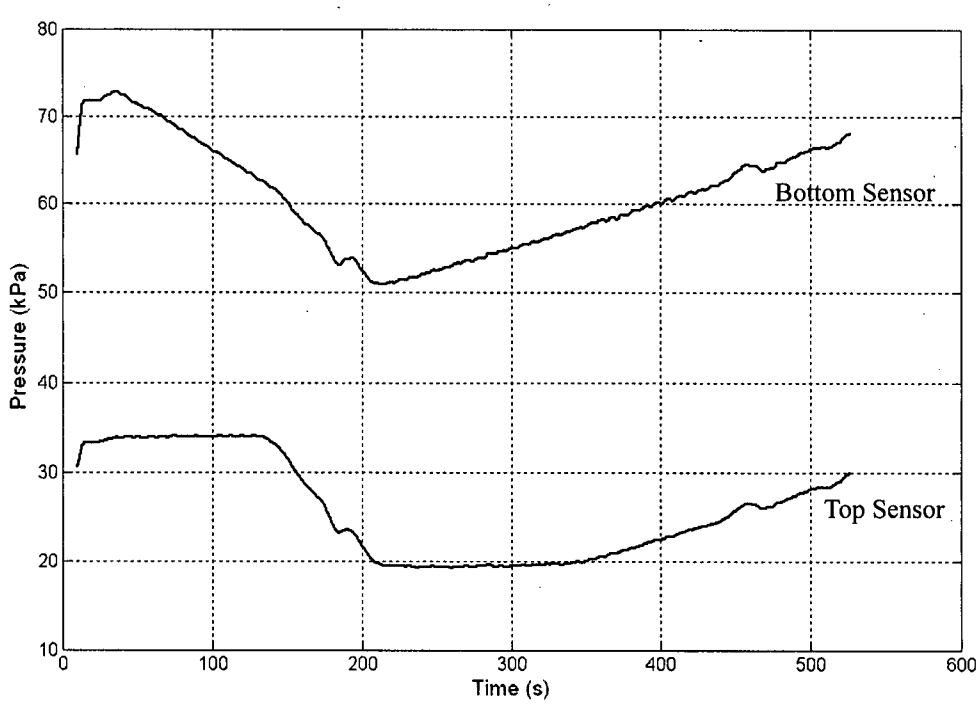

Figure 4.6: Pressure readings from bottom sensors during Set 1 Test 17.

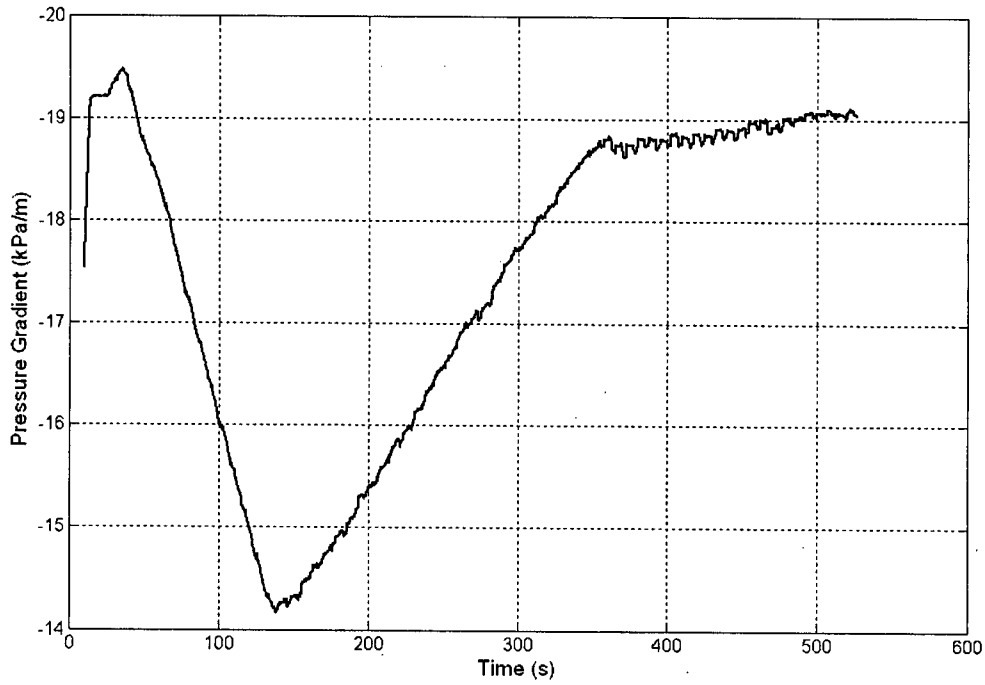

Figure 4.7: Pressure gradient along the pipe during Set 1 Test 17.

To ensure our sensors are working properly, we performed two more tests with one fluid at a time. The first test is done using water. The test results are shown in Figure 4.8 and 3.9. At $t = 0$ s, the pipe is empty and we begin pumping water into the loop. At $t = 50$ s the water column reaches the bottom sensor and at $t = 180$ s it reaches the top sensor. As soon as the water column reaches the top of the pipe at $t = 300$ s, pressure readings from both sensors approach constant. This proves that our sensors work perfectly fine with one Newtonian fluid.

The second test is done with a 0.3% Carbopol solution and results are shown in Figure 4.10 and 4.11. The procedure of this test is similar to the one done with water. At $t = 0$ s the entire pipe is empty. At $t = 130$ s the Carbopol column reaches the bottom sensor and at $t = 250$ s it reaches the top sensor. At $t = 350$ s the Carbopol column reaches the top of the pipe. The two sensors do not report a constant measurement but increase infinitely until $t = 560$ s when we run out of Carbopol solution. It is not understood why the pressure in the pipe drops after the Carbopol reaches the top of the loop and then increases again. We suspect one reason that may explain why odd things happen during this test and actual experiments is the yield stress of Carbopol.

A typical pressure sensor consists of a flexible diaphragm and a strain gauge as shown in Figure 4.12. The diaphragm expands inwards as the outside pressure increases. The strain gauge is connected to the diaphragm and used to measure the displacement of the diaphragm. A relationship is obtained by correlating the electrical output, typically voltage, of the strain gauge and the applied pressure. In general to extend the service life of a pressure sensor and to protect the diaphragm due to wall friction, the diaphragm is hidden inside the sensor body and this is exactly the case for our pressure sensors. From looking into one of our pressure sensor it is clear that the diaphragm is hidden at the end of a 1-cm long passage. This structure works perfectly fine if the working fluid is Newtonian. However, if the fluid is a yield stress fluid then measurements may be altered by the solid-like behaviour of the fluid when it is not yielded. Inside the tube the velocity of the flow should be very slow or even zero, i.e. the shear stress inside the passage approaches zero as well. In other words if the fluid is a yield stress fluid then it is possible that the fluid is not yielded and the sensor is plugged by an elastic body. Now imagine the outside pressure is increasing. The elastic body is compressed but no significant force or displacement is transferred to the diaphragm. Until the outside pressure increases to a point that the wall friction is not large enough to hold the unyielded fluid in place, then the entire plug is pushed towards the diaphragm and sensible readings may be reported. This is one possible reason which may explain the inaccurate measurements made by our sensors and the extremely long time required for our sensors to approach a steady reading. Since we are unable to explain the abnormal behaviours of our two sensors while they are used to measure the pressure of a multi-layer flow, we have decided to omit all pressure measurements in the thesis.

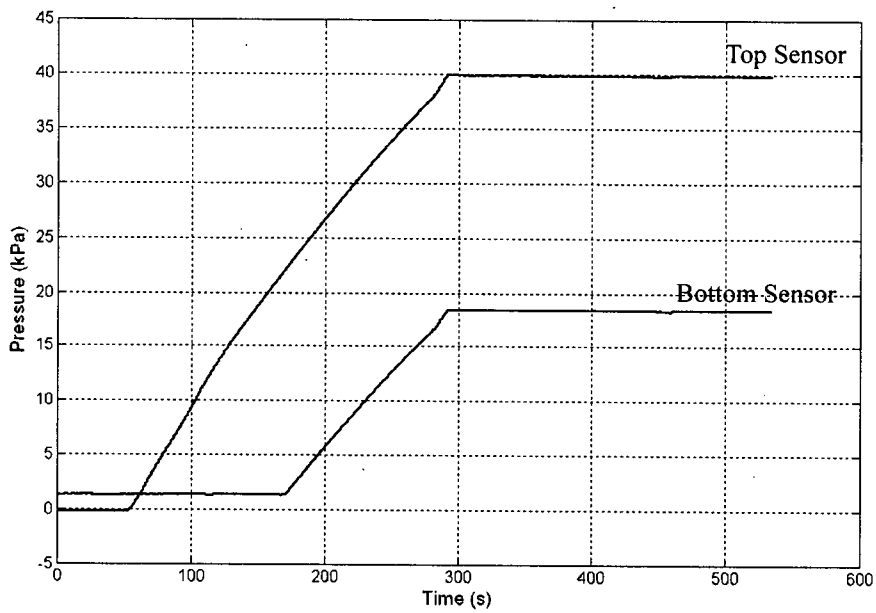

Figure 4.8: Pressure measurements from sensors. Test fluid was water. Steady measurement was achieved as soon as the water column reached the top of the loop at t = 300s.

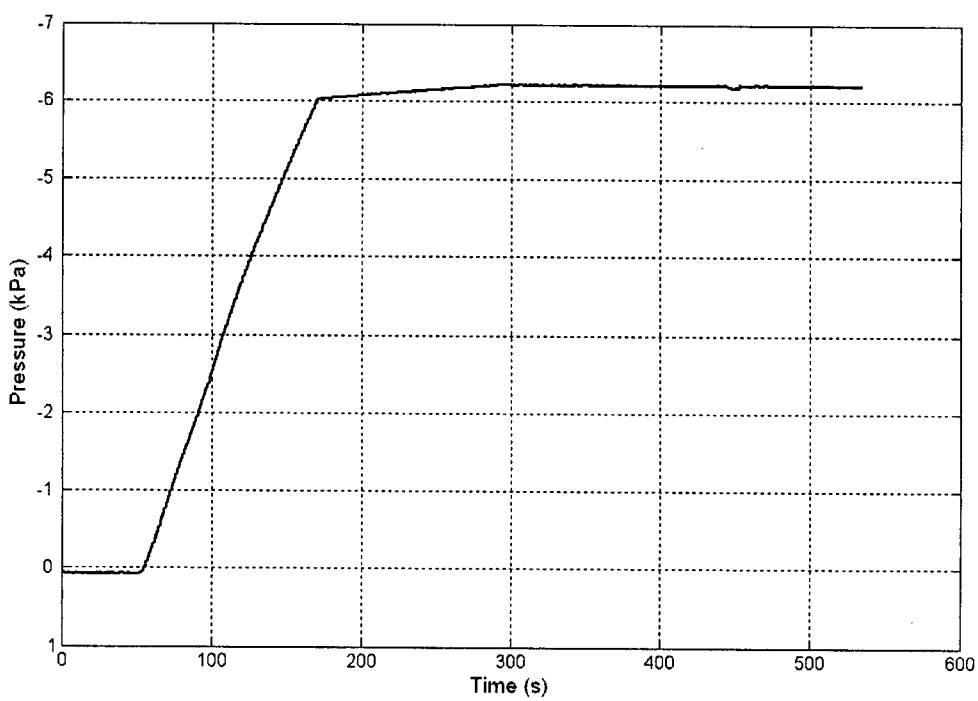

Figure 4.9: Pressure gradient calculated from Figure 4.8.

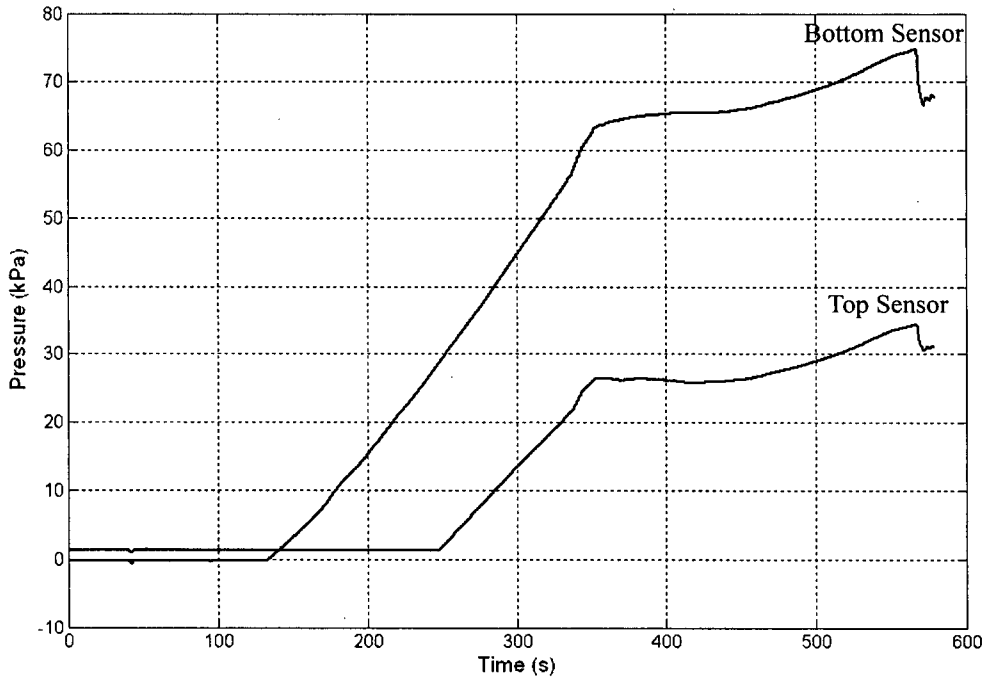

Figure 4.10: Pressure measurements from sensors. Test fluid was 0.3% Carbopol 940 solution (pH 5.0). Steady measurement was expected as soon as the fluid column reached the top of the loop at t = 350 s. Test was stopped at t = 560 s.

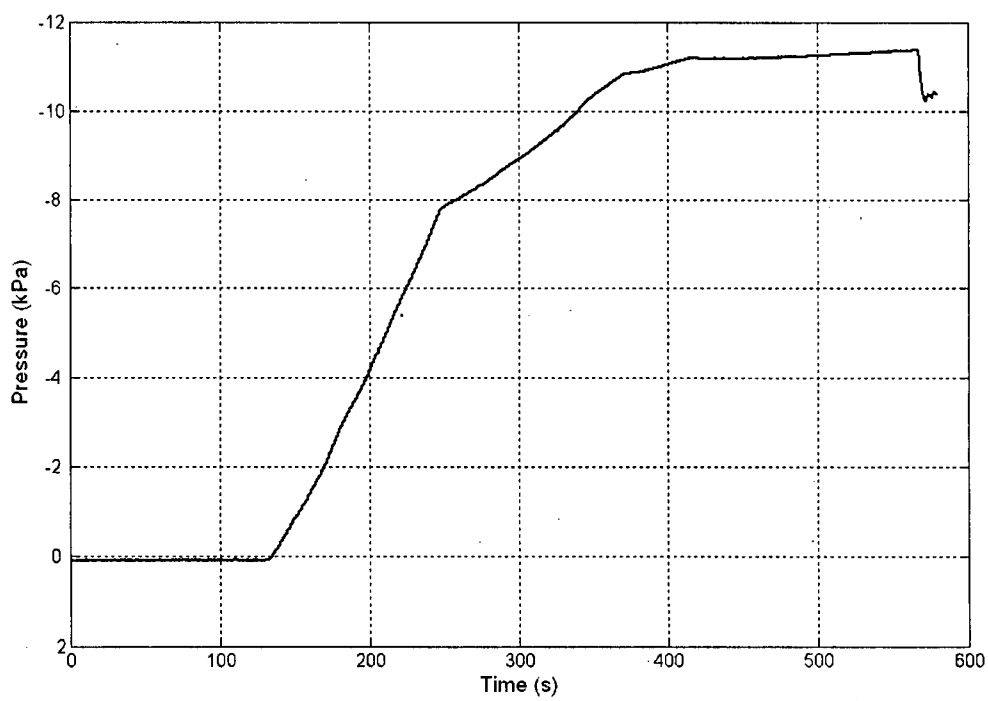

Figure 4.11: Pressure gradient calculated from Figure 4.10.

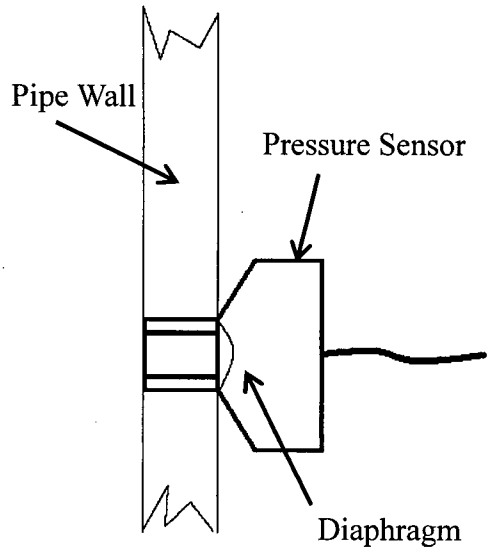

Figure 4.12: Schematics drawing of a typical pressure sensor.

Chapter 5

Discussions and Conclusions

In this thesis we have undertaken an experimental study of visco-plastic lubrication flows, where the lubricating fluid has been a Carbopol solution and the inner core fluid has been a Xanthan solution. The principal results and contributions are as follows.

5.1 Summary of Principal Results

- After conducting over 100 experiments with 4 different fluid pairs over broad flow rate range, we can unequivocally state that stable multi-layer flows, of the visco-plastic lubrication type, can be achieved in the laboratory. This was the principal objective of the thesis. An example of a stable flow is illustrated in section 3.4.2.

- The experiments have been designed with the aid of a simple control model, based on the axisymmetric flow of 2 generalized Newtonian fluids (see Chapter 2). This model predicts the boundary between stable and unstable flows. Our experimental results do approximately identify this stability boundary (see Figure 4.1 – 4.4).

- A secondary objective of the thesis was to investigate whether or not the interfacial radius, R_i, could be controlled in such flows. Results here are also promising:

  - For each of the 4 experimental fluid pairs, we have reasonable agreement between the predicted and measured R_i
  - For both our control model and experimental observations, R_i increased with Q_1 but decreased with increased Q_2.
  - For both our control model and experimental observations, R_i

increased with increased concentration of Xanthan solution and decreased with increased concentration of Carbopol solution.

Whilst the model prediction is not precisely followed, the variations of R_i with Q_1 and Q_2 suggest that online control would be possible.

5.2 Discussions

As stated above, the principal contribution of the thesis has been to provide experimental proof that visco-plastic lubrication flows can be achieved in a laboratory setting. The linear stability of these flows was predicted in [3] for a plane channel and the nonlinear stability was proven in [8] for a pipe geometry. However, there are many differences between the theoretical situation and our experiment.

- The theoretical studies consider periodic (in z) perturbations of a infinitely long base flow. The linear perturbations are temporal only.

- As the flow is infinite there are no entry or exit flow problems with development, and no difficulty to establish the flow.

- The visco-plastic fluids in [3, 8] were idealized as Bingham fluids. Our fluids have a shear thinning rheology that is approximately Herschel-Bulkley. Thus, the fluids are likely to be less stable than a Bingham-Newtonian fluid pair. Additionally, the experimental fluids may exhibit a small amount elastic and thixotropic behaviour.

Bearing in mind these differences, the stable experiments are impressive demonstrations. A stable flow has been established over 4 m, which is approximately $100R$ or $1000R_i$.

5.3 Future Work

Following suggestions are provided for future laboratory work on multi-layer flows.

- The abnormal behaviour of pressure sensors with yield stress fluid is not understood. The pressure gradient of a multi-layer flow should be measured

and compared with values predicted by the mathematical model.

- Similar experiments can be done with a manifold of different size to observe the effects of manifold size, in particular on R_i and on flow establishment.

- It was observed for each experiment the inner core fluid required some entry length, L_E, to develop from the manifold size to R_i. Experiments can be done to investigate the relationship between L_E and other flow parameters such as Q_1, Q_2, and rheologies of the two fluids etc.

- Multi-layer flow was observed evolving from stable to unstable always at the same distance from the manifold for a given combination of flow rates. This characteristic length scale can be studied more in depth.

- The assumption of our multi-layer flow is axisymmetric is to be verified.

- Effects of density difference of the two fluids are not studied yet.

- It is worth while to study behaviour of a multi-layer flow passing various angle bends, e.g. 30°, 45°, 90°, etc.

Bibliography

[1] M. Allouche, I.A. Frigaard, G. Sona, Static wall layers in the displacement of two viscoplastic fluids in a plane channel. *J. Fluid Mech.,* **424,** 243-277 (2000).

[2] E. Comparini and P. Mannucci, Flow of a Bingham fluid in contact with a Newtonian fluid. *J. Math Anal. Appl.,* **227,** 359-381 (1998).

[3] I.A. Frigaard, Super-stable parallel flows of multiple viscoplastic fluid. *J. Non-Newt. Fluid Mech.,* **100,** 49-76 (2001).

[4] I.A. Frigaard and O. Scherzer, Uniaxial exchange flows of two Bingham fluids in a cylindrical duct. *IMA J. Appl. Math.,* **61,** 237-266 (1998).

[5] I.A. Frigaard, O. Scherzer, G.. Sona, Uniqueness and non-uniqueness in the steady displacement of two viscoplastic fluids. *ZAMM,* **81(2),** 99-118 (2001).

[6] C. Gabard and J.-P. Hulin, Miscible displacement of non-Newtonian fluids in a vertical tube. *Eur. Phys. J. E,* **11,** 231-241 (2003).

[7] M.A. Moyers-Gonzalex and I.A. Frigaard, Numerical solution of duct flows of multiple visco-plastic fluids. *J. Non-Newt. Fluid Mech.,* **122,** 227-241 (2004).

[8] M.A. Moyers-Gonzalex, Nonlinearly stable multi-layer visco-plastic flows. Master Thesis, Dept. of Math and Dept. of Science at the University of British Columbia, Vancouver, Canada, (2002).

[9] C.E. Hickox, Instability due to viscosity and density stratification in axisymmetric pipe flow. *Phys. Fluids,* **14(2),** 251-262 (1971).

[10] E.J. Hinch, A note on the mechanism of the instability at the interface between two shearing fluids. *J. Fluid Mech.,* **114,** 463-465 (1984).

[11] A.P. Hooper, Long-wave instability at the interface between two viscous fluids: thin

layer effects. *Phys. Fluids*, **28,** 1613-1618 (1985).

[12] A.P. Hooper and W.G.. Boyd, Shear flow instability at the interface between two shearing fluids. *J. Fluid Mech.,* **114,** 463-465 (1984).

[13] A.P. Hooper and W.G.. Boyd, Shear flow instability due to a wall and a viscosity difference at the interface. *J. Fluid Mech.,* **179,** 201-225 (1987).

[14] A.P. Hooper and W.G. Boyd, Shear-flow instability at the interface between two viscous fluids. *J. Fluid Mech.*, **128,** 507-528 (1983).

[15] D.D. Joseph, R. Bai, K.P. Chen, Y. Renardy, Core-annular flows. *Ann. Rev. Fluid Mech.*, **29,** 65-90 (1997).

[16] D.D. Joseph and S. Carmi, Stability of Poiseuille Flow in Pipes, Annuli, and Channels. *Quart. Appl. Math.*, **26,** 575-599 (1969).

[17] D.D. Joseph, Y.Y. Renardy, M. Renardy, Instability of the flow of two immiscible liquids with different viscosities in a pipe. *J. Fluid Mech.,* **141,** 309-317 (1984).

[18] D.D. Joseph and Y.Y. Renardy, Fundamentals of Two-Fluid Dynamics Vol. I and Vol. II. *Interdisciplinary Applied Mathematics,* Springer, (1993).

[19] C. Nouar and I.A. Frigaard, Nonlinear stability of Poiseuille flow of a Bingham fluid: theoretical results and comparison with phenomenological criteria. *J. Non-Newt. Fluid Mech.,* **100,** 127-149 (2001).

[20] A. Pinarbasi and A. Liakopoulos, Stability of two-layer Poiseuille flow of Carreau-Yasuda and Bingham-like fluids. *J. Non-Newt. Fluid Mech.,* **57,** 227-241 (1995).

[21] Y. Renardy, Instability at the interface between two shearing fluids in a channel. *Phys. Fluids*, **28,** 3441-3443 (1985).

[22] S.G. Yiantsos And B.G. Higgins, Linear stability of plane Poiseuille flow of two superposed fluids. *Phys. Fluids,* **31,** 3225-3238 (1988).

[23] C.S. Yih, Instability due to viscosity stratification. *J. Fluid. Mech.,* **27(2),** 337-352 (1967).

Appendix A

Calibrations for Pressure Sensors

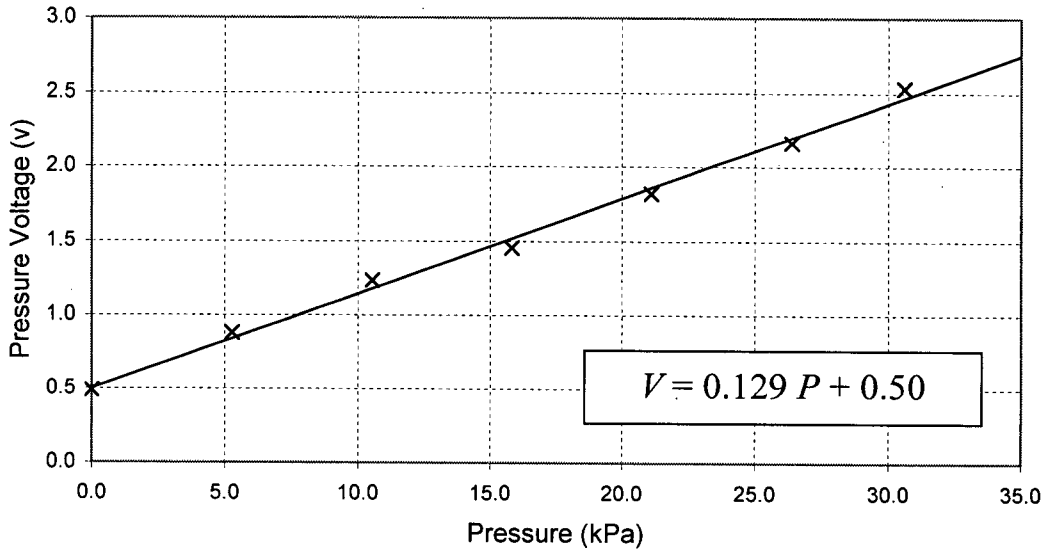

Figure A.1: Calibration plot of pressure transducer EW-68075-40.

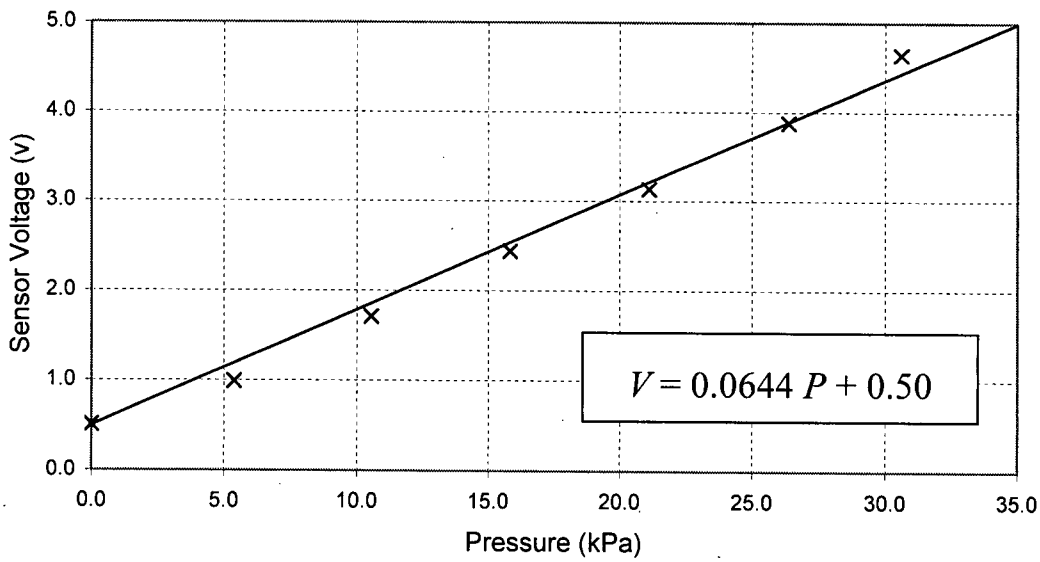

Figure A.2: Calibration plot of pressure transducer EW-68075-42.

Appendix B

Calibration for Magnetic Flowmeter and Monyo 332 PC Pump

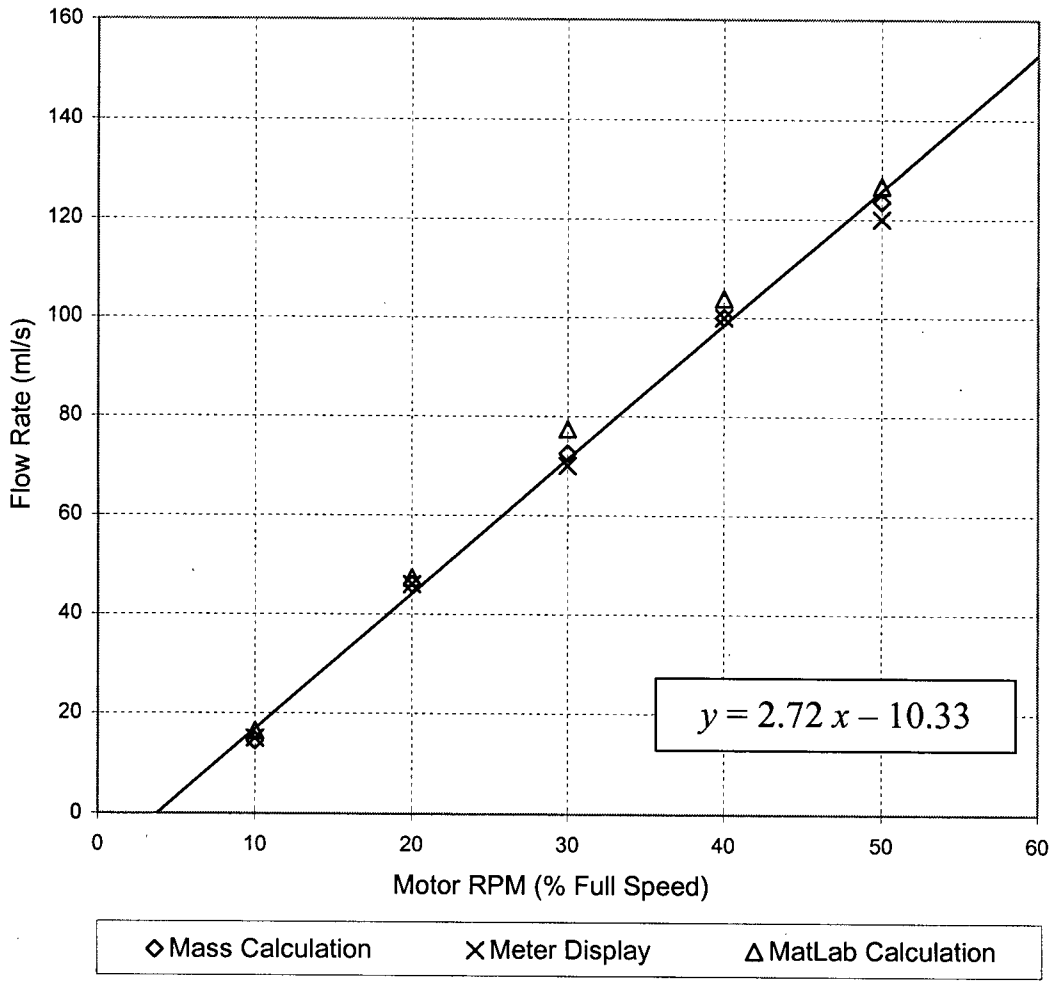

Figure B.1: Calibration plot of Monyo 332 PC pump, Omega FMG-423H magnetic flowmeter, and analog VFD. The test fluid is 0.3% Carbopol 940 solution with a pH level of 5.0.

Appendix C

Calibration for Paddle-wheel Flowmeter and Monyo 332 PC Pump

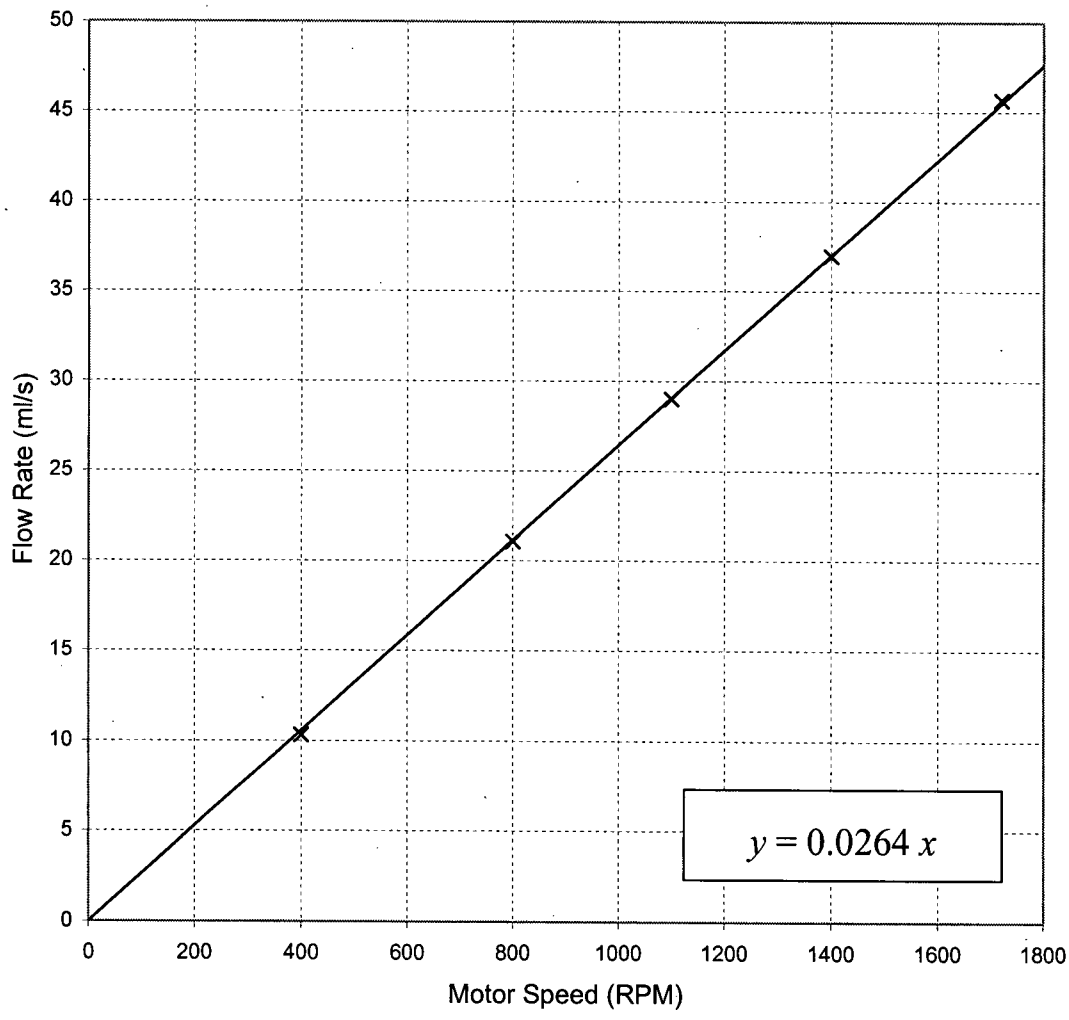

Figure C.1: Calibration plot of Monyo 1000 PC pump, Kobold DRG-1150N1F300 paddle-wheel flowmeter, and digital VFD. The test fluid is 0.3% Xanthan NF-C solution.

Appendix D

Calibrations for Video Cameras

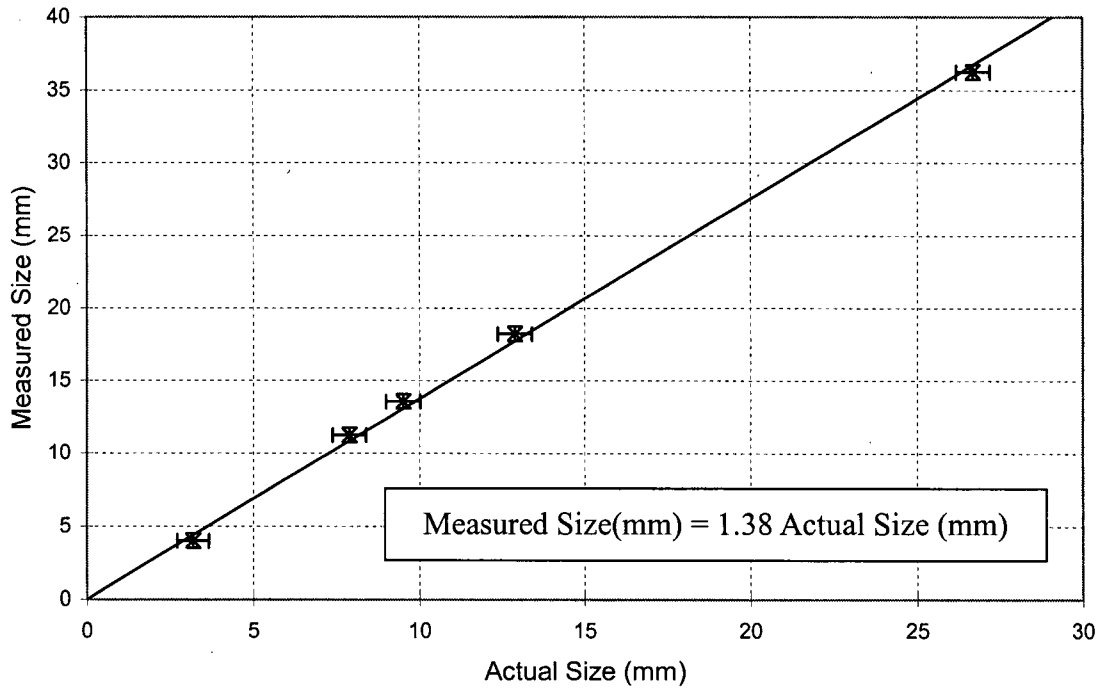

Figure D.1: Calibration plot of Canon Optura 30 video camera. The test fluid is 0.3% Carbopol 940 solution with a pH level of 5.0.

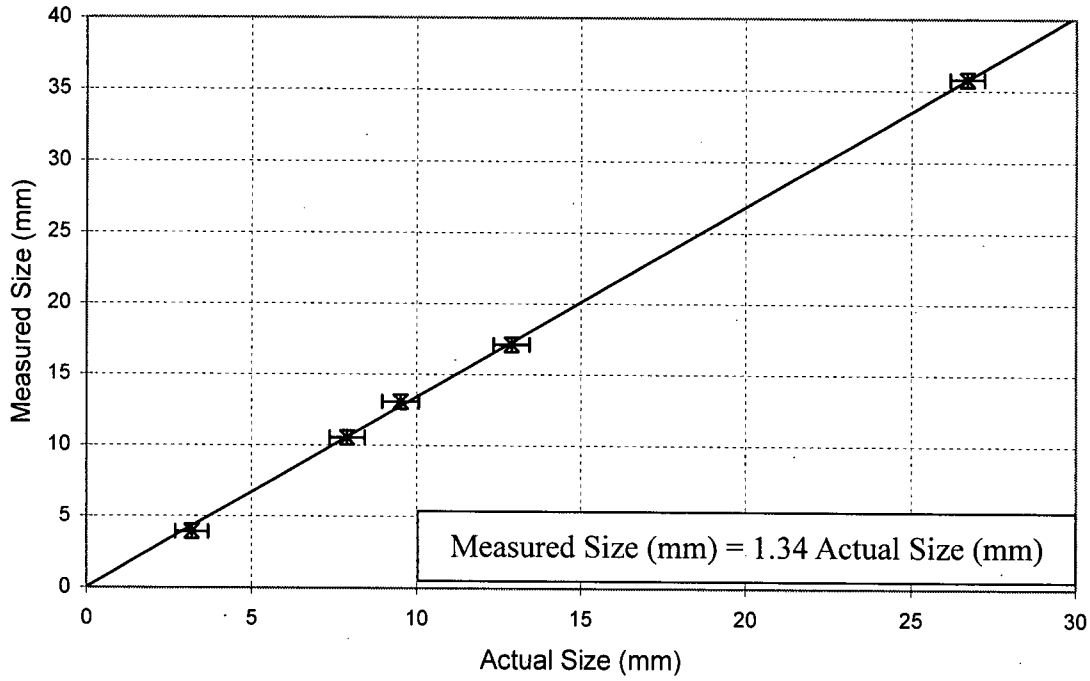

Figure D.2: Calibration plot of Panasonic PV-DV951-K video camera. The test fluid is 0.3% Carbopol 940 solution with a pH level of 5.0.

Appendix E

Flow Rate Plots for the Typical Experiment

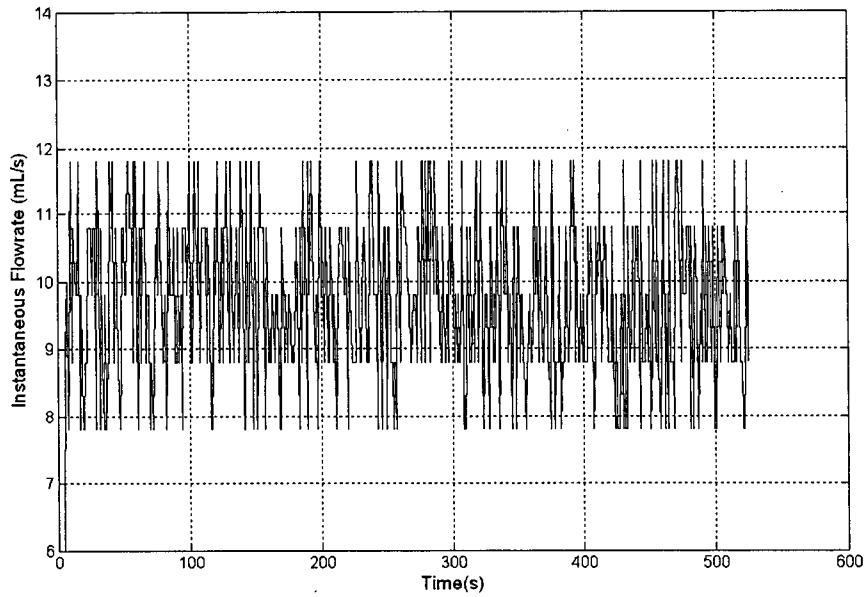

Figure E.1: Instantaneous flow rate of the inner core fluid during the typical experiment. The average flow rate is 9.7 ± 5 ml/s.

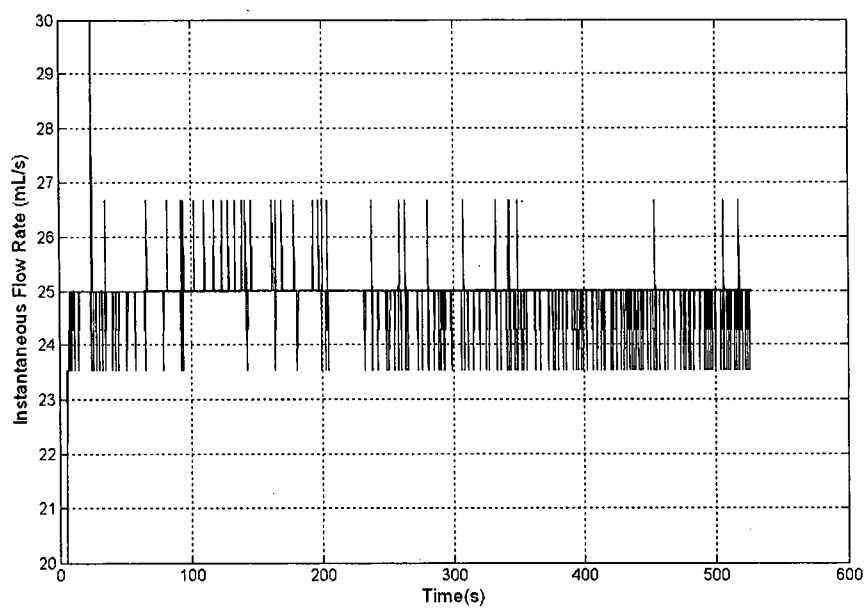

Figure 4.7: Instantaneous flow rate of the lubricating fluid during the typical experiment. The average flow rate is 24.7 ± 2 ml/s.

Appendix F

Set 1 Experimental Data Table

Test #	Inner Core Fluid	Lubricating Fluid	Q_1 (ml/s)	Q_2 (ml/s)	Measured R_i (mm)	Calculated R_i (mm)	R_i % Difference	Observ-Ation
1	0.3% Xanthan NF-C solution	0.3% Carbopol 940 solution (pH 5.0)	5.0	12.5	2.15	2.15	0.00	Stable
2			10.0	12.8	2.50	2.50	0.00	Stable
3			20.0	12.4	2.83	2.91	-2.75	Stable
4			30.0	12.5	3.23	3.18	1.57	Unstable 2
5			40.0	12.3	3.55	3.39	4.72	Unstable 2
6			5.0	15.2	2.23	2.12	5.19	Stable
7			10.0	15.5	2.97	2.47	20.24	Stable
8			15.1	15.0	2.81	2.70	4.07	Stable
9			20.0	15.7	3.04	2.87	5.92	Stable
10			25.0	14.8	3.24	3.02	7.28	Stable
11			5.1	20.0	2.20	2.09	5.26	Stable
12			10.0	19.8	2.61	2.42	7.85	Stable
13			20.0	19.9	2.80	2.82	-0.71	Unstable 1
14			30.0	20.2	3.93	3.09	27.18	Unstable 2
15			40.0	20.6	4.33	3.29	31.61	Unstable 2
16			5.0	25.0	2.15	2.05	4.88	Stable
17			9.7	24.7	2.47	2.39	3.35	Stable
18			15.0	25.2	3.04	2.61	16.48	Unstable 1
19			20.0	25.4	2.99	2.78	7.55	Unstable 2
20			5.0	25.1	2.04	1.99	2.51	Stable

Table F.1a: Results of set 1 experiment test #1 – 20

Test #	Inner Core Fluid	Lubricating Fluid	Q_1 (ml/s)	Q_2 (ml/s)	Measured R_i (mm)	Calculated R_i (mm)	R_i % Difference	Observ-ation
21	0.3% Xanthan NF-C solution	0.3% Carbopol 940 solution (pH 5.0)	10.0	34.7	2.37	2.32	2.16	Stable
22			15.0	34.5	2.65	2.55	3.92	Unstable 2
23			20.1	35.1	3.46	2.72	27.21	Unstable 2
24			5.1	38.4	2.08	1.98	5.05	Stable
25			10.2	38.9	2.23	2.32	-3.88	Stable
26			15.2	39.2	2.68	2.53	5.93	Unstable 2
27			10.0	44.9	2.26	2.28	-0.88	Stable
28			14.9	44.5	2.45	2.49	-1.61	Unstable 2
29			10.1	50.2	2.42	2.27	6.61	Stable
30			10.1	10.2	2.73	2.53	7.91	Stable
31			15.2	50.0	2.50	2.48	0.81	Unstable 1
32			20.0	5.5	3.13	3.05	2.62	Unstable 2
33			24.9	5.7	3.40	3.19	6.58	Unstable 2
34			15.1	10.2	3.01	2.77	8.66	Unstable 2

Table F.1b: Results of set 1 experiment test #21 - 34

The "Observation" column is filled with one of the followings:

1. Stable: The flow was stable and satisfied all the conditions listed in section 3.4.2.

2. Unstable 1: The flow became stable, then unstable, i.e. the flow satisfied the conditions listed in section 3.4.2 for a short duration. The interface became fuzzy and then at some height puffs of the inner core fluid appeared and perturbed the downstream of the flow either because there was no unyielded

layer of the lubricating fluid or the unyielded layer was not strong enough to suspend the puffs.

3. Unstable 2: The flow never became stable or fully developed, i.e. mixing of the two fluids was observed throughout the experiment.

Appendix G

Set 2 Experimental Data Table

Test #	Inner Core Fluid	Lubricating Fluid	Q_1 (ml/s)	Q_2 (ml/s)	Measured R_i (mm)	Calculated R_i (mm)	R_i % Difference	Observ-ation
1	0.5% Xanthan NF-C solution	0.5% Carbopol 940 solution (pH 5.0)	25.0	5.0	3.37	4.65	-27.53	Unstable 2
2			40.1	5.1	5.75	5.01	14.77	Unstable 2
3			24.9	10.0	3.92	4.14	-5.31	Stable
4			30.0	10.1	3.98	4.26	-6.57	Unstable 1
5			19.8	14.9	3.58	3.78	-5.29	Stable
6			25.1	15.0	3.72	3.93	-5.34	Stable
7			30.1	15.0	3.86	4.05	-4.69	Unstable 2
8			15.1	20.1	3.34	3.48	-4.02	Stable
9			20.0	20.1	3.30	3.65	-9.59	Stable
10			25.1	20.0	3.56	3.80	-6.32	Unstable 2
11			10.0	25.0	3.00	3.17	-5.36	Stable
12			14.9	25.0	3.53	3.39	4.13	Stable
13			20.0	25.1	3.46	3.57	-3.08	Stable
14			25.0	25.0	3.37	3.71	-9.16	Unstable 1
15			10.1	30.1	3.19	3.11	2.57	Stable
16			14.9	30.0	3.36	3.33	0.90	Unstable 1
17			5.0	30.0	2.83	2.75	2.91	Stable
18			5.0	35.0	2.88	2.71	6.27	Stable
19			10.1	34.9	3.12	3.06	1.96	Stable
20			14.9	35.0	2.95	3.28	-10.06	Unstable 2

Table 4.4a: Results of set 2 experiment test # 1 – 20

Test #	Inner Core Fluid	Lubricating Fluid	Q_1 (ml/s)	Q_2 (ml/s)	Measured R_i (mm)	Calculated R_i (mm)	R_i % Difference	Observ-ation
21	0.5% Xanthan NF-C solution	0.5% Carbopol 940 solution (pH 5.0)	5.0	40.1	2.72	2.66	2.26	Stable
22			10.1	40.1	3.13	3.01	3.99	Stable
23			14.9	39.9	3.26	3.23	0.93	Unstable 2
24			5.1	45.0	2.62	2.64	-0.76	Stable
25			9.9	45.1	2.94	2.97	-1.01	Stable
26			15.0	44.9	3.22	3.19	0.94	Unstable 2
27			5.0	50.0	2.53	2.60	-2.69	Stable
28			10.1	49.9	2.88	2.95	-2.37	Stable
29			14.9	50.0	3.28	3.16	3.80	Unstable 2

Table 4.4b: Results of set 2 experiment test # 21 - 29

Appendix H

Set 3 Experimental Data Table

Test #	Inner Core Fluid	Lubricating Fluid	Q_1 (ml/s)	Q_2 (ml/s)	Measured R_i (mm)	Calculated R_i (mm)	R_i % Difference	Observ-ation
1	0.3% Xanthan NF-C solution	0.5% Carbopol 940 solution (pH 5.0)	5.0	10.0	2.40	2.10	14.29	Stable
2			10.0	9.9	2.58	2.45	5.31	Stable
3			15.0	10.1	2.73	2.67	2.25	Stable
4			20.1	9.9	2.75	2.85	-3.51	Stable
5			24.1	10.1	2.91	2.96	-1.69	Stable
6			5.1	15.1	2.12	2.03	4.43	Stable
7			9.9	15.1	2.41	2.35	2.55	Stable
8			15.1	15.0	2.64	2.58	2.33	Stable
9			20.0	14.9	2.69	2.74	-1.82	Stable
10			25.0	15.1	2.75	2.88	-4.51	Stable
11			5.3	19.9	2.08	2.00	4.00	Stable
12			10.0	20.0	2.41	2.30	4.78	Stable
13			15.1	19.9	2.67	2.52	5.95	Stable
14			20.1	20.1	2.70	2.68	0.75	Stable
15			5.1	25.0	2.10	1.95	7.69	Stable
16			10.1	25.1	2.43	2.26	7.52	Stable
17			15.0	25.1	2.54	2.47	2.83	Stable
18			19.9	24.9	2.66	2.63	1.14	Stable
19			5.0	30.1	2.11	1.91	10.47	Stable
20			10.1	29.9	2.33	2.23	4.48	Stable

Table 4.5a: Results of set 3 experiment test # 1 - 20

Test #	Inner Core Fluid	Lubricating Fluid	Q_1 (ml/s)	Q_2 (ml/s)	Measured R_i (mm)	Calculated R_i (mm)	R_i % Difference	Observ-ation
21	0.3% Xanthan NF-C solution	0.5% Carbopol 940 solution (pH 5.0)	15.0	30.0	2.59	2.44	6.15	Stable
22			20.0	29.9	2.66	2.60	2.31	Stable
23			5.1	35.1	2.35	1.89	24.34	Stable
24			10.1	34.9	2.34	2.21	5.88	Stable
25			14.9	35.1	2.51	2.41	4.15	Stable
26			20.0	35.0	2.68	2.57	4.28	Stable
27			5.1	40.1	2.01	1.87	7.49	Stable
28			10.0	40.0	2.33	2.18	6.88	Stable
29			15.1	40.1	2.63	2.39	10.04	Stable
30			20.2	39.9	2.64	2.55	3.53	Stable
31			5.2	45.1	2.00	1.86	7.53	Stable
32			9.9	45.0	2.32	2.15	7.91	Stable
33			14.9	44.9	2.54	2.36	7.63	Stable
34			20.2	45.0	2.64	2.53	4.35	Stable
35			24.9	19.9	2.94	2.81	4.63	Stable
36			25.0	25.1	2.74	2.76	-0.72	Stable
37			25.0	30.1	2.78	2.73	1.83	Stable
38			24.9	34.9	2.89	2.70	7.04	Stable
39			25.1	40.0	2.87	2.67	7.49	Stable
40			25.1	45.1	2.81	2.65	6.04	Stable

Table 4.5b: Results of set 3 experiment test # 21 - 40

Appendix I

Set 4 Experimental Data Table

Test #	Inner Core Fluid	Lubricating Fluid	Q_1 (ml/s)	Q_2 (ml/s)	Measured R_i (mm)	Calculated R_i (mm)	R_i % Difference	Observ-ation
1	0.5% Xanthan NF-C solution	0.3% Carbopol 940 solution (pH 5.0)	5.0	50.0	2.69	2.80	-3.93	Stable
2			15.0	49.8	3.23	3.41	-5.28	Unstable 2
3			9.9	49.9	3.09	3.16	-2.22	Stable
4			5.1	40.1	2.72	2.88	-5.56	Stable
5			9.9	40.1	3.06	3.25	-5.85	Unstable 1
6			15.1	40.0	3.12	3.50	-10.86	Unstable 2
7			5.1	29.9	2.72	2.99	-9.03	Stable
8			9.9	30.0	3.26	3.36	-2.98	Unstable 2
9			15.0	29.9	3.29	3.61	-8.86	Unstable 2
10			5.1	20.1	2.76	3.12	-11.54	Stable
11			10.0	20.0	3.43	3.51	-2.28	Unstable 2
12			15.1	19.9	3.42	3.77	-9.28	Unstable 2
13			5.0	10.0	3.36	3.33	0.90	Stable
14			10.1	10.0	2.96	3.75	-21.07	Unstable 1
15			5.0	14.9	3.49	3.21	8.72	Stable
16			10.0	14.9	3.36	3.62	-7.18	Unstable 2
17			5.0	25.0	3.26	3.04	7.24	Stable
18			10.0	24.9	3.09	3.43	-9.91	Unstable 2
19			5.1	35.1	3.16	2.93	7.85	Stable
20			10.0	35.1	3.02	3.30	-8.48	Unstable 2

Table 4.6a: Results of set 4 experiment test # 1 - 20

Test #	Inner Core Fluid	Lubricating Fluid	Q_1 (ml/s)	Q_2 (ml/s)	Measured R_i (mm)	Calculated R_i (mm)	R_i % Difference	Observ-ation
21	0.5% Xanthan NF-C solution	0.3% Carbopol 940 solution (pH 5.0)	5.1	45.1	2.99	2.84	5.28	Stable
22			9.9	45.1	3.36	3.20	5.00	Unstable 2

Appendix J

Various Plots of Set 1 Experiments

Inner core fluid: 0.3% Xanthan NF-C solution.
Lubricating fluid: 0.3% Carbopol 940 solution (pH 5.0).
All plots are generated with the numerical control model.

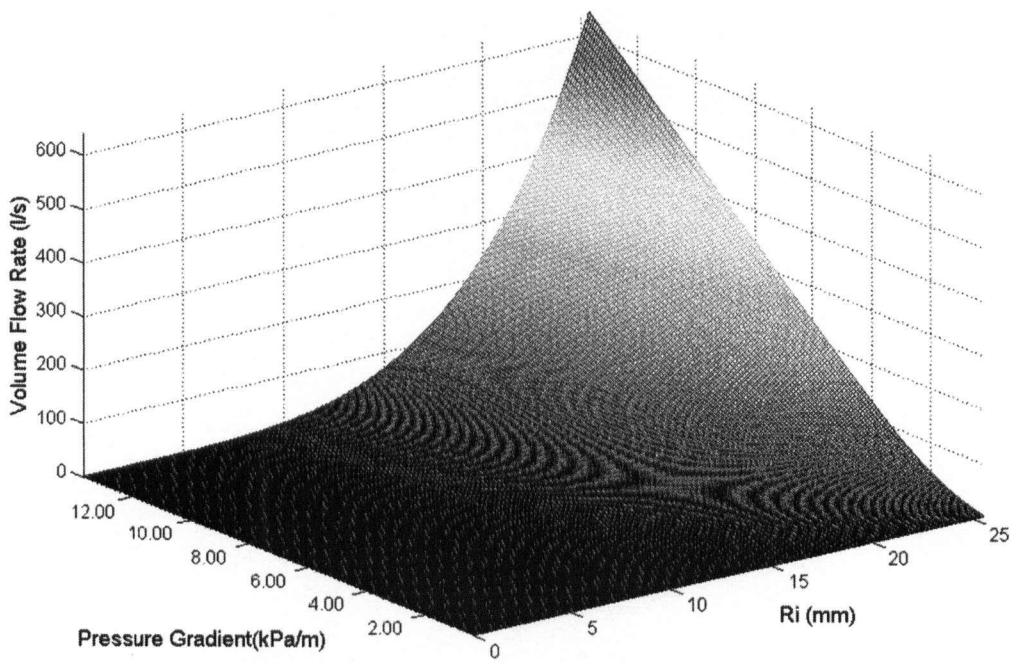

Figure J.1: Flow rate of the inner core fluid versus the pressure gradient along the axis of the pipe and interfacial radius.

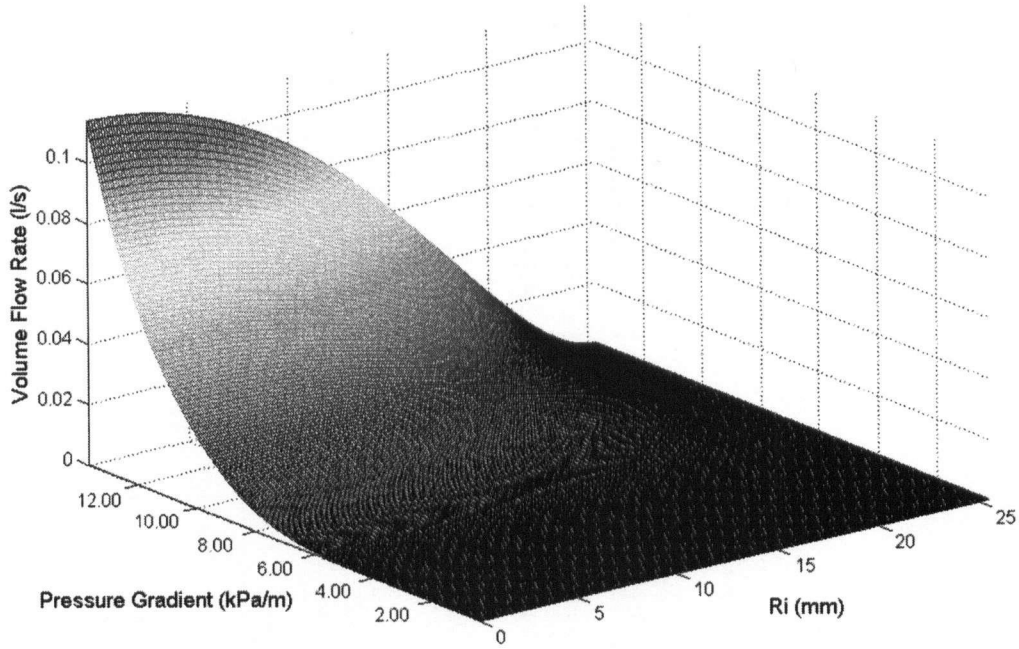

Figure J.2: Flow rate of the lubricating fluid versus the pressure gradient along the axis of the pipe and interfacial radius.

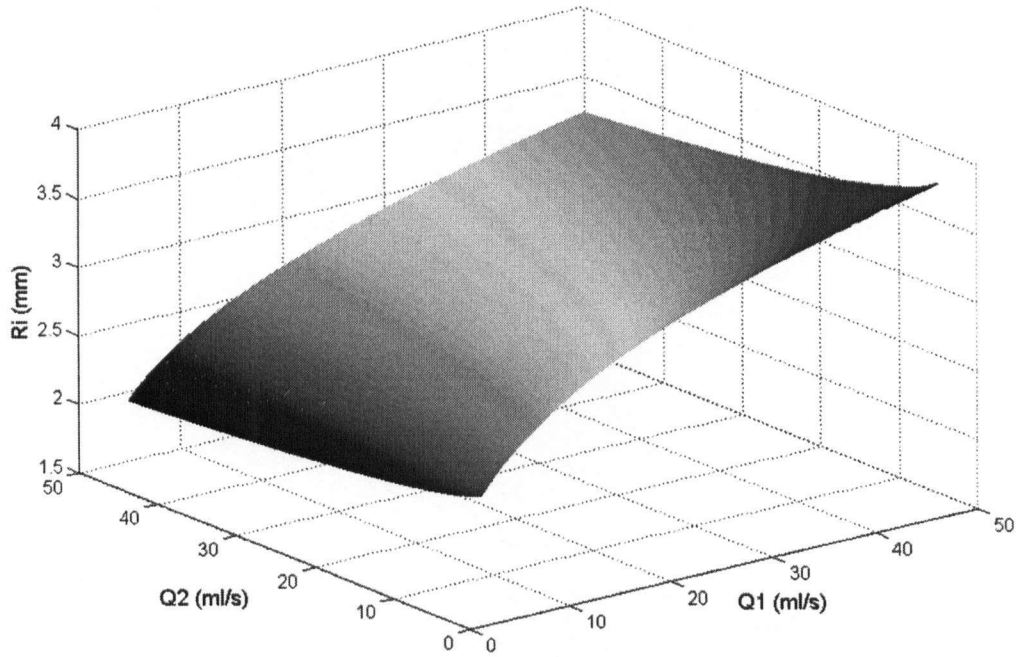

Figure J.3: Interfacial radius versus the flow rates of the two fluids.

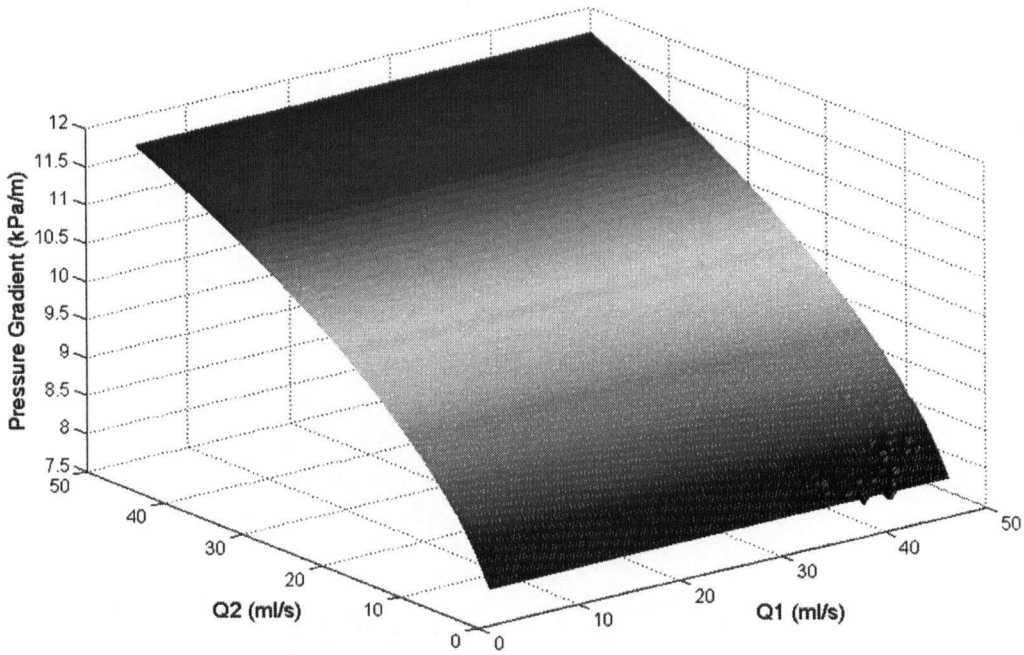

Figure J.4: Pressure gradient along the axis of the pipe versus the flow rate of the two fluids.

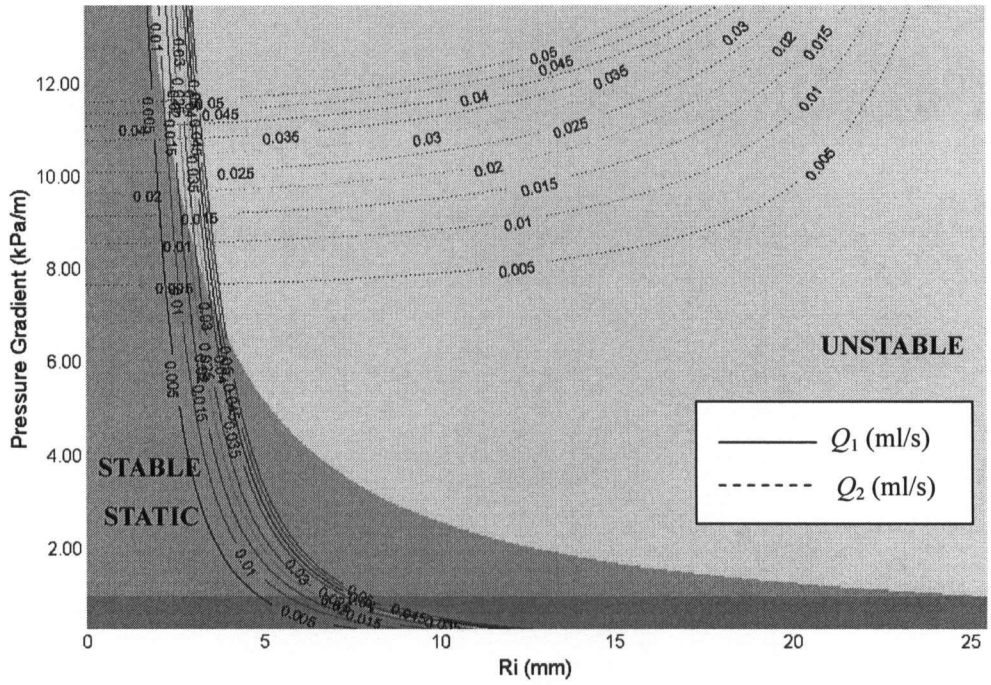

Figure J.5: Contours of flow rates versus the pressure gradient and interfacial radius.

Appendix K

Various Plots of Set 2 Experiments

Inner core fluid: 0.5% Xanthan NF-C solution.
Lubricating fluid: 0.5% Carbopol 940 solution (pH 5.0).
All plots are generated with the numerical approach.

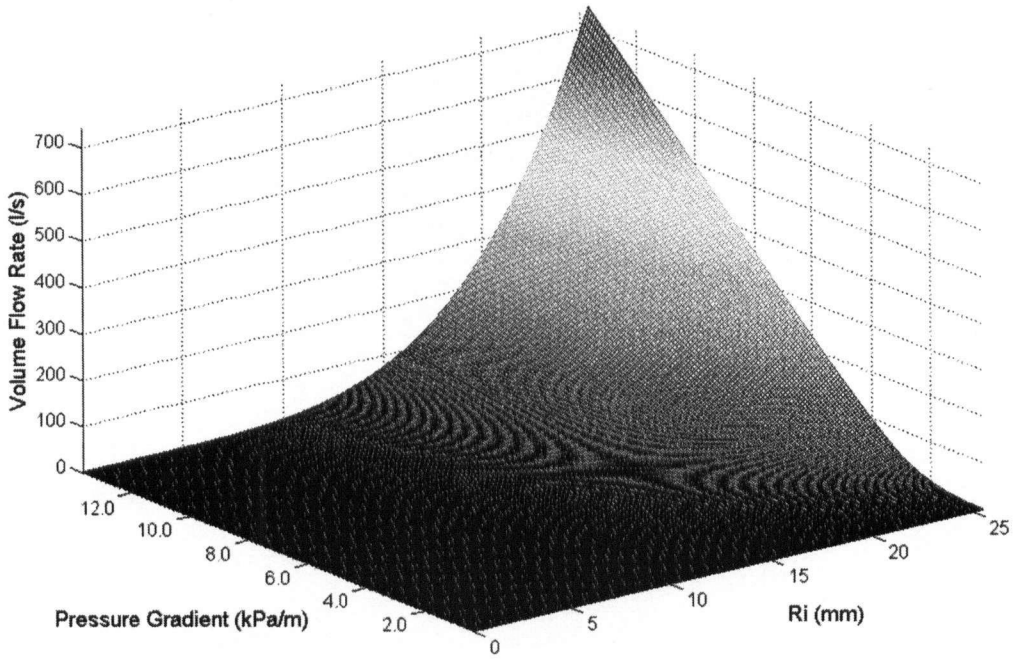

Figure K.1: Flow rate of the inner core fluid versus the pressure gradient along the axis of the pipe and interfacial radius.

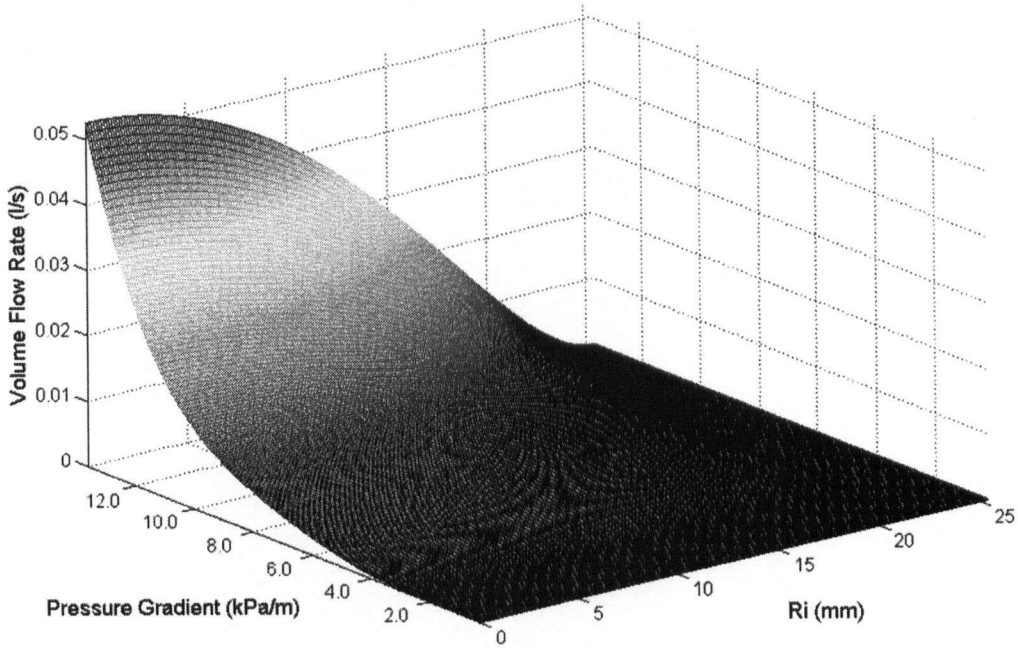

Figure K.2: Flow rate of the lubricating fluid versus the pressure gradient along the axis of the pipe and interfacial radius.

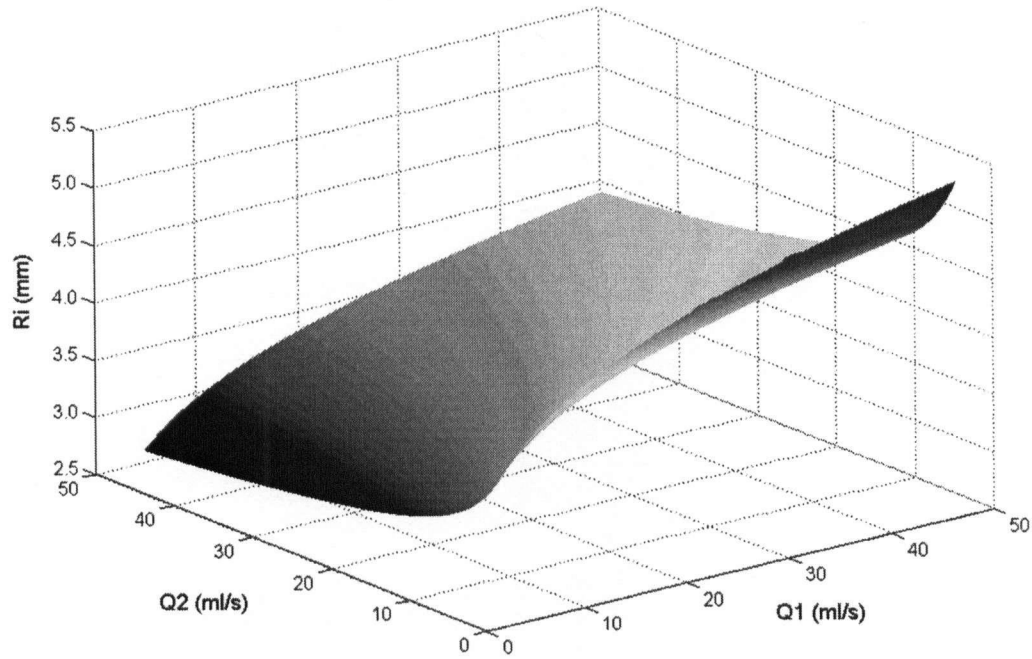

Figure K.3: Interfacial radius versus the flow rates of the two fluids.

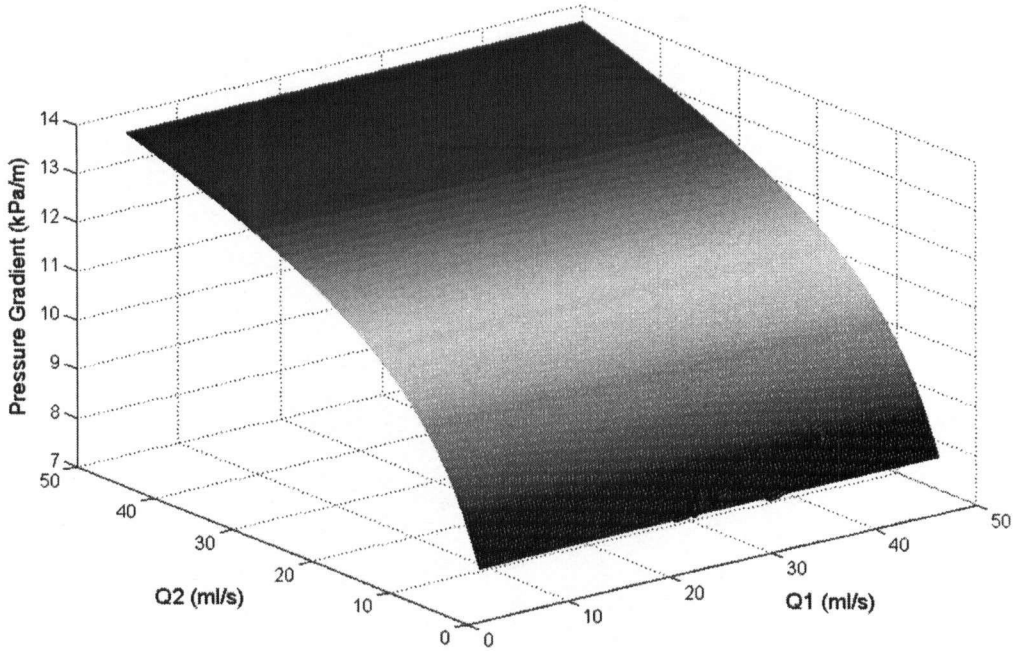

Figure K.4: Pressure gradient along the axis of the pipe versus the flow rate of the two fluids.

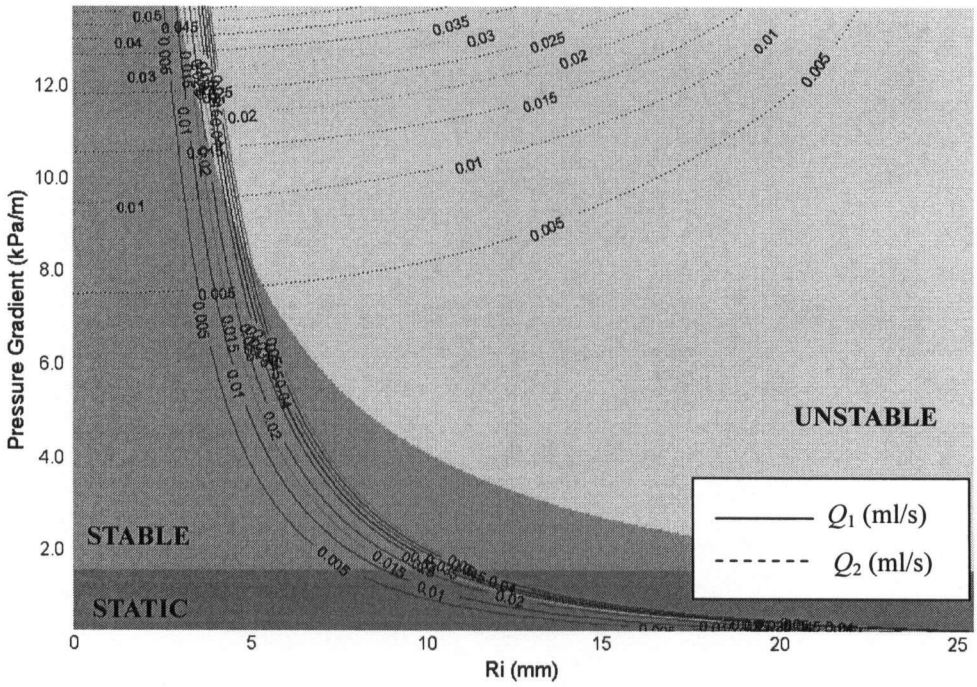

Figure K.5: Contours of flow rates versus the pressure gradient and interfacial radius.

Appendix L

Various Plots of Set 3 Experiments

Inner core fluid: 0.3% Xanthan NF-C solution.
Lubricating fluid: 0.5% Carbopol 940 solution (pH 5.0).
All plots are generated with the numerical control model.

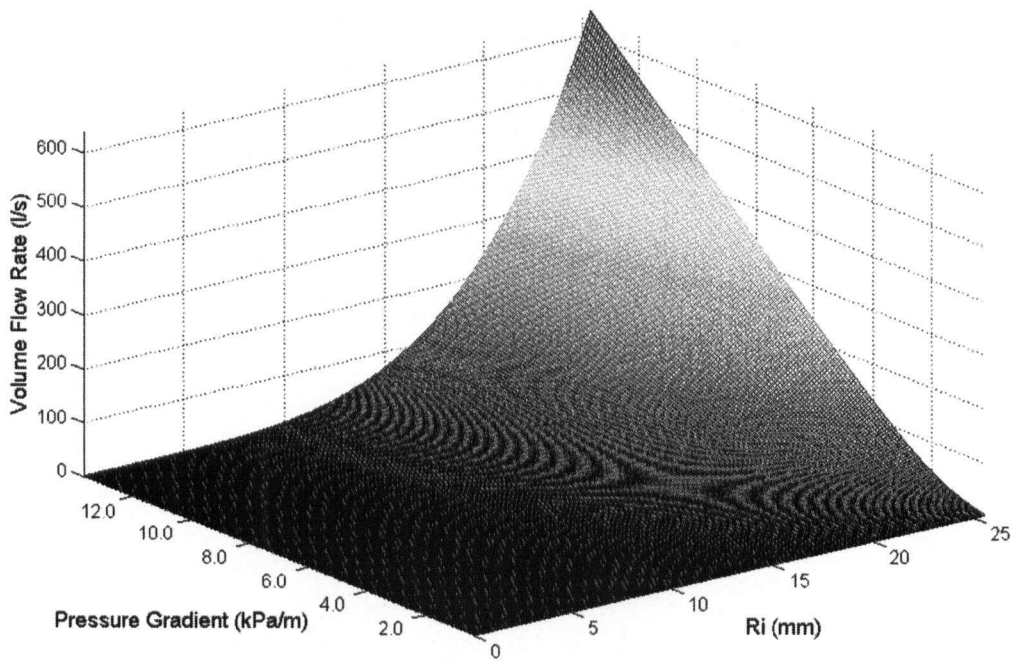

Figure L.1: Flow rate of the inner core fluid versus the pressure gradient along the axis of the pipe and interfacial radius.

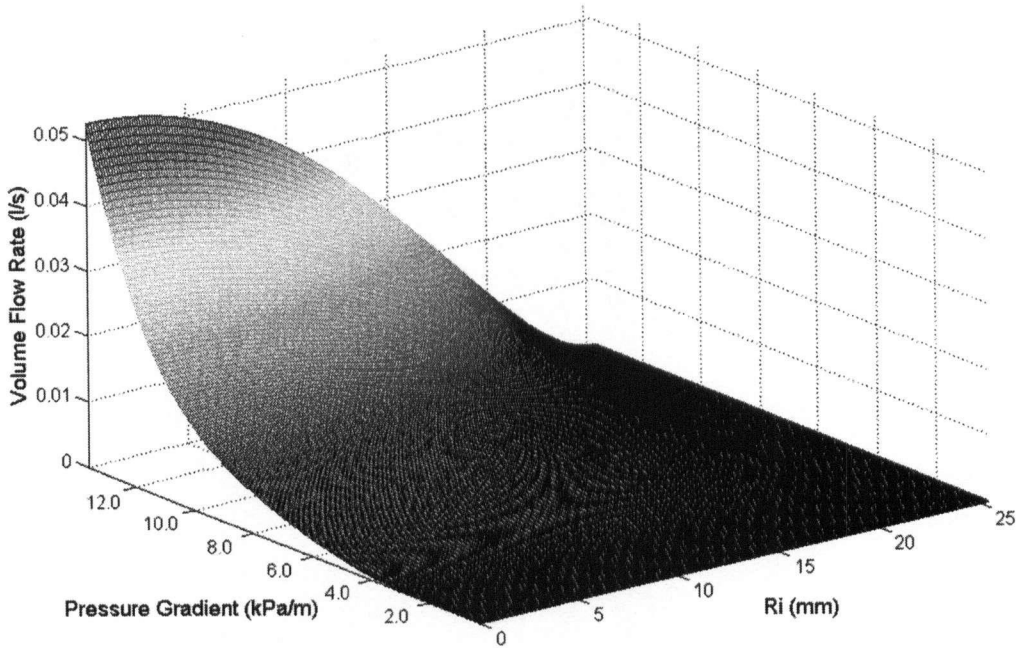

Figure L.2: Flow rate of the lubricating fluid versus the pressure gradient along the axis of the pipe and interfacial radius.

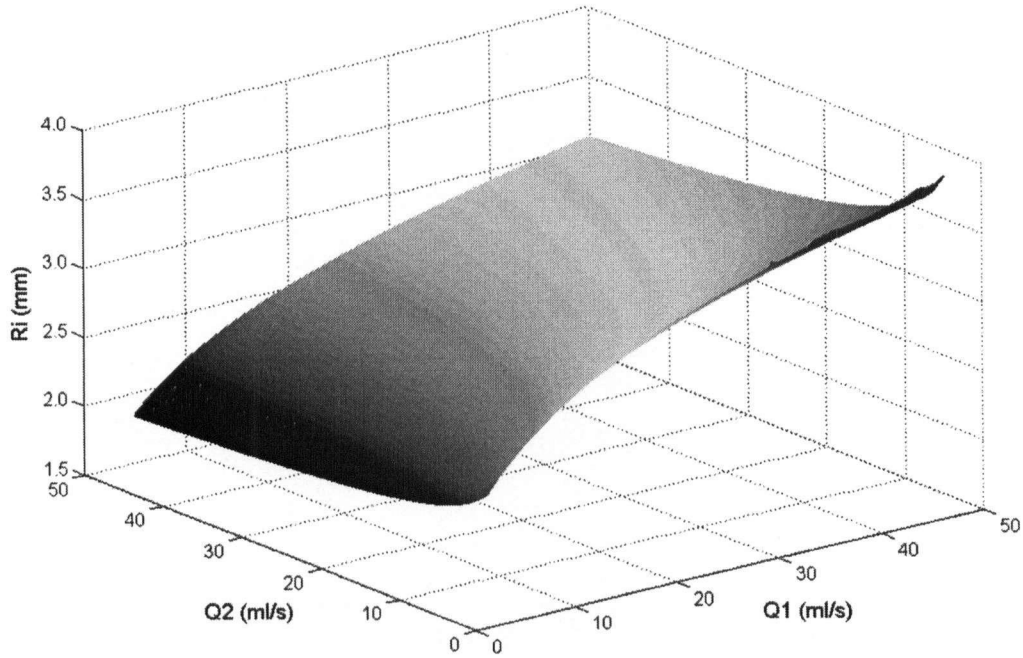

Figure L.3: Interfacial radius versus the flow rates of the two fluids.

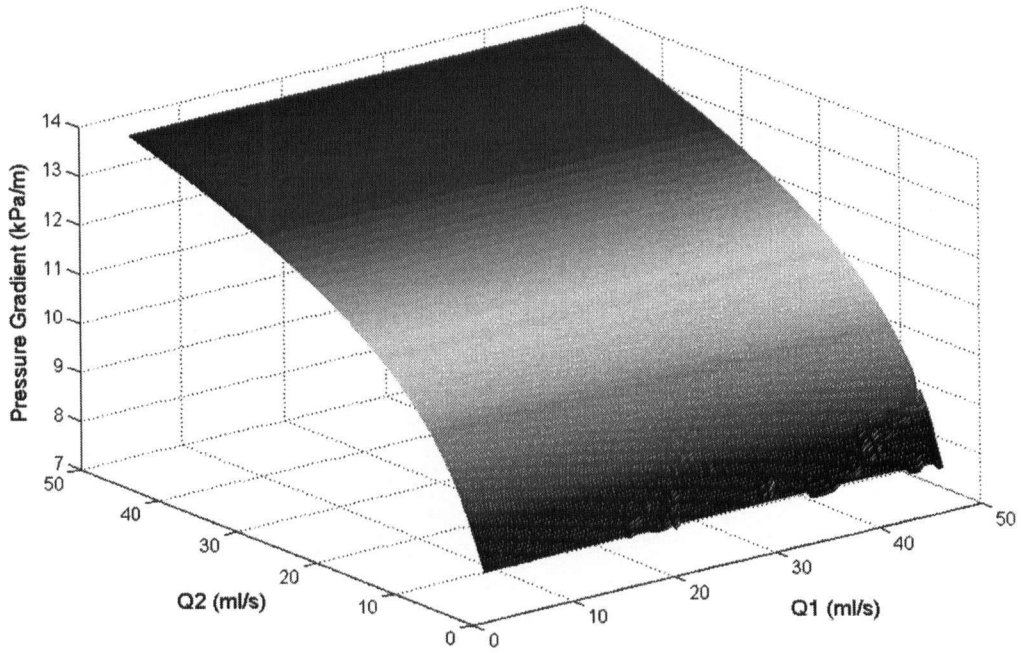

Figure L.4: Pressure gradient along the axis of the pipe versus the flow rate of the two fluids.

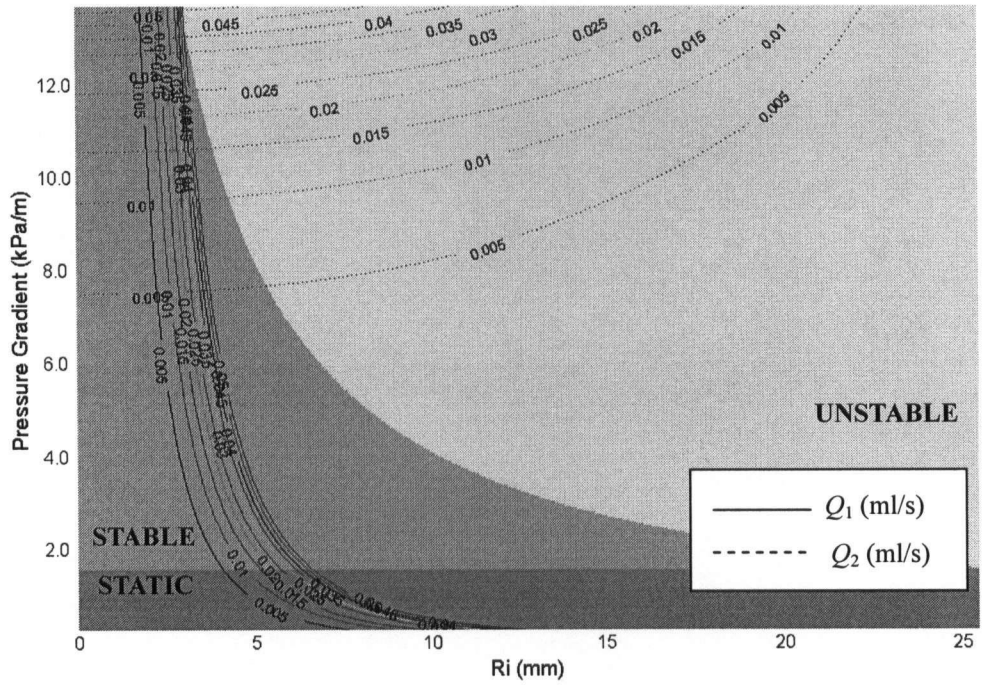

Figure L.5: Contours of flow rates versus the pressure gradient and interfacial radius.

Appendix M

Various Plots of Set 4 Experiments

Inner core fluid: 0.5% Xanthan NF-C solution.
Lubricating fluid: 0.3% Carbopol 940 solution (pH 5.0).
All plots are generated with the numerical control model.

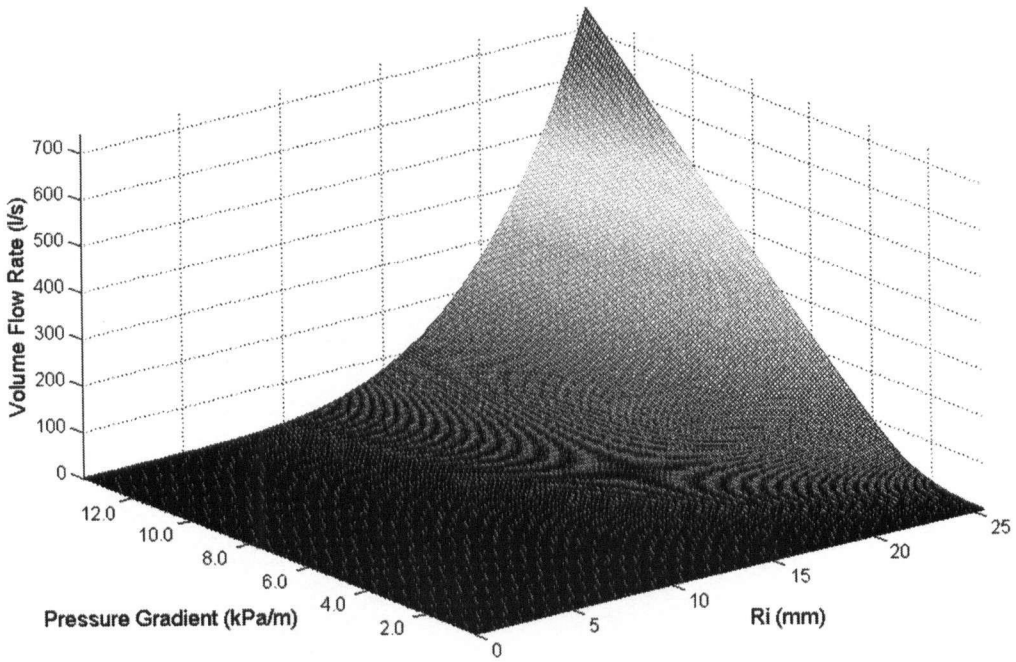

Figure M.1: Flow rate of the inner core fluid versus the pressure gradient along the axis of the pipe and interfacial radius.

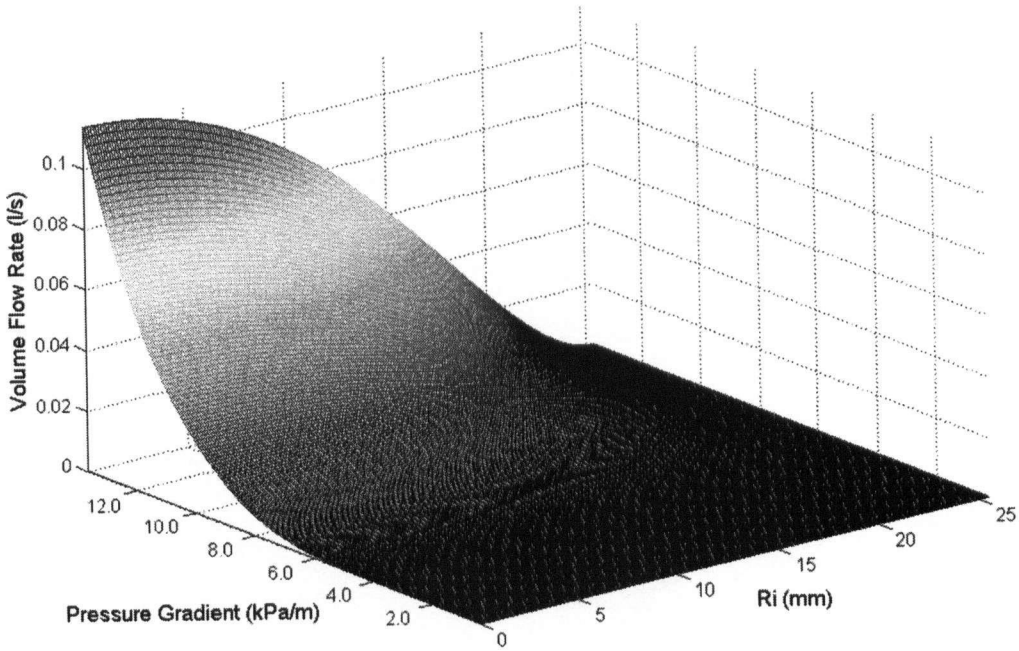

Figure M.2: Flow rate of the lubricating fluid versus the pressure gradient along the axis of the pipe and interfacial radius.

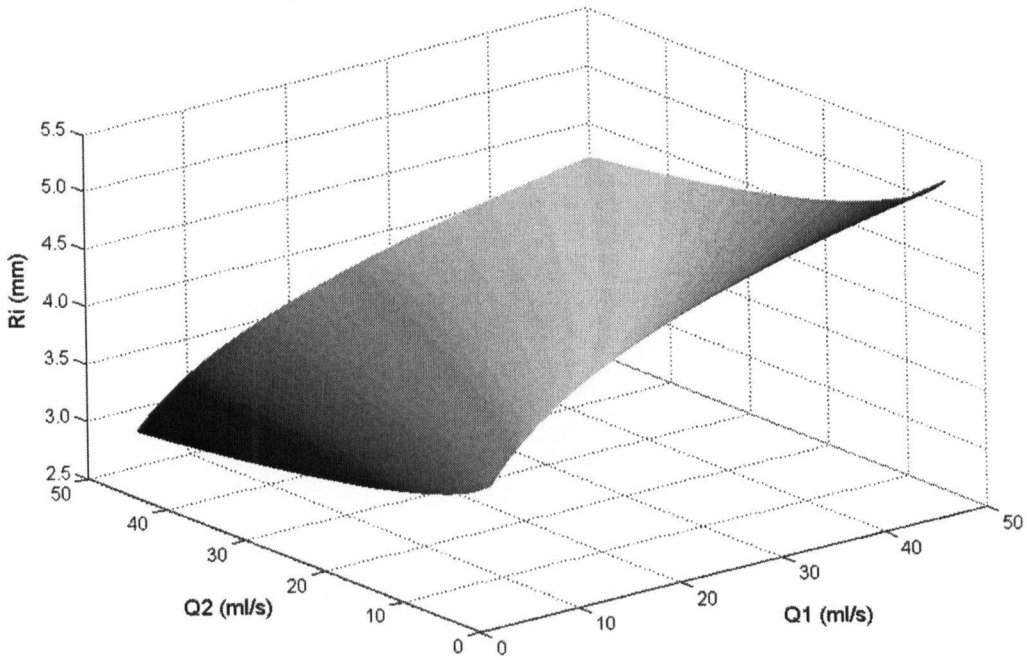

Figure M.3: Interfacial radius versus the flow rates of the two fluids.

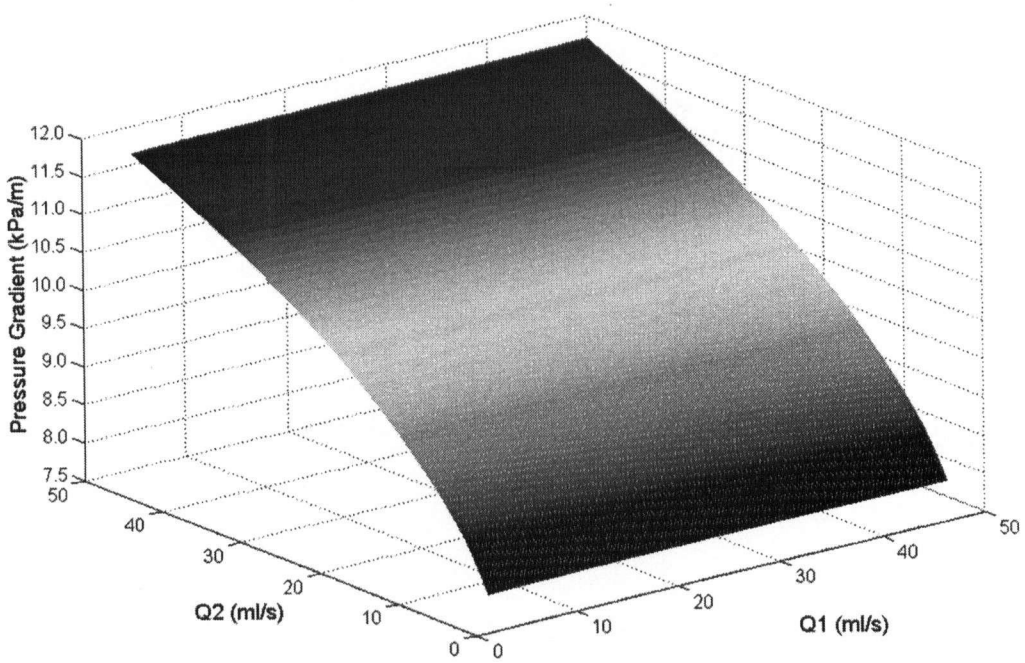

Figure M.4: Pressure gradient along the axis of the pipe versus the flow rate of the two fluids.

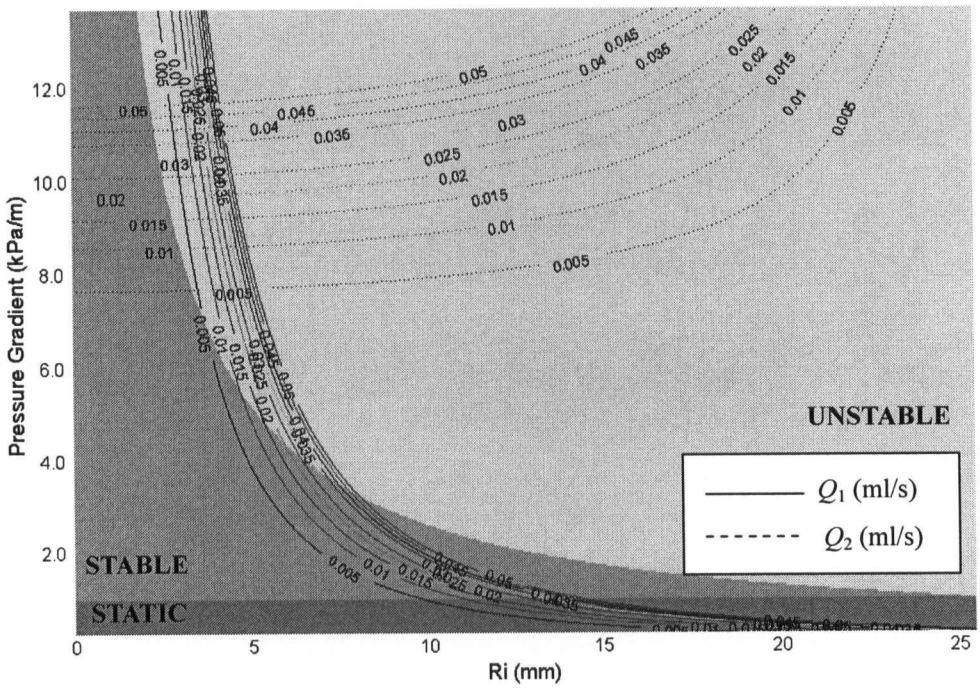

Figure M.5: Contours of flow rates versus the pressure gradient and interfacial radius.

Appendix N

Specifications of Monyo 332 Progressive Cavity Pump

SPECIFICATION DATA

MOYNO® 500 PUMPS

300 SERIES
331, 332, 333, 344, 356 AND 367 MODELS

DIMENSIONS

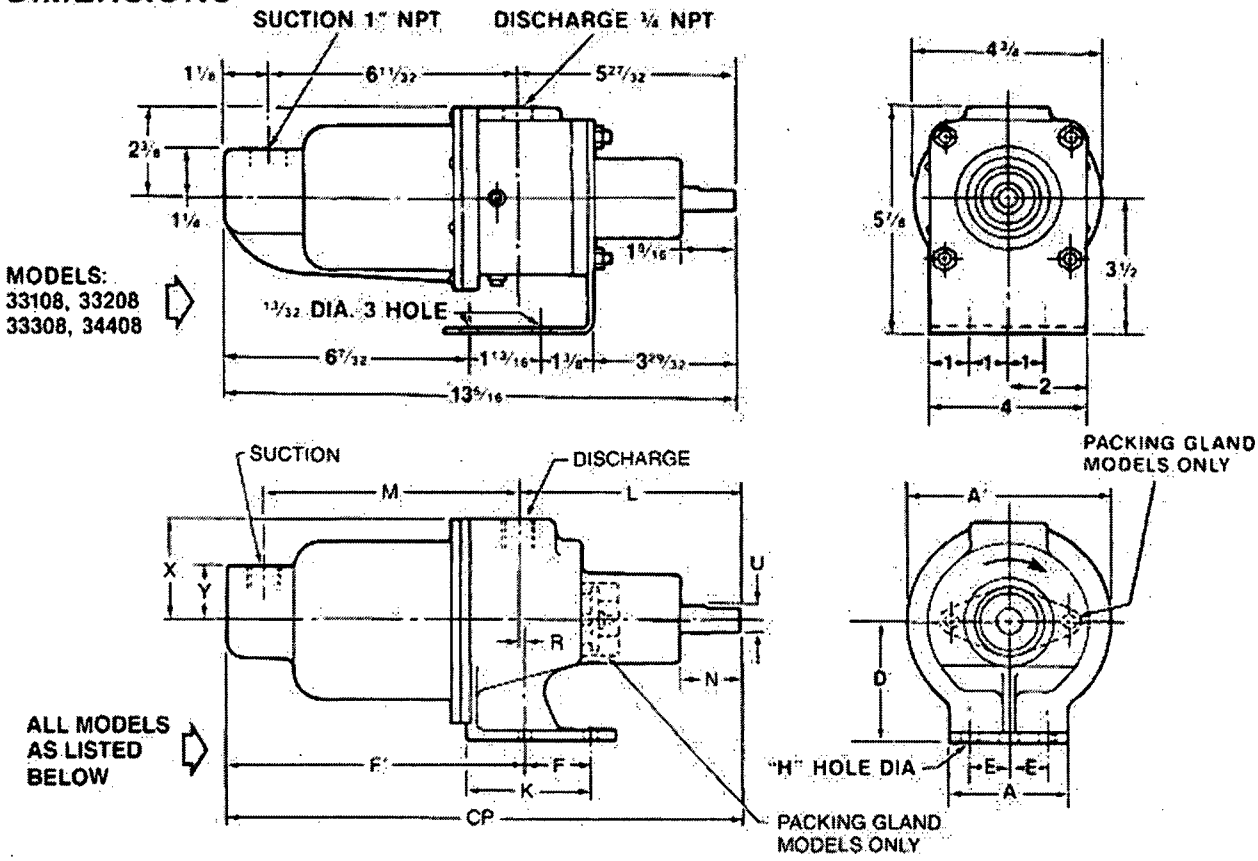

MODELS	CP	A	A¹	D	E	F	F¹	H	K	L	M	N	R	U	X	Y	SUCT (NPT)	DISCH (NPT)
33101, 33201 33301, 33104 33204, 33304 34401, 34404	12 5/8	3 1/8	4 3/4	2 3/4	1	1 13/16	6 15/16	13/32	3 1/32	5 11/16	6 1/16	1 7/16	—	5/8	2 3/8	1 1/4	3/4	3/4
*34411	13 15/16	3 1/4	4 3/4	2 3/4	1 1/8	—	7 3/16	13/32	2 7/8	7	6 1/16	1 3/8	1/4	5/8	2 5/16	1 1/4	3/4	3/4
35601, 35604	17 1/2	6 1/2	7 9/16	4 9/32	1 3/4	2	10 19/32	13/32	4 1/2	7 3/8	8 5/8	2 3/8	15/32	3/4	3 25/32	2 1/8	1 1/2	1 1/4
*35611, *35613	19 3/8	6 1/2	7 9/16	4 9/32	1 3/4	2 1/2	10 19/32	13/32	4	9 11/32	8 5/8	2 13/32	9/16	3/4	3 25/32	2 1/8	1 1/2	1 1/4
36701, 36704	20 15/16	5 1/4	8	4 1/2	2	2 5/16	13	9/16	4 1/16	7 15/16	11 3/16	2 1/8	—	1	4	2 1/2	2	2

*Packing Gland Model

All dimensions are in inches. Specifications subject to change without notice.

331, 332, 333 and 344 MODELS PERFORMANCE (water at 70°F)

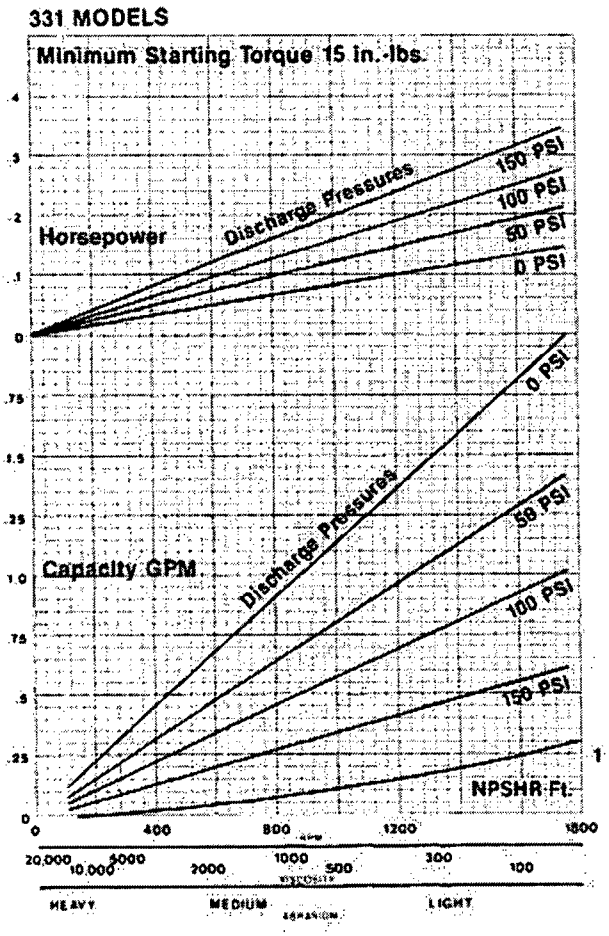

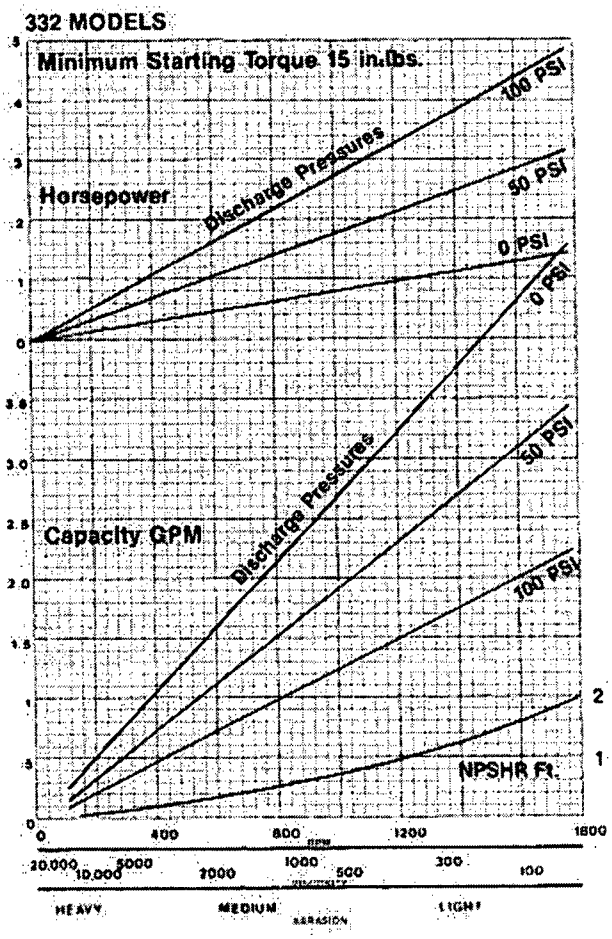

NOTE: For fluids with viscosity over 200 CP (1000 SSU), pump capacity is reduced by 20%.

MATERIALS OF CONSTRUCTION

COMPONENT	MODELS			
	33101, 33201 33301, 34401	33104, 33204 33304, 34404	33108, 33208 33308, 34408	*34411
Housing	Cast iron	316 SS	Nylon	Cast iron
Rotor	416 SS/CP	316 SS/CP	416 SS/CP	416 SS/CP
Stator	NBR (Nitrile)	NBR (Nitrile)	NBR (Nitrile)	NBR (Nitrile)
Weight (lbs)	16	16	8	16

* Packing Gland Model
CP = Chrome plated

333 MODELS

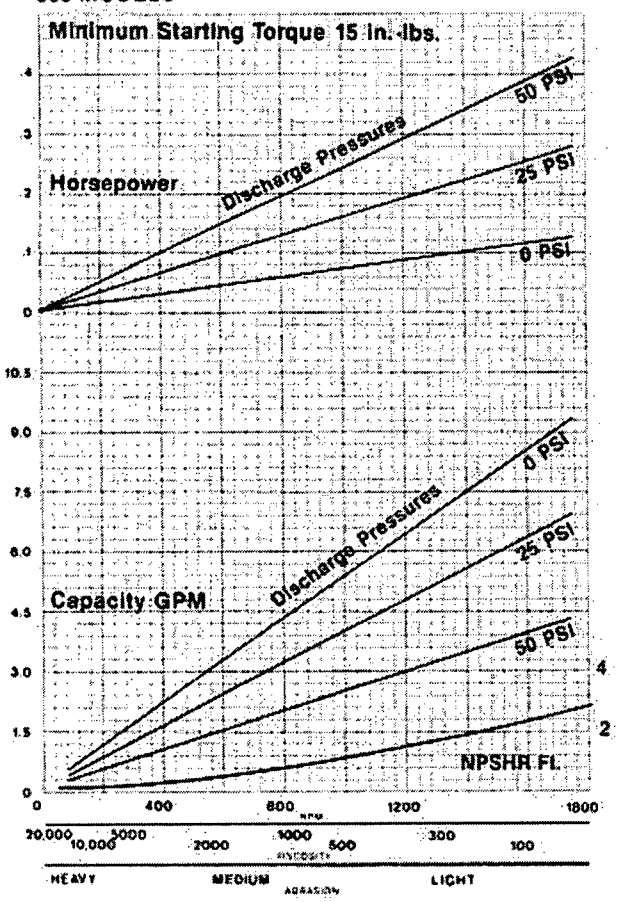

344 MODELS

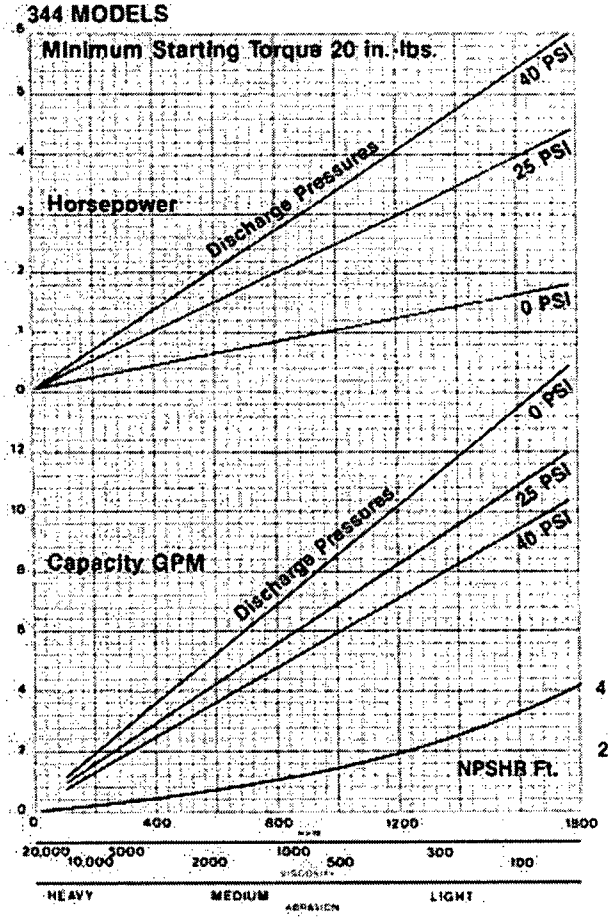

NOTE: For fluids with viscosity over 200 CP (1000 SSU), pump capacity is reduced by 20%.

356 and 367 MODELS PERFORMANCE (water at 70°F)

356 MODELS

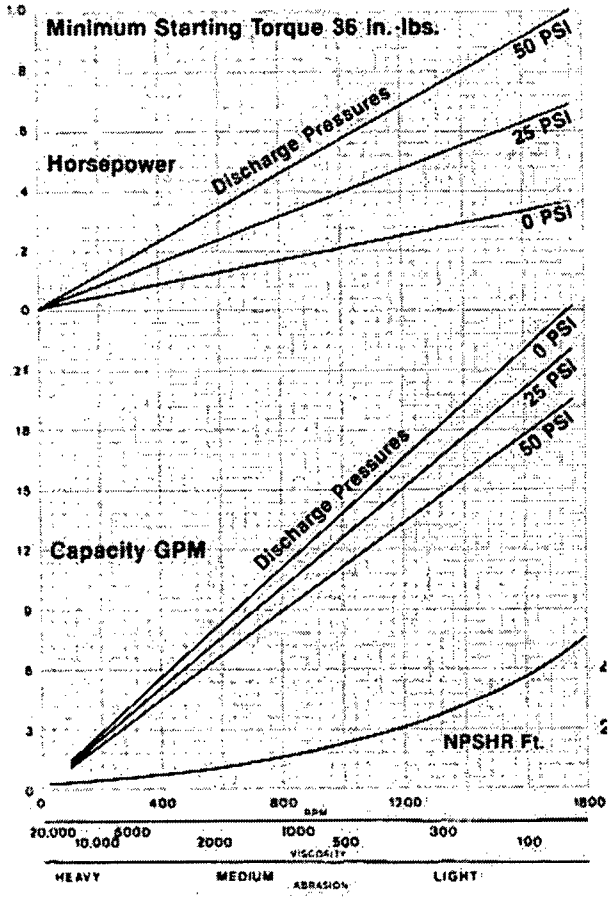

367 MODELS

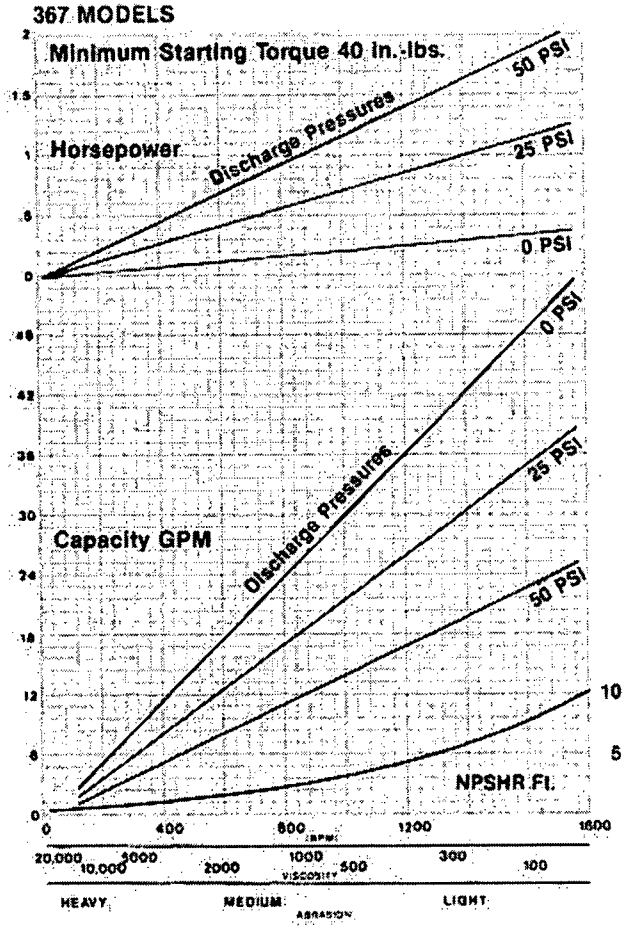

NOTE: For fluids with viscosity over 200 CP (1,000 SSU), pump capacity is reduced by 20%.

MATERIALS OF CONSTRUCTION

COMPONENT	MODELS					
	35601, 35611		35604, 35613		36701	36704
Housing	Cast iron		316 SS		Cast iron	316 SS
Rotor	416 SS/CP		316 SS/CP		416 SS/CP	316 SS/CP
Stator	NBR (Nitrile)		NBR (Nitrile)		NBR (Nitrile)	NBR (Nitrile)
Weight (lbs)	37	40	37	40	54	54

CP=Chrome plated

© 1999 by Moyno, Inc.
® Moyno is a registered trademark of Moyno, Inc.

Printed in U.S.A.

Appendix O

Specifications of Monyo 1000 Progressive Cavity Pump

Moyno® 1000 Pumps

The Competitive Edge in Pumping Solutions

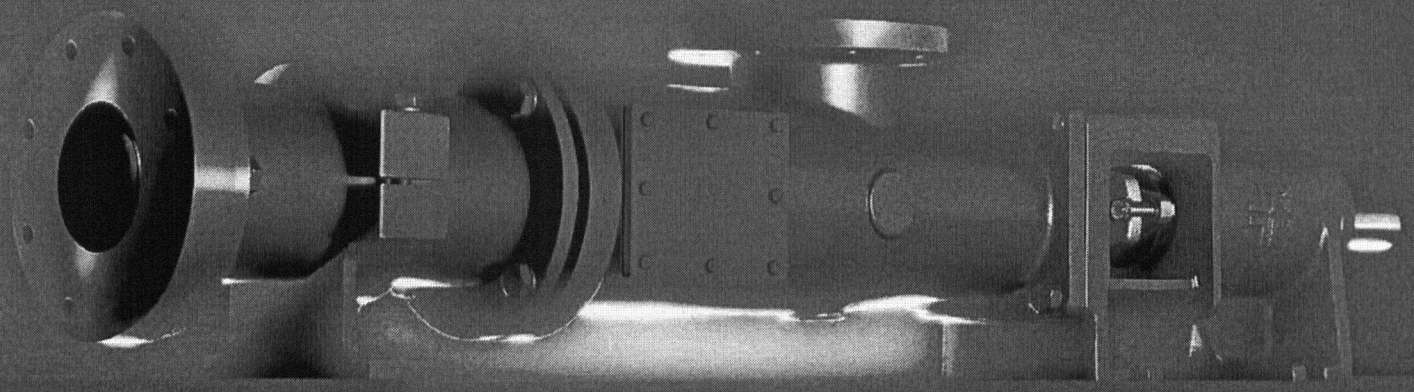

CERTIFICATE No. 101442

MOYNO

Always the Right Solution™

Moyno® 1000 Pumps

Outstanding Benefits Provide the Competitive Edge

Economical, high-efficiency performance with application versatility and maintenance simplicity...the Moyno 1000 pump offers you an unparalleled combination of benefits and features other positive displacement pumps cannot match.

- Sealed pin joint for longer life
- Easy to maintain; low cost of ownership
- Standard flange, close-coupled and open throat hopper models
- Wide range of materials of construction
- High volumetric and mechanical efficiency
- Minimal power consumption and operating costs
- No valves to clog, stick or vapor lock
- Handle clean water to viscous, abrasive fluids and slurries
- Efficient and economical fluid transfer, extraction, feeding and metering
- Smooth non-pulsating flow
- Head independent of pump speed
- Low NPSH requirement
- Self-priming
- Low shear
- Viscosities over 1,000,000 cps.
- High suction lift to 28 feet
- Entrained solids to 1.1 inches in diameter
- Fluid temperature range to 400˚F

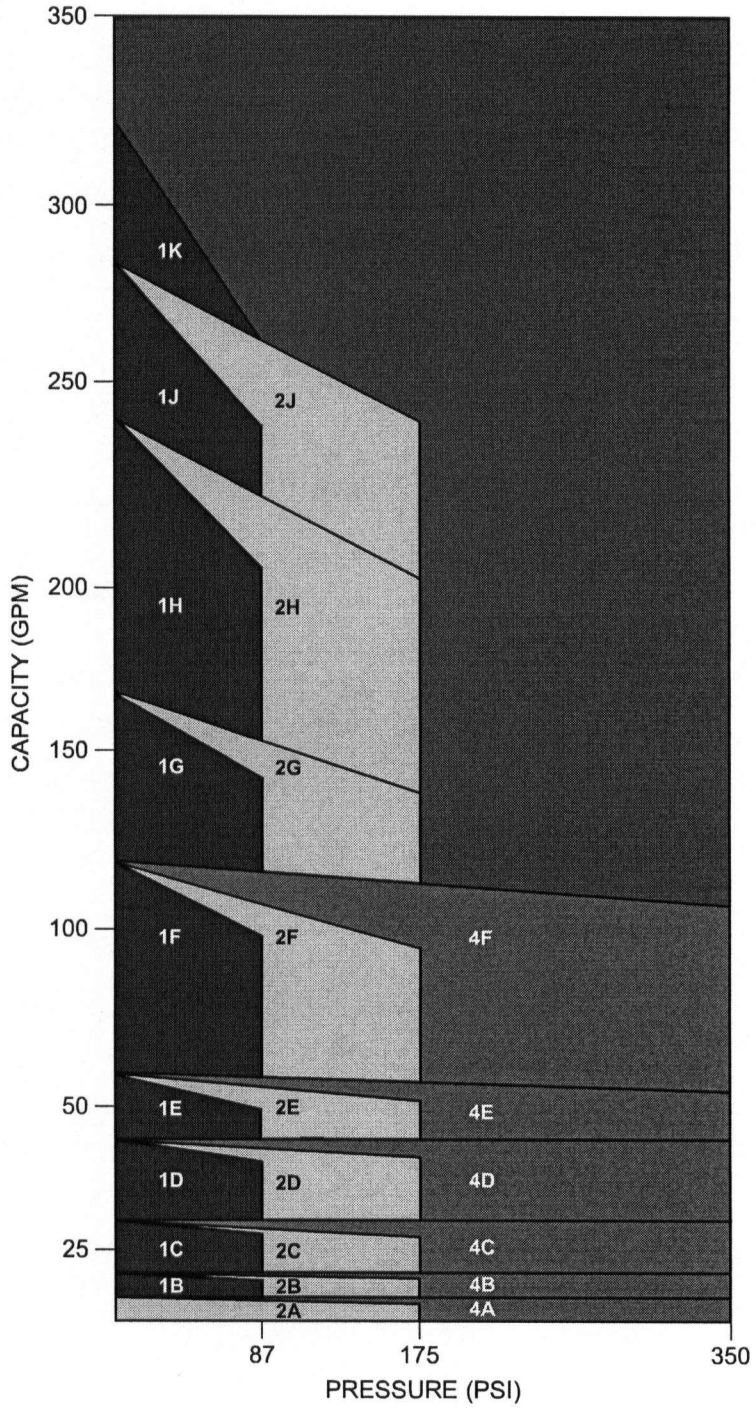

Moyno® 1000 Pumps

Uncompromising Quality Design and Materials of Construction

Moyno 1000 pumps combine design excellence, quality materials and state-of-the-art manufacturing to offer you...

Two-Piece Drive Shaft Now Available On All Bare Shaft Models

- Easy mechanical seal and pump maintenance

Highest Grade Components

1. Abrasion-resistant chrome-plated rotors in high grade carbon steel or 316 stainless. New Ultra-Shield® rotor coatings are available on all models.
2. Wide variety of Ultra-Flex® stator elastomers to meet specific application needs.
3. Wettable pump body parts in cast iron or 316 stainless.

Versatile Piping Connections

4. Flanges available in 125 or 150 lb. flat face, cast iron or stainless steel on pump suction and discharge ends.
   - 300 lb. raised face flanges on discharge end of four-stage, high-pressure pumps.
5. Suction port can be rotated to four positions, 90° apart.
   - Open throat with large suction hopper allows smooth flow of viscous materials from auger assembly to rotor/stator elements.

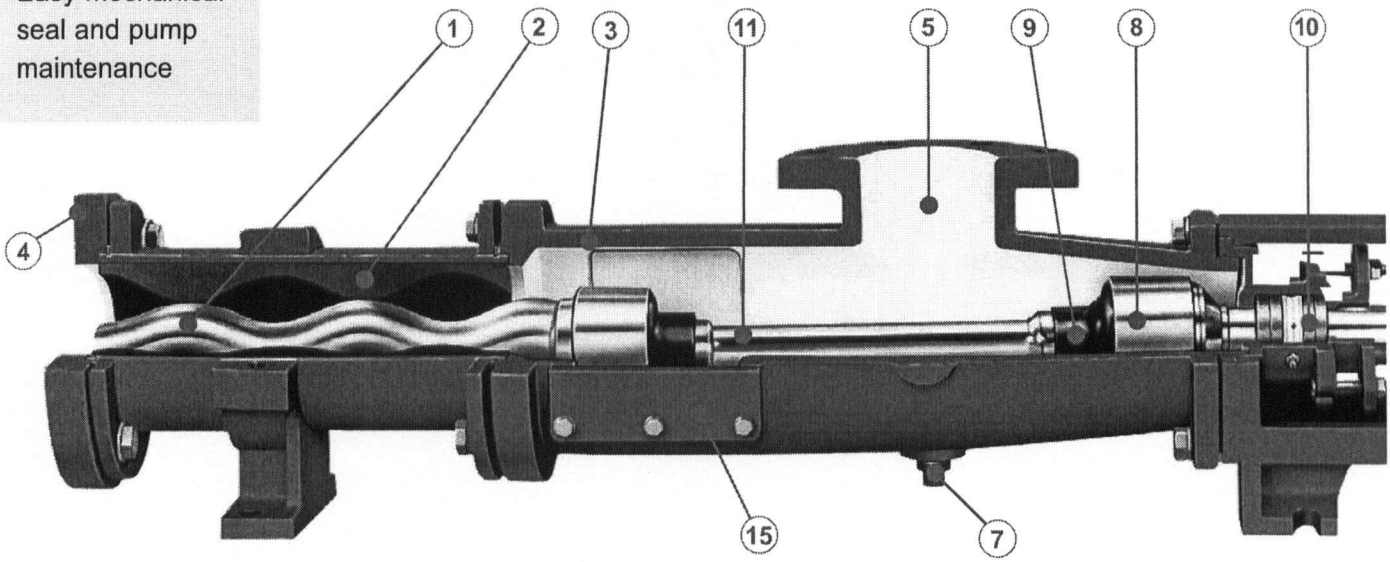

How a Progressing Cavity Pump Works

Although the geometry of its pumping elements may seem somewhat complex, the principle of
progressing cavity pump operation is deceptively simple.

The key components are the rotor and stator. The rotor is a single external helix with a round cross-section, precision machined from high-strength steel. The stator is a double internal helix molded of tough, abrasion-resistant elastomer, permanently bonded within an alloy steel tube. As the rotor turns within the stator, cavities are formed which progress from the suction to the discharge end of the pump, conveying the pumped material. The continuous seal between the rotor and the stator helices keeps the fluid moving steadily at a fixed flow rate proportional to the pump's rotational speed.

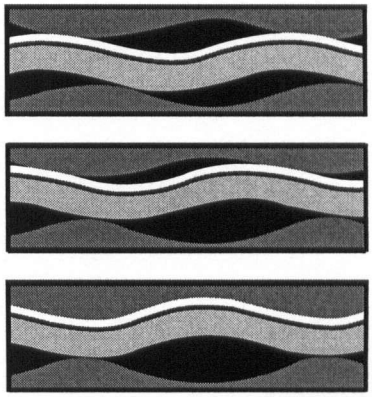

Easy Assembly and Disassembly

6. Only standard tools needed for repairs.

7. Drain plug allows easy, complete drainage of suction housing for pump inspection or maintenance.

Low-Maintenance Drive Trains

8. Hardened pin-type universal joints are sealed and lubricated for long life and easy maintenance.
   - Low angularity minimizes wear.
   - Durable connecting rod and rotor/shaft head.
   - No thin bushings used.
   - Spare set of pin holes extends service life.

9. Universal joint seal design increases service life three to five times over unprotected joints.
   - No metal bands or special tools required.

10. High-quality pump packing.
    - Grease lubrication extends packing life.
    - Stuffing box water flush system is an option.
    - Mechanical seals available.

Longer Lasting Drive Ends

11. Connecting rod is precision machined from high-quality alloy steel or 316 stainless.
    - Provides low angularity, minimum velocity and smaller universal joint contact area.
    - Reduces friction heat and increases service life and maximum torque to easily handle heavy fluids.

12. Heavy-duty, grease-lubricated bearings absorb radial and thrust loads.
    - Longer packing or mechanical seal life.
    - Meet ANSI B.10 requirements.
    - No relubrication needed until pump disassembly.

13. Precision-machined chrome-plated carbon steel or 316 stainless drive shaft.

14. Standard high-quality gear drives for close-coupled units.
    - Available with integral motors, C-face reducers with AC or DC motors and mechanical variable speed drives.

15. Optional inspection ports on "E" size and larger for internal inspection without moving piping.

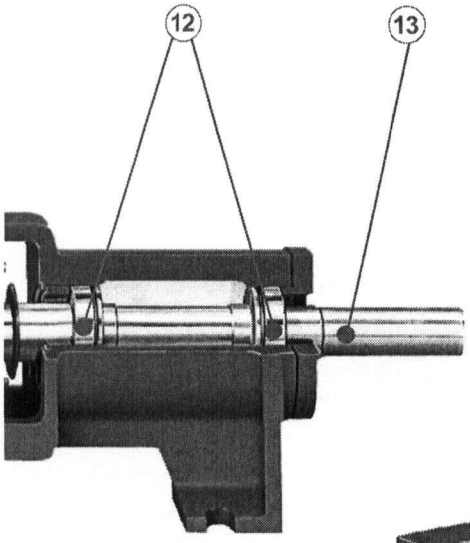

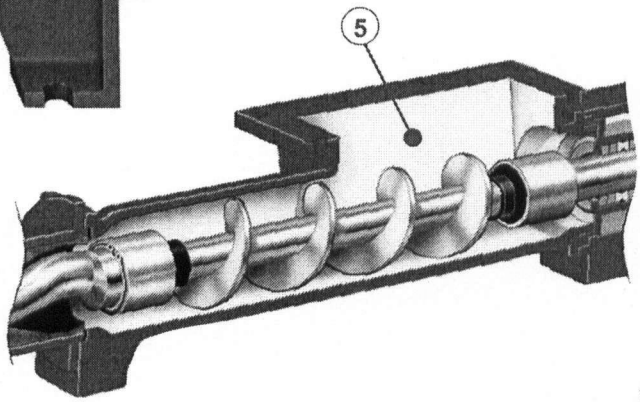

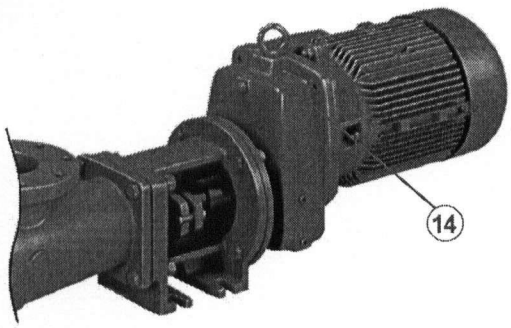

Moyno® 1000 Pumps

Field-Proven Performance

Moyno 1000 pumps successfully serve in thousands of applications worldwide across a broad range of industries that include:

Water & Wastewater Treatment

Chemical dosing
Scum and grease
Sampling
Lime slurries

Pulp & Paper

Chemical metering
Coating color
Starch
Stock transfer
Mill wastewater

Chemical

Polyester blend
Calcium carbonate slurry
Polymer metering
Soaps and detergents

Pharmaceutical

Pill pastes
Hand lotions

Petroleum

Oily water separation
Offshore oil platform transfer
Polymer flooding

Miscellaneous

Adhesives and mastics
Grout
High-pressure water
Gels
Lubricants

Transferring dewatered filter cake at 20 gpm and 20 psig.

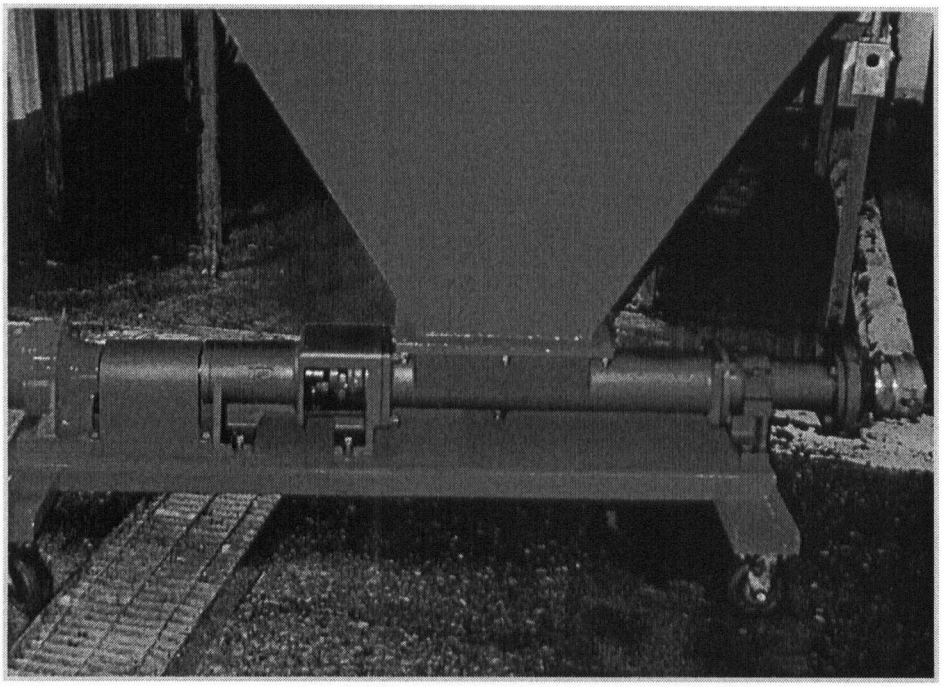

...And many more!

Moyno® Progressing Cavity Pumps

Parts and Services

Your critical applications demand responsive service and support. Our network of authorized representatives and stocking distributors are seasoned professionals with many years of experience specifying, installing and maintaining fluids handling equipment.

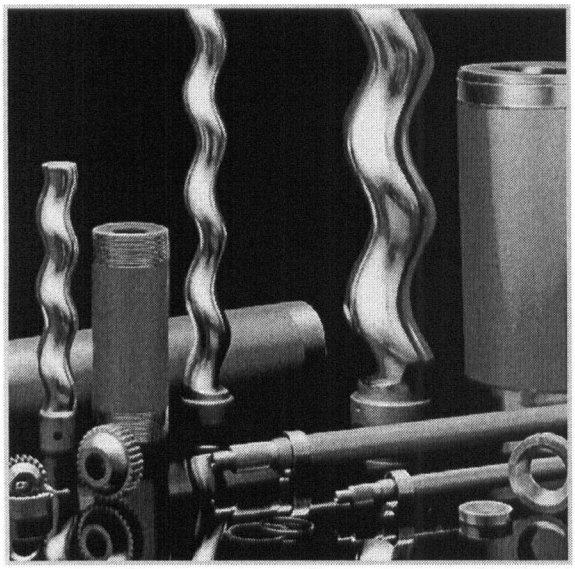

Certified Service Facilities...Sustaining Standards of Excellence

When you purchase genuine Moyno replacement parts and service from one of our Certified Service Facilities, you can be confident that you are receiving the highest quality service and parts available for your Moyno pump. Certified distributors meet stringent capabilities standards in the areas of repair, service, inventory and physical facility layout. They must also successfully complete our Product Services Training Program. Only then are they designated a Certified Service Facility.

Moyno distributors offer you:

- Maintenance cost reduction ideas
- Preventative maintenance programs and service contracts
- Extensive local inventory of genuine Moyno replacement parts
- On-site maintenance seminar
- Troubleshooting assistance
- Warrantied repairs
- 24-hour service and support
- Convenience

Always Specify Genuine Moyno Replacement Parts!

For information about Moyno products or for technical assistance, write or call:

Moyno, Inc.
P.O. Box 960
Springfield, OH 45501-0960
U.S.A.
Telephone:.....1-877-4UMOYNO
Facsimile: 937-327-3572
Web site: www.moyno.com

Note: Information contained herein is subject to change without notice. Before making a final product selection, please contact a Moyno representative.

Your Moyno Authorized Distributor is:

Bulletin 114-M

MOYNO

Always the Right Solution™

© 1999 by Moyno, Inc.
® Moyno, Ultra-Shield and Ultra-Flex are registered trademarks of Moyno, Inc.
Moyno, Inc. is a Unit of Robbins & Myers, Inc.

Printed in U.S.A.
5M EDGE 403

MOYNO

Always the Right Solution™

Section:
1000 Pumps
Date: February 1, 2001

Performance Data

Curve 1.02

Models: A2A, B2A, A4A, B4A

Use appropriate HP and pressure scales for the number of stages required.

Note: Pressure limits rated at 87 psi/ stage (70 Duro). Some models have additional limits. Please consult factory before making final selection.

		RPM	200	400	600	800	1000	1200	1500
NPSH Required – (Ft.)			0.47	0.94	1.41	1.88	2.35	2.82	3.53
STARTING TORQUE, Minimum Recommended Motor HP*	*49 IN/LB*	2 STG	0.25	0.33	0.33	0.50	0.75	1.00	1.00
	62 IN/LB	4 STG	0.25	0.50	0.50	0.75	0.75	1.00	1.00
Drive End HP Must be added to HP value from curve.		2, 4 STG	0.04	0.08	0.12	0.16	0.20	0.24	0.30

*Based on drives supplying 150% starting torque.

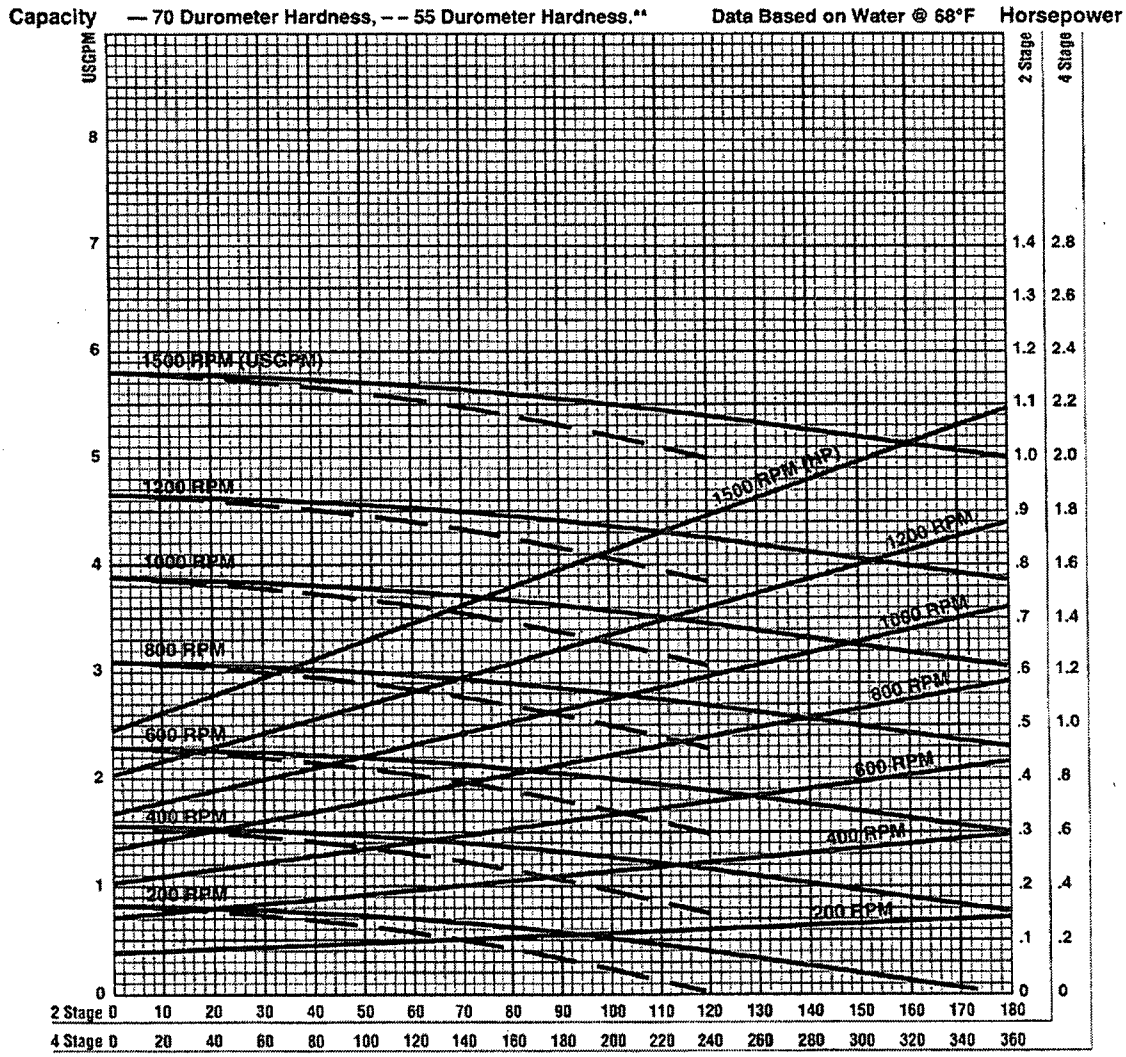

**Std. Nitrile, EPDM, and Fluoroelastomer = 70 Duro.
Std. Natural Rubber = 55 Duro.

(BAR x 1.0197 = kg/cm²)
(BAR x 14.504 = PSI)
(USGPM = 227.1 L/HR)
(1 kW = 1.3410 HP)

A2A, B2A, A4A, B4A

HORSEPOWER MULTIPLIERS:

Pump horsepower from the reverse side can be broken into three components: drive end, rotor/stator, and hydraulic.

Temperature affects the rotor/stator HP component only. For applications involving temperatures above 70°F, it is necessary to adjust the rotor/stator HP component of the horsepower obtained from the reverse side (i.e., the greater of the water HP or Minimum Recommended HP). This new horsepower is referred to as the **Temperature Corrected Horsepower**.

Rotor/stator horsepower can be found from the curve on the previous page. It is the HP at zero pressure for the corresponding RPM and number of stages.

To calculate the Temperature Corrected Horsepower, subtract the rotor/stator HP from the greater of the water or minimum recommended HP. This gives you the drive end/hydraulic HP. Multiply the rotor/stator HP by the appropriate temperature multiplier listed below. Add this adjusted value to the drive end/hydraulic HP to get the total Temperature Corrected Horsepower.

(Degrees F = 9/5 C + 32)

FLUID TEMPERATURE	70°F	100°F	125°F	150°F	175°F	200°F
HORSEPOWER MULTIPLIERS						
- Standard Size Rotor	1.00	1.10	1.30	1.60	2.00	2.50
- Undersize Rotor	0.75	0.80	0.85	0.95	1.10	1.60

For applications involving temperatures greater than 200°F, consult the factory.

HORSEPOWER ADDITIVES:

Shown below are HP additives for both water base slurries and for viscous materials. To use these tables, first determine which table applies to your product and enter that table with the appropriate fluid characteristics. Determine the HP additive per 100 RPM and multiply it by the speed of your pump divided by 100. Add the resulting figure to the HP for water from the curve on the preceding page or to the minimum HP for starting from the table at the top of the preceding page, whichever is larger.

If your product is a combination of a slurry and viscous material, determine the appropriate HP additive from both tables below and use whichever is greater.

TABLE I – WATER BASE SLURRIES

HP ADDER/100 RPM

% Solids	Fine 16 Mesh (1.0 mm) (.039")		Medium 16 to 9 Mesh (1.0-2.0 mm) (.039-.078")		Coarse 9 to 4 Mesh (2.0-5.0 mm) (.078-.185")	
	Number of Stages					
	2	4	2	4	2	4
10	.02	.04	.05	.07	.09	.10
30	.05	.06	.13	.17	.27	.33
50	.09	.13	.21	.27	.44	.55

TABLE II – VISCOSITY (NEWTONIAN FLUIDS):

HP ADDER/100 RPM/STAGE

Viscosity (Centipoise)						
1	2,500	5,000	10,000	50,000	100,000	150,000
0	.013	.017	.023	.050	.065	.080

© 2001 by Moyno, Inc.
Moyno, Inc. is a Unit of Robbins & Myers, Inc. Printed In U.S.A.

Appendix P

Top Pressure Sensor: EW-68075-40
Bottom Pressure Sensor: EW-68075-42

Cole-Parmer Economical ±0.25% Accuracy Pressure Transmitters

- Suitable for high shock/vibration applications; no seals or O-rings to cause leakage
- Stainless steel sensor attached to SS electrode forms a variable capacitor.

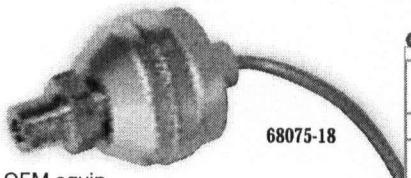

68075-18

Economical, excellent accuracy, and high performance. Ideal for industrial OEM equipment, industrial engines, hydraulic systems, and compressor control.

Transmitters with 4 to 20 mA output have red (positive power) and black (output) wires. Transmitters with 0.5 to 5.5 V output have red (positive power), green (output), and black/white (common) wires.

Specifications

ISO 9000 REGISTERED SUPPLIER CE

Accuracy: ±0.25% full-scale
Temperature range (compensated): -4° to 176°F (-20° to 80°C)
Operating temperature range: -40° to 260°F (-40° to 125°C)
Process connection: ¼" NPT(M)
Power: 9 to 30 VDC
Electrical connection: 2-ft cable
Media compatibility: gases or liquids compatible with 17-4 PH stainless steel
Dimensions: 2¾"L x 1½" diameter
Shpg wt: 1 lb (0.5 kg)

Ordering Information

Range	4 to 20 mA output		0.5 to 5.5 V output	
	Catalog number	Price	Catalog number	Price
Compound transmitters				
-14.7 to 0 psig	A-68075-00		A-68075-30	
-14.7 to 15 psig	A-68075-02		A-68075-32	
-14.7 to 30 psig	A-68075-04		A-68075-34	
-14.7 to 60 psig	A-68075-06		A-68075-36	
-14.7 to 100 psig	A-68075-08		A-68075-38	
Gauge pressure transmitters				
0 to 5 psig	A-68075-10		A-68075-40	
0 to 10 psig	A-68075-12		A-68075-42	
0 to 25 psig	A-68075-14		A-68075-44	
0 to 50 psig	A-68075-16		A-68075-46	
0 to 100 psig	A-68075-18		A-68075-48	
0 to 250 psig	A-68075-20		A-68075-50	
0 to 500 psig	A-68075-22		A-68075-52	
0 to 1000 psig	A-68075-24		A-68075-54	
0 to 3000 psig	A-68075-26		A-68075-56	
0 to 10,000 psig	A-68075-28		A-68075-58	

Cole-Parmer High-Accuracy Industrial Pressure Transmitters

- **Welded stainless steel (SS) housing rated to NEMA 4 (IP65) standards**

Transmitters feature SS capacitive sensor for your more demanding systems—even withstands high shock and vibration applications. ElectroMagnetic Interference (EMI)/Radio Frequency Interference (RFI) resistance ensures accurate and consistent performance in any environment.

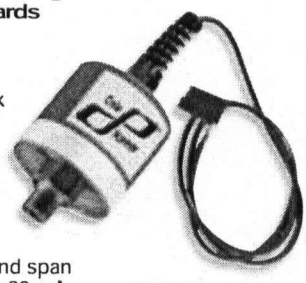

68073-14

Transmitters feature adjustable zero and span potentiometers. Transmitters with 4 to 20 mA output have red (positive power) and black (output) wires. Transmitters with 0.1 to 5.1 V output have red (positive power), green (output), and white/black (common) wires.

Specifications

ISO 9000 REGISTERED SUPPLIER CE

Accuracy: ±0.13% full scale
Temperature range (compensated): -4 to 176°F (-20 to 80°C)
Operating temperature: -40 to 260°F (-40 to 126°C)
Process connection: ¼" NPT(M)
Power: 12 to 28 VDC (unregulated)
Electrical connection: 2-ft L cable
Media compatibility: gases or liquids compatible with 17-4 PH stainless steel
Dimensions: 5"L x 2" diameter
Shpg wt: 1 lb (0.5 kg)

Range	4 to 20 mA output		0.1 to 5.1 V output	
	Catalog number	Price	Catalog number	Price
Compound transmitters				
-14.7 to 15 psi	A-68073-00		A-68074-00	
-14.7 to 30 psi	A-68073-02		A-68074-02	
-14.7 to 60 psi	A-68073-04		A-68074-04	
-14.7 to 100 psi	A-68073-06		A-68074-06	
Gauge pressure transmitters				
0 to 25 psig	A-68073-08		A-68074-08	
0 to 50 psig	A-68073-10		A-68074-10	
0 to 100 psig	A-68073-12		A-68074-12	
0 to 500 psig	A-68073-14		A-68074-14	
0 to 1000 psig	A-68073-16		A-68074-16	
0 to 3000 psig	A-68073-18		A-68074-18	
0 to 5000 psig	A-68073-20		A-68074-20	
0 to 10,000 psig	A-68073-22		A-68074-22	

Cole-Parmer Economical Pressure Transmitters

- True 1% interchangeability from unit to unit—laser trimmed technology
- Wide compensated temperature range
- Superior linearity, repeatability performance, and proof-and-burst pressure tolerance
- ElectroMagnetic Interference (EMI) and Radio Frequency Interference (RFI) shielding

68848-08

These economical transmitters feature reverse polarity protection, fused silicone strain gauge technology, NEMA 4X enclosure, and high over-temperature protection.

Transmitters with 4 to 20 mA output have red (positive power) and black (output) wires; transmitters with 1 to 5 V output have red (positive power), white (output), and black (common) wires.

Specifications

Accuracy: ±1% full scale
Temp range (compensated): -40 to 212°F (-40 to 100°C)
Operating temperature range: -40 to 250°F (-40 to 121°C)
Process connections: ¼" NPT(M)
Power: 8 to 30 VDC
Electrical connection: 3-ft cable
Media compatibility: gases or liquids compatible with 17-4 PH SS
Dimensions: 4"L x 1¾" dia
Shpg wt: 1 lb (0.5 kg)

Range	4 to 20 mA output		1 to 5 VDC output	
	Catalog number	Price	Catalog number	Price
Vacuum and compound transmitters				
-14.7 to 0 psig	A-68848-00		—	—
-14.7 to 30 psig	A-68848-02		A-68848-26	
Gauge pressure transmitters				
0 to 30 psig	A-68848-04		A-68848-28	
0 to 60 psig	A-68848-06		A-68848-30	
0 to 100 psig	A-68848-08		A-68848-32	
0 to 200 psig	A-68848-10		A-68848-34	
0 to 300 psig	A-68848-12		A-68848-36	
0 to 500 psig	A-68848-14		A-68848-38	
0 to 1000 psig	A-68848-16		A-68848-40	
0 to 3000 psig	A-68848-18		A-68848-42	
0 to 5000 psig	A-68848-20		A-68848-44	
0 to 10,000 psig	A-68848-22		A-68848-46	

Appendix Q

Specifications of Magnetic Flowmeter FMG 423H

NEW™ ELECTROMAGNETIC FLOWMETERS

1 YEAR WARRANTY · YEAR 2000 COMPLIANT · CE

FMG-400 Series

$2500

Basic Model

- **±0.5% Accuracy**
- **Clear, Backlit LCD Display**
- **Rotational Display**
- **Easily Programmed**
- **Easy Wiring**
- **Unique Noise Suppressor**

These cost-effective magnetic flowmeters combine superior noise immunity with high purity Alumina ceramic detection tubes, allowing precise measurements in a wide range of applications. Available in pipe sizes from ½" up to 16" to accommodate many materials: chemicals, corrosives, foods, pulp and other solid matter slurry flows. Unique noise-suppression circuitry utilizes the optimum square-waved excitation frequency, eliminating various noises generated by slurries, making this flowmeter ideal for pulp, food and grout applications.

SPECIFICATIONS

Accuracy:
±0.25% FS or ±0.5% of rate at <1.0 m/s
±0.1% FS or ± 0.5% of rate at 1.0 to 10 m/s
Fluid Electrical Conductivity Minimum: 5 µS/cm
Fluid Temperature:
-10 to 120°C (14 to 250°F)
Ambient Temperature:
-10 to 60°C (14 to 140°F)
Fluid Pressure: 290 psig
Enclosure: NEMA-4X (IP-67) corrosion-resistance type
Metering Tube Case: Carbon steel
Electronic Housing: Aluminum alloy
Display: LCD,16-column, 2-row LCD, alphanumeric with backlight
16 Engineering Programmable Units Including: %, MPS, GPM, LPM, m^3/s
Output: 4-20 mA/dc current with digital I/O provided, 1 open collector
Load Resistance: 0-1 k ohm
Capacity: 30 mA dc max 200 mA

ANSI 150 Connection Flange
316L Stainless Steel Electrode (Hastelloy and Tantalum Optional)
316L Grounding Ring
Wafer: ½" to 4": Ceramic lining 6" to 8": Teflon® PFA lining; no coating for sizes 1" to 4" sizes; all other sizes have phthalic acid resin coating

Flanged: Teflon® PFA lining; phthalic acid resin coating
Power Supply: 100 to 240 Vac, 50/60 Hz power supply (24 Vdc option)
Cable Connection Ports: A cable gland with a cap nut is provided for each port
Power Cable Requirements: Dia: 11 to 13 mm (0.43 to 0.51"), 3-wire sheathed (not included)
Cable Gland Material: Nylon 66
Port Holes in the Housing: G(PF) ½" female screw
Vibration Resistance: No resonance to the following levels of vibration:
10 to 60 Hz, amplitude 0.07 mm
60 to 150 Hz with acceleration of 9.8 m/s^2
Heat shock resistance for ceramic tube detector:
Heating: $\Delta T \leq 150°C/0.5s$
Cooling: $\Delta T \leq 100°C/0.5s$
Note: Avoid constant vibration environments

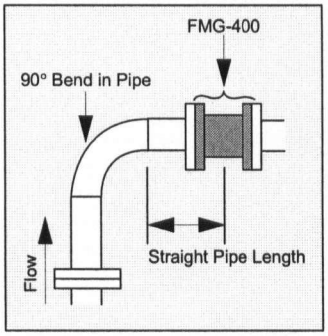

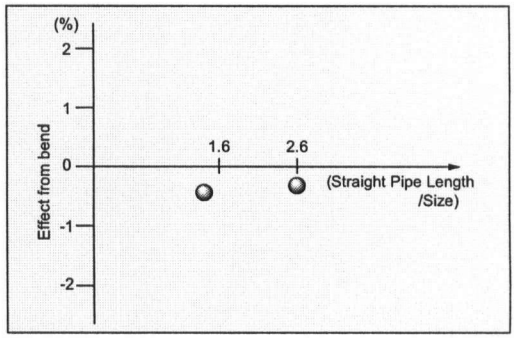

High accuracy is assured even when a magnetic flowmeter is mounted downstream of a 90-degree bend in pipe

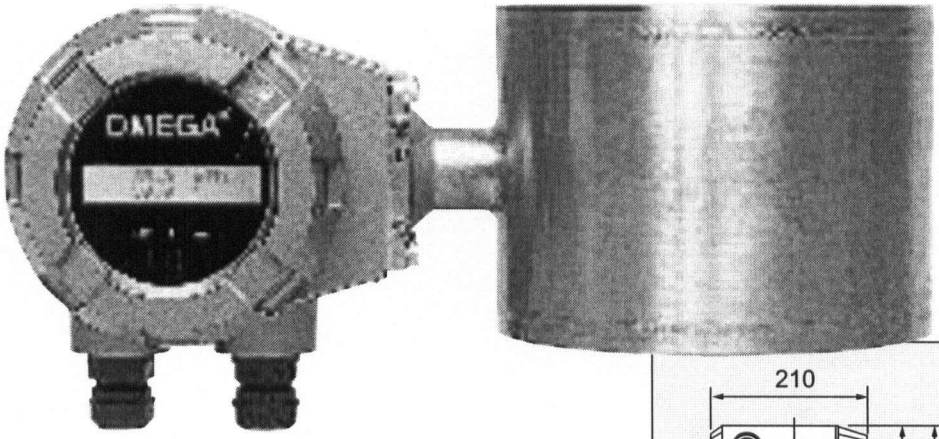

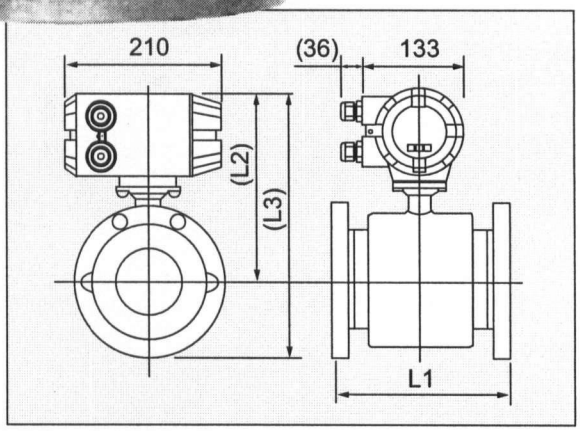

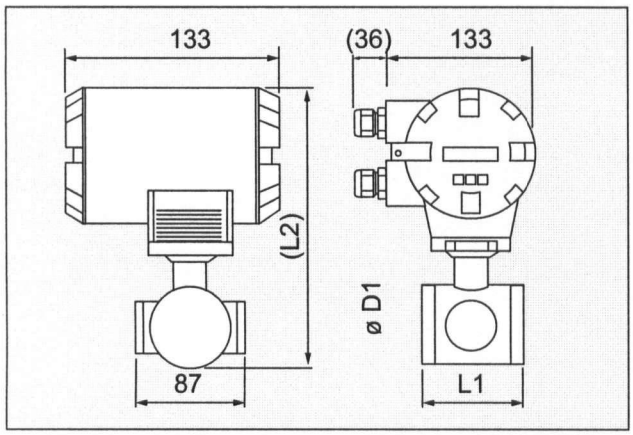

Meter Size(in)	Wafer Dimensions			Weight (lb)
	L1 (in)	L2 (in)	D1 (in)	
½	2¾	9¾	1⅞	approx. 9
1	3⅛	9¼	2⅝	approx. 11
1½	4	10¼	3⅜	approx. 13
2	4⅜	10⅞	4	approx. 16
3	4⅜	11⅞	5	approx. 18
4	4¾	13⅛	6¼	approx. 22
6	9	15⅜	8½	approx. 49
8	11¾	17⅜	10½	approx. 80

Flange Dimensions

Meter Size (in)	L1 (in)	L2 (in)	L3 (in)	No. of bolts	Weight (lb)
1½	5½	8½	9¼	4	approx. 14
1	6¼	8⅝	10	4	approx. 18
1½	6¾	8⅞	10⅝	4	approx. 25
2	7½	9¼	11¼	4	approx. 27
3	9	9¾	12⅜	4	approx. 40
4	9½	10½	13⅝	8	approx. 49
6	10¼	11¾	16⅛	8	approx. 82
8	11¾	12¾	18⅛	12	approx. 111
10	13¾	13⅝	20⅜	12	approx. 234
12	15¾	14⅝	22⅜	12	approx. 250
14	17¾	15⅜	23⅞	12	approx. 287
16	19⅝	16⅛	26⅛	16	approx. 393

To Order *(Specify Model Number)*

Model No. Wafer Style	Price	Model No. Flange Style	Price	Pipe Size	Flow Rate 0.1 m/s	0.3 m/s	1 m/s	10 m/s
FMG-401	**$2500**	**FMG-421**	**$2645**	0.5"	.28 GPM	.84 GPM	2.80 GPM	28.00 GPM
FMG-402	**2600**	**FMG-422**	**2645**	1.0"	.77 GPM	2.33 GPM	7.77 GPM	77.79 GPM
FMG-403	**2600**	**FMG-423**	**2776**	1.5"	1.99 GPM	5.97 GPM	19.91 GPM	199.13 GPM
FMG-404	**2679**	**FMG-424**	**2978**	2.0"	3.11 GPM	9.33 GPM	31.11 GPM	311.14 GPM
FMG-405	**2825**	**FMG-425**	**3219**	3.0"	7.96 GPM	23.89 GPM	79.64 GPM	796.46 GPM
FMG-406	**3145**	**FMG-426**	**3330**	4.0"	12.44 GPM	37.34 GPM	124.46 GPM	1244.66 GPM
FMG-407	**3292**	**FMG-427**	**3588**	6.0"	28.00 GPM	84.00 GPM	280.06 GPM	2800.60 GPM
FMG-408	**3767**	**FMG-428**	**4116**	8.0"	49.79 GPM	149.38 GPM	497.75 GPM	4979.54 GPM
-	-	**FMG-429**	**4937**	10.0"		233.39 GPM	777.97 GPM	7779.70 GPM
-	-	**FMG-430**	**6183**	12.0"		336.10 GPM	1120.50 GPM	11205.06 GPM
-	-	**FMG-431**	**6722**	14.0"		457.44 GPM	1525.12 GPM	15251.22 GPM
-	-	**FMG-432**	**7330**	16.0"		597.45 GPM	1991.37 GPM	19913.76 GPM

Ordering Examples: FMG-401**, wafer-style electromagnetic flowmeter for 0.5" diameter pipe, **$2500;
***FMG-432**, flange-style electromagnetic flowmeter for 16" diameter pipe, **$7330**.*

Appendix R

Specifications of Paddle Wheel Flowmeter DRG-1150N1F300

DRG PADDLE FLOW SENSOR

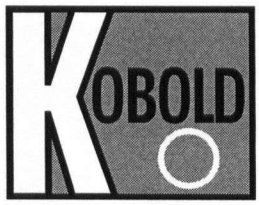

Flow
Pressure
Level
Temperature
measurement
monitoring
control

- **Economically Priced**
- **Perfect OEM Flow Sensor**
- **Five Material Combinations**
- **Flow Ranges 0.15-3 GPM to 3-37 GPM**
- **Frequency, 4-20 mA Transmitters or Compact Electronics**
- **All Plastic Versions Available**

S4

USA

KOBOLD Instruments Inc.
1801 Parkway View Drive
USA-Pittsburgh, PA 15205
☎ +1 412-788-2830
Fax +1 412-788-4890
E-mail: info@koboldusa.com

CANADA

KOBOLD Instruments Canada Inc.
9A Aviation
Pointe-Claire, QC H9R 4Z2
☎ +1 514-428-8090
Fax +1 514-428-8899
E-mail: kobold@kobold.ca

Visit KOBOLD Online at
www.kobold.com

Model:
DRG

Features

- Economically Priced
- Perfect OEM Flow Sensor
- Five Material Combinations
- Flow Ranges 0.15-3 GPM to 3-37 GPM
- Frequency, 4-20 mA Transmitters or Compact Electronics
- All Plastic Versions Available

The KOBOLD series DRG has the winning combination of compact size, low cost and versatility which makes it the perfect product for OEM flow measuring applications. The DRG series is a paddle flow sensor which uses a Hall effect sensor to detect the passing of permanent magnets imbedded in the rotating paddle. The DRG can be supplied with a frequency output, 4-20 mA output or a versatile compact electronics package providing an LED display, 4-20 mA output or programmable setpoint switches. The DRG series is offered in five material combinations. An all plastic version is available which makes the DRG series suitable for use with high purity water and many types of aggressive chemicals.

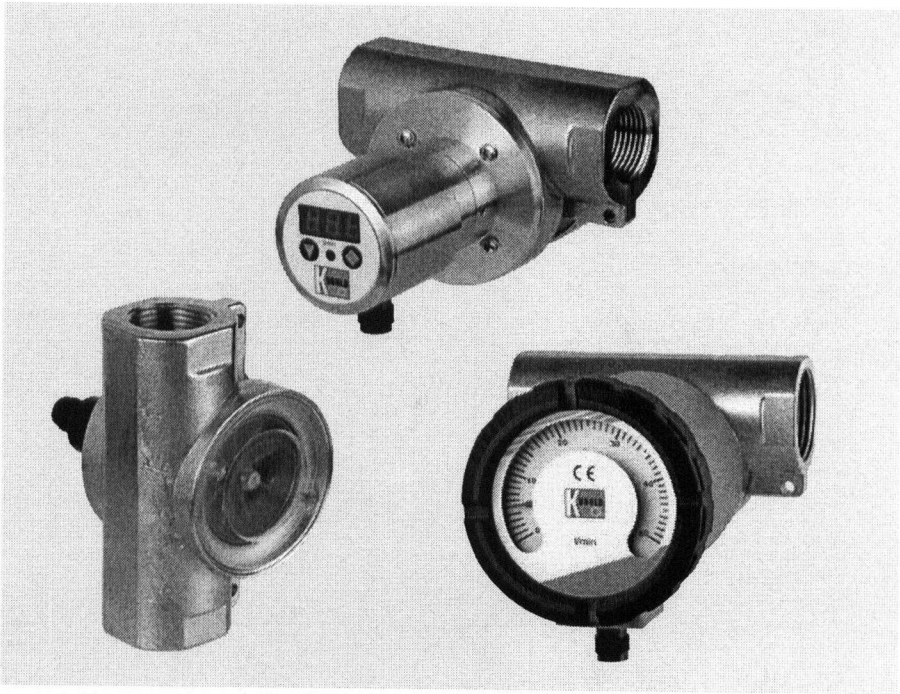

KOBOLD DRG Series Paddle Flow Sensor

Specifications

Accuracy: ±3% of full scale

Output:

- **Frequency:** PNP, 25 mA max. 14-28 VDC
- **Analog:** 4-20 mA, 2-wire or 3-wire, 24 VDC power

Elec. Protection: NEMA 4X

Elec. Connection: Micro-DC plug, 4-pin male or DIN 43650 Plug

Sensor Pressure Drop: 14.5 PSI @ 100% rated flow

Compact Electronics (optional)

Programmable Functions: Lockout code, dampening, transmitter span, switch setpoint

Output Types: 4-20 mA, 3-wire flow transmitter and PNP flow switch or 2 PNP switches depending on model code

Switch Type: Adjustable, PNP open collector, 300 mA Max. short circuit protected, programmable as a flow switch or frequency transmitter

Display: LED 3-digit

Electrical Protection: NEMA 4X

Electrical Connection: Micro-DC plug, 5-pin male

Material Combinations

	DRG-11	DRG-12	DRG-14	DRG-15	DRG-18
Housing	Bronze	Bronze	316L SS	316L SS	Polypropylene
Housing Cover	Acrylic	Bronze	Acrylic	316L SS	Polypropylene
O-ring	Buna-N	Buna-N	Viton	Viton	Buna-N
Paddle	Teflon	Teflon	Teflon	Teflon	Teflon
Axle	Ceramic	Ceramic	Ceramic	Ceramic	Ceramic
Axle Support	Teflon	Teflon	Teflon	Teflon	Teflon
Max. Temp.	176˚F	212˚F	176˚F	212˚F	176˚F
Max. Press.	230 PSIG	580 PSIG	230 PSIG	580 PSIG	230 PSIG

Subject to change without prior notice.

DRG Series Ordering Codes

Flow Range GPM Water	Material Combination & Flow Ranges					Fitting (NPT)					Output
	DRG-11...	DRG-12...	DRG-14...	DRG-15...	DRG-18...	1/8"	1/4"	1/2"	3/4"	1"	
0.15-3	...50	...50	...50	...50	...50	N1	-	-	-	-	F300= Frequency Micro-DC Plug
0.15-6.6	...55	...55	...55	...55	...55	-	N2	-	-	-	
0.3-8	...60	...60	...60	...60	...60	-	N2	N4	-	-	L342= 4-20 mA, 2-wire, Micro-DC Plug
0.6-12	...65	...65	...65	...65	...65	-	-	N4	N5	N6	L343= 4-20 mA, 3-wire,Micro-DC Plug
0.8-23	...70	...70	...70	...70	...70	-	-	N4	N5	N6	
1.5-37	...75	...75	...75	...75	...75	-	-	-	N5	N6	L442= 4-20 mA, 2-wire DIN 43650 Plug
3-37	...80	...80	...80	...80	...80	-	-	-	N5	N6	C34P= Compact Electronics, 4-20mA +1 PNP Switch
											C30R= Compact Elec. 2 PNP Switches
											Z340= Analog Indicator + 4-20mA, 3-wire

Accessories

Part Number 807.037 - Mating 4-pin Micro-DC plug with 6 ft. cable for output F300, L342, L343 & Z340
807.007 - Mating 5-pin Micro-DC plug with 6ft. cable for output C34P & C30R

Example Part Number: DRG-1150N1F300

DIMENSIONS

DRG Frequency and 4-20 mA

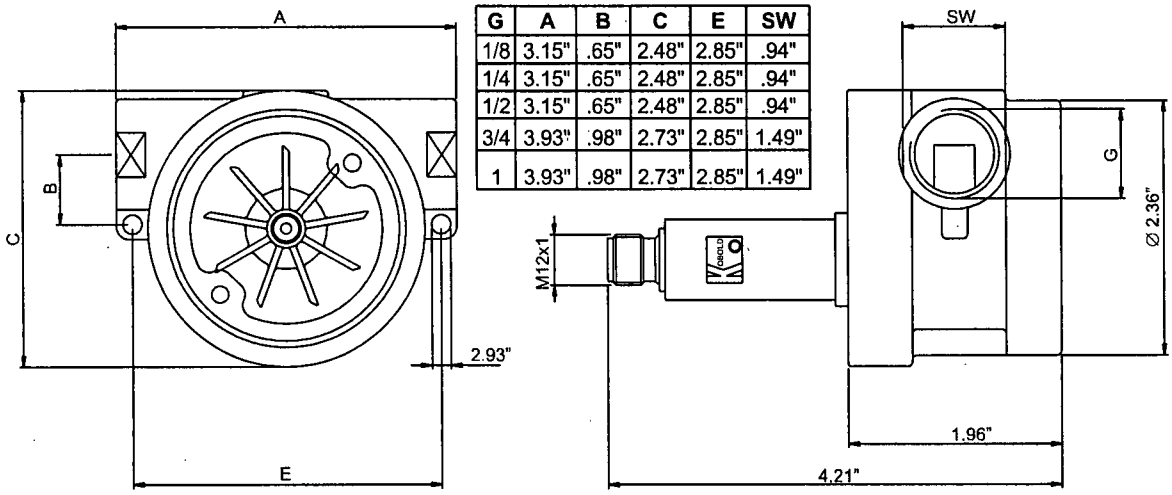

G	A	B	C	E	SW
1/8	3.15"	.65"	2.48"	2.85"	.94"
1/4	3.15"	.65"	2.48"	2.85"	.94"
1/2	3.15"	.65"	2.48"	2.85"	.94"
3/4	3.93"	.98"	2.73"	2.85"	1.49"
1	3.93"	.98"	2.73"	2.85"	1.49"

S4

DIMENSIONS

DRG w/ Compact Electronics

G	A	B	C	E	SW
1/8	3.15"	.65"	2.48"	2.85"	.94"
1/4	3.15"	.65"	2.48"	2.85"	.94"
1/2	3.15"	.65"	2.48"	2.85"	.94"
3/4	3.93"	.98"	2.73"	3.54"	1.49"
1	3.93"	.98"	2.73"	3.54"	1.49"

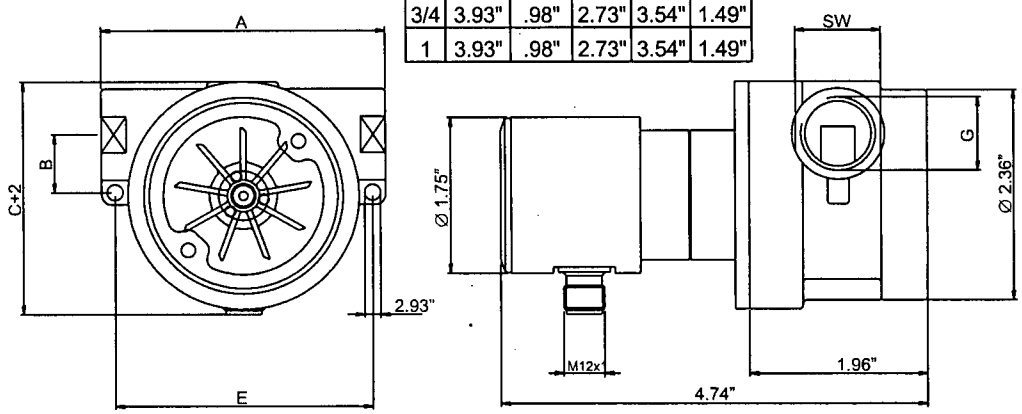

Subject to change without prior notice.

Appendix S

Specifications of Data Acquisition System

DaqBoard/2000™ Series

16-Bit, 200-kHz PCI & CompactPCI® Data Acquisition Boards

Features

- Five DaqBoard/2000 series PCI boards and the DaqBoard/2001c CompactPCI® version are available
- 16-bit, 200-kHz A/D converter
- 8 differential or 16 single-ended analog inputs (software selectable per channel)
- Expandable up to 256 analog input channels, while maintaining 200 kHz (5 ∝s per channel) scan rate
- Up to four boards can be installed into one PC for up to 1024 analog input channels
- 100% digital calibration
- 512 location channel/gain FIFO, capable of scanning all channels, including 256 analog expansion channels and digital/counter channels, at 5 ∝s per channel
- DMA bus mastering for synchronous analog I/O, digital I/O, and counter inputs
- Trigger modes include analog, digital, and software, with <5 ∝s latency
- Virtually infinite pre-trigger buffer*
- Up to four 16-bit, 100-kHz analog outputs with infinite continuous waveform output capability*
- 40 digital I/O lines, can be scanned synchronously or asynchronously with analog inputs
- Digital I/O is expandable up to 272 lines, including optional isolation and relay closure
- Four counter/pulse input channels can be scanned synchronously or asynchronously with analog inputs
- Two timer/pulse output channels

Signal Conditioning Options

- Signal conditioning and expansion options for thermocouples, strain gages, accelerometers, isolation, RTDs, etc.—over 40 options in all

Software

- Includes support for Visual Basic®, C/C++, ActiveX/COM, Linux, LabVIEW®, MATLAB®, and DASYLab®
- Optional DaqView2000™ software package

* Limited only by available PC RAM and hard disk space

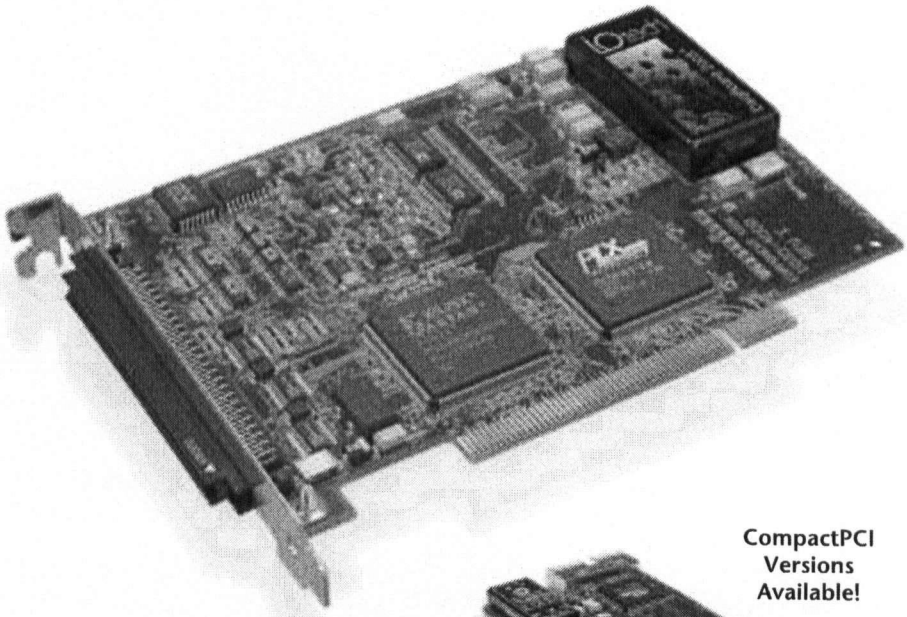

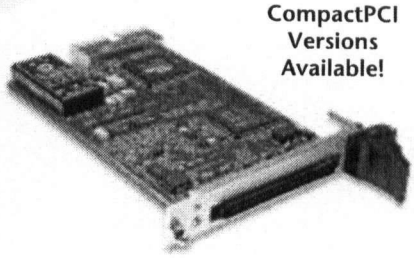

CompactPCI Versions Available!

The DaqBoard/2000 series plug-in boards provide cost-effective, high-speed data acquisition

The DaqBoard/2000™ series sets the price/performance benchmark for high-speed, multifunction plug-and-play data acquisition for PCI bus computers. The DaqBoard/2000 series hardware design offers all of the features normally found on significantly more expensive boards, including 16-bit, 200-kHz A/D, 100% digital calibration, bus mastering, two or four 16-bit, 100-kHz D/A converters, 40 digital I/O lines, four counters and two timers.

DaqBoard/2000 series is supported by a growing family of over 40 signal conditioning and expansion options, offering signal conditioning for thermocouples, RTDs, accelerometers, isolation, high-voltage, strain gages, and much more. Up to 528 channels of analog and digital I/O can be accessed using one DaqBoard/2000, while maintaining the 5 ∝s per channel update rate. Up to four DaqBoard/2000s can be installed into one PC.

Software support is the most extensive of any board, including comprehensive drivers and new ActiveX/COM-based programming tools for nearly every programming environment under Windows® 95 and higher. Included in this list are Visual Basic, C/C++, Linux, LabVIEW, MATLAB, and DASYLab. Also available is a suite of DaqView™ software options for *Out-of-the-Box*™ setup, acquisition, display, and analysis of acquired data—no programming required. DaqView2000™ combines DaqView, DaqViewXL™, and eZ-PostView™ in one software package for use with the DaqBoard/2000 series.

In total, the DaqBoard/2000 series sets the industry standard for plug-and-play PCI data acquisition.

tel: 440-439-4091 fax: 440-439-4093 sales@iotech.com www.iotech.com

DaqBoard/2000™ Series

General Information

DaqBoard/2000™ Series Selection Chart					
	Multifunction I/O			Digital I/O	Analog Output
Feature	/2001 & /2001c	/2000	/2005	/2002	/2004
Analog inputs (16 bit/200 kHz)	16	16	16	—	—
Analog outputs (16 bit/100 kHz)	4	2	—	—	4
Digital I/O	40	40	40	40	40
Freq./pulse I/O	6	6	6	6	6

Synchronous I/O for High-Speed Applications

The DaqBoard/2000 series sets a new standard with its ability to make analog measurements, read digital inputs, and read counter inputs, while synchronously generating up to four analog outputs and/or a 16-bit digital pattern output. Most other boards require CPU interaction to access I/O other than analog input, making it impossible to generate time-critical analog waveforms or digital patterns. With the DaqBoard/2000 series, the true power of today's PCI-based PCs can be unleashed.

The same synchronous features of the DaqBoard extend to its family of DBK signal conditioning and expansion options. Up to 256 analog input channels and 272 (256, P2 only) digital I/O channels can also be accessed synchronously to one another, with precise and deterministic channel-to-channel timing. Up to four DaqBoards can be installed in one PC, quadrupling the channel capacity to over 1000 analog input channels, 1000 digital I/O channels and 16 high-speed analog output channels.

Signal I/O

One 100-pin connector on the DaqBoard/2000 series provides access to all of the input and output signals. Unlike other multifunction boards that require multiple PC slots in order to access all of the I/O, careful design of the DaqBoard/2000 series accommodates all I/O using one cable, and utilizing a single PCI slot.

The 100-pin DaqBoard/2000 series I/O connector, **P4**, is logically divided into three sub-ports, P1, P2, and P3. **P1**, the analog input port, contains all of the analog input channels, as well as the sequencer control signals for accessing external analog input options. All analog expansion options attach to the P1 port. **P2**, the general purpose digital I/O port, can be used directly to control and monitor 24 digital I/O lines. P2 can also function as the digital I/O expansion port, whereby the 24 lines are exclusively used to control external digital DBK expansion options, for up to 256 lines of digital input or output. **P3** contains an additional 16-bit digital I/O port, as well as the counter inputs, timer outputs, and analog outputs. Several options are available to provide easy user access to all of the I/O signals on P4.

Analog Input (P1)

The DaqBoard/2000 series has a 16-bit, 200-kHz A/D coupled with 16 single-ended, or 8 differential analog inputs. Thirteen software programmable ranges provide inputs from ±10V to ±156 mV full scale. Each channel can be software-configured for a different range, as well as for single-ended or differential, and unipolar or bipolar input. Beyond the 16 built-in analog inputs, the user can expand the DaqBoard/2000 series up to 256 analog inputs using external DBK signal conditioning and expansion options. As with the on-board channels, expansion channels are scanned at the same 5 ∝s/channel rate (200 kHz), and most are software-programmable for range. There is *no* speed penalty for scanning expansion channels versus built-in channels. The DBK expansion options offer a wide variety of signal measurements, including thermocouples, RTDs, strain gages, accelerometers, high voltage, isolation, current, and much more.

DaqBoard/2000™ Series

General Information

DaqBoard/2000, /2001, /2001c, and /2005 Block Diagram

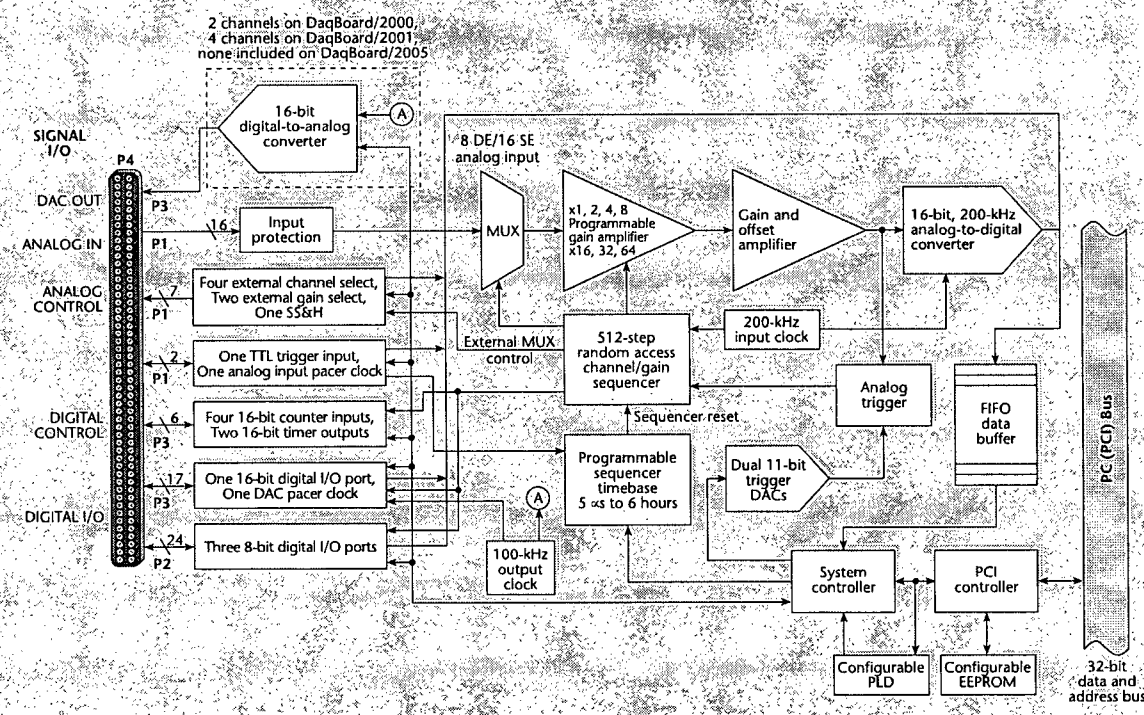

DaqBoard/2002 Block Diagram

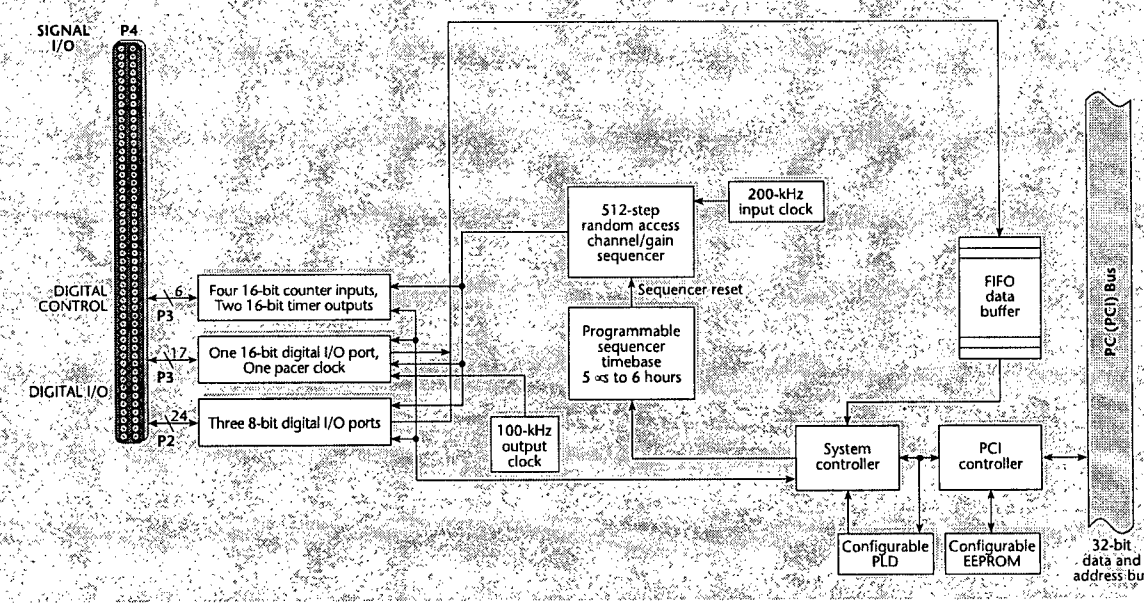

DaqBoard/2000™ Series

General Information

DaqBoard/2004 Block Diagram

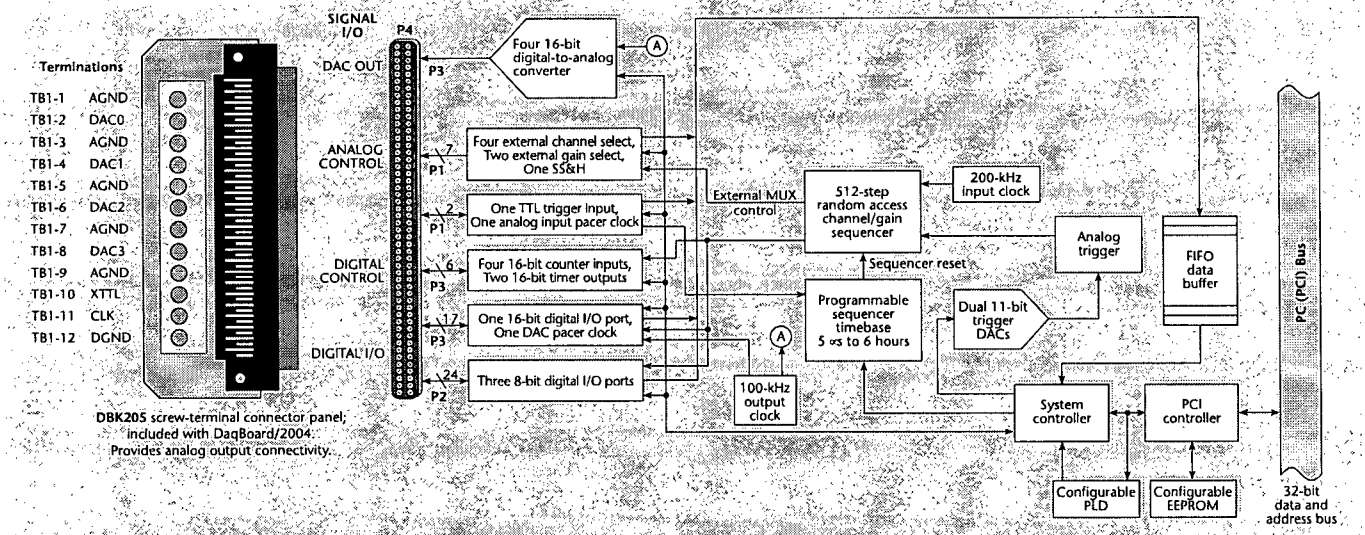

DaqBoard/2000™ Series

General Information

Scanning

The DaqBoard/2000 series has an on-board scan sequencer that permits the user to select any combination of up to 512 channel/range combinations. The sequencer scans all channels contained in the sequence at the fastest rate of 5 ∝s/channel, thereby minimizing the time-skew from channel-to-channel. The user can also set the time between scan groups, from 0 to 6 hours. In addition to scanning analog inputs, the sequencer can scan digital inputs and counter inputs.

Bus Mastering DMA

The DaqBoard/2000 series supports Bus Mastering DMA, which allows analog and digital/counter input data, as well as analog and digital output data to flow between the PC and the DaqBoard/2000 series without consuming valuable CPU time. The driver supplied with the DaqBoard/2000, as well as all other third-party software support such as MATLAB®, LabVIEW®, and DASYLab®, automatically utilize Bus Mastering DMA to efficiently conduct I/O from the PC to the DaqBoard.

Triggering

Triggering can be the most critical aspect of a data acquisition application. The DaqBoard/2000 series supports a full complement of trigger modes to accommodate any measurement situation.

Hardware Analog Triggering. Many data acquisition boards claim analog triggering, but rely on the PC to take readings and make a decision, which leads to uncertain and potentially long latencies. The DaqBoard/2000 series uses true analog triggering, whereby the trigger level programmed by the user sets an analog DAC, which is then compared in hardware to the analog input level on the selected channel. The result is analog trigger latency which is guaranteed to be less than 5 ∝s, significantly shorter than most data acquisition boards. Any analog channel can be selected as the trigger channel, including built-in or expansion channels. The user can program both the trigger level, as well as the edge (rising or falling).

Channel-Scanning Flexibility

The DaqBoard/2000 series offers a 512-location scan sequencer that allows you to select each channel and associated input amplifier gain at random. The sequencer circuitry circumvents a major limitation encountered with many plug-in data acquisition boards—a drastic reduction in the scan rate for external expansion channels. All DaqBoard/2000 series channels, including the 528 potential expansion channels, are scanned at 100K or 200 kHz (1 or 5 ∝s/channel), software programmable per channel. In addition, the digital and frequency inputs can be scanned using the same scan sequence employed for analog inputs, enabling the time correlation of acquired digital data to acquired analog data. The DaqBoard/2000 series permits each scan group, which can contain up to 512 channel/gain combinations, to be repeated immediately or at programmable intervals of up to 6 hours. Within each scan group, consecutive channels are measured at a fixed 5 ∝s/channel rate.

DaqBoard/2000 Series Scanning Example

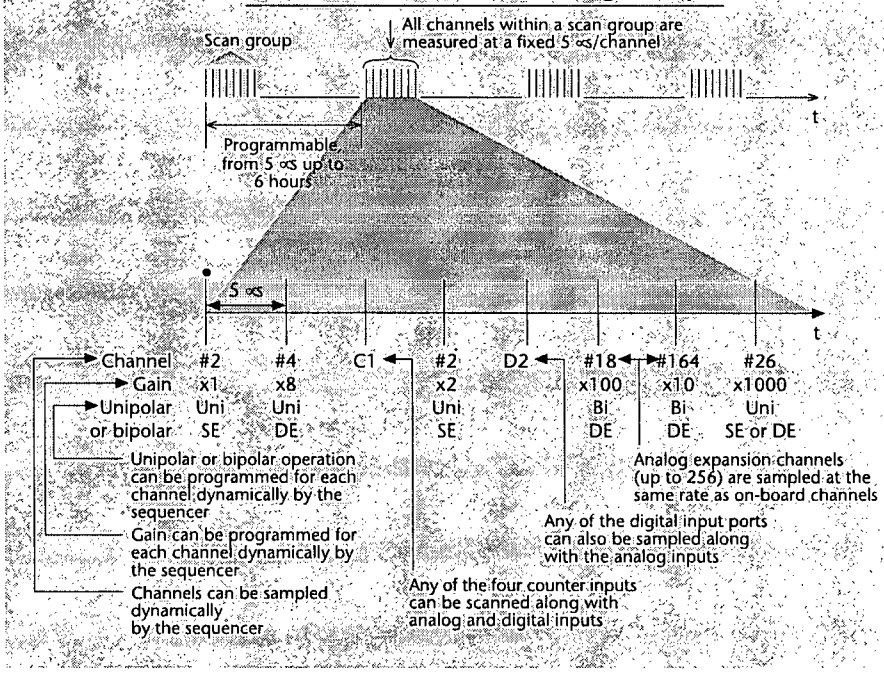

Digital and Pattern Triggering (P1). A separate digital trigger input line is provided, allowing TTL-level triggering, again with latencies guaranteed to be less than 5 ∝s. Both the logic levels (1 or 0), as well as the edge (rising or falling), can be programmed for the discrete digital trigger input.

Software-Based Triggering. Software-based triggering differs from the modes described above because the readings, analog, digital, or counter, are interrogated by the PC to detect the trigger event, not in the hardware as described above. The advantage of this mode is to permit triggering based on more complex situations, such as on a specific temperature, which was derived from the acquisition of at least two analog measurements, plus the calculation of the measured temperature using linearization algorithms.

The DaqBoard/2000 series also supports digital pattern triggering, whereby the user can designate any of the digital input ports as the trigger port. The programmed

digital pattern, including the ability to mask or ignore specific bits, is then compared to the actual input until a match is detected, after which the sequencer begins the scan sequence.

Triggering can also be programmed to occur when one of the counters reaches, exceeds, or is within a programmed level. Any of the built-in counter/totalizer channels can be programmed as a trigger source.

Normally software-based triggering results in long latencies from the time that a trigger condition is detected, until the actual capturing of data commences. However, the DaqBoard/2000 series circumvents this undesirable phenomenon by use of pre-trigger data. Specifically, when software-based triggering is employed, and the PC detects that a trigger condition has occurred, (which may be thousands of readings later than the actual occurrence of the signal), the DaqBoard driver automatically looks back to the location in memory where the actual trigger-causing measurement occurred. The acquired data that is presented to the user actually begins at the point where the trigger-causing measurement occurs. The latency in this mode is equal to one scan cycle.

Stop Trigger. Any of the software trigger modes described above can also be used to stop an acquisition. Thus an acquisition can be programmed to begin on one event, such as a temperature level, and then can stop on another event, such as a digital pattern.

Pre- and Post-Triggering Modes. Six modes of pre- and post-triggering are supported, providing a wide variety of options to accommodate any measurement requirement. When using pre-trigger, the user must use software-based triggering to initiate an acquisition.

No pre-trigger, post-trigger stop event. This, the simplest of modes, acquires data upon receipt of the trigger, and stops acquiring upon receipt of the stop-trigger event.

Fixed pre-trigger with post-trigger stop event. In this mode, the user specifies the number of pre-trigger readings to be acquired, after which, acquisition continues until a stop-trigger event occurs.

No pre-trigger, infinite post-trigger. No pre-trigger data is acquired in this mode. Instead, data is acquired beginning with the trigger event, and is terminated when the operator issues a command to halt the acquisition.

Fixed pre-trigger with infinite post-trigger. The user specifies the amount of pre-trigger data to acquire, after which the system continues to acquire data until the program issues a command to halt acquisition.

Variable pre-trigger with post-trigger stop event*. Unlike the previous pre-trigger modes, this mode does not have to satisfy the pre-trigger number of readings before recognizing the trigger event. Thus the number of pre-trigger readings acquired is variable and dependent on the time of the trigger event relative to the start. In this mode, data continues to be acquired until the stop trigger event is detected.

Variable pre-trigger with infinite post trigger*. This is similar to the mode described above, except that the acquisition is terminated upon receipt of a command from the program to halt the acquisition.

Calibration

Every range on the DaqBoard/2000 series is calibrated from the factory using a digital calibration method. This method works by storing a correction factor for each range on the DaqBoard/2000 series at the time of calibration. Whenever a particular range is selected, the appropriate calibration constant is automatically applied to a compensating DAC, thereby calibrating the specific range. The result is that readings generated by the A/D are already calibrated, and do not require additional processing.

This is significantly better than other boards, that merely adjust the readings in software after they are transferred to the PC. That method has the disadvantage of reducing the dynamic range of the A/D, and can adversely affect the speed at which the PC can obtain a calibrated reading.

The DaqBoard/2000 series also has a user-cal mode, whereby the user can adjust the calibration of the board in their system, without destroying the factory calibration supplied with the board. This is accomplished by having 2 distinct calibration tables in the DaqBoard/2000 series on-board EPROM, one which contains the factory cal, and the other which is available for user calibration.

Analog Output (P3)

DaqBoard/2000, /2001, & /2004 Only

Two or four 16-bit, 100-kHz analog output channels are built into the DaqBoard/2000 series, with an output from –10V to +10V. These outputs are entirely separate from the D/As which are used to determine analog trigger level (some data acquisition board suppliers confusingly refer to trigger D/As as if they are available to the user). Through the use of Bus Mastering DMA, each D/A output can continuously output a waveform, which can be read from PC RAM or a file on the hard disk. In addition, a program can asynchronously output a value to either of the D/As for non-waveform applications, presuming that the D/A is not already being used in the waveform output mode. Additional low-speed D/A channels can be added to the DaqBoard through the use of the DBK2 analog output option card.

When used to generate waveforms, the D/As can be clocked in several different modes. Each D/A can be separately selected to be clocked from one of the sources described below.

Asynchronous Internal Clock. The on-board programmable clock can generate updates ranging from 1.5 Hz to 100 kHz, independent of any acquisition rate.

Synchronous Internal Clock. The rate of analog output update can be synchronized to the acquisition rate derived from 100 kHz to once every 5.96 hours.

Asynchronous External Clock. A user-supplied external input clock can be used to pace the D/A, entirely independent of analog inputs.

Synchronous External Clock. A user-supplied external input clock can pace both the D/A and the analog input.

* Driver support only

DaqBoard/2000™ Series

General Information

Digital Pattern Generation (P3)

The DaqBoard/2000 series supports digital pattern generation via Bus Mastering DMA on the 16-bit high-speed digital I/O port. In the same manner as Analog Output, the digital pattern can be read from PC RAM or a file on the hard disk. Digital pattern generation is clocked in the same four modes as described above with analog output*.

Digital Inputs and Outputs (P2, P3)

Forty TTL-level digital I/O lines are included in the DaqBoard/2000 series. They are divided into three 8-bit ports (P2) and one 16-bit port (P3). The P2 ports can be programmed in 8-bit groups as either input or output. The 16-bit P3 port can be programmed as all inputs or all outputs. Ports programmed as inputs can be part of the scan group and scanned along with other analog and digital input channels, or can be asynchronously accessed via the PC at any time, including when a scanned acquisition is occurring.

In addition, the P2 ports can be expanded up to 256 digital I/O lines using external DBK digital options. These options are available as TTL-level I/O, relay output, or optically isolated input and output. Whenever expansion digital I/O is attached to the DaqBoard/2000 series, the P2 I/O lines are no longer user-programmable, and are instead used to communicate with the digital expansion options.

Counter Inputs (P3)

Four 16-bit counters are built into the DaqBoard/2000, each capable of counting up to 65,536 TTL-level transitions. Each of the four counters will accept frequency inputs up to 10 MHz, and can be configured for pulse count or totalize mode. The counters can also be cascaded, allowing over four billion counts to be accumulated. As with all other inputs to the DaqBoard/2000 series, the counter inputs can be read asynchronously under program control, or synchronously as part of an analog and digital scan group.

* When digital pattern generation is used, one of the analog output channels is limited to asynchronous output mode

DaqBoard/2000 Series Signal Conditioning & Expansion Options

Product	Description	Capacity	Page
DBK1	16-connector BNC interface module	16 connectors	116
DBK2	D/A voltage-output card	4 channels	117
DBK4	Dynamic signal-input card	2 channels	118
DBK5	Current output card	4 channels	120
DBK7	Frequency-to-voltage input card	4 channels	122
DBK8	High-voltage input card	8 channels	124
DBK9	RTD measurement card	8 channels	125
DBK10	Expansion-card enclosure module	3 cards	126
DBK11A	Screw-terminal card	40 terminals	127
DBK15	Universal current/voltage input card	16 channels	128
DBK16	Strain gage measurement card	2 channels	130
DBK17	Simultaneous sample and hold card	4 channels	132
DBK18	Low-pass filter card	4 channels	134
DBK20	Digital I/O card (screw-terminal connectors)	48 channels	136
DBK21	Digital I/O card (male DB37 connectors)	48 channels	136
DBK23	Optically isolated digital-input module	24 channels	137
DBK24	Optically isolated digital-output module	24 channels	139
DBK25	Relay output card	8 channels	141
DBK30A	Rechargeable battery/excitation module	14.4 or 28.8 VDC	142
DBK32A	Auxiliary power supply card	±15 VDC @ 500 mA	143
DBK40	BNC interface module	18 connectors	145
DBK41	Analog expansion enclosure module	10 cards	146
DBK42	5B isolated signal-conditioning module	16 channels	148
DBK43A	Strain gage module	8 channels	150
DBK44	5B isolated signal conditioning card	2 channels	152
DBK45	SS&H card with low-pass filter	4 channels	154
DBK50	Isolated high-voltage input module	8 channels	156
DBK51	Isolated low-voltage input module	8 channels	156
DBK55	Frequency-to-voltage input module	8 channels	158
DBK60	3-slot expansion module w/customizable panels	3 cards	160
DBK65	Transducer interface module	8 channels	162
DBK70	Vehicle network interface module	16 channels	164
DBK80	Differential voltage input card with excitation output	16 channels	169
DBK81	TC/mV card with screw-terminal connections	7 channels	170
DBK82	TC/mV card with screw-terminal connections	14 channels	170
DBK83	TC/mV card with external screw-terminal Pod and 3 ft. cable	14 channels	170
DBK84	TC/mV module with mini TC connector jacks	14 channels	170
DBK85	Differential voltage input module	16 channels	172
DBK200	Adapter board for analog inputs	P1	199
DBK201	Panel-mount adapter board with three (DBK) expansion ports	P1, P2, P3	199
DBK202	Screw-terminal adapter board, solder locations for user-supplied resistors and R/C networks, with three expansion ports	120 terminals, P1, P2, P3	200
DBK203	Same as DBK202 adapter board with a rugged metal enclosure	120 terminals, P1, P2, P3	200
DBK206	Adapter board with removable screw-terminals with three expansion ports	120 terminals, P1, P2, P3	177
DBK207	5B-isolated analog input signal conditioning board with two expansion ports	P1 (2)	178
DBK207/CJC	Same as DBK207 plus on-board, cold-junction compensation; two expansion ports	P1 (2)	178
DBK208	Opto-22® signal conditioning board for isolated (solid-state-relay) digital I/O, with two P2 digital I/O expansion ports	P2 (2)	180
DBK209	Same as DBK201 but rack and DIN-rail mountable with optional kits	P1, P2, P3	199
DBK210	Isolated high-density digital I/O board	32 channels	182

Timer Outputs (P3)

Two 16-bit timer outputs are built into the DaqBoard/2000, each capable of generating different square waves with a programmable frequency range from 16 Hz to 1 MHz.

Multiple DaqBoards per PC

All of the features described for the DaqBoard/2000 can be replicated with up to four DaqBoard/2000s (PCI and cPCI) installed in the same PC. The serial number on each DaqBoard/2000 is used to differentiate one from another, and a user-selected name can be assigned to each board for easy program documentation. Thus, with four boards installed along with DBK expansion options, over 1,000 analog input channels and over 1,000 digital I/O channels could be accessed from one PC. When multiple boards are installed, all boards can be operated synchronously.

DaqBoard/2000™ Series

Expansion Options

The DaqBoard/2000 series provides all I/O signals on one 100-pin connector. The following adapter options make it easy for the user to attach signals and expansion options.

DBK200™ Adapter Board

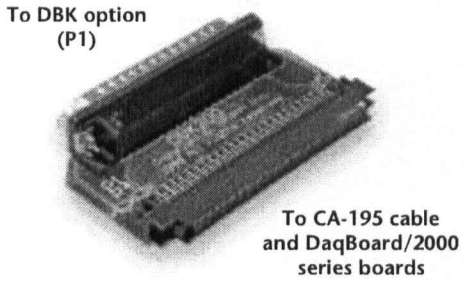

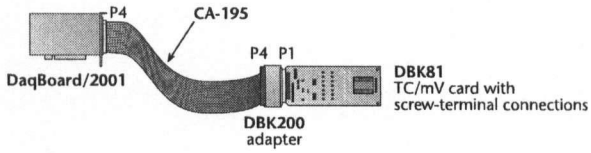

The DBK200 adapter mates directly with analog DBK signal conditioning options

Suitable exclusively for analog-signal expansion, the DBK200 adapter board contains one 100-pin connector which connects to the DaqBoard/2000 series via the CA-195 cable, and one female DB37 connector that mates directly with the P1 port of any of the DBK analog signal conditioning and expansion options. This is the most convenient way to add analog expansion options if access to the DaqBoard/2000 series digital I/O or frequency signals is not required. Access to P1 analog signals is also possible via included female-mating solder-lug connectors or optional CA-37-x* or CA-37-xT* expansion cables.

DBK201™ & DBK209™ Adapter Boards

For both analog and digital expansion, the DBK201 adapter board mates with the DaqBoard/2000 series via a 3-ft. CA-195 cable. The DBK209 provides three male DB37 connectors, divided into P1 analog input, P2 digital I/O, and P3 analog output and counter/timer I/O. Each port on the DBK201 connects to DBK expansion options via an optional CA-37-x* or CA-37-xT* expansion cable. Alternatively, users can solder wires to the included DB37 female-mating solder-lug connectors, or custom make their own cables that are terminated with a female DB37. An optional 6 ft. cable is available that contains a mating female DB37 connector at one end, and is unterminated at the other end (CA-113). The DBK209 is identical in function to the DBK201 but is snap-track (DIN-rail), and rack-mountable with optional mounting kits.

DBK201

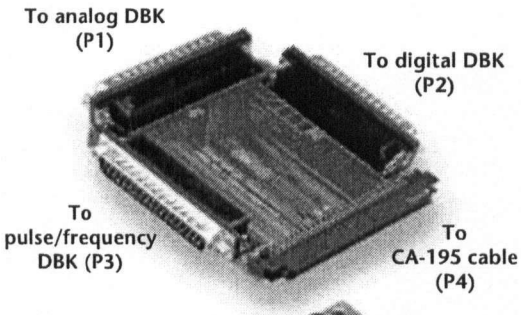

DBK209

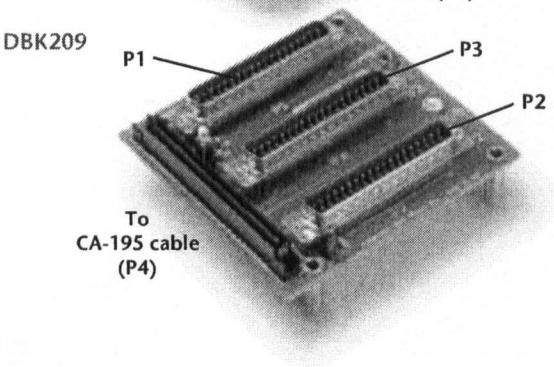

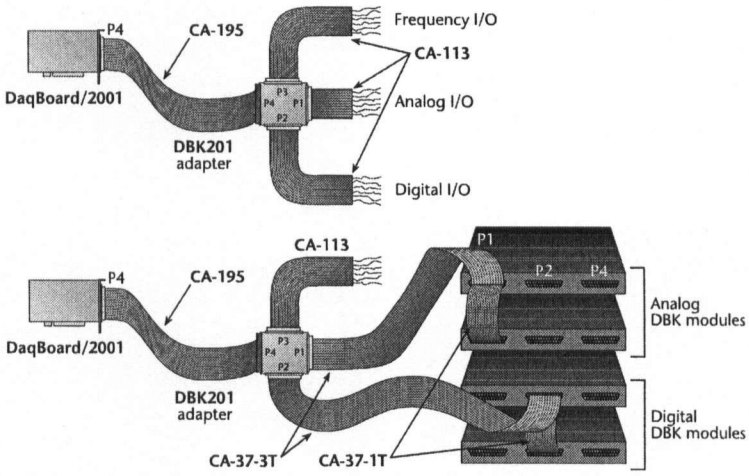

The DBK201 adapter with analog and digital DBK signal conditioning and expansion modules

* The "x" in the cable part numbers should be replaced by the number of expansion products to be connected

DaqBoard/2000™ Series

Expansion Options

DBK202™ Screw-Terminal Adapter Board

The DBK202 screw-terminal board provides convenient screw-terminal access to all signals from the DaqBoard/2000 series. Divided into three ports (P1, P2, and P3), the DBK202 also provides another way to access signals. There are male DB37 connectors on P1 and P2, and an adapter cable (CA-60) can be used to connect to the P3 header for connection to DBK signal conditioning and expansion options. Mounting holes in the DBK202 permit it to be easily screw-mounted into a user-provided enclosure.

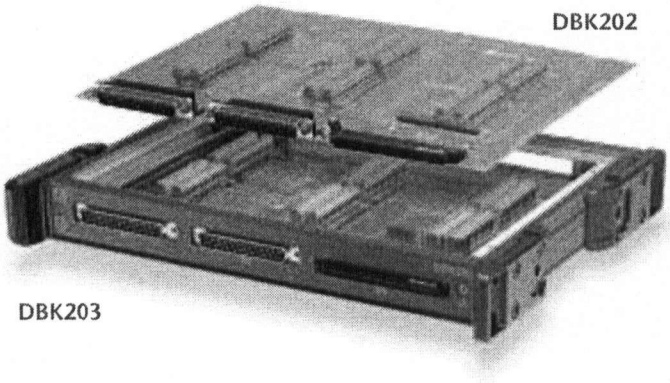

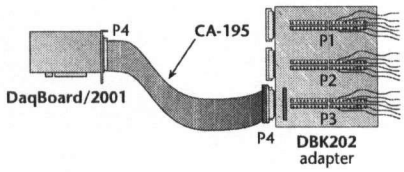

The DBK202 adapter with screw-terminal connectors

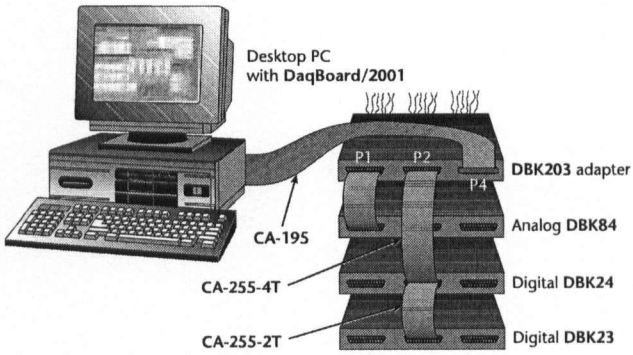

The DBK203 adapter with screw-terminal connectors

DBK203™ Screw-Terminal Adapter Module

The DBK203 is identical to the DBK202, except that it is housed in a shielded metal enclosure, which easily mounts to other DBK signal conditioning and expansion modules.

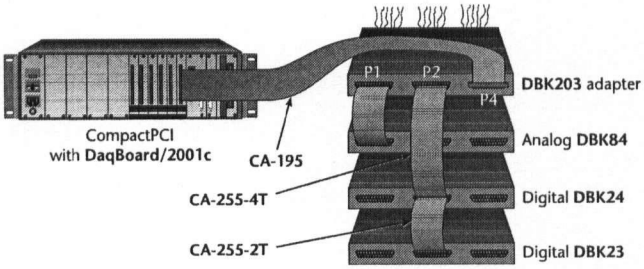

The DBK203 adapter with screw-terminal connectors

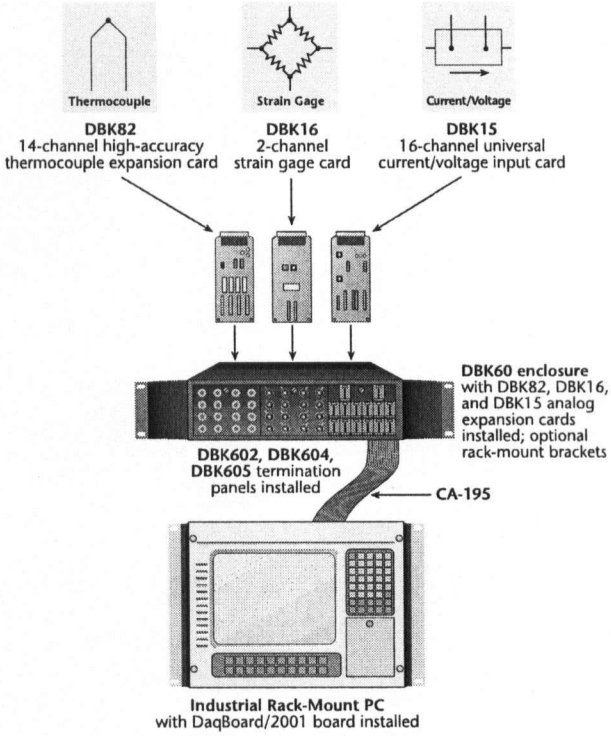

The DBK60 ruggedized rack-mount enclosure with optional signal conditioning and termination panels

DaqBoard/2000™ Series

Expansion Options

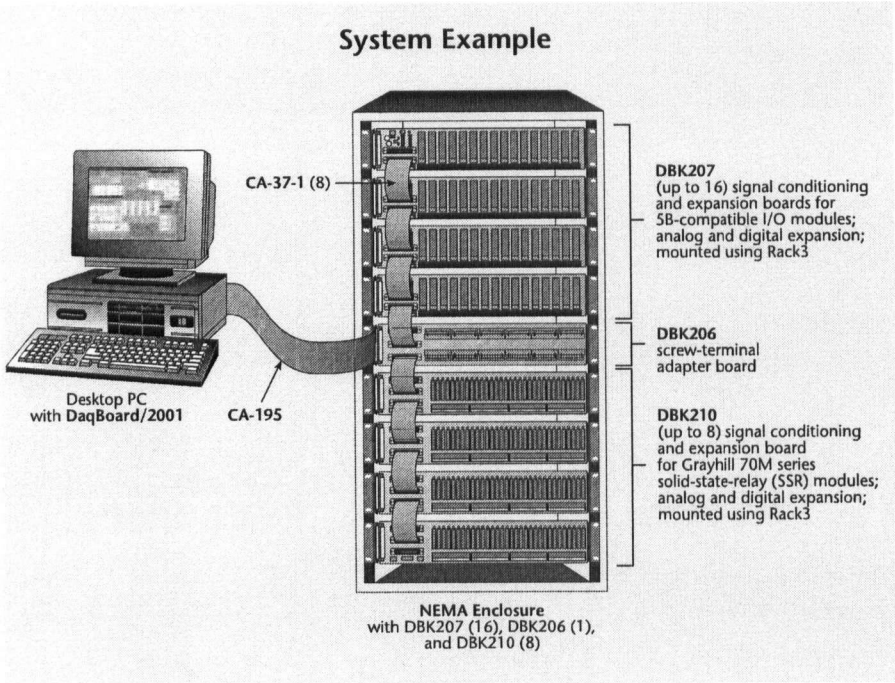

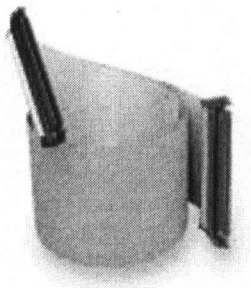

The CA-195 100-pin conductor cable connects the DaqBoard/2000 series boards with the DBK200 series adapters

DaqBoard/2000 Series Expansion Options for Rack-Mount Systems

The DaqBoard/2000 series can be expanded up to 100s of analog and digital channels in a rack-mount system, with only *one* cable back to the DaqBoard. This is possible because of the unique capability built into the DaqBoard/2000 series and the DBK200™ series options. Specifically, the DBK206™, DBK207™, DBK208™, and DBK210™ have on-board multiplexing and daisy chain capability, which means that only one DBK board within the rack system is connected to the DaqBoard, and all other DBK boards are daisy-chained together (see diagram).

In the example system described here, one CA-195 connects the DBK206 screw-terminal board to the PC, while up to 16 DBK207 analog input boards are daisy chained to the DBK206, and 8 DBK210 boards are daisy chained to the DBK206. The total I/O in such a system is 256 analog input channels (via DBK207), 256 digital I/O channels (via DBK210), plus 4 frequency inputs, 2 timer outputs, 4 analog outputs and 16 TTL digital I/O via the DBK206. All analog, digital and frequency channels can be scanned at 5 ∝sec/channel (in the case of digital I/O, 16 channels per 5 ∝sec is possible).

For applications with higher channel requirements, up to 4 DaqBoards can be installed into one PC, for a total channel capacity that is 4x a single DaqBoard system.

DaqBoard/2000™ Series

Expansion Options

DBK206™ Screw-Terminal Adapter

Similar in function to the DBK202, but designed for mounting in 19-inch enclosures, the DBK206 features three vertically mounted straight male DB37 connectors for analog and digital channel expansion (P1 analog I/O, P2 digital I/O, and P3 digital and counter-timer, and analog output).

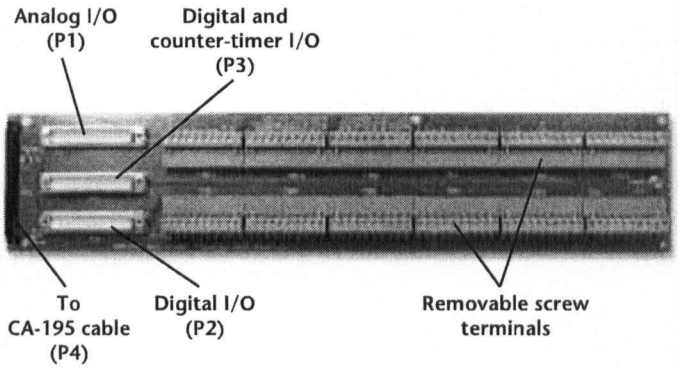

DBK207™ & DBK207/CJC™ Multiplexing Isolated Analog Input

The DBK207 provides sockets for 16 channels of isolated analog input when populated with industry standard 5B-style or compatible signal conditioning modules (sold separately).

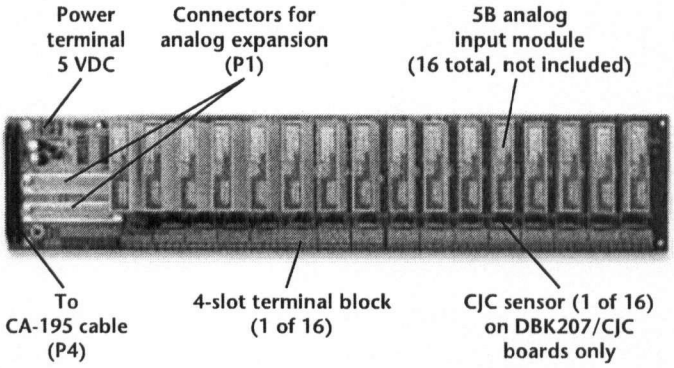

DBK208™ Multiplexing Isolated Digital I/O

The DBK208 provides sockets for 16 channels of isolated digital I/O when populated with industry standard Opto-22®-style or compatible solid-state-relay modules (sold separately).

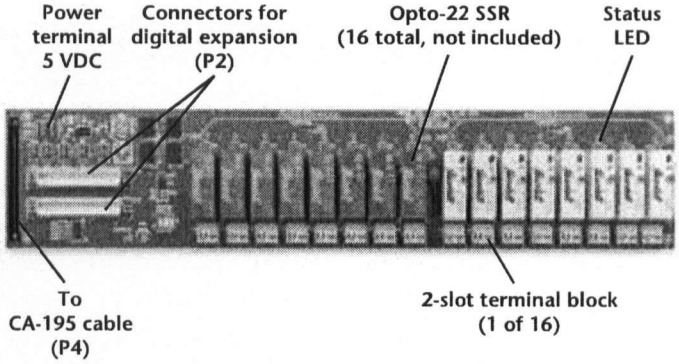

DBK210™ Multiplexing Isolated High-Density Digital I/O

The DBK210 offers similar functionality as the DBK208 but with twice the channel capacity per board. The DBK210 is the same size physically as the DBK208 but by using the Grayhill 70M series solid state relay modules (sold separately), provides space for 32 isolated digital I/O. These modules feature a narrower footprint allowing for high-density channel capacity.

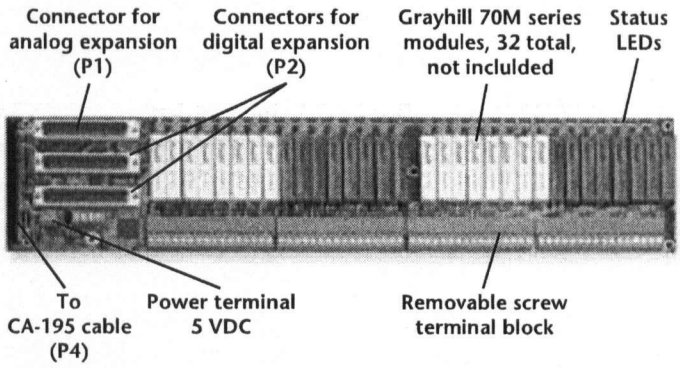

Rack3™ Rack-Mount Kit

Rack-mount kit for the DBK206, DBK207, DBK207/CJC, DBK208, DBK209, and DBK210 signal termination and expansion boards.

DIN1™ & DIN2™ DIN-Rail Kit

Snap-track (DIN-rail) mounting kit for the DBK206, DBK207, DBK207/CJC, DBK208, and DBK210 signal termination and expansion boards. Specify DIN2 for DBK209 only.

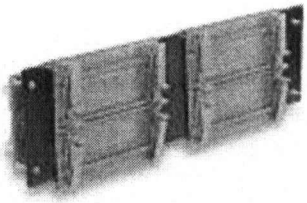

Software Support

Included Software for DaqBoard/1000™ & DaqBoard/2000™ Series

The DaqBoard/1000™ and DaqBoard/2000™ series are supported by several levels of software support, allowing you to select the software environment that best fits your application and skill set. The next page is an overview of optional software available for the DaqBoard/1000 and DaqBoard/2000 series.

DaqX API Libraries

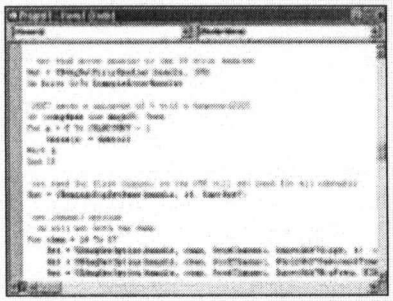

DaqBoards are supplied with free DaqX Subroutine API Libraries providing complete support for all of the functionality available on each data acquisition device in Visual Basic®, and C/C++. Further, DaqX is supported under all versions of Windows®. Included with DaqX Subroutine API Libraries are over 100 example programs, and online comprehensive API documentation.

LabVIEW® Support

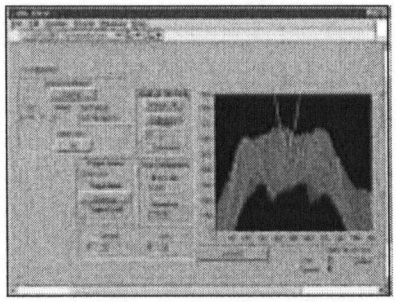

IOtech offers extensive LabVIEW® support for the DaqBoard series, including expansion and signal conditioning modules. IOtech data acquisition VIs for LabVIEW are more than just simple hardware access VIs, they are full blown examples complete with engineering data conversion, data display and logging capabilities.

DaqCOM™ ActiveX/COM

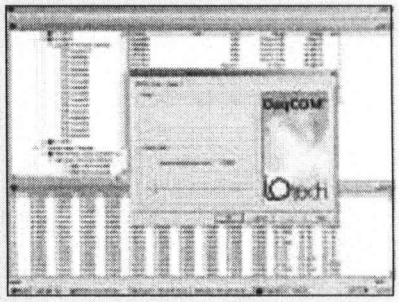

DaqCOM™ programming tools allow applications developers to rapidly develop and deploy custom systems by leveraging COM (Component Object Model) technology. DaqCOM provides an easy-to-use interface for most programming languages including, Visual Basic®, VBA, C++, and J++. DaqCOM support for Windows.NET is accomplished by utiltizing the COM interoperability layer included with VisualStudio.NET.

Linux Support

Linux drivers are included with each DaqBoard series board. These drivers provide an effective and robust alternative for non-Windows® based data acquisition applications. Designed for use with version 2.4 and 2.4x releases of the Linux kernel (Debian Gnu/Linux2.4, RedHat Linux 7.x, and SuSE 7.x) or greater. The IOtech Linux driver addresses the need for an economical "open source" development platform.

IOtech's DaqX-library for Linux is functionally equivalent to the DaqX driver for Windows. This allows for easy migration from Windows to Linux or from the Linux environment to Windows based applications with a minimum of effort. Extensive example applications are included.

MATLAB® Support

MATLAB® drivers are included with each DaqBoard series board. Drivers provide synchronous analog, digital, and counter input as well as asynchronous digital and analog output capabilities. Contact factory for availability.

MATLAB tools can be used to communicate with the DaqBoard series and allow measured data to be streamed live. The data collected using the test and measurement tools can be brought directly into the MATLAB workspace for fast and accurate data analysis, data manipulation, and pre- and post-processing. Analysis on collected data is easy to perform with MATLAB, the Data Acquisition Toolboxes and their built-in analysis functions.

Software Support

Optional Software for DaqBoard/1000™ & DaqBoard/2000™ Series

DaqView2000™ & eZ-PostView™

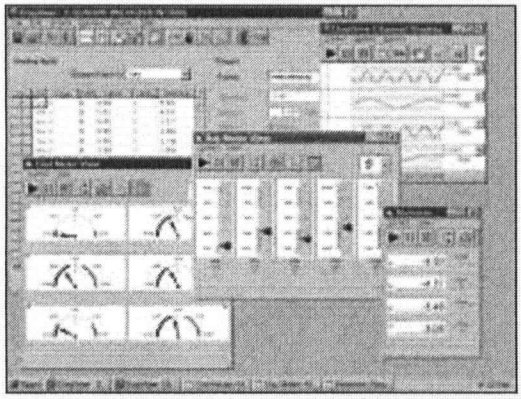

DaqView2000™ graphical data acquisition and display software is available for all DaqBoard series systems. Using DaqView software's spreadsheet-style interface, you can easily set up your application and begin taking data within minutes of connecting your hardware, with no programming required. Included with DaqView2000 is eZ-PostView, a post-acquisition data viewer application, which makes it simple to visually inspect acquired waveforms from multiple channels within seconds of acquiring the data.

eZ-TimeView™ & eZ-FrequencyView™

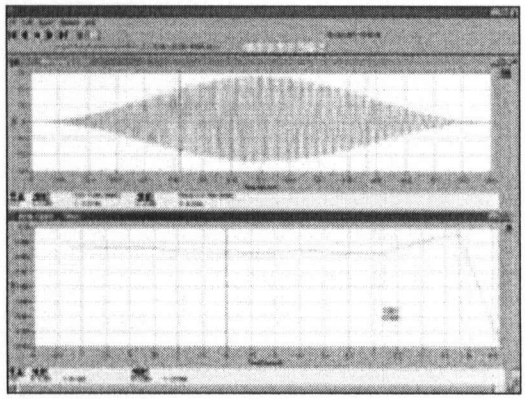

eZ-TimeView™ and eZ-FrequencyView™ are post-acquisition analysis packages for data acquired from the DaqBoard series. eZ-TimeView is targeted at time-domain analysis, including min/max, peak-peak, mean, RMS, plus a wide variety of plotting and waveform viewing capabilities. eZ-FrequencyView is targeted at post-acquisition frequency-domain analysis, including FFT's, octave analysis, plus dozens of other analysis features.

DASYLab® (DaqBoard/2000 series only)

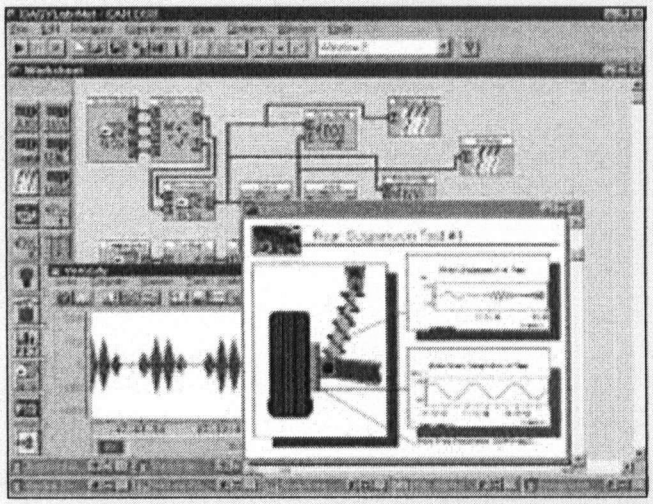

If your application requirements go beyond the scope of DaqView™, DASYLab® software offers a greater degree of flexibility and customization. You can learn DASYLab in a matter of days, without the weeks of training required for some other icon-based application-development software.

DaqBoard/2000™ Series

Specifications

Specifications

General (all boards)

Power Consumption (per board): 3.5W (up to 10W with external accessories)
Power Available for External Signal Conditioning and Expansion Options: 5V at 1A (all boards); ±15V at 75 mA each (except for /2002)
Operating Temperature: 0° to +60°C
Vibration: MIL STD 810E
Signal I/O Connector: 100-pin high-density edge-type carries all analog and digital I/O signals
Dimensions: 165 mm W x 15 mm D x 108 mm H (6.5" x 0.6" x 4.2")

Analog Inputs (/2000, /2001, & /2005)

Channels: 16 single-ended or 8 differential, programmable on a per-channel basis as single-ended or differential and unipolar or bipolar
Expansion: Up to 256 channels per board (4 boards per PC), without degradation in maximum channel-to-channel scan rate (5 ∝s/channel)
Bandwidth: 500 kHz
Settling Time: 5 ∝s to 1 LSB for full-scale step
Maximum Input Voltage: ±11V relative to analog common
Over-Voltage Protection: ±35V
Ranges: Software or sequencer selectable on a per-channel basis
Input Impedance: 10M Ohm single-ended, 20M Ohm differential

Voltage Range*	Accuracy** One Year, 0-35°C (% reading+% range) Absolute
0 to +10V	0.015 + 0.005
0 to +5V	0.015 + 0.005
0 to +2.5V	0.015 + 0.005
0 to +1.25V	0.015 + 0.008
0 to +0.625V	0.015 + 0.008
0 to +0.3125V	0.015 + 0.008
-10 to +10V	0.015 + 0.005
-5 to +5V	0.015 + 0.005
-2.5 to +2.5V	0.015 + 0.005
-1.25 to +1.25V	0.015 + 0.005
-0.625 to +0.625V	0.015 + 0.008
-0.3125 to +0.3125V	0.015 + 0.008
-0.156 to +0.156V	0.02 + 0.008

* Specifications assume differential input single channel scan, 200-kHz scan rate, unfiltered
** Accuracy specification is exclusive of noise

A/D Specifications (/2000, /2001, & /2005)

Type: Successive approximation
Resolution: 16 bit
Conversion Time: 5 ∝s
Maximum Sample Rate: 200 kHz
Nonlinearity (Integral): ±1 LSB
Nonlinearity (Differential): No missing codes

Input Sequencer (/2000, /2001, /2002, /2004, & /2005)

Analog, digital and counter inputs can be scanned synchronously, based on either an internal programmable timer, or an external clock source. Analog and digital outputs can be synchronized to either of these clocks.
Scan Clock Sources: 2
1. Internal, programmable from 5 ∝s to 5.96 hours in 1 ∝s steps
2. External, TTL level input up to 200 kHz max

Programmable Parameters per Scan: Channel (random order), gain, unipolar/bipolar
Depth: 512 location
On-Board Channel-to-Channel Scan Rate: 5 or 10 ∝s per channel, programmable
Expansion Channel Scan Rate: 5 or 10 ∝s per channel, programmable

External Acquisition Scan Clock Input (/2000, /2001, & /2005)

Maximum Rate: 200 kHz
Clock Signal Range: 0V to +5V
Minimum Pulse Width: 50 ns high, 50 ns low

Triggering

Trigger Sources: 6, individually selectable for starting and stopping an acquisition. Stop acquisition can occur on a different trigger source other than start acquisition, and can be triggered via modes 2, 4, 5, or 6. Pre-trigger is supported with fixed or variable pre-trigger periods.
1. Single-Channel Analog Hardware Trigger
   Latency: 5 ∝s max (/2000, /2001, & /2005)
2. Single-Channel Analog Software Trigger
   Latency: One scan period max (/2000, /2001, & /2005)
3. Single-Channel Digital Trigger
   Latency: 5 ∝s max (/2000, /2001, /2002, /2004, & /2005)
4. Digital Pattern Triggering
   Latency: One scan period max (/2000, /2001, /2002, /2004, & /2005)
5. Counter/Totalizer Triggering (/2000, /2001, /2002, /2004, & /2005)
   Latency: One scan period, max (all boards)
6. Software Triggering (all boards)
   Trigger can be initiated under program control.

Analog Outputs (/2000, /2001, & /2004)

The two or four analog output channels are updated synchronously relative to scanned inputs, and clocked from either an internal onboard clock, or an external clock source. Analog outputs can be updated asynchronously, independent of any other scanning in the system. Bus Mastering DMA provides CPU and system-independent data transfers, ensuring accurate outputs independent of other system activities. Streaming from disk or memory is supported, allowing continuous, nearly-infinite length, waveform outputs (limited only by available PC system resources).
Channels: 2 (/2000); 4 (/2001, & /2004)
Resolution: 16 bits
Output Voltage Range: ±10V
Clock Sources: 4, programmable
1. Onboard D/A clock, independent of scanning input clock
2. Onboard scanning input clock (/2000, /2001, & /2004 only)
3. External D/A input clock, independent of external scanning input clock
4. External scanning input clock (/2000, /2001, & /2004 only)

Digital I/O (/2000, /2001, /2002, /2004, & /2005)

Channels: 40, expandable up to 208 with DBK options
Input Scanning Modes: 2, programmable
1. Asynchronous, under program control at anytime
2. Synchronous with input scanning

Ports: 3 x 8-bit (82C55 emulation), and 1 x 16-bit. Each port is software programmable as input or output
Input Characteristics: 100 Ohm series, 20 pF to common
I/O Levels: TTL
Sampling/Update Rate: 200 kHz max
Output Characteristics: Output 12 mA per pin, 200 mA total continuous (per bank of 40 outputs)

Pattern Generation Output (/2000, /2001, /2002, /2004, & /2005)

The P3 16-bit digital I/O port can be configured for 16-bit pattern generation. The pattern can be updated synchronously with an acquisition.

Counter (/2000, /2001, /2002, /2004, & /2005)

Counter inputs can be scanned synchronously along with analog and digital scanned inputs, based either on internal programmable timer, or an external clock source. Counter can also be read asynchronously.
Channels: 4 x 16-bit; cascadable as 2 x 32-bit
Frequency Measurement Rate: 10 MHz max
Trigger Level: TTL

Frequency/Pulse Generators (/2000, /2001, /2002, /2004, & /2005)

Channels: 2 x 16-bit
Output: 1-MHz base rate divided by 1 to 65,535 (programmable)

DaqBoard/2000™ Series

Ordering Information

Ordering Information

Description	Part No.
16-bit, 200-kHz data acquisition board for PCI-bus PCs with 16 analog inputs, two 16-bit, 100-kHz analog outputs, 40 digital I/O, four 16-bit counter-timers, and two 16-bit frequency/pulse generators; includes DaqX API library, drivers for Visual Basic®, and C++ for Windows® 95 and higher; C++ for Linux, DASYLab®, MATLAB®, & LabVIEW®; plus DaqCOM™	DaqBoard/2000
Same as DaqBoard/2000 but with four 16-bit, 100-kHz analog outputs	DaqBoard/2001
CompactPCI version of /2001	DaqBoard/2001c
Same as DaqBoard/2001 but with no analog I/O	DaqBoard/2002
Same as DaqBoard/2001 but with no analog inputs	DaqBoard/2004
Same as DaqBoard/2001 but with no analog outputs	DaqBoard/2005
DaqBoard/2000, DaqView2000 software, DBK202, and CA-195	DAQ2000/STR-KIT

Accessories

Description	Part No.
Adapter board, directly connects DBK signal conditioning and expansion options (P1, analog only) to a CA-195 or CA-209 expansion cable	DBK200
Adapter board, connects all DBK signal conditioning and expansion options to a CA-195 or CA-209 expansion cable	DBK201
Adapter board with screw terminals, also connects DBK signal conditioning and expansion options to a CA-195 or CA-209 expansion cable	DBK202
Same as DBK202 but housed in a shielded metal enclosure	DBK203
Termination and expansion board with removable screw terminals for access to all DaqBoard/2000 series I/O with direct connection for DBK signal conditioning and expansion options (P1, P2, and P3 for analog and digital I/O) via CA-37-1 cable(s); connects to DaqBoard/2000 series P4 connector via a CA-195 or CA-209 cable	DBK206
Termination and (P1) expansion board with fixed screw terminals and sockets for up to 16 multiplexed 5B-compatible isolated analog input modules; connects to DaqBoard/2000 series (P4) connector via a CA-195 or CA-209 cable and to LogBook or DaqBook series devices (P1) connector via CA-37-1	DBK207
Same as DBK207 but with on board, cold-junction compensation and two (P1) expansion ports	DBK207/CJC
Termination and expansion board with fixed screw terminals (12 to 26 AWG wire), sockets for up to sixteen Opto-22®-compatible isolated solid-state-relay (SSR) digital I/O modules, and status LEDs per channel; connects to DaqBoard/2000 series P4 connector via a CA-195 or CA-209 cable	DBK208
Same as DBK201 but rack and DIN-rail mountable with optional kits	DBK209
32-channel isolated high-density digital I/O board	DBK210
Rack-mount kit for DBK206, DBK207, DBK207/CJC, DBK208, DBK209, and DBK210 signal termination and expansion boards	Rack3
DIN-rail adapter kit for DBK206, DBK207, DBK207/CJC, DBK208, and DBK210 signal termination and expansion boards	DIN1
DIN-rail adapter kit for DBK209 signal termination and expansion board	DIN2
Optional hardcopy manual set (3); includes programmer's manual, DaqBoard/2000 and DaqBoard/2000c series user's manual, DBK option cards and modules user's manual	1033-0900

Cables

Description	Part No.
Expansion-card cable for connecting DBK series expansion options; specify number of option cards (x) to be connected	CA-37-x
Ribbon cable with female DB37 connector, provides convenient wiring to P1, P2, and P3 ports without requiring soldering to DB37 connectors, 6 ft.	CA-113
100-conductor expansion cable, mates with the DaqBoard/2000 series boards and the DBK200, DBK201, DBK202, DBK203, DBK206, DBK207, DBK207/CJC, DBK208, DBK209, and DBK210; 3 ft. expansion cable	CA-195
6 ft. expansion cable	CA-195-6
Same as CA-195 with CE compliance; 3 ft.	CA-209
Molded expansion cable from DaqBook to DBK modules; 2 in.	CA-255-2T
Molded expansion cable from DaqBook to DBK modules; 4 in.	CA-255-4T

Software

Description	Part No.
DaqView™ for setup, data acquisition, display, and analysis; DaqViewXL™ for seamless execution within Microsoft® Excel's tool palette, and eZ-PostView™ for post-acquisition viewing and analysis	DaqView2000
Icon-based data acquisition, graphics, control, and analysis software	DASYLab
Post-acquisition time-domain analysis software for data acquired from the DaqBoard/2000	eZ-TimeView
Post-acquisition fequency-domain analysis software for data acquired from the DaqBoard/2000	eZ-FrequencyView

For complete information on accessories and cables, visit **www.iotech.com/acc**

Related Products

Expansion Hardware
DBK1 p. 116
DBK2 p. 117
DBK4 p. 118
DBK5 p. 121
DBK7 p. 122
DBK8 p. 124
DBK9 p. 125
DBK10 p. 126
DBK11A p. 127
DBK15 p. 128
DBK16 p. 130
DBK17 p. 132
DBK18 p. 134
DBK20 p. 136
DBK21 p. 136
DBK23 p. 137
DBK24 p. 139
DBK25 p. 141
DBK30A p. 142
DBK32A p. 143
DBK40 p. 145
DBK41 p. 146
DBK42 p. 148
DBK43A p. 150
DBK44 p. 152
DBK45 p. 154
DBK50 p. 156
DBK51 p. 156
DBK55 p. 158
DBK60 p. 161
DBK65 p. 162
DBK70 p. 164
DBK80 p. 169
DBK81 p. 170
DBK82 p. 170
DBK83 p. 170
DBK84 p. 170
DBK85 p. 170
DBK200 p. 199
DBK201 p. 199
DBK202 p. 200
DBK203 p. 200
DBK206 p. 177
DBK207 p. 178
DBK207/CJC p. 178
DBK208 p. 180
DBK209 p. 199
DBK210 p. 182

Software
Linux Support p. 203
DaqView p. 217
DaqViewXL p. 221
DaqCOM p. 232
DASYLab p. 234

Appendix T

Rheology of a 0.3% Xanthan NF-C Solution

Shear Stress (Pa)	Shear Rate (Trial 1) (1/s)	Shear Rate (Trial 2) (1/s)	Shear Rate (Trial 3) (1/s)	Standard Deviation of Shear Rate Measurements
0.0102	0.0852	0.0844	0.0853	0.00051
0.0106	0.0639	0.0641	0.0644	0.00028
0.0111	0.0652	0.0651	0.0647	0.00030
0.0116	0.0603	0.0602	0.0598	0.00030
0.0121	0.0627	0.0634	0.0637	0.00051
0.0126	0.0657	0.0648	0.0658	0.00053
0.0131	0.0594	0.0602	0.0587	0.00075
0.0137	0.0611	0.0618	0.0605	0.00063
0.0142	0.0638	0.0644	0.0634	0.00051
0.0148	0.0596	0.0599	0.0601	0.00030
0.0155	0.0569	0.0571	0.0561	0.00055
0.0161	0.0633	0.0630	0.0630	0.00017
0.0168	0.0682	0.0676	0.0687	0.00055
0.0175	0.0711	0.0711	0.0710	0.00010
0.0182	0.0674	0.0682	0.0672	0.00053
0.0190	0.0721	0.0721	0.0722	0.00004
0.0198	0.0725	0.0719	0.0719	0.00032
0.0207	0.0758	0.0767	0.0752	0.00075
0.0215	0.0785	0.0794	0.0789	0.00048
0.0224	0.0840	0.0831	0.0831	0.00055
0.0234	0.0886	0.0884	0.0892	0.00044
0.0244	0.0852	0.0860	0.0852	0.00043
0.0254	0.0937	0.0931	0.0947	0.00078
0.0265	0.0923	0.0913	0.0930	0.00086
0.0276	0.1058	0.1049	0.1054	0.00046
0.0288	0.1023	0.1023	0.1026	0.00020
0.0300	0.1147	0.1141	0.1137	0.00050
0.0313	0.1155	0.1149	0.1152	0.00029
0.0326	0.1186	0.1186	0.1183	0.00020

0.0339	0.1264	0.1261	0.1267	0.00028
0.0354	0.1296	0.1289	0.1292	0.00032
0.0369	0.1381	0.1387	0.1388	0.00037
0.0384	0.1396	0.1397	0.1403	0.00035
0.0401	0.1516	0.1511	0.1517	0.00031
0.0418	0.1511	0.1505	0.1516	0.00054
0.0435	0.1702	0.1710	0.1697	0.00069
0.0454	0.1706	0.1716	0.1699	0.00083
0.0473	0.1764	0.1755	0.1757	0.00047
0.0493	0.1826	0.1827	0.1831	0.00023
0.0514	0.1943	0.1945	0.1946	0.00015
0.0535	0.1997	0.2006	0.2004	0.00051
0.0558	0.2118	0.2127	0.2114	0.00067
0.0582	0.2251	0.2242	0.2250	0.00049
0.0606	0.2450	0.2450	0.2440	0.00054
0.0632	0.2619	0.2609	0.2614	0.00047
0.0659	0.2755	0.2754	0.2764	0.00054
0.0686	0.2947	0.2939	0.2957	0.00091
0.0715	0.3144	0.3148	0.3148	0.00026
0.0746	0.3385	0.3392	0.3376	0.00080
0.0777	0.3590	0.3583	0.3588	0.00036
0.0811	0.3853	0.3854	0.3851	0.00017
0.0844	0.4126	0.4119	0.4130	0.00056
0.0880	0.4432	0.4427	0.4441	0.00073
0.0917	0.4748	0.4755	0.4744	0.00056
0.0957	0.5216	0.5221	0.5213	0.00042
0.0997	0.5612	0.5619	0.5603	0.00082
0.1039	0.6036	0.6029	0.6038	0.00049
0.1084	0.6584	0.6587	0.6574	0.00065
0.1129	0.7174	0.7178	0.7172	0.00029
0.1176	0.7845	0.7845	0.7837	0.00044
0.1227	0.8615	0.8609	0.8619	0.00049
0.1279	0.9289	0.9286	0.9289	0.00019
0.1333	1.0002	0.9992	1.0006	0.00072
0.1389	1.0751	1.0751	1.0745	0.00032

0.1448	1.1576	1.1568	1.1584	0.00084
0.1509	1.2569	1.2568	1.2576	0.00043
0.1573	1.3633	1.3636	1.3632	0.00021
0.1640	1.4458	1.4459	1.4455	0.00020
0.1709	1.5405	1.5408	1.5414	0.00045
0.1781	1.6557	1.6564	1.6558	0.00040
0.1857	1.7871	1.7875	1.7877	0.00030
0.1935	1.8957	1.8951	1.8955	0.00031
0.2017	2.0076	2.0080	2.0073	0.00032
0.2102	2.1281	2.1287	2.1277	0.00048
0.2191	2.2352	2.2355	2.2343	0.00063
0.2284	2.3143	2.3142	2.3151	0.00048
0.2380	2.3551	2.3561	2.3560	0.00054
0.2481	2.3527	2.3520	2.3518	0.00046
0.2586	2.3455	2.3464	2.3460	0.00043
0.2695	2.3319	2.3324	2.3310	0.00067
0.2809	2.3367	2.3369	2.3357	0.00064
0.2928	2.4002	2.4001	2.4010	0.00050
0.3052	2.5478	2.5485	2.5480	0.00036
0.3181	2.7731	2.7729	2.7735	0.00032
0.3315	3.0816	3.0811	3.0826	0.00076
0.3455	3.3956	3.3952	3.3952	0.00025
0.3601	3.6935	3.6927	3.6933	0.00041
0.3754	3.9851	3.9844	3.9844	0.00038
0.3912	4.2983	4.2980	4.2974	0.00044
0.4078	4.5907	4.5913	4.5913	0.00035
0.4250	4.7991	4.7995	4.7983	0.00061
0.4430	4.8116	4.8119	4.8117	0.00016
0.4617	4.7410	4.7416	4.7419	0.00044
0.4818	4.8133	4.8127	4.8133	0.00034
0.5016	5.2218	5.2211	5.2227	0.00083
0.5228	5.8480	5.8484	5.8472	0.00058
0.5449	6.4174	6.4180	6.4171	0.00049
0.5680	6.9707	6.9701	6.9706	0.00034
0.5920	7.4070	7.4072	7.4075	0.00026

0.6177	7.4259	7.4258	7.4260	0.00009
0.6431	7.3989	7.3980	7.3997	0.00087
0.6703	8.0746	8.0748	8.0737	0.00059
0.6994	9.0334	9.0334	9.0328	0.00034
0.7282	9.8427	9.8423	9.8436	0.00069
0.7590	10.2240	10.2231	10.2237	0.00043
0.7919	10.1940	10.1932	10.1936	0.00041
0.8245	11.1520	11.1522	11.1522	0.00012
0.8594	12.3680	12.3678	12.3688	0.00056
0.8966	13.0550	13.0554	13.0550	0.00022
0.9336	13.2010	13.2013	13.2015	0.00028
0.9730	14.5920	14.5913	14.5929	0.00084
1.0152	15.8750	15.8753	15.8746	0.00034
1.0582	16.1830	16.1828	16.1829	0.00011
1.1018	17.7390	17.7391	17.7398	0.00043
1.1496	18.9140	18.9145	18.9138	0.00034
1.1982	19.9300	19.9304	19.9307	0.00034
1.2475	21.7250	21.7259	21.7256	0.00047
1.3016	22.7450	22.7451	22.7442	0.00053
1.3567	24.7530	24.7525	24.7522	0.00042
1.4126	26.0930	26.0930	26.0930	0.00004
1.4738	28.1350	28.1342	28.1342	0.00047
1.5361	30.2830	30.2822	30.2831	0.00047
1.5994	32.1200	32.1196	32.1205	0.00047
1.6688	34.5810	34.5813	34.5805	0.00040
1.7376	37.1680	37.1674	37.1674	0.00037
1.8129	39.9490	39.9486	39.9489	0.00022
1.8896	42.8630	42.8635	42.8627	0.00036
1.9694	46.0210	46.0217	46.0200	0.00083
2.0527	49.4530	49.4533	49.4530	0.00020
2.1395	53.1760	53.1755	53.1758	0.00025
2.2300	56.5650	56.5642	56.5650	0.00045
2.3243	61.5920	61.5916	61.5923	0.00033
2.4226	66.2720	66.2713	66.2720	0.00037
2.5250	71.3860	71.3861	71.3859	0.00011

2.6318	76.9080	76.9088	76.9079	0.00049
2.7430	82.8970	82.8979	82.8977	0.00049
2.8590	89.3830	89.3839	89.3826	0.00069
2.9799	96.4450	96.4460	96.4443	0.00086
3.1059	104.0800	104.0795	104.0792	0.00040
3.2373	112.3300	112.3299	112.3299	0.00007
3.3741	121.2300	121.2294	121.2291	0.00047
3.5168	130.8400	130.8409	130.8395	0.00069
3.6655	141.2100	141.2091	141.2091	0.00051
3.8204	152.4100	152.4106	152.4106	0.00034
3.9861	164.8300	164.8303	164.8299	0.00022
4.1504	177.5500	177.5495	177.5492	0.00042
4.3259	191.5800	191.5794	191.5807	0.00066
4.5135	207.1300	207.1299	207.1305	0.00033
4.6995	223.0400	223.0402	223.0396	0.00033
4.8982	240.5500	240.5509	240.5496	0.00065
5.3982	287.0850	287.0846	287.0853	0.00033
5.8982	333.4787	333.4791	333.4791	0.00022
6.3982	382.6739	382.6736	382.6745	0.00044
6.8982	430.7600	430.7599	430.7608	0.00050
7.3982	484.8736	484.8728	484.8728	0.00044
7.8982	541.5759	541.5766	541.5756	0.00053
8.3982	590.3240	590.3244	590.3231	0.00069
8.8982	650.9747	650.9756	650.9755	0.00050
9.3982	714.0278	714.0284	714.0271	0.00063
9.8982	765.9720	765.9710	765.9713	0.00051
10.3982	832.5413	832.5423	832.5419	0.00048
10.8982	901.3606	901.3614	901.3615	0.00052
11.3982	955.7613	955.7605	955.7612	0.00048
11.8982	1027.7324	1027.7321	1027.7334	0.00066
12.3982	1101.8248	1101.8256	1101.8239	0.00086
12.8982	1158.0597	1158.0597	1158.0606	0.00055
13.3982	1234.9902	1234.9901	1234.9906	0.00024
13.8982	1313.9308	1313.9316	1313.9314	0.00042
14.3982	1371.4687	1371.4696	1371.4682	0.00071

14.8982	1452.9729	1452.9732	1452.9723	0.00044
15.3982	1536.3899	1536.3903	1536.3898	0.00027
15.8982	1621.7002	1621.7004	1621.7005	0.00017
16.3982	1708.8853	1708.8860	1708.8855	0.00036
16.8982	1797.9272	1797.9274	1797.9265	0.00044
17.3982	1888.8089	1888.8099	1888.8088	0.00060
17.8982	1981.5138	1981.5146	1981.5148	0.00050
18.3982	2076.0261	2076.0263	2076.0261	0.00010
18.8982	2172.3304	2172.3314	2172.3313	0.00055
19.3982	2270.4120	2270.4128	2270.4129	0.00050
19.8982	2370.2565	2370.2571	2370.2561	0.00049
20.3982	2471.8502	2471.8503	2471.8496	0.00038
20.8982	2575.1797	2575.1791	2575.1790	0.00037
21.3982	2680.2321	2680.2329	2680.2312	0.00084
21.8982	2786.9948	2786.9939	2786.9953	0.00071
22.3982	2895.4556	2895.4561	2895.4555	0.00033
22.8982	3005.6028	3005.6037	3005.6033	0.00046
23.3982	3117.4249	3117.4251	3117.4243	0.00043
23.8982	3230.9108	3230.9105	3230.9113	0.00043
24.3982	3346.0496	3346.0494	3346.0501	0.00039
24.8982	3462.8308	3462.8303	3462.8305	0.00023
25.3982	3581.2441	3581.2445	3581.2431	0.00070
25.8982	3701.2796	3701.2792	3701.2793	0.00021
			Mean of Standard Deviation:	0.00045

Table T.1: Rheological data table of a 0.3% Xanthan NF-C solution. $T = 22^{o}C$.

Appendix U

Model Utility Test for Set 1 Experiments

Null hypothesis (H_0): $\beta_1 = 0$

Test statistic value: $t = \dfrac{\hat{\beta}_1}{S_{\hat{\beta}_1}}$

Alternative Hypothesis (H_a): $\beta_1 \neq 0$ Rejection Region: $t \geq t_{\alpha/2,\, n\text{-}2}$ or $t \leq -t_{\alpha/2,\, n\text{-}2}$

	x	y	x^2	xy	y^2
Sum	47.56	49.82	114.8722	120.3242	126.3808
Mean	2.378	2.491	5.74361	6.01621	6.31904

x = predicted R_i (mm), and y = experimental R_i (mm)

Number of sample, n	20	$\hat{\beta}_0$	0.00885
Significance level (α)	0.01	S	0.13861
S_{xx}	1.77452	$S_{\hat{\beta}_1}$	0.10405
S_{xy}	1.85224	t	10.0316
$\hat{\beta}_1$	1.0438	$t_{\alpha/2,\, n\text{-}2}$	2.87844

$$S_{xy} = \sum x_i y_i - (\sum x_i)(\sum y_i)/n \qquad S_{xx} = \sum x_i^2 - (\sum x_i)^2/n$$

$$\hat{\beta}_1 = \frac{S_{xy}}{S_{xx}} \qquad \hat{\beta}_0 = \bar{y} - \hat{\beta}_1 \bar{x}$$

$$S^2 = \frac{\Sigma y_i^2 - \hat{\beta}_0 \Sigma y_i - \hat{\beta}_1 \Sigma x_i y_i}{n-2} \qquad S_{\hat{\beta}_1} = \frac{S}{\sqrt{S_{xx}}}$$

$t \geq t_{\alpha/2,\, n\text{-}2}$ therefore H_0 is rejected. The test suggests the following relation:

$$\textit{Measured } R_i = 1.04 \cdot \textit{Predicted } R_i + 0.0089$$

Appendix V

Model Utility Test for Set 2 Experiments

Null hypothesis (H_0): $\beta_1 = 0$

Test statistic value: $t = \dfrac{\hat{\beta}_1}{S_{\hat{\beta}_1}}$

Alternative Hypothesis (H_a): $\beta_1 \neq 0$ Rejection Region: $t \geq t_{\alpha/2,\, n\text{-}2}$ or $t \leq -t_{\alpha/2,\, n\text{-}2}$

	x	y	x^2	xy	y^2
Sum	57.57	56.69	187.9227	184.3124	181.1117
Mean	3.19833	3.149444	10.44015	10.23958	10.06176

x = predicted R_i (mm), and y = experimental R_i (mm)

Number of sample, n	18	$\hat{\beta}_0$	0.62183
Significance level (α)	0.01	S	0.11172
S_{xx}	3.79465	$S_{\hat{\beta}_1}$	0.05735
S_{xy}	2.99888	t	13.7799
$\hat{\beta}_1$	0.79029	$t_{\alpha/2,\, n\text{-}2}$	2.92079

$$S_{xy} = \sum x_i y_i - (\sum x_i)(\sum y_i)/n \qquad S_{xx} = \sum x_i^2 - (\sum x_i)^2/n$$

$$\hat{\beta}_1 = \frac{S_{xy}}{S_{xx}} \qquad \hat{\beta}_0 = \bar{y} - \hat{\beta}_1 \bar{x}$$

$$S^2 = \frac{\Sigma y_i^{\,2} - \hat{\beta}_0 \Sigma y_i - \hat{\beta}_1 \Sigma x_i y_i}{n-2} \qquad S_{\hat{\beta}_1} = \frac{S}{\sqrt{S_{xx}}}$$

$t \geq t_{\alpha/2,\, n\text{-}2}$ therefore H_0 is rejected. The test suggests the following relation:

$$\textit{Measured } R_i = 0.79 \cdot \textit{Predicted } R_i + 0.62$$

Appendix W

Model Utility Test for Set 3 Experiments

Null hypothesis (H_0): $\beta_1 = 0$

Test statistic value: $t = \dfrac{\hat{\beta}_1}{S_{\hat{\beta}_1}}$

Alternative Hypothesis (H_a): $\beta_1 \neq 0$ Rejection Region: $t \geq t_{\alpha/2,\, n-2}$ or $t \leq -t_{\alpha/2,\, n-2}$

	x	y	x^2	xy	y^2
Sum	96.89	101.28	238.4063	248.2681	259.0352
Mean	2.42225	2.532	5.960158	6.206703	6.47588

x = predicted R_i (mm), and y = experimental R_i (mm)

Number of sample, n	40	$\hat{\beta}_0$	0.6131
Significance level (α)	0.01	S	0.08321
S_{xx}	3.7145	$S_{\hat{\beta}_1}$	0.04317
S_{xy}	2.94262	t	18.3491
$\hat{\beta}_1$	0.7922	$t_{\alpha/2,\, n-2}$	2.71157

$$S_{xy} = \sum x_i y_i - (\sum x_i)(\sum y_i)/n \qquad S_{xx} = \sum x_i^2 - (\sum x_i)^2/n$$

$$\hat{\beta}_1 = \frac{S_{xy}}{S_{xx}} \qquad \hat{\beta}_0 = \bar{y} - \hat{\beta}_1 \bar{x}$$

$$S^2 = \frac{\Sigma y_i^{\,2} - \hat{\beta}_0 \Sigma y_i - \hat{\beta}_1 \Sigma x_i y_i}{n-2} \qquad S_{\hat{\beta}_1} = \frac{S}{\sqrt{S_{xx}}}$$

$t \geq t_{\alpha/2,\, n-2}$ therefore H_0 is rejected. The test suggests the following relation:

$$\textit{Measured } R_i = 0.79 \cdot \textit{Predicted } R_i + 0.61$$

Appendix X

Model Utility Test for Set 4 Experiments

Null hypothesis (H_0): $\beta_1 = 0$

Test statistic value: $t = \dfrac{\hat{\beta}_1}{S_{\hat{\beta}_1}}$

Alternative Hypothesis (H_a): $\beta_1 \neq 0$ Rejection Region: $t \geq t_{\alpha/2,\, n\text{-}2}$ or $t \leq -t_{\alpha/2,\, n\text{-}2}$

	x	y	x^2	xy	y^2
Sum	27.14	27.15	82.094	82.1621	82.6735
Mean	3.01556	3.016667	9.121556	9.129122	9.185944

x = predicted R_i (mm), and y = experimental R_i (mm)

Number of sample, n	9	$\hat{\beta}_0$	-0.4533
Significance level (α)	0.01	S	0.25002
S_{xx}	0.25182	$S_{\hat{\beta}_1}$	0.49823
S_{xy}	0.28977	t	2.30954
$\hat{\beta}_1$	1.15068	$t_{\alpha/2,\, n\text{-}2}$	3.49948

$$S_{xy} = \sum x_i y_i - (\sum x_i)(\sum y_i)/n \qquad S_{xx} = \sum x_i^2 - (\sum x_i)^2/n$$

$$\hat{\beta}_1 = \frac{S_{xy}}{S_{xx}} \qquad \hat{\beta}_0 = \bar{y} - \hat{\beta}_1 \bar{x}$$

$$S^2 = \frac{\Sigma y_i^{\,2} - \hat{\beta}_0 \Sigma y_i - \hat{\beta}_1 \Sigma x_i y_i}{n-2} \qquad S_{\hat{\beta}_1} = \frac{S}{\sqrt{S_{xx}}}$$

$t \leq t_{\alpha/2,\, n\text{-}2}$ therefore H_0 is not rejected however, this could be due to the small number of sample data. The test suggests the following relation:

$$\textit{Measured } R_i = 1.15 \cdot \textit{Predicted } R_i - 0.45$$